Dynamik, Stabilitäts- und Bifurkationsanalyse von Rotorsystemen mit Luftlagern: Numerische Untersuchung und Optimierung

Dynamics, stability and bifurcation analysis of rotor systems with air bearings: Numerical investigation and optimization

Zur Erlangung des akademischen Grades Doktor-Ingenieur (Dr.-Ing.)
Genehmigte Dissertation von Pascal Zeise aus Frankfurt am Main
Tag der Einreichung: 22. April 2024, Tag der Prüfung: 19. Juni 2024

1. Gutachten: Prof. Dr.-Ing. Bernhard Schweizer
2. Gutachten: Prof. Dr. Peter Hagedorn
Darmstadt, Technische Universität Darmstadt

TECHNISCHE UNIVERSITÄT DARMSTADT

Fachbereich Maschinenbau
Institut für Angewandte Dynamik

Dynamik, Stabilitäts- und Bifurkationsanalyse von Rotorsystemen mit Luftlagern: Numerische Untersuchung und Optimierung
Dynamics, stability and bifurcation analysis of rotor systems with air bearings: Numerical investigation and optimization

Genehmigte Dissertation von Pascal Zeise

Tag der Einreichung: 22. April 2024
Tag der Prüfung: 19. Juni 2024

Darmstadt, Technische Universität Darmstadt

Erklärungen laut Promotionsordnung

§ 8 Abs. 1 lit. c PromO

Ich versichere hiermit, dass die elektronische Version meiner Dissertation mit der schriftlichen Version übereinstimmt.

§ 8 Abs. 1 lit. d PromO

Ich versichere hiermit, dass zu einem vorherigen Zeitpunkt noch keine Promotion versucht wurde. In diesem Fall sind nähere Angaben über Zeitpunkt, Hochschule, Dissertationsthema und Ergebnis dieses Versuchs mitzuteilen.

§ 9 Abs. 1 PromO

Ich versichere hiermit, dass die vorliegende Dissertation – abgesehen von den in ihr ausdrücklich genannten Hilfen – selbstständig verfasst wurde und dass die „Grundsätze zur Sicherung guter wissenschaftlicher Praxis an der Technischen Universität Darmstadt“ und die „Leitlinien zum Umgang mit digitalen Forschungsdaten an der TU Darmstadt“ in den jeweils aktuellen Versionen bei der Verfassung der Dissertation beachtet wurden.

§ 9 Abs. 2 PromO

Die Arbeit hat bisher noch nicht zu Prüfungszwecken gedient.

Darmstadt, 22. April 2024

Pascal Zeise

Kurzfassung

Luftlager eignen sich zur Lagerung schnell drehender Rotorsysteme in Umgebungen mit höchsten Reinheitsanforderungen, z. B. in Brennstoffzellen. Weit verbreitet sind Luftlager mit starrem Gehäuse, die aufgrund der geringen Dämpfungseigenschaften von Luft unterhalb der Stabilitätsgrenze betrieben werden müssen. Auch Folienluftlager mit einer zusätzlich dämpfenden Folienstruktur zwischen dem Luftfilm und dem Gehäuse kommen zum Einsatz. Aufgrund der starken Kopplung der Struktur mit dem Luftfilm können Vorspannungen in der Struktur jedoch zu höheren Abhebedrehzahlen und damit zu erhöhtem Verschleiß beim Start/Stopp des Rotorsystems führen.

Im Rahmen dieser Arbeit wird ein weiterer Typ von Luftlagern, hier bezeichnet als Air Ring Bearing, untersucht, der als eine Kombination der oben genannten Lagertypen angesehen werden kann. Dabei wird eine starre Buchse beweglich zwischen der Folienstruktur und dem Rotor angeordnet. Alternativ zur Folienstruktur kann auch ein Elastomer verwendet werden. Durch die externe, zusätzliche Dämpfung der Folienstruktur ist mit Air Ring Bearings auch ein Betrieb des Rotorsystems oberhalb der Stabilitätsgrenze möglich. Durch die starre Buchse werden Luftfilm und Struktur entkoppelt, wodurch der Rotor früher abhebt und der Lagerverschleiß beim Start/Stopp deutlich reduziert wird.

In dieser Arbeit wird ein schnelldrehendes Rotorsystem mit zwei Air Ring Bearings betrachtet. Ziel ist der Betrieb des Systems oberhalb der Stabilitätsgrenze bei selbsterregten Schwingungen mit tolerierbaren, moderaten Amplituden. Mithilfe von Hochlaufsimulationen wird das stark nichtlineare Verhalten des Rotorsystems untersucht und anhand von Bifurkationspfaden systematisch beschrieben. Auftretende dynamische Effekte und Bifurkationseffekte aufgrund der Nichtlinearität werden physikalisch ausführlich erklärt. In anschließenden Optimierungsstudien werden weite Parameterbereiche ermittelt, in denen ein technisch sicherer Betrieb des Rotorsystems möglich ist.

Zur Untersuchung des stark nichtlinearen Systems wird ein komplexes Co-Simulationsmodell verwendet. Dieses besteht zum einen aus einem Mehrkörpersystem, in dem die Bewegungen des Rotors und der Buchsen modelliert werden, und zum anderen aus Finite-Elemente-Systemen, die die Luftfilme modellieren.

Abstract

Air bearings are suitable for mounting high-speed rotor systems in environments with high purity requirements, such as fuel cells. Air bearings with rigid housings are widely used, which must be operated below the stability limit due to the low damping properties of air. Air foil bearings with an additional damping foil structure between the air film and the housing are also used. However, due to the strong coupling with the air film, preloads in the structure can result in higher lift-off speeds and thus increased wear during start/stop of the rotor system.

Another type of air bearing, referred to here as an air ring bearing, which can be regarded as a combination of the above types of bearings, is investigated in this thesis. Here, a rigid bushing is movably arranged between the foil structure and the rotor. As an alternative to the foil structure, an elastomer can also be used. Due to the additional external damping, rotor systems with air ring bearings can be operated above the stability limit. The rigid bushing decouples the air film from the structure, allowing the rotor to lift off earlier and improving the wear properties of the bearing.

This thesis considers a high-speed rotor system with two air ring bearings. The objective is to operate the system above the stability limit with self-excited vibrations of tolerable moderate amplitudes. The highly nonlinear behavior of the rotor system is studied using run-up simulations and systematically described using bifurcation paths. Dynamic and bifurcation effects due to the nonlinearity are explained in physical detail. In subsequent optimization studies, large parameter ranges are determined in which technically safe operation of the rotor systems is possible.

A complex co-simulation model is used to study the highly nonlinear system. It consists of a multi-body system, in which the movements of the rotor and the bushings are modeled, and finite element systems, in which the air films are modeled.

Danksagung

Diese Arbeit ist während meiner Zeit als wissenschaftlicher Mitarbeiter am Institut für Angewandte Dynamik unter der Leitung von Professor Schweizer entstanden.

Mein besonderer Dank gilt Professor Schweizer für die Bereitstellung des spannenden Forschungsthemas, die intensive fachliche Betreuung und die gewährten Freiräume für die wissenschaftliche Arbeit. Ich erinnere mich gerne an die vielseitige und abwechslungsreiche Zeit am Institut. Professor Hagedorn danke ich für die Übernahme des Zweitgutachtens und für seine wertvollen fachlichen Hinweise. Professor Lu danke ich für seine stets geduldige und zuverlässige Unterstützung während meiner Anfangszeit am Institut.

Meinen (ehemaligen) Kolleginnen und Kollegen am Institut Marcel Bauer, Dr. Ioannis Chatzisavvas, Huaxin Dong, Markus Eickhoff, Dennis Heyser, Jan Jäckel, Stefan Klimmek, Dr. Jan Kraft, Debora Linn, Dr. Marcel Mahner, Bianca Mehlhose, Dr. Tobias Meyer, Dr. Gerrit Nowald, Dr. Bastian Pfau und Johannis Triebwasser danke ich für den fachlichen Austausch und die angenehme Zusammenarbeit. Mein besonderer Dank gilt Bianca Mehlhose für das Korrekturlesen meiner Dissertation sowie meinem Bürokollegen Markus Eickhoff für seine angenehme und humorvolle Art und für seine grenzenlose Hilfsbereitschaft in allen beruflichen und privaten Belangen. Während meiner Zeit am Institut durfte ich die studentischen Arbeiten von Sebastian Armbruster, Shadi Ghanbari, Bianca Mehlhose, Wanglun Yin, Timo Weber und Maximilian Michel betreuen, was mir sehr viel Freude bereitet hat. Dafür möchte ich mich herzlich bedanken.

Helga Lorenz und Maria Rauck danke ich für die offene Tür und die stets zuverlässige Unterstützung in allen administrativen Belangen.

Meiner Mutter danke ich für die große Unterstützung im Alltag und für die vielen Stunden der Betreuung von Julian, insbesondere während der Erstellung der Dissertation. Meinem Vater danke ich für das Korrekturlesen der Arbeit und die vielen Formulierungsvorschläge.

Mein ganz besonderer Dank gilt meiner Frau Huaxin für ihre seelische und fachliche Unterstützung sowie meinem Sohn Julian und seinem Geschwisterchen, auf dessen Geburt wir uns sehr freuen.

Darmstadt, im April 2024 Pascal Zeise

Inhaltsverzeichnis

Publikationsverzeichnis

Die unten aufgeführte Liste enthält alle Publikationen des Autors. Die Liste umfasst Veröffentlichungen in Fachzeitschriften, Konferenzbeiträge, sowie die Bachelor- und Master-Abschlussarbeiten. Die vorliegende, kumulative Dissertation basiert auf den hervorgehobenen Veröffentlichungen.

P. Zeise, Entwicklung einer Methode zur Abschätzung und Minimierung von Mapping Fehlern in mehrstufigen FEM Simulationen, Bachelor Thesis, 2013, Technische Universität Darmstadt.

J. Yanagimoto, Y. Wake, P. Zeise, H. Mao, N. Shikazono, Design and optimization of stamping process of ultra-thin stainless sheet into bidirectionally corrugated shape for finless high-efficiency heat exchanger, CIRP Annals 65 (1) (2016) 289-292.

P. Zeise, Erstellung eines Numerischen Wälzlagermodells für Abgasturbolader-Rotoren, Master Thesis, 2017, Technische Universität Darmstadt.

P. Zeise, M. Mahner, M. Bauer, M. Rieken, B. Schweizer, A Reduced Model for Air Foil Journal Bearings for Time-Efficient Run-Up Simulations, Proceedings of the ASME Turbo Expo 2019: Turbomachinery Technical Conference and Exposition. Volume 7B: Structures and Dynamics. Phoenix, Arizona, June 17–21, 2019.

P. Zeise, M. Mahner, M. Bauer, M. Rieken, B. Schweizer, A reduced semi-analytical gas foil bearing model for transient run-up simulations, Proceedings of the 12th virtual Conference on Vibrations in Rotating Machinery XII (VIRM 12), October 14-15, 2020.

[1] **P. Zeise, B. Schweizer, Dynamics, stability and bifurcation analysis of rotors in air ring bearings, Journal of Sound and Vibration 521 (2022) 116392.**

[2] **P. Zeise, B. Schweizer, Vibration and bifurcation analysis of rotor systems with air ring bearings including ring tilting, Journal of Sound and Vibration 571 (2024) 118079.**

[3] **P. Zeise, B. Schweizer, Numerical investigations on high-speed turbo-compressor rotor systems with air ring bearings: Nonlinear vibration behavior and optimization, Applied and Computational Mechanics 17 (2023) 169–190.**

Darstellung zum Eigenanteil an den Veröffentlichungen

[1] P. Zeise, B. Schweizer, Dynamics, stability and bifurcation analysis of rotors in air ring bearings, *Journal of Sound and Vibration* 521 (2022) 116392.

- **Pascal Zeise:** Conceptualization; Data Curation; Formal Analysis; Methodology; Software; Visualization; Writing - original draft; Writing - review & editing.
- **Bernhard Schweizer:** Conceptualization; Writing - review & editing.

[2] P. Zeise, B. Schweizer, Vibration and bifurcation analysis of rotor systems with air ring bearings including ring rilting, *Journal of Sound and Vibration* 571 (2024) 118079.

- **Pascal Zeise:** Conceptualization; Data Curation; Formal Analysis; Methodology; Software; Visualization; Writing - original draft; Writing - review & editing.
- **Bernhard Schweizer:** Conceptualization; Writing - review & editing.

[3] P. Zeise, B. Schweizer, Numerical investigations on high-speed turbo-compressor rotor systems with air ring bearings: Nonlinear vibration behavior and optimization, *Applied and Computational Mechanics* 17 (2023) 169-190.

- **Pascal Zeise:** Conceptualization; Data Curation; Formal Analysis; Methodology; Software; Visualization; Writing - original draft; Writing - review & editing.
- **Bernhard Schweizer:** Conceptualization; Writing - review & editing.

Symbole und Abkürzungen

Symbole

Lateinische Symbole

Symbol	Einheit	Bedeutung
a	mm	Hebelarm der elastischen Struktur
b	mm	Breite der Buchse
C	µm	Nominalspiel zwischen Rotorzapfen und Buchse
c_{Buchse}	N mm^{-1}	Ersatzsteifigkeit der elastischen Struktur
c_{con}	N mm^{-3}	Kontaktsteifigkeit pro Fläche
c_{elast}	N mm^{-1}	Steifigkeitskoeffizient des Elastomers
c_{foil}	N mm^{-1}	Steifigkeitskoeffizient der Folienstruktur
$c_{\text{luft,tilt}}$	N mm rad^{-1}	Ersatzdrehsteifigkeit des Luftfilms
$c_{\text{luft,trans}}$	N mm^{-1}	Ersatzsteifigkeit des Luftfilms
d_{con}	N ms mm^{-3}	Kontaktdämpfung pro Fläche
d_{visc}	N s m^{-1}	Dämpfungskoeffizient des Elastomers
$\boldsymbol{F}_{\text{con},N}$	N	Normale Kontaktkraft
$\boldsymbol{F}_{\text{con},T}$	N	Tangentiale Kontaktkraft
$\boldsymbol{F}_{\text{ges}}$	N	Resultierende Lagerkraft
$\boldsymbol{F}_{p}$	N	Resultierende hydrodynamische Kraft
$\boldsymbol{F}_{\tau}$	N	Resultierende Kraft der Fluidfilmscherung
F_{fric}	N	Reibkraft der Folienstruktur
$\boldsymbol{f}_{e}$		Äußere Kräfte des Mehrkörpersystems
$\boldsymbol{G}$		Jacobi-Matrix der Bindungsgleichungen des Mehrkörpersystems

$\boldsymbol{g}$		Bindungsgleichungen des Mehrkörpersystems
g	m s^{-2}	Ortsfaktor
H_N		Makroschrittweite der numerischen Zeitintegration
h	µm	Höhenfunktion zwischen Rotorzapfen und Buchse
h_{con}	µm	Festgelegter Parameter zur Kontaktabfrage
h_n		Mikroschrittweite der numerischen Zeitintegration
$\boldsymbol{J}_{\text{Buchse}}$	kg mm^2	Trägheitsmatrix der Buchse
$\boldsymbol{J}_{\text{Rotor}}$	kg mm^2	Trägheitsmatrix des gesamten Rotors
l_{Rotor}	mm	Länge des Rotors
$\boldsymbol{M}$	kg	Massenmatrix des Mehrkörpersystems
$\boldsymbol{M}_{\text{con},N}$	N mm	Moment der normalen Kontaktkraft
$\boldsymbol{M}_{\text{con},T}$	N mm	Moment der tangentialen Kontaktkraft
$\boldsymbol{M}_{\text{ges}}$	N mm	Resultierendes Lagermoment
$\boldsymbol{M}_p$	N mm	Resultierendes hydrodynamisches Moment
$\boldsymbol{M}_\tau$	N mm	Resultierendes Moment der Fluidfilmscherung
M_B		Mittelpunkt der Buchse
M_{Keil}		Keilflächen der Buchse
M_Z		Mittelpunkt des Zapfenquerschnitts
m_{Buchse}	g	Masse der Buchse
m_{Rotor}	g	Masse des Rotors
n_k		Anzahl der diskreten Druckvariablen
O		Ursprung im Mittelpunkt des Lagergehäuses
$\boldsymbol{p}$	Pa	Vektor der diskreten Druckvariablen
p	Pa	Druck im Fluidfilm
p_a	Pa	Umgebungsdruck
p_{con}	Pa	Kontaktpressung
$\boldsymbol{R}$		Drehmatrix
r	mm	Radius des Rotorzapfens
$\boldsymbol{r}_B$	mm	Verschiebung der Buchse

$\boldsymbol{r}_Z$	mm	Verschiebung des Zapfens
S_{Rotor}		Schwerpunkt des gesamten Rotors
S_T		Schwerpunkt des Turbinenrads
S_V		Schwerpunkt des Verdichterrads
T_N		Makrozeitpunkt
t	s	Zeit
$\boldsymbol{v}$		Geschwindigkeiten des Mehrkörpersystems
u_{FEM}		Eingangsvariablen des Finite-Elemente-Systems
u_{MKS}		Eingangsvariablen des Mehrkörpersystems
v_{step}	m s^{-1}	Numerische Konstante
v_{tan}	m s^{-1}	Relative Oberflächengeschwindigkeit zwischen Rotorzapfen und Buchse
$\boldsymbol{x}$		Positionen des Mehrkörpersystems
x, y, z	m	Raumfestes Referenzsystem
x_B, y_B, z_B	m	Buchsenfestes Koordinatensystem
x_Z, y_Z, z_Z	m	Zapfenfestes Koordinatensystem
y_{BT}	mm	Vertikale Buchsenposition am Turbinenlager
y_{BV}	mm	Vertikale Buchsenposition am Verdichterlager
y_{FEM}		Ausgabevariablen des Finite-Elemente-Systems
y_{MKS}		Ausgabevariablen des Mehrkörpersystems
y_{ZT}	mm	Vertikale Zapfenposition am Turbinenlager
y_{ZV}	mm	Vertikale Zapfenposition am Verdichterlager
z_T	mm	Axiale Position des Turbinenrads
z_V	mm	Axiale Position des Verdichterrads
z_{ZT}	mm	Axiale Position der Turbinenbuchse
z_{ZV}	mm	Axiale Position der Verdichterbuchse

Griechische Symbole

Symbol	**Einheit**	**Bedeutung**
α	rad	Ausrichtungswinkel der Buchseninnenkontur

α_{tilt}	rad	Erster körperfester Kardanwinkel des Zapfens relativ zur Buchse
β_{tilt}	rad	Zweiter körperfester Kardanwinkel des Zapfens relativ zur Buchse
ΔH	µm	Keilhöhe der Buchseninnenkontur
$\Delta \boldsymbol{r}$	mm	Einfluss der relativen Zapfentranslation auf die Höhenfunktion
$\Delta r, \delta$	mm, rad	Komponenten von $\Delta \boldsymbol{r}$ zerlegt im Polarkoordinatensystem
$\Delta \boldsymbol{r}_{\text{tilt}}$	mm	Einfluss der relativen Zapfenverkippung auf die Höhenfunktion
$\Delta r_{\text{tilt}}, \delta_{\text{tilt}}$	mm, rad	Komponenten von $\Delta \boldsymbol{r}_{\text{tilt}}$ zerlegt im Polarkoordinatensystem
δ_{pen}	µm	Durchdringungstiefe bei Kontakt
ε_T		Rotorexzentrizität im Turbinenlager
ε_V		Rotorexzentrizität im Verdichterlager
η	kg m^{-1} s^{-1}	Viskosität von Luft
κ		Anzahl der generalisierten Koordinaten des Mehrkörpersystems
κ_C		Anzahl der Bindungsgleichungen des Mehrkörpersystems
$\boldsymbol{\lambda}$		Langrange-Multiplikatoren durch die Bindungsgleichungen auf Lageebene
$\boldsymbol{\mu}$		Langrange-Multiplikatoren durch die Bindungsgleichungen auf Geschwindigkeitsebene
μ		Reibungskoeffizient
π		Kreiszahl
τ_{con}	Pa	Tangentiale Reibspannung des Kontakts
φ	rad	Umfangskoordinate der Buchse
φ_t	rad	Keilänge
Ω	s^{-1}	Rotordrehzahl
$\omega_{Z,z}$	s^{-1}	Winkelgeschwindigkeit des Rotorzapfens um seine Längsachse

Sonstige Symbole

Symbol	Bedeutung
$\lfloor \ldots \rfloor$	Abrundungsfunktion

Abkürzungen

Abkürzung	Bedeutung
Abb.	Abbildung
atan2	Erweiterte Arkustangensfunktion
BDF	Backward differentiation formula (Implizites Mehrschrittverfahren zur Lösung von Anfangswertproblemen)
DAE	Differential-algebraic system of equations (System differential-algebraischer Gleichungen)
dt.	Deutsch
engl.	Englisch
FEM	Finite-Elemente-Methode
FFT	Fast Fourier Transformation (Schnelle Fourier-Transformation)
MKS	Mehrkörpersystem
Mode_1(b)	Erste Rückwärtsmode des linearisierten Rotorsystems
Mode_1(f)	Erste Vorwärtsmode des linearisierten Rotorsystems
step	Geglättete Approximation der Stufenfunktion
step_{SL}	Geglättete Approximation der Vorzeichenfunktion

1 Einleitung

Die vorliegende kumulative Dissertation basiert auf den Veröffentlichungen [1–3] und behandelt die Dynamik, die Stabilitäts- und die Bifurkationseigenschaften von Rotorsystemen mit elastisch gebetteten Luftlagern. Dieser Lagertyp wird hier als *Air Ring Bearing* bezeichnet. Die Einleitung beginnt mit einem kurzen Überblick über Luftlager in Abschnitt 1.1 und erläutert anschließend in Abschnitt 1.2 die Ziele der Dissertation und die einzelnen Beiträge der Veröffentlichungen [1–3]. Abschnitt 1.3 beschreibt das entwickelte numerische Modell für Rotorsysteme mit Air Ring Bearings. Die Parameter des Rotorsystems für die durchgeführten Hochlaufsimulationen sind in Abschnitt 1.4 aufgeführt.

1.1 Luftlager

Luftlager oder aerodynamische Lager werden den Gleitlagern zugeordnet. Sie bestehen im Wesentlichen aus einem Rotor und einem Gehäuse, die durch einen schmalen Luftspalt voneinander getrennt sind. Mit Beginn der Rotordrehung wird die an der Rotoroberfläche haftende Luft unter den Rotor geführt und dabei verdichtet. Ab einer bestimmten Drehzahl, der Abhebedrehzahl, gleicht der Überdruck im Luftspalt unter dem Rotor die Gewichtskraft des Rotors aus. Der Rotor ist nun durch einen Luftfilm vollständig vom Gehäuse getrennt. In diesem Zustand arbeitet das Rotorsystem nahezu verschleißfrei. Da keine zusätzlichen Schmiermittel wie Öl oder Fett erforderlich sind, lassen sich aerodynamische Lager in Umgebungen mit höchsten Reinheitsanforderungen einsetzen, z. B. in Brennstoffzellen oder in Kühlaggregaten von Flugzeugen.

Luftlager lassen sich in weitere Arten unterteilen: In Abb. 1.1a ist ein Luftlager mit starrem Gehäuse abgebildet. Abb. 1.1b zeigt ein Folienluftlager mit einer elastischen Folienstruktur bestehend aus einer Wellfolie (engl. *Bump Foil*) und einer Deckfolie (engl. *Top Foil*), die zwischen dem Luftfilm und dem Gehäuse eingesetzt wird. In Abb. 1.1c ist ein Air Ring Bearing abgebildet, das eine starre Buchse zwischen dem Luftfilm und der Folienstruktur aufweist.

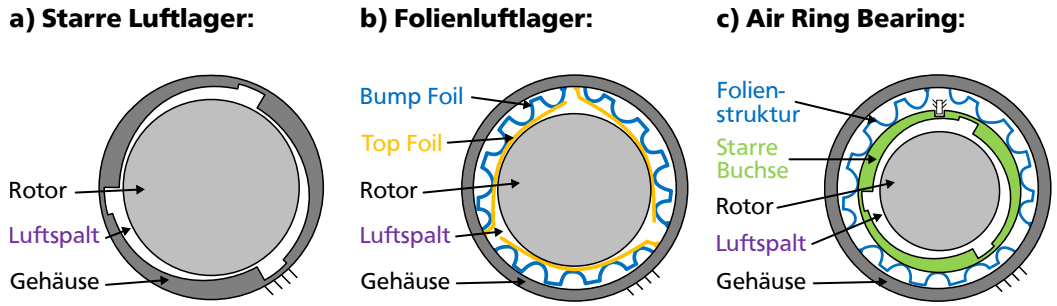

Abbildung 1.1: Beispiele von verschiedenen Luftlagertypen [1–3].

Die Stabilitätseigenschaften sind bei Luftlagern von hoher Bedeutung. Ab einer bestimmten Drehzahl wird bei Luftlagern das Gleichgewicht zwischen Rotorgewicht und Druck im Luftfilm instabil und das System neigt dazu, in einen Zustand mit selbsterregten Schwingungen (Whirl/Whip-Oszillationen) überzugehen. Aufgrund der geringen Viskosität von Luft wird zum einen das Rotorsystem bereits bei sehr niedrigen Drehzahlen instabil. Zum anderen reichen die Dämpfungseigenschaften von Luft nicht aus, um die dann auftretenden Whirl/Whip-Oszillationen ausreichend zu begrenzen. In diesem Fall ist mit gefährlichen Kontakten zwischen Rotor und Gehäuse zu rechnen, die zu schweren Maschinenschäden führen können. Aus diesem Grund ist ein Ziel bei der Auslegung von Luftlagern den Eintritt der Instabilität durch konstruktive Maßnahmen soweit zu verzögern, dass dieser außerhalb des Betriebsbereichs des Systems liegt. Ebenfalls ist es möglich die selbsterregten Oszillationen mit externer Dämpfung ausreichend zu begrenzen. In [4] wird das Stabilitätsproblem von Luftlagern detailliert erläutert.

In den folgenden Abschnitten werden die Luftlagertypen aus Abb. 1.1 genauer vorgestellt.

1.1.1 Luftlager mit starrem Gehäuse

Luftlager mit starrem Gehäuse lassen sich anhand der Innengeometrie des Lagergehäuses einteilen. In der einfachsten Ausführung kann eine rein kreisförmige Geometrie verwendet werden, siehe Abb. 1.2a. Diese Art der Lagerung weist jedoch ein sehr schlechtes Stabilitätsverhalten auf, d. h. die Instabilität tritt bereits bei sehr niedrigen Rotordrehzahlen ein. Die Verwendung einer Dreikeilgeometrie, siehe Abb. 1.2b, erhöht die Drehzahlgrenze bis zum Eintreten der Instabilität. Im Allgemeinen liegt diese jedoch weiterhin innerhalb des Betriebsbereichs. Anstelle einer Keilgeometrie können auch Spiralrillen zur Stabilisierung

des Lagers verwendet werden. Die Spiralrillen können sowohl in die Rotor- als auch in die Gehäuseflächen eingebracht werden. Insbesondere ist die Anordnung der Rillen als Fischgrätenmuster (engl. *Herringbone Grooves*) weit verbreitet, siehe Abb. 1.2c. Durch die Anordnung der Rillen tritt während dem Betrieb ein Pumpeffekt im Luftfilm auf, der sich stabilisierend auf das dynamische System auswirkt. Bei richtiger Wahl der Konstruktionsparameter ist ein stabiler Betrieb des Rotorsystems über den gesamten Drehzahlbereich möglich [5, 6]. Für einen stabilen Betrieb sind jedoch auch bei Herringbone-Lagern Spaltmaße im unteren Mikrometerbereich notwendig. Die kleinen Spaltmaße führen zwar zu kleinen Amplituden der Unwuchtsschwingungen, wodurch z. B. die Spalte zwischen Verdichter- bzw. Turbinenrad und Gehäuse kleiner dimensioniert werden können, um den Wirkungsgrad der gesamten Maschine zu erhöhen. Jedoch erfordern die geringen Spaltmaße auch sehr enge Toleranzen und ein umfassendes Thermomanagement, da bereits kleinste Änderungen der Spalthöhe (z. B. durch Fliehkraftaufweitung des Rotors oder durch Wärmeausdehnung) das dynamische Verhalten beeinflussen können. Im Extremfall ist sogar ein Verklemmen des Rotors im Gehäuse möglich. Aufgrund der hohen Toleranzanforderungen ist bei diesem Lagertyp mit einem hohen Fertigungsaufwand zu rechnen. Einen grundlegenden Überblick über Luftlager mit starrem Gehäuse gibt [4]. Die Dynamik und das Stabilitätsverhalten von Rotorsystemen mit Herringbone-Lagern werden z. B. in [7, 8] diskutiert. Untersuchungen zur Optimierung der Rillengeometrie finden sich in [9]. Thermische Aspekte im Zusammenhang mit Herringbone-Lagern werden z. B. in [10] betrachtet. Eine ausführliche Literaturübersicht zu Herringbone-Lagern findet sich in [11].

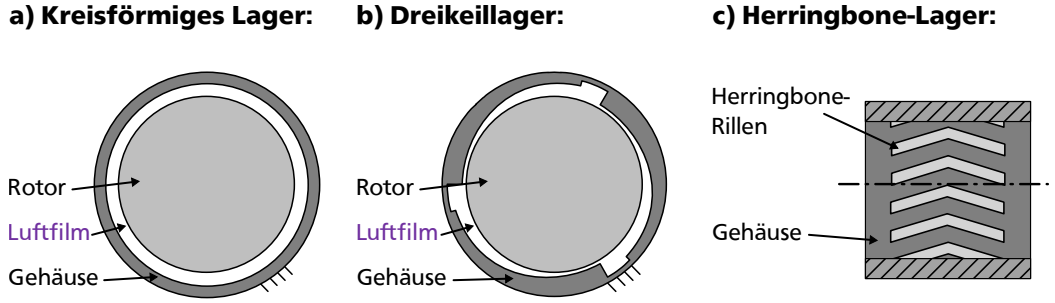

Abbildung 1.2: Beispiele von unterschiedlichen Luftlagern mit starrem Gehäuse.

1.1.2 Folienluftlager

Bei Folienlagern wird zwischen Luftfilm und Gehäuse eine elastische Folienstruktur eingefügt. Die Struktur besteht in der Regel aus einem beschichteten Top Foil, das von einer Unterstruktur aus Bump Foils [12–14] oder *Beam Foils* (dt. Balkenfolien) [15, 16] getragen wird. Beide Varianten sind in Abb. 1.3 dargestellt. Weiterhin werden Folienlager mit *Wing Foils* (dt. Flügelfolien) [17, 18], Federn [19], einem Metallvlies [20] oder einem Polymer [21, 22] untersucht. Die Folienstruktur kann den Rotor komplett umschließen, alternativ ist auch eine Unterteilung der Struktur in Segmente (engl. *Pads*) möglich. Neben der vollständig umschließenden Variante sind Drei-Pad-Varianten in der Literatur weit verbreitet. Das Bump Foil Lager und das Beam Foil Lager sind in Abb. 1.3 als Drei-Pad-Variante dargestellt. Die elastische Folienstruktur kann das Rotorsystem zusätzlich dämpfen und mögliche Fehlstellungen im Lager ausgleichen.

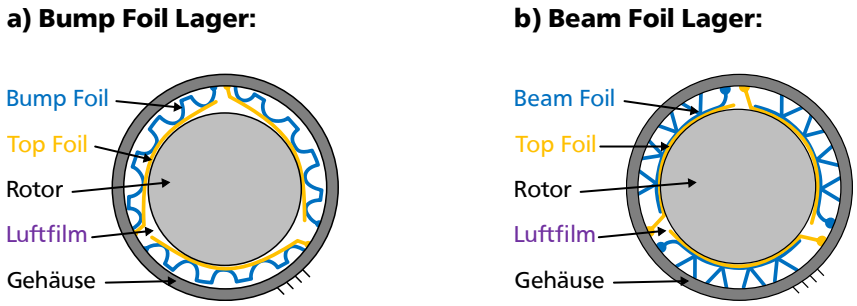

Abbildung 1.3: Bump Foil und Beam Foil Lager mit drei Pads [1].

Je nach Bauart weisen Folienluftlager unterschiedliche Steifigkeits- und Dämpfungs- bzw. Reibungseigenschaften auf. Diese Eigenschaften beeinflussen das dynamische Verhalten, sowie das Stabilitäts- und Bifurkationsverhalten des Rotorsystems maßgeblich. Folienlager mit einem Drei-Pad-Design zeichnen sich im Allgemeinen durch verbesserte Stabilitätseigenschaften im Vergleich zu Lagern mit einer vollständig umschließenden Folienstruktur aus [13, 14]. Die Stabilität kann auch durch eine gezielte Modifikation der Geometrie der Gehäuseinnenfläche [23], durch den Einsatz von Unterlegblechen [24, 25] oder durch eine Vorspannung der Folienstruktur [26] verbessert werden. Allerdings kann die Vorspannung auch zu einem verzögerten Abheben des Rotors und damit zu erhöhtem Verschleiß während des Start/Stopps des Rotorsystems führen. Aktive Änderungen der Geometrie der Gehäuseinnenfläche zur Stabilisierung von Rotorsystemen mit Folienlagern werden in [27, 28] diskutiert. Lager mit aktiver Gasinjektion werden in [29, 30] untersucht. Das ther-

mische Verhalten von Folienlagern wird z. B. in [31, 32] behandelt. Eine experimentelle Analyse der Abhebedrehzahl von vorgespannten Folienluftlagern findet sich in [33].

Aufgrund des stark nichtlinearen Verhaltens und der starken Kopplung mit dem Luftfilm stellt die Folienstruktur eine immense Herausforderung für die numerische Modellierung und Vorhersage des dynamischen Verhaltens sowie der Stabilitätseigenschaften dar. Diese sind jedoch für den sicheren Betrieb von Rotorsystemen mit Folienluftlagern von großer Relevanz. Klassische Stabilitätsberechnungen, bei denen die dynamischen Eigenschaften des Luftfilms durch Feder-Dämpfer-Elemente für eine Eigenwertberechnung approximiert werden (siehe z. B. [34, 35]), sind je nach Lagertyp nicht hinreichend genau [36–38]. Verbesserte Ansätze zur Berechnung der Stabilität werden in [39–41] vorgestellt. In [42–44] wird das dynamische Verhalten von Rotorsystemen mit Folienluftlagern numerisch und experimentell untersucht. Ein Literaturüberblick über Folienlager wird in [45] gegeben.

1.1.3 Air Ring Bearings

Das Air Ring Bearing, siehe Abb. 1.4, versteht sich als eine Kombination der in Abschnitt 1.1.1 und 1.1.2 genannten Ansätze. Hierbei wird zwischen dem Rotor und der Folienstruktur eine starre Buchse eingesetzt, die in radialer Richtung verschiebbar und um die radialen Achsen verkippbar ist. Die axiale Translation und die axiale Rotation werden verhindert. Bei Bewegung der Buchse, z. B. durch selbsterregte Schwingungen, wird Energie durch die Folienstruktur dissipiert und so die Schwingungsamplituden begrenzt. Alternativ zur Folienstruktur [1–3] kann auch ein Elastomer [1–3, 46–48] als elastische Struktur in Betracht gezogen werden. Die beiden Ansätze unterscheiden sich in der Art der Dissipation: Bei einer Folienstruktur dominiert die Festkörperreibung, bei einem Elastomer ist die viskose Dämpfung ausschlaggebend. Neben einer Folienstruktur oder einem Elastomer gibt es Ansätze, die Elastizität durch eine flexible Membran [49] oder durch Federstahldrähte [50] zu realisieren. Durch die starre Buchse entfällt die Vorspannung zwischen dem Rotor und der Folienstruktur, wodurch der Rotor früher abheben kann. Außerdem werden der Luftfilm und die elastische Struktur durch die Buchse vollständig entkoppelt, was den Simulationsaufwand erheblich reduziert. Dies ermöglicht die Simulation transienter Hochläufe mit tolerierbaren Rechenzeiten für detaillierte Untersuchungen der Dynamik und den Stabilitätseigenschaften des Rotorsystems.

Die Untersuchungen zu aerodynamischen Lagern mit elastisch gelagerten Buchsen in [46–50] haben zum Ziel, das Auftreten von Instabilitäten über den Betriebsbereich des Rotors hinaus zu verzögern und damit einen stabilen Betrieb des Rotorsystems über den gesamten Drehzahlbereich zu gewährleisten. Hiervon unterscheidet sich das Air Ring Bearing in den vorliegenden Veröffentlichungen [1–3]: Das Air Ring Bearing soll insbesondere auch nach dem Eintritt der Instabilität, d. h. bei Whirl/Whip-Oszillationen, betrieben

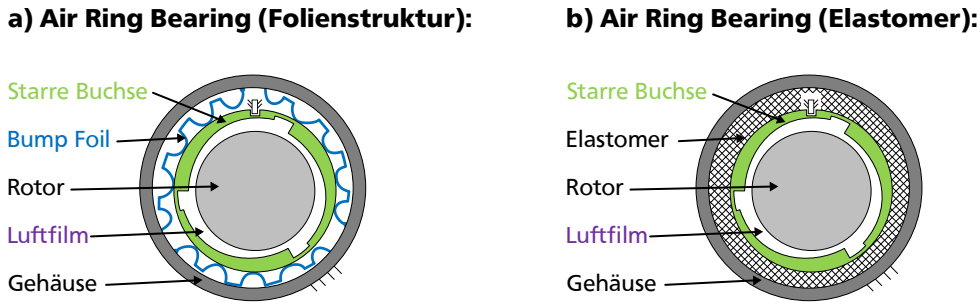

Abbildung 1.4: Air Ring Bearing mit einer Dreikeilinnenkontur der Buchse [1–3].

werden. Dabei begrenzt die elastische Struktur bzw. das Elastomer des Air Ring Bearings die Amplituden der Schwingungen, sodass ein sicherer Betrieb des Rotorsystems weiterhin gewährleistet ist. Die Inkaufnahme der auftretenden Whirl/Whirl-Oszillationen ermöglicht es einen größeren Luftspalt zwischen Rotor und Buchse zu realisieren. Das hat zur Folge, dass die Anforderungen an die Fertigungsgenauigkeit und an das Thermomanagement des Lagers deutlich reduziert und damit einhergehend die Herstellungskosten gesenkt werden können. Ein optimales Air Ring Bearing der Veröffentlichungen [1–3] hat daher einen maximal großen Luftspalt bei gleichzeitig tolerierbaren Oszillationen innerhalb des Drehzahlbereichs.

In den Veröffentlichungen [1–3] werden die Buchsen zur Stabilisierung zusätzlich mit einer Dreikeilinnenkontur versehen, siehe Abb. 1.4. Die Innenkontur hat eine $120°$-Symmetrie.

1.2 Zielsetzung und Aufbau der Dissertation

Die Veröffentlichungen der kumulativen Dissertation [1–3] sollen zu einem besseren Verständnis der Dynamik, der Stabilitäts- und der Bifurkationseigenschaften von Rotorsystemen mit Air Ring Bearings beitragen. Eine Neuheit der Veröffentlichungen ist hierbei der besondere Fokus auf das Verhalten des Systems nach Eintritt der Instabilität, d. h. bei selbsterregten (Whirl/Whip-)Oszillationen. Durch das Inkaufnehmen selbsterregter Schwingungen können die Fertigungs- und Toleranzanforderungen gegenüber einem komplett stabilen Betrieb reduziert werden, wodurch Air Ring Bearings wirtschaftlicher hergestellt werden können.

Als Grundlage für die systematische Beschreibung von Rotorsystemen mit Air Ring Bearings werden drei Bifurkationspfade vorgestellt, die in der Regel beobachtet werden können. Die drei Bifurkationspfade werden hier als *Bifurkationspfad 1*, *Bifurkationspfad 2a* und *Bifurkationspfad 2b* bezeichnet. Es wird gezeigt, welche Bifurkationspfade für einen sicheren Betrieb des Rotorsystems wünschenswert sind und welche Bifurkationspfade vermieden werden sollten. Darüber hinaus wird der Einfluss relevanter Lagerparameter auf das Bifurkationsverhalten des Lagers untersucht. Aus den Ergebnissen umfangreicher Parameterstudien werden Empfehlungen für die Lagerauslegung abgeleitet. Außerdem werden verschiedene nichtlineare Effekte von Rotorsystemen mit Air Ring Bearings (Synchronisationseffekte, Modenkopplung, selbsterregte Schwingungen, Chaos, etc.) vorgestellt und physikalisch interpretiert. Die Veröffentlichungen sollen eine grundlegende Unterstützung bei der Auslegung von Rotorsystemen mit Air Ring Bearings bieten.

Durch eine Eigenwertanalyse des linearisierten Rotorsystems kann zwar der Eintritt der Instabilität abgeschätzt werden, für eine Analyse des Systems nach der Instabilität sind jedoch komplexere nichtlineare Modelle erforderlich. Aus diesem Grund ist für die Untersuchungen in den Veröffentlichungen [1–3] ein detailliertes Modell eines Rotorsystems mit zwei Air Ring Bearings entwickelt worden. Die beiden Luftfilme werden durch die Finite-Elemente-Methode modelliert, der Rotor und die Buchsen werden als Mehrkörpermodell implementiert. Die insgesamt drei Subsysteme werden über eine Co-Simulationsschnittstelle miteinander gekoppelt und lassen sich auf diese Weise simultan im Zeitbereich lösen. Dieser Ansatz ermöglicht es, transiente Simulationen von Hochläufen des Rotorsystems durchzuführen. Eine Vielzahl von Hochläufen mit unterschiedlichen Rotor- und Lagerparametern gibt einen umfassenden Einblick in die dynamischen Eigenschaften, sowie in das Stabilitäts- und Bifurkationsverhalten des Systems.

Die einzelnen Veröffentlichungen liefern hierbei die folgenden Beiträge:

1. Veröffentlichung [1]: In der ersten Veröffentlichung wird erstmals der Ansatz vorgestellt, Rotorsysteme mit Air Ring Bearings bewusst nach Eintritt der Instabilität unter selbsterregten Schwingungen mit moderaten Amplituden zu betreiben. Ferner wird das Co-Simulationsmodell zur transienten Simulation der Hochläufe ausführlich erklärt. Zur Erläuterung der Bifukationspfade werden Hochlaufsimulationen mit einem symmetrischen und einem asymmetrischen Rotor durchgeführt. Die elastische Struktur der Buchsen wird in den Hochläufen entweder als eine Folienstruktur oder als ein Elastomer modelliert. Die Parameterstudien umfassen im Wesentlichen die Variation der Steifigkeit der elastischen Struktur sowie dessen Reibkraft bzw. dessen viskose Dämpfung. Auch der Einfluss von Unwuchten und der Einfluss der Rotorasymmetrie auf das dynamische Verhalten werden untersucht. Die auftretenden nichtlinearen Effekte werden physikalisch erklärt und inter-

pretiert. Aus den gewonnenen Ergebnissen werden erste Empfehlungen für die Auslegung eines Rotorsystems mit Air Ring Bearings abgeleitet.

2. Veröffentlichung [2]: In der zweiten Veröffentlichung wird das Modell um die Verkippung der Buchsen erweitert. Da bei extremen Exzentrizitäten des Rotorzapfens und/oder Verkippungen Kontakt zwischen Buchse und Zapfen entstehen kann, wird das Finite-Elemente-System des Luftfilms um eine Kontaktmodellierung ergänzt. Der Einfluss der neuen Verkippungsfreiheitsgrade auf das Bifurkationsverhalten wird durch verschiedene Parameterstudien untersucht. Darüber hinaus werden die Übergänge zwischen den Bifurkationspfaden näher betrachtet. Die Untersuchungen konzentrieren sich auf die Steifigkeit und Reibung bzw. viskose Dämpfung der Folienstruktur oder des Elastomers. Für bestimmte Parameter ist eine nichtlineare Modenkopplung (1:2 Modensynchronisation) als Folge der Buchsenverkippung entdeckt worden. Dieser Effekt wird ausführlich physikalisch beschrieben und erklärt.

3. Veröffentlichung [3]: In der dritten Veröffentlichung wird nun die Innenkontur der Buchse (und somit auch die Geometrie des Luftspalts) genauer betrachtet. Es zeigt sich, dass die Innenkontur der Buchse das dynamische Verhalten von Rotorsystemen mit Air Ring Bearings maßgeblich beeinflusst. Durch umfassende Parameterstudien der Kontur sowie des Elastomers werden mehrere Bifurkationskarten erstellt, die bei dem Design eines optimalen Air Ring Bearings unterstützen. Die Bifurkationskarten zeigen einen großen Bereich der Lagerparameter mit denen das Rotorsystem technisch sicher betrieben werden kann.

Die Beiträge der Veröffentlichungen sind in Tabelle 1.1 zusammengefasst. Die variierten Parameter sind hierbei unter anderem das Nominalspiel C und die Keilhöhe ΔH des Luftspalts (Definitionen im Abschnitt 1.3.1), der Hebelarm a, die Steifigkeit c_{foil} und die Strukturreibung F_{fric} der Folienstruktur, die Steifigkeit c_{elast} und die Dämpfung d_{visc} des Elastomers (Definitionen im Abschnitt 1.3.2), sowie die Buchsenmasse m_{Buchse}.

Tabelle 1.1: Beiträge der Veröffentlichungen im Überblick

	Veröffentlichung [1]	**Veröffentlichung [2]**	**Veröffentlichung [3]**
Eigenschaften der Buchse/des Luftfilms			
Translation der Buchse	✔	✔	✔
Verkippung der Buchse		✔	
Kontaktmodellierung		✔	✔
Variierte Parameter			
C			✔
ΔH			✔
a		✔	
c_{foil}	✔	✔	
F_{fric}	✔	✔	
c_{elast}	✔	✔	✔
d_{visc}	✔	✔	✔
m_{Buchse}	✔	✔	✔
Inhalt der Veröffentlichung			
	• Definition Bifurkationspfade • Einfluss Unwucht • Einfluss Asymmetrie	• Einfluss Verkippung • Übergänge Bifurkationspfade • Modensynchronisation	• Einfluss Innenkontur • Optimierung • Bifurkationskarten

1.3 Modellierung von Rotorsystemen mit Air Ring Bearings

In diesem Kapitel wird die Modellierung von Rotorsystemen mit Air Ring Bearings vorgestellt, die in den Veröffentlichungen [1–3] Anwendung findet. Das Modell besteht aus verschiedenen Subsystemen, die mit unterschiedlichen Methoden berechnet werden. Die Luftfilme werden mittels der Finite-Elemente-Methode (FEM) modelliert, siehe Abschnitt 1.3.1. Der Rotor und die Buchsen werden in einem Mehrkörpersystem (MKS) dargestellt, siehe Abschnitt 1.3.2. Die mathematische Kopplung der Subsysteme mittels Co-Simulation wird im Abschnitt 1.3.3 erläutert.

1.3.1 Finite-Elemente-Modell des Luftfilms

Das Ziel der Modellierung des Luftfilms ist die Berechnung der resultierenden Kräfte und Momente. Als Eingabewerte erhält das Finite-Elemente-System die Position (translatorisch und rotatorisch) des Rotorzapfens relativ zur Buchse. Mit diesen kinematischen Größen lässt sich die Geometrie des Luftspalts, die Höhenfunktion $h(\varphi, z_B)$, ermitteln. In der Höhenfunktion ist auch die Dreikeilinnenkontur der Buchse berücksichtigt. Die Höhenfunktion wird in die *Reynolds-Gleichung* eingesetzt, um die Druckverteilung $p(\varphi, z_B)$ im Luftfilm mithilfe der Finite-Elemente-Methode zu berechnen. Die Integration des Drucks führt zu den hydrodynamischen Kräften und Momenten des Luftfilms. Da in bestimmten Situationen auch Kontakt zwischen dem Rotorzapfen und der Buchse wahrscheinlich ist, werden auch mögliche Kontaktkräfte und -momente modelliert.

Hydrodynamische Kräfte und Momente

Zur Ermittlung der Höhenfunktion muss die Relativbewegung zwischen Rotorzapfen und Buchse bekannt sein. Die dazu notwendigen kinematischen Größen erhält das Finite-Elemente-System durch die Co-Simulationsschnittstelle. Abb. 1.5 zeigt den Rotorzapfen und die Buchse in einer beliebigen Lage. In der ersten und dritten Veröffentlichung [1, 3] ist die Rotation der Buchse vollständig durch Bindungsgleichungen bestimmt, sodass nur die translatorische Bewegung zur Ermittlung der Höhenfunktion notwendig ist. In der zweiten Veröffentlichung [2] können die Buchsen zusätzlich relativ zum Rotor frei verkippen, wodurch auch die relative Drehung der Buchsen in der Höhenfunktion berücksichtigt werden muss.

Zur Beschreibung der Translation der beiden Körper wird als Bezugssystem ein raumfestes x, y, z-Koordinatensystem definiert, dessen Ursprung O im Mittelpunkt des Lagergehäuses liegt. Es wird angenommen, dass sich der Mittelpunkt M_B der Buchse nur innerhalb der x, y-Ebene bewegen kann. Die Verschiebung von M_B im raumfesten Koordinatensystem

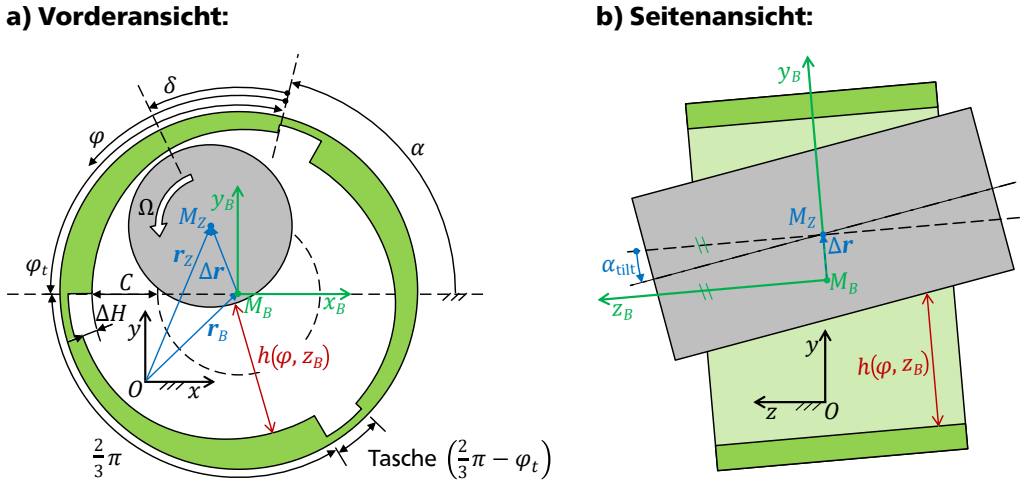

Abbildung 1.5: Dreikeilgeometrie des Air Ring Bearings [1–3].

wird durch den Vektor $\boldsymbol{r}_B = [x_B, y_B, 0]^T$ dargestellt. Analog zur Buchse wird die Verschiebung des Zapfens M_Z durch den Vektor $\boldsymbol{r}_Z = [x_Z, y_Z, 0]^T$ beschrieben. Daraus ergibt sich die Relativposition zwischen Rotorzapfen und Buchse $\Delta\boldsymbol{r} = \boldsymbol{r}_Z - \boldsymbol{r}_B = [\Delta x, \Delta y, 0]^T$. Im Anschluss wird $\Delta\boldsymbol{r}$ in Polarkoordinaten Δr, δ transformiert. Die Transformation erfolgt anhand der folgenden Gleichungen:

$$\Delta r = \sqrt{\Delta x^2 + \Delta y^2}\,, \tag{1.1}$$

$$\delta = \operatorname{atan2}\left(\Delta y, \Delta x\right) - \alpha\,. \tag{1.2}$$

Der konstante Winkel α in Gleichung (1.2) beschreibt dabei die Ausrichtung der Innenkontur der Buchse in Bezug zum Gehäuse, siehe Abb. 1.5a. Die Innenkontur besteht aus drei Keilen, deren Längen durch den Winkel φ_t definiert sind. Zwischen den Keilen befinden sich Taschen mit den Längen $2/3\pi - \varphi_t$. Die Höhe des Luftspalts ergibt sich aus dem Lagerspiel C und der Keilhöhe ΔH.

In der zweiten Veröffentlichung [2] wird die Verkippung des Zapfens gegenüber dem x_B, y_B, z_B-Koordinatensystem der Buchse durch Kardanwinkel modelliert. Dabei beschreibt α_{tilt} die erste Drehung um die körperfeste x_Z-Achse des Rotorzapfens, siehe Abb. 1.5b. Die zweite Drehung um die y_Z-Achse wird durch β_{tilt} definiert. Die dritte Drehung ist für die Berechnung der Höhenfunktion nicht notwendig. Aufgrund der geringen

Spalthöhe im Verhältnis zum Zapfenradius und zur Buchsenbreite sind α_{tilt} und β_{tilt} sehr klein, $\alpha_{\text{tilt}}, \beta_{\text{tilt}} \ll 1$. Aus den ersten beiden Kardanwinkeln lässt sich die resultierende Drehmatrix $\boldsymbol{R}$ herleiten:

$$\boldsymbol{R} = \begin{pmatrix} \cos\beta_{\text{tilt}} & 0 & \sin\beta_{\text{tilt}} \\ \sin\alpha_{\text{tilt}}\ \sin\beta_{\text{tilt}} & \cos\alpha_{\text{tilt}} & -\sin\alpha_{\text{tilt}}\ \cos\beta_{\text{tilt}} \\ -\cos\alpha_{\text{tilt}}\ \sin\beta_{\text{tilt}} & \sin\alpha_{\text{tilt}} & \cos\alpha_{\text{tilt}}\ \cos\beta_{\text{tilt}} \end{pmatrix} . \tag{1.3}$$

Die Änderung des Luftspalts aufgrund der Verkippung $\Delta\boldsymbol{r}_{\text{tilt}}$ lässt sich mit $\boldsymbol{R}$ und z_B berechnen:

$$\Delta\boldsymbol{r}_{\text{tilt}} = \begin{pmatrix} \Delta x_{\text{tilt}} \\ \Delta y_{\text{tilt}} \\ \Delta z_{\text{tilt}} \end{pmatrix} = \boldsymbol{R} \cdot \begin{pmatrix} 0 \\ 0 \\ z_B \end{pmatrix} = z_B \cdot \begin{pmatrix} \sin\beta_{\text{tilt}} \\ -\sin\alpha_{\text{tilt}}\ \cos\beta_{\text{tilt}} \\ \cos\alpha_{\text{tilt}}\ \cos\beta_{\text{tilt}} \end{pmatrix} . \tag{1.4}$$

Der Vektor $\Delta\boldsymbol{r}_{\text{tilt}}$ wird ebenfalls in ein Polarkoordinatensystem transformiert:

$$\Delta r_{\text{tilt}} = \sqrt{\Delta x_{\text{tilt}}^2 + \Delta y_{\text{tilt}}^2}\,, \tag{1.5}$$

$$\delta_{\text{tilt}} = \text{atan2}\left(\Delta y_{\text{tilt}}, \Delta x_{\text{tilt}}\right) - \alpha\,. \tag{1.6}$$

Mit Δr_{tilt} und δr_{tilt} wird der Einfluss der Verkippung des Zapfens auf die Höhenfunktion dargestellt. Zusammen mit Δr und δ kann nun die Höhenfunktion $h(\varphi, z_B)$ des Luftfilms beschrieben werden:

$$\begin{aligned} h\left(\varphi, z_B, t\right) = C &- \Delta r \cdot \cos\left(\varphi - \delta\right) \\ &- \Delta r_{\text{tilt}} \cdot \cos\left(\varphi - \delta_{\text{tilt}}\right) \\ &+ \Delta H \cdot \left(1 + \frac{2\pi}{3\varphi_t} \cdot \left\lfloor \frac{3\varphi}{2\pi} \right\rfloor - \frac{\varphi}{\varphi_t}\right) , \\ &\varphi \in M_{\text{Keil}}\,. \end{aligned} \tag{1.7}$$

Dabei entspricht $\lfloor ... \rfloor$ der Abrundungsfunktion. Die Höhenfunktion ist nur auf den Keilflächen der Buchse definiert $M_{\text{Keil}} = \{[0, \varphi_t], [\frac{2\pi}{3}, \frac{2\pi}{3} + \varphi_t], [\frac{4\pi}{3}, \frac{4\pi}{3} + \varphi_t]\}$. Der Term $-\Delta r_{\text{tilt}} \cdot \cos(\varphi - \delta_{\text{tilt}})$ beschreibt die Höhenänderung aufgrund der relativen Verkippung zwischen Buchse und Rotor und ist daher nur in der Höhenfunktion in der zweiten Veröffentlichung [2] vorzufinden. Die Höhenfunktion wird in die isotherme, kompressible Reynolds-Gleichung [51, 52] eingesetzt, die die Druckverteilung $p(\varphi, z_B, t)$ auf den Keilflächen beschreibt:

$$\frac{1}{r^2}\frac{\partial}{\partial\varphi}\left(ph^3\frac{\partial p}{\partial\varphi}\right)+\frac{\partial}{\partial z_B}\left(ph^3\frac{\partial p}{\partial z_B}\right)=6\Omega\eta\frac{\partial\left(ph\right)}{\partial\varphi}+12\eta\frac{\partial\left(ph\right)}{\partial t}\,. \tag{1.8}$$

In der Gleichung ist r der Radius des Rotorzapfens, η die dynamische Viskosität der Luft und Ω die Winkelgeschwindigkeit des Rotors. Die Luft im Spalt wird als ideales Gas betrachtet. In den Taschen der Buchse wird die Spalthöhe als ausreichend groß angenommen, sodass in diesem Bereich der Umgebungsdruck p_a herrscht. Abb. 1.6 zeigt die Druckverteilung auf den Keilflächen über den Umfang und über die Breite b der Buchse. An den Rändern des Gebiets wird Umgebungsdruck angenommen (Dirichlet-Randbedingung $p = p_a$).

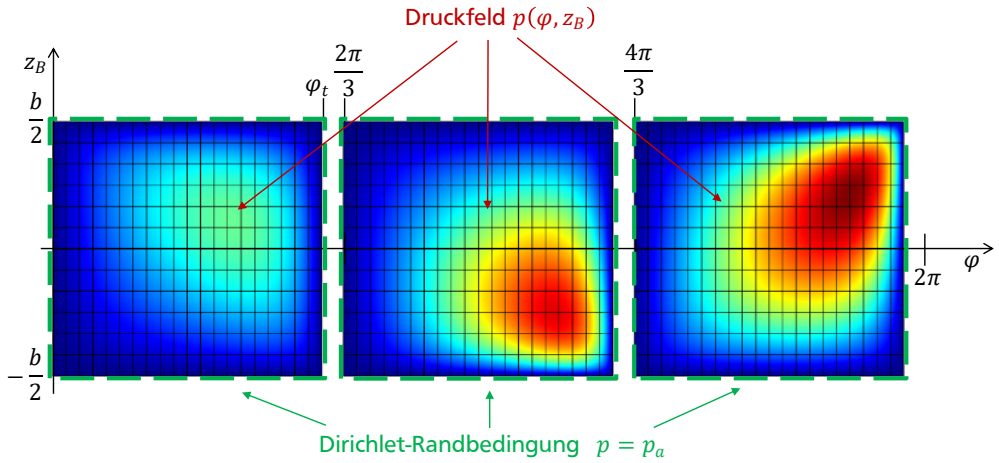

Abbildung 1.6: Druckverteilung auf den Keilflächen des Air Ring Bearings [1, 2].

Zur Berechnung der Druckverteilung $p\left(\varphi, z_B, t\right)$ wird die Reynolds-Gleichung (1.8) mit einem Finite-Elemente-Ansatz diskretisiert. Daraus resultieren 720 Elemente in Kombination mit einer quadratischen Ansatzfunktion. Dies ergibt $n_k = 3075$ Freiheitsgrade für die Druckverteilung. Die n_k diskreten Druckvariablen werden in dem Vektor $\boldsymbol{p} = [p_1, \ldots, p_{n_k}]^T$ zusammengefasst. Die diskretisierte Reynolds-Gleichung kann formal als ein System nichtlinearer gewöhnlicher Differentialgleichungen geschrieben werden:

$$\boldsymbol{f}\left(\boldsymbol{p}, \dot{\boldsymbol{p}}, t\right) = \boldsymbol{0}\,. \tag{1.9}$$

Das Gleichungssystem wird anschließend mit einem BDF-Verfahren (*Backward Differentiation Formula*, variable Integrationsordnung und variable Schrittweite [53]) numerisch integriert. Nach jedem Zeitschritt werden die hydrodynamischen Kräfte $\boldsymbol{F}_p$ und Momente $\boldsymbol{M}_p$ durch Integration des Drucks auf den Keilflächen berechnet:

$$\boldsymbol{F}_p = \begin{bmatrix} F_{p,x_B} \\ F_{p,y_B} \end{bmatrix} = \int_0^{2\pi} \int_{-\frac{b}{2}}^{\frac{b}{2}} p\left(\varphi, z_B\right) \cdot r \cdot \begin{bmatrix} \cos\left(\varphi + \alpha\right) \\ \sin\left(\varphi + \alpha\right) \end{bmatrix} \mathrm{d}z_B \ \mathrm{d}\varphi \,, \tag{1.10}$$

$$\boldsymbol{M}_p = \begin{bmatrix} M_{p,x_B} \\ M_{p,y_B} \end{bmatrix} = \int_0^{2\pi} \int_{-\frac{b}{2}}^{\frac{b}{2}} z_B \cdot p\left(\varphi, z_B\right) \cdot r \cdot \begin{bmatrix} -\sin\left(\varphi + \alpha\right) \\ \cos\left(\varphi + \alpha\right) \end{bmatrix} \mathrm{d}z_B \ \mathrm{d}\varphi \,. \tag{1.11}$$

In der zweiten Veröffentlichung [2] wird zusätzlich die Scherspannung τ des Luftfilms an der Innenfläche der Buchse berücksichtigt. Die Scherspannung τ wird durch folgende Gleichung beschrieben:

$$\tau\left(\varphi, z_B\right) = \frac{h}{2r} \cdot \frac{\partial p\left(\varphi, z_B\right)}{\partial \varphi} - \eta \frac{r\Omega}{h} \,. \tag{1.12}$$

Eine Integration von τ über den Keilflächen der Buchse führt zu den Kräften $\boldsymbol{F}_\tau$ und Momenten $\boldsymbol{M}_\tau$ der Scherspannung:

$$\boldsymbol{F}_\tau = \begin{bmatrix} F_{\tau,x_B} \\ F_{\tau,y_B} \end{bmatrix} = \int_0^{2\pi} \int_{-\frac{b}{2}}^{\frac{b}{2}} \tau\left(\varphi, z_B\right) \cdot r \cdot \begin{bmatrix} \sin\left(\varphi + \alpha\right) \\ -\cos\left(\varphi + \alpha\right) \end{bmatrix} \mathrm{d}z_B \ \mathrm{d}\varphi \,, \tag{1.13}$$

$$\boldsymbol{M}_\tau = \begin{bmatrix} M_{\tau,x_B} \\ M_{\tau,y_B} \end{bmatrix} = \int_0^{2\pi} \int_{-\frac{b}{2}}^{\frac{b}{2}} z_B \cdot \tau\left(\varphi, z_B\right) \cdot r \cdot \begin{bmatrix} \cos\left(\varphi + \alpha\right) \\ \sin\left(\varphi + \alpha\right) \end{bmatrix} \mathrm{d}z_B \ \mathrm{d}\varphi \,. \tag{1.14}$$

Aufgrund der geringen Viskosität von Luft sind $\boldsymbol{F}_\tau$ und $\boldsymbol{M}_\tau$ jedoch vergleichsweise klein. Eine detaillierte Herleitung von $\boldsymbol{F}_\tau$ und $\boldsymbol{M}_\tau$ ist [2] zu entnehmen. Die resultierenden Kräfte $\boldsymbol{F}_p$, $\boldsymbol{F}_\tau$ und Momente $\boldsymbol{M}_p$, $\boldsymbol{M}_\tau$ sind oben im buchsenfesten x_B, y_B, z_B-Koordinatensystem zerlegt und wirken auf die Buchse.

Mischreibung und Kontakt

Bei großen Exzentrizitäten des Rotorzapfens oder bei Verkippung der Buchsen ist mit Kontakt zwischen der Innenseite der Buchsen und dem Zapfen zu rechnen, siehe Abb. 1.7. In diesem Fall tritt Mischreibung auf. Damit ist ein rein hydrodynamischer Ansatz durch die Reynolds-Gleichung nicht mehr ausreichend, um die wechselwirkenden Kräfte zwischen

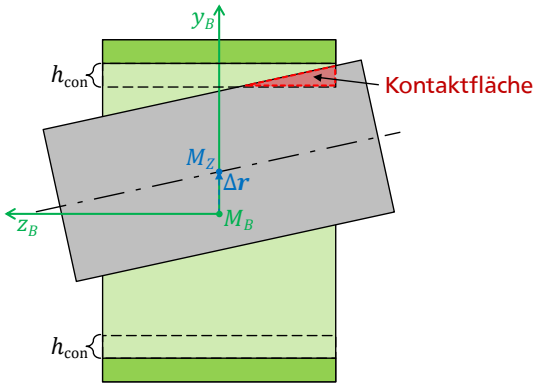

Abbildung 1.7: Kontakt zwischen Rotor und Buchse [2].

Buchse und Zapfen zu berechnen. Aus diesem Grund wird in der zweiten Veröffentlichung [2] ein Kontaktmodell entwickelt, das die Mischreibungseffekte berücksichtigt.

Zunächst wird der Parameter h_{con} zur Bestimmung von Mischreibungsgebieten eingeführt [54, 55]. Zusammen mit der Höhenfunktion $h(\varphi, z_B)$ wird die Kontaktabfrage formuliert:

i) In den Gebieten des Luftfilms, die $h(\varphi, z_B) \leq h_{\text{con}}$ erfüllen, herrscht Mischreibung. In diesem Fall sind zusätzlich zu den hydrodynamischen Kräften auch die Kontaktkräfte zu berücksichtigen.

ii) Für die Gebiete, in denen $h(\varphi, z_B) > h_{\text{con}}$ gilt, liegt keine Mischreibung vor und eine rein hydrodynamische Modellierung der Kräfte und Momente ist ausreichend.

Die Kontaktkräfte werden mit einem *Penalty-Ansatz* berechnet, der die Kontaktsteifigkeiten und die Kontaktdämpfungen berücksichtigt. Zunächst wird die lokale Eindringtiefe δ_{pen} berechnet durch:

$$\delta_{\text{pen}}\left(\varphi, z_B\right) = \max\left(h_{\text{con}} - h\left(\varphi, z_B\right), 0\right) \ . \tag{1.15}$$

Durch die Kontaktsteifigkeit pro Fläche c_{con} und die Kontaktdämpfung pro Fläche $d_{\text{con}}($ $\delta_{\text{pen}}(\varphi, z_B))$ kann die Kontaktpressung $p_{\text{con}}(\varphi, z_B)$ berechnet werden:

$$p_{\text{con}}\left(\varphi, z_B\right) = \max\left(c_{\text{con}} \cdot \delta_{\text{pen}}\left(\varphi, z_B\right) - d_{\text{con}}\left(\delta_{\text{pen}}\left(\varphi, z_B\right)\right) \cdot \frac{\mathrm{d}}{\mathrm{d}t} h\left(\varphi, z_B\right), 0\right) \ . \tag{1.16}$$

Hierbei ist die Kontaktdämpfung $d_{\text{con}}(\delta_{\text{pen}}(\varphi, z_B))$ eine nichtlineare Funktion der Eindringtiefe $\delta_{\text{pen}}(\varphi, z_B)$, um Unstetigkeiten in der Dämpfung bei Kontaktbeginn zu vermeiden [56]. Die Definition von $d_{\text{con}}(\delta_{\text{pen}}(\varphi, z_B))$ ist [2] zu entnehmen. Durch Integration von $p_{\text{con}}(\varphi, z_B)$ über die Keilflächen der Buchse werden die resultierenden Kontaktnormalkräfte $\boldsymbol{F}_{\text{con},N}$ und die resultierenden Momente $\boldsymbol{M}_{\text{con},N}$ berechnet:

$$\boldsymbol{F}_{\text{con},N} = \begin{bmatrix} F_{\text{con},N,x_B} \\ F_{\text{con},N,y_B} \end{bmatrix} = \int_0^{2\pi} \int_{-\frac{b}{2}}^{\frac{b}{2}} p_{\text{con}}(\varphi, z_B) \cdot r \cdot \begin{bmatrix} \cos(\varphi+\alpha) \\ \sin(\varphi+\alpha) \end{bmatrix} \, \mathrm{d}z_B \, \mathrm{d}\varphi \,, \tag{1.17}$$

$$\boldsymbol{M}_{\text{con},N} = \begin{bmatrix} M_{\text{con},N,x_B} \\ M_{\text{con},N,y_B} \end{bmatrix} = \int_0^{2\pi} \int_{-\frac{b}{2}}^{\frac{b}{2}} z_B \cdot p_{\text{con}}(\varphi, z_B) \cdot r \cdot \begin{bmatrix} -\sin(\varphi+\alpha) \\ \cos(\varphi+\alpha) \end{bmatrix} \, \mathrm{d}z_B \, \mathrm{d}\varphi \,. \tag{1.18}$$

Die tangentialen Reibspannungen des Kontakts $\tau_{\text{con}}(\varphi, z_B)$ werden anhand der Coulombschen Reibung mit dem Reibungskoeffizienten $\mu = 0.1$ berechnet:

$$\tau_{\text{con}}(\varphi, z_B) = \text{step}_{SL}(v_{\text{tan}}(\varphi, z_B)) \cdot \mu \cdot p_{\text{con}}(\varphi, z_B) \,. \tag{1.19}$$

Dabei entspricht $\text{step}_{SL}(v_{\text{tan}}(\varphi, z_B))$ einer geglätteten (stetigen) Approximation der Signumfunktion und $v_{\text{tan}}(\varphi, z_B)$ der relativen Oberflächengeschwindigkeit in tangentialer Richtung zwischen Rotorzapfen und Buchse, siehe [2]. Die Integration von $\tau_{\text{con}}(\varphi, z_B)$ über die Keilflächen führt zu den resultierenden tangentialen Reibungskräften $\boldsymbol{F}_{\text{con},T}$ und Momenten $\boldsymbol{M}_{\text{con},T}$:

$$\boldsymbol{F}_{\text{con},T} = \begin{bmatrix} F_{\text{con},T,x_B} \\ F_{\text{con},T,y_B} \end{bmatrix} = \int_0^{2\pi} \int_{-\frac{b}{2}}^{\frac{b}{2}} \tau_{\text{con}}(\varphi, z_B) \cdot r \cdot \begin{bmatrix} -\sin(\varphi+\alpha) \\ \cos(\varphi+\alpha) \end{bmatrix} \, \mathrm{d}z_B \, \mathrm{d}\varphi \,, \tag{1.20}$$

$$\boldsymbol{M}_{\text{con},T} = \begin{bmatrix} M_{\text{con},T,x_B} \\ M_{\text{con},T,y_B} \end{bmatrix} = \int_0^{2\pi} \int_{-\frac{b}{2}}^{\frac{b}{2}} z_B \cdot \tau_{\text{con}}(\varphi, z_B) \cdot r \cdot \begin{bmatrix} -\cos(\varphi+\alpha) \\ -\sin(\varphi+\alpha) \end{bmatrix} \, \mathrm{d}z_B \, \mathrm{d}\varphi \,. \tag{1.21}$$

Die detaillierte Beschreibung der Kontaktkräfte kann [2] entnommen werden. Die resultierenden Kontaktkräfte $\boldsymbol{F}_{\text{con},N}$, $\boldsymbol{F}_{\text{con},T}$ und Momente $\boldsymbol{M}_{\text{con},N}$, $\boldsymbol{M}_{\text{con},T}$ sind oben auch im buchsenfesten x_B, y_B, z_B-Koordinatensystem zerlegt und wirken auf die Buchse.

Resultierende Kräfte und Momente des Air Ring Bearings

Die resultierenden Lagerkräfte und -momente ergeben sich aus der Summation der Teilkräfte und -momente:

$$\boldsymbol{F}_{\text{ges}} = \begin{bmatrix} F_{\text{res},x_B} \\ F_{\text{res},y_B} \end{bmatrix} = \boldsymbol{F}_p + \boldsymbol{F}_\tau + \boldsymbol{F}_{\text{con},N} + \boldsymbol{F}_{\text{con},T}\,, \tag{1.22}$$

$$\boldsymbol{M}_{\text{ges}} = \begin{bmatrix} M_{\text{res},x_B} \\ M_{\text{res},y_B} \end{bmatrix} = \boldsymbol{M}_p + \boldsymbol{M}_\tau + \boldsymbol{M}_{\text{con},N} + \boldsymbol{M}_{\text{con},T}\,. \tag{1.23}$$

Die Berechnung der Momente $\boldsymbol{M}_{\text{ges}}$ des Air Ring Bearings ist nur bei einer Verkippung der Buchsen (d. h. in [2]) notwendig. Die resultierenden Kräfte und Momente entsprechen den Ausgangsvariablen des Finite-Elemente-Systems und werden in dem Vektor $\boldsymbol{y}_{\text{FEM}}$ zusammengefasst. Da das Rotorsystem aus zwei Buchsen besteht, werden insgesamt zwei Vektoren definiert: $\boldsymbol{y}_{\text{FEM1}} = [\boldsymbol{F}_{\text{ges1}}^T, \boldsymbol{M}_{\text{ges1}}^T]^T$ und $\boldsymbol{y}_{\text{FEM2}} = [\boldsymbol{F}_{\text{ges2}}^T, \boldsymbol{M}_{\text{ges2}}^T]^T$.

1.3.2 Mehrkörpermodell der Starrkörper

Das Rotorsystem wird in den Veröffentlichungen [1–3] als Mehrkörpersystem [57, 58] modelliert. Nach einer kurzen Beschreibung des Mehrkörpermodells wird die Modellierung der elastischen Struktur (Folienstruktur und Elastomer) erläutert. Anschließend wird auf die Bewegungsgleichungen des Mehrkörpersystems eingegangen. Das Rotorsystem mit Air Ring Bearings ist in Abb. 1.8 dargestellt.

Das Mehrkörpermodell beinhaltet den Rotor (bestehend aus einer Welle und einem Verdichter- und Turbinenrad), zwei Buchsen und die elastische Struktur (entweder als Folienstruktur oder Elastomer). Der Rotor lässt sich als Starrkörper modellieren, da die Eigenfrequenz seiner ersten frei-frei Biegemode mit ca. 2600 Hz deutlich über der Maximaldrehzahl der Simulationen von 2000 Hz liegt. Die Verschiebung des Rotors in z-Richtung wird verhindert, die Drehgeschwindigkeit des Rotors wird durch die Bindungsgleichung $\omega_{Z,z} - \Omega(t) = 0$ vorgegeben. Der Rotor verfügt somit über zwei translatorische und zwei rotatorische Freiheitsgrade. Die Positionen der Buchsen werden durch die axialen Koordinaten z_{ZV} und z_{ZT} beschrieben, eine axiale Verschiebung der Buchsen wird ebenfalls verhindert. In der ersten und dritten Veröffentlichung [1, 3] ist die Drehung der Buchsen relativ zum Rotor vollständig durch Bindungsgleichungen vorgegeben, in der zweiten Veröffentlichung [2] sind Verkippungen um die radialen x_B- und y_B-Achsen möglich. Die Buchsen besitzen somit jeweils zwei translatorische und in [2] zusätzlich zwei rotatorische Freiheitsgrade. Das Mehrkörpermodell hat demnach in [1, 3] insgesamt acht Freiheitsgrade und in [2] insgesamt zwölf Freiheitsgrade.

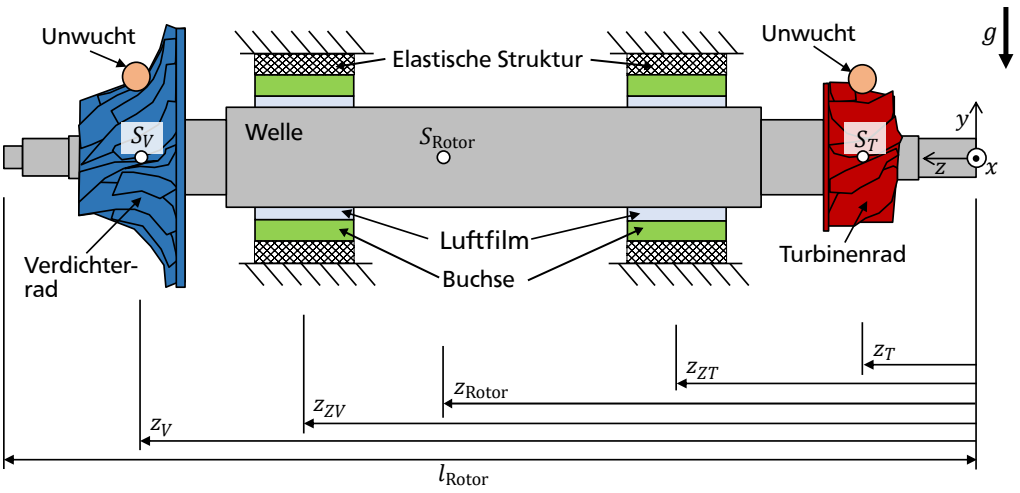

Abbildung 1.8: Übersicht des Rotorsystems mit Air Ring Bearings [1–3].

Modellierung der Folienstruktur

Je nach Design verhält sich die Folienstruktur stark anisotrop und nichtlinear [26, 42, 59]. In dieser Arbeit ist jedoch die Auswirkung des Luftfilms auf das dynamische und das Bifurkationsverhalten des Rotorsystems von besonderem Interesse. Aus diesem Grund wird für die Folienstruktur ein isotropes, linear-elastisches Hystereseverhalten angenommen, sodass die nichtlinearen Effekte des Luftfilms in den Simulationen deutlich zu erkennen sind. Die Steifigkeit der Struktur wird durch den Koeffizienten c_{foil} beschrieben. Da in Folienstrukturen hauptsächlich Dissipation durch Reibeffekte entsteht, wird Reibung nach Coulomb angenommen. Es wird eine konstante Reibkraft F_{fric} eingeführt, die stets entgegen der Bewegungsrichtung der Buchse wirkt. Eine Erweiterung des verwendeten Hystereseansatzes ist in [60, 61] beschrieben, indem die Folienstruktur durch ein 2D-Hysteresekennfeld mit nichtlinearen Steifigkeiten und veränderlichen Reibkräften modelliert wird.

Da in der zweiten Veröffentlichung [2] eine Verkippung der Buchsen möglich ist, werden auch die Drehsteifigkeiten und die Reibmomente der Folienstruktur modelliert. Dazu wird die Folienstruktur in eine linke und rechte Struktur aufgeteilt, siehe Abb. 1.9. Die Strukturen befinden sich an den Punkten $M_{B,\text{links}}$ bzw. $M_{B,\text{rechts}}$, die beide mit dem Abstand a von der Buchsenmitte M_B entfernt sind. Beide Strukturen haben eine Steifigkeit von $c_{\text{foil}}/2$ und eine Reibkraft von $F_{\text{fric}}/2$. Mit den Verschiebungen der Buchse $\boldsymbol{r}_{B,\text{links}}$ und

$\boldsymbol{r}_{B,\text{rechts}}$ an den Punkten $M_{B,\text{links}}$ und $M_{B,\text{rechts}}$ können die resultierenden Kräfte durch die folgenden Gleichungen berechnet werden:

$$\boldsymbol{F}_{\text{links}} = -\frac{c_{\text{foil}}}{2}\boldsymbol{r}_{B,\text{links}} - \frac{F_{\text{fric}}}{2}\frac{\dot{\boldsymbol{r}}_{B,\text{links}}}{\max\left(\left|\dot{\boldsymbol{r}}_{B,\text{links}}\right|, v_{\text{step}}\right)}\text{step}\left(\left|\dot{\boldsymbol{r}}_{B,\text{links}}\right|\right) , \tag{1.24}$$

$$\boldsymbol{F}_{\text{rechts}} = -\frac{c_{\text{foil}}}{2}\boldsymbol{r}_{B,\text{rechts}} - \frac{F_{\text{fric}}}{2}\frac{\dot{\boldsymbol{r}}_{B,\text{rechts}}}{\max\left(\left|\dot{\boldsymbol{r}}_{B,\text{rechts}}\right|, v_{\text{step}}\right)}\text{step}\left(\left|\dot{\boldsymbol{r}}_{B,\text{rechts}}\right|\right) . \tag{1.25}$$

Dabei ist $v_{\text{step}} = 1\text{E-}6\ \text{m s}^{-1}$ eine numerische Konstante und step(...) eine geglättete Approximation der Stufenfunktion um Unstetigkeiten sowie Nulldivisionen zu vermeiden. Die Definition von step(...) ist in [2] nachzulesen. Durch die Multiplikation des Hebelarms a mit den resultierenden Kräften werden die Momente der Folienstruktur berechnet.

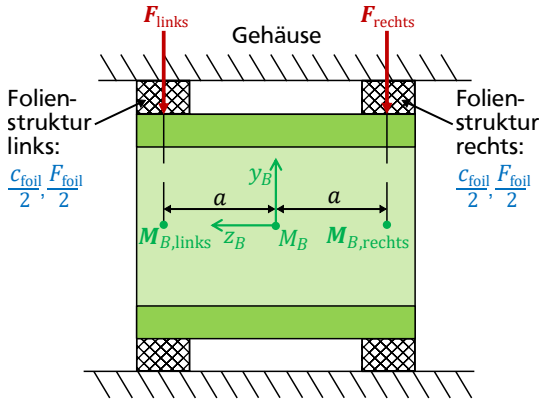

Abbildung 1.9: Seitenansicht des Air Ring Bearings mit einer Folienstruktur [2].

Modellierung des Elastomers

Bei Verwendung eines Elastomers wird isotropes, linear visko-elastisches Materialverhalten angenommen. Nichtlineare Steifigkeits- und Dämpfungseffekte, sowie frequenzabhängige Materialeigenschaften des Elastomers werden vernachlässigt, sodass die nichtlinearen Effekte des Luftfilms in den Simulationen deutlich zu erkennen sind. Die Eigenschaften des Elastomers werden durch den Steifigkeitskoeffienten c_{elast} und den Dämpfungskoeffizienten d_{visc} beschrieben. Analog zur Folienstruktur werden auch beim Elastomer Drehsteifigkeiten und Dämpfungsmomente modelliert, indem das Elastomer in ein linkes

und rechtes Elastomer an den Punkten $M_{B,\text{links}}$ bzw. $M_{B,\text{rechts}}$ aufgeteilt wird. Beide Elastomere haben eine Stefigkeit von $c_{\text{elast}}/2$ und eine Dämpfung von $d_{\text{visc}}/2$. Die Momente des Elastomers werden durch Multiplikation des Hebelarms a mit den Kräften berechnet. Mit den Verschiebungen der Buchse $\boldsymbol{r}_{B,\text{links}}$ und $\boldsymbol{r}_{B,\text{rechts}}$ an den Punkten $M_{B,\text{links}}$ und $M_{B,\text{rechts}}$ werden die Kräfte des Elastomers folgendermaßen berechnet:

$$\boldsymbol{F}_{\text{links}} = -\frac{c_{\text{elast}}}{2}\boldsymbol{r}_{B,\text{links}} - \frac{d_{\text{visc}}}{2}\dot{\boldsymbol{r}}_{B,\text{links}}\,, \tag{1.26}$$

$$\boldsymbol{F}_{\text{rechts}} = -\frac{c_{\text{elast}}}{2}\boldsymbol{r}_{B,\text{rechts}} - \frac{d_{\text{visc}}}{2}\dot{\boldsymbol{r}}_{B,\text{rechts}}\,. \tag{1.27}$$

Bewegungsgleichungen des Mehrkörpersystems

Die Bewegungsgleichungen des Mehrkörpersystems werden als differential-algebraisches Gleichungssystem (DAE) in der stabilisierten Index-2 Notation [62] formuliert:

$$\boldsymbol{M}\left(t,\boldsymbol{x}\right)\dot{\boldsymbol{x}} = \boldsymbol{M}\left(t,\boldsymbol{x}\right)\boldsymbol{v} - \boldsymbol{G}^{T}\left(t,\boldsymbol{x}\right)\boldsymbol{\mu}\,, \tag{1.28}$$

$$\boldsymbol{M}\left(t,\boldsymbol{x}\right)\dot{\boldsymbol{v}} = \boldsymbol{f}_{e}\left(t,\boldsymbol{x},\boldsymbol{v},\boldsymbol{u}_{\text{MKS}}\right) - \boldsymbol{G}^{T}\left(t,\boldsymbol{x}\right)\boldsymbol{\lambda}\,, \tag{1.29}$$

$$\boldsymbol{0} = \boldsymbol{g}\left(t,\boldsymbol{x}\right)\,, \tag{1.30}$$

$$\boldsymbol{0} = \dot{\boldsymbol{g}}\left(t,\boldsymbol{x},\boldsymbol{v}\right)\,. \tag{1.31}$$

Hierbei enthält der Vektor $\boldsymbol{x} \in \mathbb{R}^{\kappa}$ die Positionen und $\boldsymbol{v} \in \mathbb{R}^{\kappa}$ die Geschwindigkeiten des Mehrkörpersystems. Des Weiteren ist $\boldsymbol{M}\left(t,\boldsymbol{x}\right) \in \mathbb{R}^{\kappa\times\kappa}$ die Massenmatrix. Die äußeren Kräfte (z. B. die Kräfte der elastischen Struktur) sowie die Zentrifugal- und die Corioliskräfte sind in dem Vektor $f_e\left(t,\boldsymbol{x},\boldsymbol{v},\boldsymbol{u}_{\text{MKS}}\right)$ enthalten. Dabei entspricht $\boldsymbol{u}_{\text{MKS}}$ den Kräften und den Momenten aus den Luftfilmen, die das Mehrkörpersystem als Eingabevariablen über die Co-Simulationsschnittstelle erhält. Aus den κ_c algebraischen Bindungsgleichungen $\boldsymbol{g}\left(t,\boldsymbol{x}\right) = \boldsymbol{0}$, $\boldsymbol{g} \in \mathbb{R}^{\kappa_c}$ in Gleichung (1.30) ergeben sich die Bindungskräfte oder Bindungsmomente $\boldsymbol{G}^{T}\left(t,\boldsymbol{x}\right)\boldsymbol{\lambda}$. Dabei ist $\boldsymbol{G} = \frac{\partial \boldsymbol{g}}{\partial \boldsymbol{x}} \in \mathbb{R}^{\kappa_c\times\kappa}$ die Jacobi-Matrix der Bindungsgleichungen und $\boldsymbol{\lambda} \in \mathbb{R}^{\kappa_c}$ der Vektor der unbekannten Lagrange-Multiplikatoren. In der Index-2 Notation werden die Bindungsgleichungen $\dot{\boldsymbol{g}}\left(t,\boldsymbol{x},\boldsymbol{v}\right) = \boldsymbol{0}$ zusätzlich auf der Geschwindigkeitsebene angewendtet und damit weitere unbekannte Lagrange-Multiplikatoren $\boldsymbol{\mu} \in \mathbb{R}^{\kappa_c}$ eingeführt. Zur Lösung des differential-algebraischen Gleichungssystems findet ein BDF-Verfahren (variable Integrationsordnung, variable Schrittweite [53]) Anwendung.

Aus den Positionen $\boldsymbol{x}$ und den Geschwindigkeiten $\boldsymbol{v}$ werden die relativen Positionen zwischen Rotor und Zapfen $\Delta\boldsymbol{r}_V$, $\Delta\boldsymbol{r}_T$, $\alpha_{\text{tilt},V}$, $\beta_{\text{tilt},V}$, $\alpha_{\text{tilt},T}$ und $\beta_{\text{tilt},T}$ sowie deren Zeitableitungen an den Lagerstellen berechnet. Diese kinematischen Größen werden inklusive der Rotordrehzahl $\Omega(t)$ an die Finite-Elemente-Systeme übergeben.

1.3.3 Co-Simulationsmodell des gesamten Rotorsystems

Nachdem in den Abschnitten 1.3.1 und 1.3.2 sowohl das Finite-Elemente-System als auch das Mehrkörpersystem erläutert worden sind, behandelt dieser Abschnitt das Co-Simulationsmodell des Rotorsystems. Das Co-Simulationsmodell besteht aus insgesamt drei Subsystemen. Das erste Subsystem ist das Mehrkörpersystem (MKS) bestehend aus Rotor und Buchsen. Die anderen beiden Subsysteme sind die Finite-Elemente-Systeme (FEM1 und FEM2) der beiden Luftfilme in den Air Ring Bearings. Die drei Subsysteme werden durch einen sequentiellen, expliziten Co-Simulationsansatz (Gauss-Seidel-Verfahren) gekoppelt [63].

Für die Kommunikation zwischen den Subsystemen werden Kopplungsvariablen (Eingangsvariablen $\boldsymbol{u}$ und Ausgangsvariablen $\boldsymbol{y}$) definiert. Die Eingangsvariablen des Mehrkörpersystems entsprechen den Ausgangsvariablen der Finite-Elemente-Systeme. Im Einzelnen sind dies die resultierenden Kräfte und Momente der beiden Luftfilme $\boldsymbol{u}_{\text{MKS}} = [\boldsymbol{y}_{\text{FEM1}}^T, \boldsymbol{y}_{\text{FEM2}}^T]^T = [\boldsymbol{F}_{\text{FEM1}}^T, \boldsymbol{M}_{\text{FEM1}}^T, \boldsymbol{F}_{\text{FEM2}}^T, \boldsymbol{M}_{\text{FEM2}}^T]^T$. Die Ausgangsvariablen des Mehrkörpersystems sind die kinematischen Größen an den Lagerstellen $\boldsymbol{y}_{\text{MKS}} = [\Delta\boldsymbol{r}_1^T, \Delta\dot{\boldsymbol{r}}_1^T, \Delta\boldsymbol{r}_2^T, \Delta\dot{\boldsymbol{r}}_2^T, \alpha_{\text{tilt1}}, \beta_{\text{tilt1}}, \dot{\alpha}_{\text{tilt1}}, \dot{\beta}_{\text{tilt1}}, \alpha_{\text{tilt2}}, \beta_{\text{tilt2}}, \dot{\alpha}_{\text{tilt2}}, \dot{\beta}_{\text{tilt2}}, \Omega]^T$. Aus $\boldsymbol{y}_{\text{MKS}}$ ergeben sich die Eingangsvariablen der beiden Finite-Elemente-Systeme $\boldsymbol{u}_{\text{FEM1}}$ und $\boldsymbol{u}_{\text{FEM2}}$. Die strukturelle Anordnung der Subsysteme ist in Abb. 1.10 dargestellt.

Neben den Schnittstellen der Subsysteme wird auch der Variablenaustausch während der Co-Simulation zeitlich festgelegt. Die Subsysteme tauschen die Kopplungsvariablen nur zu festgelegten Makrozeitpunkten T_N ($N = 0, 1, ...$) aus. Zwischen den Zeitpunkten findet keine Kommunikation statt und die Subsysteme werden unabhängig voneinander integriert. Die benötigten Kopplungsvariablen werden dabei durch Polynomansätze extrapoliert bzw. interpoliert [64, 65]. Die Integration des Mehrkörpersystems bestimmt das Gitter der Makrozeitpunkte: Die Abstände der Makrozeitpunkte (Makroschrittweite H_N) entsprechen den Integrationsschrittweiten des Mehrkörpersystems.

Die Integration in jedem Zeitschritt erfolgt abwechselnd im Mehrkörpersystem und in den Finite-Elemente-Systemen: Sobald die Integration im Mehrkörpersystem abgeschlossen ist, ruht das System solange, bis die anschließende Integration in allen Finite-Elemente-Systemen abgeschlossen ist. Anschließend ruhen die Finite-Elemente-Systeme bis die Integration des nächsten Zeitschritts im Mehrkörpersystem beendet ist.

Die Integration über das Zeitintervall $[T_N, T_{N+1}]$ wird wie folgt durchgeführt:

1) **Integration des Mehrkörpersystems, Finite-Elemente-Systeme ruhen:**
   Zunächst findet die Integration von T_N nach T_{N+1} im Mehrkörpersystem statt. Die erforderlichen Lagerkräfte und Momente (Eingangsvariablen $\boldsymbol{u}_{\text{MKS}}$) sind in diesem Zeitintervall jedoch unbekannt. Daher wird auf vergangene Makrozeitpunkte T_N, T_{N-1}, T_{N-2}, etc. zurückgegriffen, zu denen $\boldsymbol{u}_{\text{MKS}}$ bekannt ist. Mithilfe eines

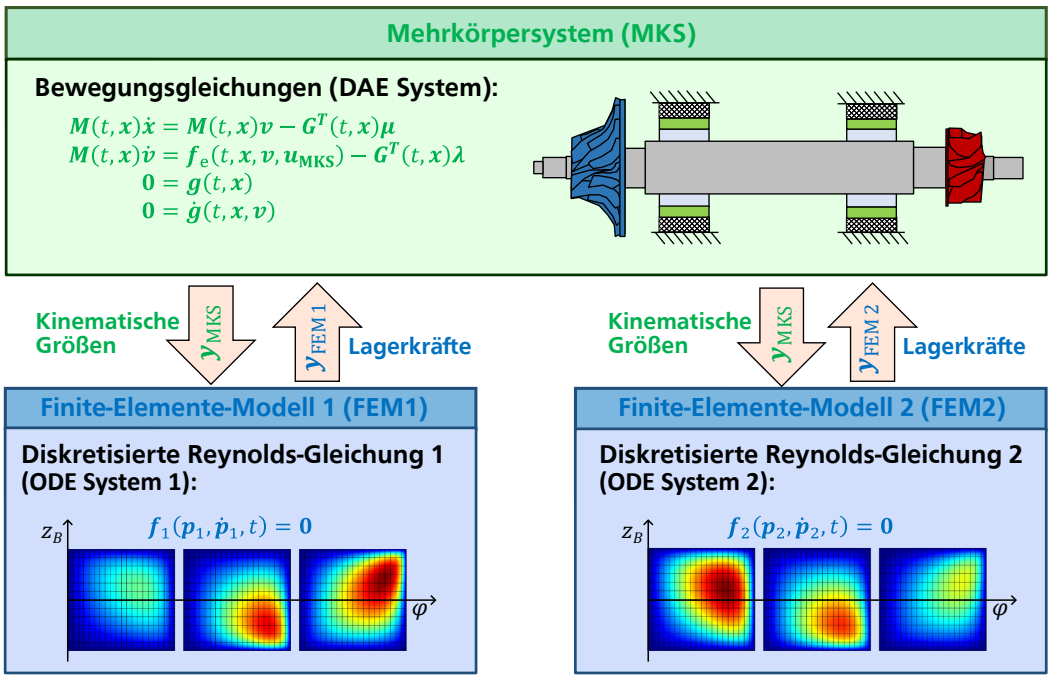

Abbildung 1.10: Gekoppelte Subsysteme des Air Ring Bearings [2].

Polynoms werden die Eingangsvariablen im Intervall $[T_N, T_{N+1}]$ extrapoliert. In dieser Arbeit wird dafür ein quadratisches Polynom verwendet. Mit den extrapolierten Kräften und Momenten kann nun die Integration im Mehrkörpersystem durchgeführt werden. Nach erfolgter Integration werden die Ausgangsvariablen des Mehrkörpersystems $\boldsymbol{y}_{\text{MKS}}$ berechnet und an die Finite-Elemente-Systeme übergeben. Anschließend ruht das Mehrkörpersystem, bis es die Lagerkräfte und Momente von allen Finite-Elemente-Systemen zum Zeitpunkt T_{N+1} erhalten hat, um die Integration über dem nächsten Zeitintervall fortzusetzen.

2) **Mehrkörpersubsystem ruht, Integration der Finite-Elemente-Systeme:**
Jedes Finite-Elemente-System erhält aus dem Mehrkörpersystem die kinematischen Größen (Eingangsvariablen $\boldsymbol{u}_{\text{FEM1}}$ bzw. $\boldsymbol{u}_{\text{FEM2}}$) zum Zeitpunkt T_{N+1}. Die Eingangsvariablen sind zu den Makrozeitpunkten T_{N+1}, T_N, T_{N-1} etc. bekannt und werden durch ein Polynom im Intervall $[T_N, T_{N+1}]$ interpoliert. In dieser Arbeit kommt dafür ebenfalls ein quadratisches Polynom zur Anwendung. Mit den interpolierten Eingangsgrößen findet nun die Integration der Finite-Elemente-Systeme statt. Die

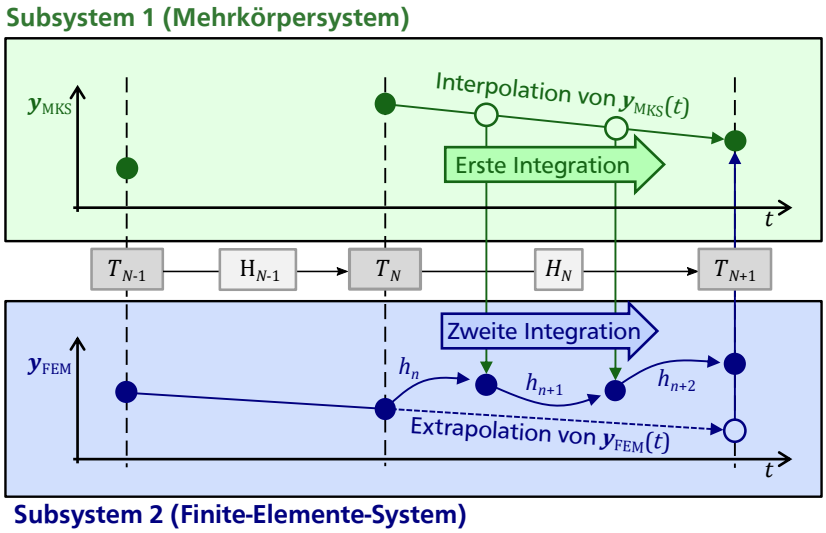

Abbildung 1.11: Explizites Gauss-Seidel-Verfahren für zwei Subsysteme mit linearen Extra- und Interpolationspolynomen [2, 66].

berechneten Kräfte und Momente $\boldsymbol{y}_{\text{FEM1}}$ und $\boldsymbol{y}_{\text{FEM2}}$ zum Zeitpunkt T_{N+1} werden nun an das Mehrkörpersystem übermittelt. Anschließend ruhen die Finite-Elemente-Systeme, bis sie die Eingangsvariablen für die Integration des nächsten Intervalls erhalten. Es ist möglich, dass die Finite-Elemente-Systeme die Integration in mehreren kleinen Integrationsschritten (Mikroschrittweite h_n) durchführen. Die Finite-Elemente-Systeme rechnen unabhängig voneinander und kommunizieren direkt mit dem Mehrkörpersystem.

Abb. 1.11 veranschaulicht die Integration über das Intervall $[T_N, T_{N+1}]$ mit linearen Extra- und Interpolationspolynomen.

1.4 Modellparameter des Rotorsystems

Als Grundlage für die Untersuchungen des Rotorsystems mit Air Ring Bearings dienen Hochlaufsimulationen. Dabei wird die Drehgeschwindigkeit des Rotors kinematisch mit $\Omega(t) = 2\pi/3 \cdot 2000 \cdot t \text{ s}^{-2}$ vorgegeben, was einem linearen Hochlauf von 0 auf 2000 Hz in 3 Sekunden entspricht. Zu Beginn der Simulationen befinden sich sowohl der Rotor als auch die Buchsen ruhend auf der z-Achse des raumfesten Referenzsystems. Die drei Körper sind ohne Verkippung entlang der z-Achse ausgerichtet. Um die nichtlinearen Effekte der

Luftfilme in den Air Ring Bearings besser sichtbar zu machen, wird in den Simulationen auf zusätzliche Unwuchten verzichtet. Untersuchungen in der ersten Veröffentlichung [1] haben gezeigt, dass Unwuchten nur einen geringen Einfluss auf das Verhalten des Rotorsystems dieser Arbeit haben.

In Tabelle 1.2 sind wichtige Parameter des Rotorsystems mit Air Ring Bearings zur Übersicht aufgelistet. Die Steifigkeiten der elastischen Struktur c_{foil} bzw. c_{elast} sowie die Reibkraft F_{fric} bzw. die viskose Dämpfung d_{visc} sind in der Tabelle nicht enthalten. Aufgrund ihres großen Einflusses auf das dynamische Verhalten des Rotorsystems werden sie für die Hochläufe stets variiert und für jede Simulation einzeln angegeben. In der dritten Veröffentlichung [3] wird zusätzlich das Lagerspiel C und die Keilhöhe ΔH in Parameterstudien variiert. Beide Parameter zeigen ebenfalls einen großen Einfluss auf das dynamische Verhalten des Rotorsystems.

Tabelle 1.2: Parameter des Rotorsystems

Rotor		
Masse	$m_{\text{Rotor}} = 830$ g	
Trägheit	$\boldsymbol{J}_{\text{Rotor}} = \text{diag}(2500 \text{ kg mm}^2, 2500 \text{ kg mm}^2, 120 \text{ kg mm}^2)$	
Radius Zapfen	$r = 15$ mm	
Länge	$l_{\text{Rotor}} = 250$ mm	
Position Schwerpunkt	$z_{\text{Rotor}} = 125$ mm	
Position Verdichterlager	$z_{ZV} = 170$ mm	
Position Turbinenlager	$z_{ZT} = 60$ mm	
Buchse		
Masse	$m_{\text{Buchse}} = 50$ g	
Trägheit	$\boldsymbol{J}_{\text{Buchse}} = \text{diag}(10.3 \text{ kg mm}^2, 10.3 \text{ kg mm}^2, 13.7 \text{ kg mm}^2)$	
Breite	$b = 28.6$ mm	
Luftspalt		
Lagerspiel	$C = 30$ µm	(Warmspiel, Rotoraufweitung durch die Fliehkraft wird vernachlässigt)
Keilhöhe	$\Delta H = 20$ µm	
Keillänge	$\varphi_t = 110°$	
Einbauwinkel	$\alpha = 180° - \varphi_t$	
Hebelarm	$a = 10$ mm	
Viskosität Luft	$\eta = 20.936$E-6 kg m^{-1} s^{-1} (angenommene Temperatur der Luft: $80°$C)	

2 Ergebnisse

Dieses Kapitel behandelt das dynamische Verhalten von Rotorsystemen mit Air Ring Bearings. Zunächst zeigt Abschnitt 2.1 die Eigenmoden des linearisierten Rotorsystems. In Abschnitt 2.2 werden die drei gängigen Bifurkationspfade des Rotorsystems (*Bifurkationspfad 1*, *Bifurkationspfad 2a* und *Bifurkationspfad 2b*) anhand von Beispielsimulationen erläutert. Anhand der Bifurkationspfade wird in Abschnitt 2.3 die Dynamik, das Stabilitäts- und das Bifurkationsverhalten von Rotorsystemen mit Air Ring Bearings beschrieben. In Abschnitt 2.4 werden schließlich Optimierungsstudien des Rotorsystems vorgestellt, die sich insbesondere auch mit der Innengeometrie der Buchsen befassen.

2.1 Modalanalyse des linearisierten Rotorsystems

Für die Modalanalyse werden die Luftilme im Modell durch lineare (Dreh-)Federn mit den geschätzten Steifigkeiten von $c_{\text{luft,tilt},\alpha} = c_{\text{luft,tilt},\beta} \approx 2.6\text{E+4 N mm rad}^{-1}$ und $c_{\text{luft,trans},x} = c_{\text{luft,trans},y} \approx 755\ \text{N mm}^{-1}$ ersetzt. Zur Abschätzung der Federsteifigkeiten sind stationäre Finite-Elemente-Simulationen des Luftfilms durchgeführt worden, die in der zweiten Veröffentlichung [2] ausführlich beschrieben sind. Die elastische Struktur (Folienstruktur oder Elastomer) wird durch lineare Federn (Steifigkeit $c_{\text{Buchse},x} = c_{\text{Buchse},y} = 100\,\text{N mm}^{-1}$) modelliert. Dissipationseffekte werden bei der Eigenwertanalyse nicht berücksichtigt. Es wird eine Rotordrehzahl von $\Omega = 1500$ Hz angenommen. Die Berechnung der Eigenmoden liefert dabei die folgenden Ergebnisse [2]:

- *Mode_1(b)* und *Mode_1(f)* sind konische Moden mit einem Schwingungsknoten am turbinenseitigen Lager (Rückwärtsmode *Mode_1(b)* hat eine Eigenfrequenz von ca. 45 Hz; die Eigenfrequenz der entsprechenden Vorwärtsmode *Mode_1(f)* beträgt ca. 69 Hz; Rotor und Buchsen oszillieren gleichphasig).
- *Mode_2(b)* und *Mode_2(f)* sind konische Moden mit einem Schwingungsknoten am verdichterseitigen Lager (Rückwärtsmode *Mode_2(b)*: ca. 71 Hz; Vorwärtsmode *Mode_2(f)*: ca. 112 Hz; Rotor und Buchsen oszillieren gleichphasig).

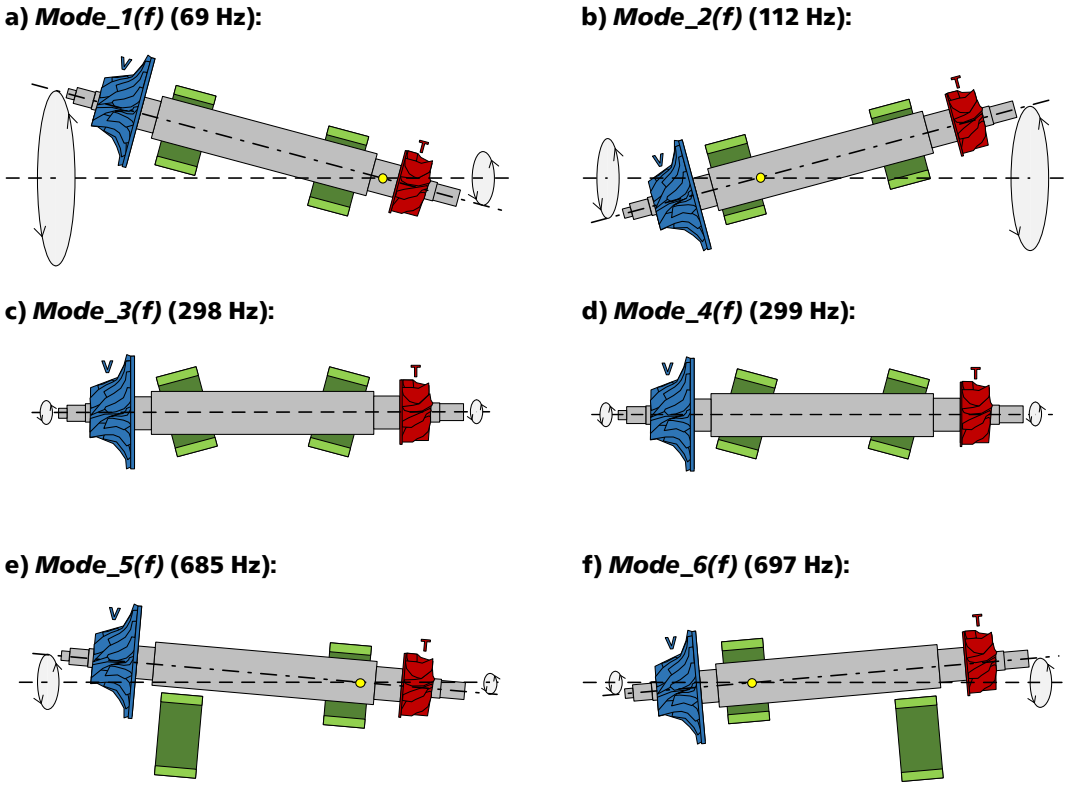

Abbildung 2.1: Vorwärtsmoden des linearisierten Rotorsystems mit Air Ring Bearings [2].

- *Mode_3(b)* und *Mode_3(f)* sind Verkippungsmoden der Buchsen (Rückwärtsmode *Mode_3(b)*: ca. 298 Hz; Vorwärtsmode *Mode_3(f)*: ca. 298 Hz; die Buchsen oszillieren gegenphasig; der Rotor bewegt sich nur geringfügig).

- *Mode_4(b)* und *Mode_4(f)* sind ebenfalls Verkippungsmoden der Buchsen (Rückwärtsmode *Mode_4(b)*: ca. 299 Hz; Vorwärtsmode *Mode_4(f)* ca. 299 Hz; die Buchsen oszillieren gleichphasig; der Rotor bewegt sich nur geringfügig).

- *Mode_5(b)* und *Mode_5(f)* sind translatorische Buchsenmoden mit einem Schwingungsknoten am turbinenseitigen Lager (Rückwärtsmode *Mode_5(b)*: ca. 682 Hz; Vorwärtsmode *Mode_5(f)*: ca. 685 Hz; Rotor und Buchsen oszillieren gegenphasig).

- *Mode_6(b)* und *Mode_6(f)* sind translatorische Buchsenmoden mit einem Schwingungsknoten am verdichterseitigen Lager (Rückwärtsmode *Mode_6(b)*: ca. 693 Hz; Vorwärtsmode *Mode_6(f)*: ca. 697 Hz; Rotor und Buchsen oszillieren gegenphasig).

In Abb. 2.1 sind die resultierenden Vorwärtsmoden dargestellt.

2.2 Hochlaufsimulationen von Rotorsystemen mit Air Ring Bearings

Dieser Abschnitt stellt die drei gängigen Bifurkationspfade des Rotorsystems (Bifurkationspfad 1, Bifurkationspfad 2a und Bifurkationspfad 2b) anhand konkreter Simulationen vor. Für die Hochläufe werden Air Ring Bearings mit einer Folienstruktur verwendet. Die Rotorsysteme der Simulationen unterscheiden sich in der Steifigkeit c_{foil} und in der Reibkraft F_{fric} der Folienstruktur. Zusätzlich wird für Bifurkationspfad 2b die Buchsenmasse m_{Buchse} erhöht. Alle weiteren Parameter der Rotorsysteme bleiben in den Simulationen unverändert. Die Hochläufe sind ebenfalls in der zweiten Veröffentlichung [2] beschrieben.

2.2.1 Bifurkationspfad 1

Zur Veranschaulichung des Bifurkationspfads 1 ist in Abb. 2.2 ein Rotorhochlauf mit einer Steifigkeit $c_{\text{foil}} = 600$ N mm^{-1} und einer Reibkraft $F_{\text{fric}} = 6$ N dargestellt. Dabei zeigt Abb. 2.2a die dimensionslosen Exzentrizitäten $\varepsilon_V = \Delta r_V / C$ und $\varepsilon_T = \Delta r_T / C$ des Rotorzapfens in der Verdichter- und der Turbinenbuchse. Aufgrund der Keilgeometrie des Luftspalts sind Werte von ε_V und ε_T größer 1 möglich. Das nachfolgend beschriebene Verhalten des Rotorsystems ist in Abb. 2.2 dargestellt.

- Im Bereich $0 \leq t \leq 700$ ms rotiert der Rotor in einem stabilen Gleichgewicht.
- Bei einer Zeit von $t \approx 700$ ms ist eine subkritische Hopf-Bifurkation zu erkennen und das System geht in einen Zustand stabiler, quasiperiodischer Oszillationen (Whirl/Whip-Oszillationen) über. Der verdichterseitige Whirl/Whip regt dabei die konische Vorwärtsmode *Mode_1(f)* an, der turbinenseitige Whirl/Whip regt die konische Vorwärtsmode *Mode_2(f)* an, siehe Abschnitt 2.1.
- Eine zweite Bifurkation tritt zum Zeitpunkt $t \approx 1700$ ms ein. Bei der Frequenz des turbinenseitigen Whirl/Whips ist ein Sprung zu erkennen. Nach diesem verlaufen die verdichter- und turbinenseitigen Whirl/Whip-Oszillationen synchron und eine zylindrische Mode wird angeregt.

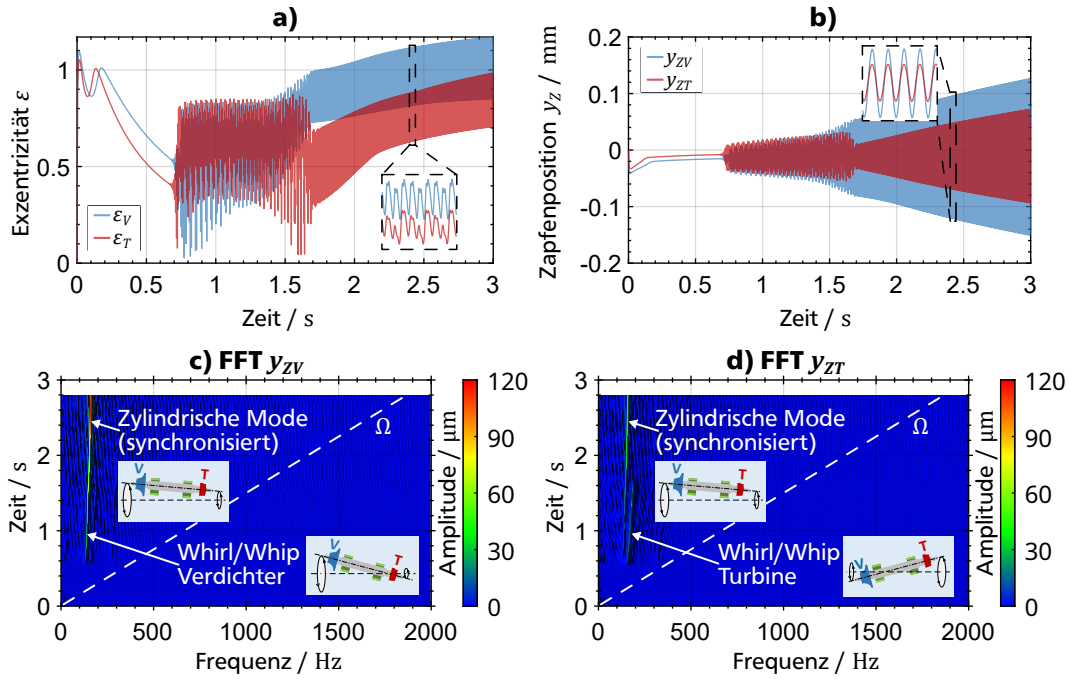

Abbildung 2.2: Hochlaufsimulation mit $c_{\text{foil}} = 600\ \text{N mm}^{-1}$ und $F_{\text{fric}} = 6\ \text{N}$ (Bifurkationspfad 1) [2]: (a) Verdichter- und turbinenseitige dimensionslose Exzentrizitäten ε_V, ε_T; (b) Verdichter- und turbinenseitige vertikale Zapfenpositionen y_{ZV}, y_{ZT}; (c) Frequenzsprektrum von y_{ZV}; (d) Frequenzsprektrum von y_{ZT}.

- Trotz weiterer Zunahme der Rotordrehzahl bleibt die Frequenz der Whirl/Whip-Oszillationen nahezu konstant. Dagegen nehmen Amplituden der Schwingungen jedoch deutlich zu.

Obwohl die selbsterregten Whirl/Whip-Oszillationen rechnerisch stabil sind, kommt der Rotorzapfen der Innenfläche der Buchsen gefährlich nahe, siehe Abb. 2.2a. Es ist daher von einem Kontakt zwischen Rotor und Buchse auszugehen. Aus technischer Sicht sollte daher der Betrieb des Rotorsystems in Kombination mit Bifurkationspfad 1 vermieden werden.

2.2.2 Bifurkationspfad 2a

Für die Darstellung von Bifurkationspfad 2a wird die Steifigkeit auf $c_{\text{foil}} = 400\ \text{N mm}^{-1}$ gesenkt, die Reibkraft bleibt unverändert $F_{\text{fric}} = 6\ \text{N}$. Das Ergebnis des simulierten Rotorhochlaufs ist Abb. 2.3 zu entnehmen. Das charakteristische Verhalten lässt sich wie folgt beschreiben:

- In dem Zeitraum $0 \leq t \leq 700$ ms befindet sich das Rotorsystem in einem stabilen Gleichgewicht.
- Zum Zeitpunkt $t \approx 700$ ms ist eine Bifurkation in eine quasiperiodische Oszillation (Whirl/Whip-Oszillation) zu erkennen. Dabei regt der verdichterseitige Whirl/Whip die konische Vorwärtsmode *Mode_1(f)* und der turbinenseitige Whirl/Whip die konische Vorwärtsmode *Mode_2(f)* an, siehe Abschnitt 2.1.

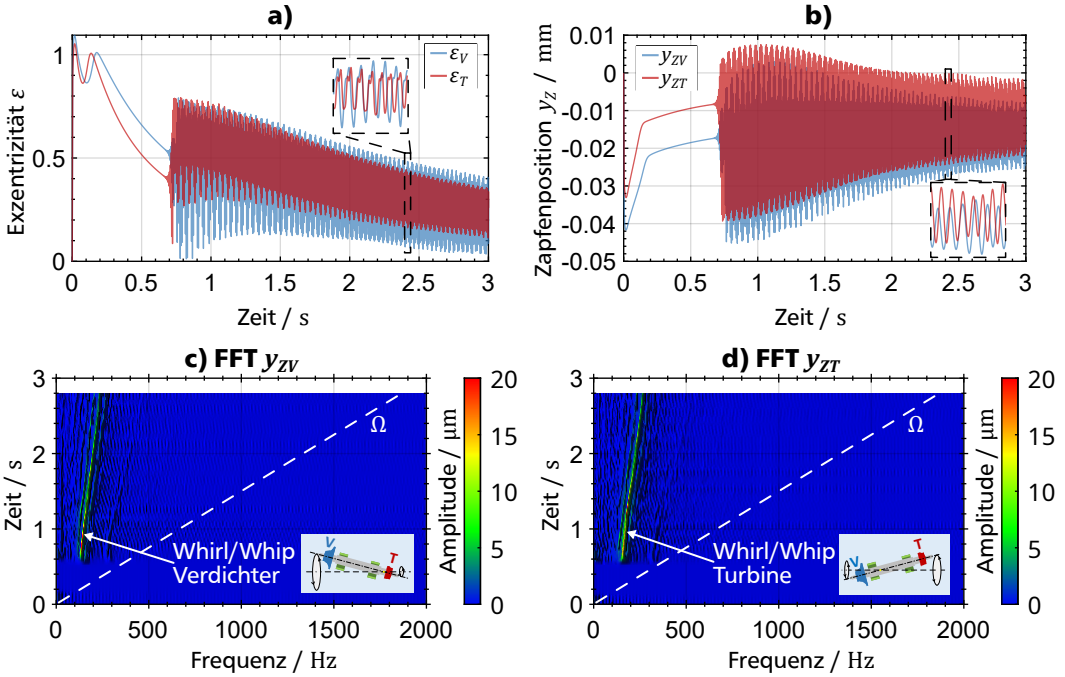

Abbildung 2.3: Hochlaufsimulation mit $c_{\text{foil}} = 400\ \text{N mm}^{-1}$ und $F_{\text{fric}} = 6\ \text{N}$ (Bifurkationspfad 2a) [2]: (a) Dimensionslose Exzentrizitäten ε_V, ε_T; (b) Zapfenpositionen y_{ZV}, y_{ZT}; (c) Frequenzsprektrum von y_{ZV}; (d) Frequenzsprektrum von y_{ZT}.

- Bei weiterer Erhöhung der Rotordrehgeschwindigkeit nimmt auch die Frequenz der Whirl/Whip-Oszillationen zu. Dagegen ist eine deutliche Abnahme in der Amplitude der Schwingungen zu erkennen.

Die Amplituden der gezeigten Simulation sind moderat (ε_V, ε_T liegen im höheren Drehzahlbereich deutlich unter 1), sodass ein technisch sicherer Betrieb von Rotorsystemen mit Air Ring Bearings möglich ist.

2.2.3 Bifurkationspfad 2b

Für die Simulation von Bifurkationspfad 2b wird die Foliensteifigkeit erneut auf $c_{\text{foil}} = 100\ \text{N mm}^{-1}$ und die Reibkraft auf $F_{\text{fric}} = 1\ \text{N}$ reduziert. Darüber hinaus wird die Masse der Buchsen erhöht auf $m_{\text{Buchse}} = 100\ \text{g}$. Die Ergebnisse der Simulation sind in Abb. 2.4 dargestellt.

- In dem Zeitintervall $0 \leq t \leq 700$ ms befindet sich der Rotor in einer stabilen Gleichgewichtslage.
- Bei $t \approx 700$ ms wird das Gleichgewicht instabil und das Rotorsystem geht in einen Zustand selbsterregter Whirl/Whip-Oszillationen über. Der verdichterseitige Whirl/Whip regt die konische Vorwärtsmode *Mode_1(f)* an, und der turbinenseitige Whirl/Whip regt die konische Vorwärtsmode *Mode_2(f)* an, siehe Abschnitt 2.1.
- Bei weiterer Erhöhung der Rotordrehzahl sind in den Spektrogrammen weitere subsynchrone Frequenzen zu erkennen. Eine mögliche Ursache hierfür sind Stick/Slip-Effekte in der Folienstruktur. Insgesamt erscheint die Schwingung in diesem Bereich chaotisch.
- Bei einer Zeit von $t \approx 2400$ ms ist eine weitere Bifurkation festzustellen. Die Whirl/Whips regen nun die Verkippungsmoden der Buchsen *Mode_3(f)* aus Abschnitt 2.1 an. Die Kardanwinkel der Buchsen zeigen einen Amplitudensprung, siehe Abb. 2.4h. In den Spektrogrammen der Kardanwinkel in Abb. 2.4i-j ist ab dem Zeitpunkt der Bifurkation eine Oszillation mit einer Frequenz von ca. 300 Hz zu Beginn zu erkennen. Mit Blick auf die Buchsenposition in Abb. 2.4e-g fällt auf, dass die Luftfilme auch die translatorischen Buchsenmoden *Mode_5(f)* und *Mode_6(f)* anregen. Die Frequenz der translatorischen Moden beträgt ca. 600 Hz und ist damit doppelt so groß wie die Frequenz der Verkippungsmoden. Dieser Effekt der 1:2 Modensynchronisation ist in der zweiten Veröffentlichung [2] ausführlich beschrieben und erklärt.

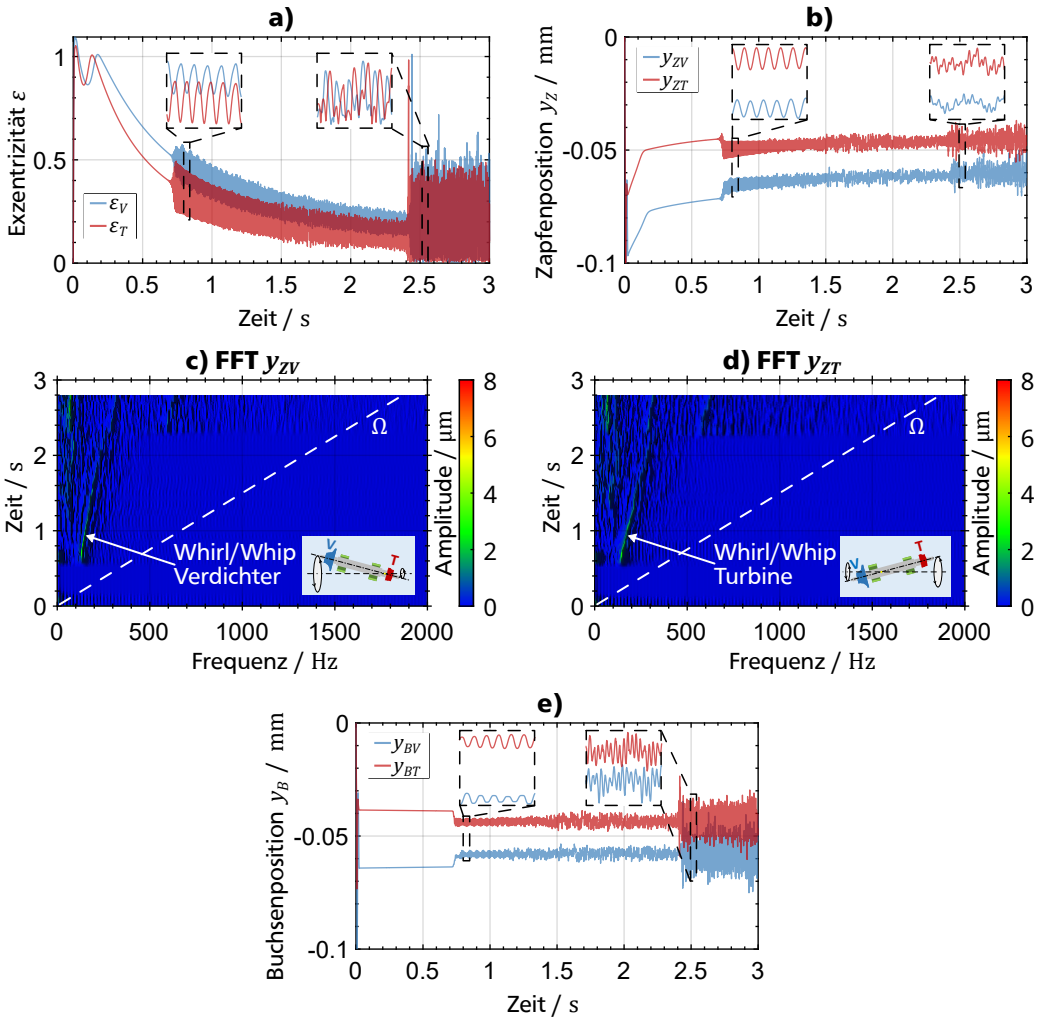

Abbildung 2.4: Hochlaufsimulation mit $c_{\text{foil}} = 100\ \text{N mm}^{-1}$, $F_{\text{fric}} = 1\ \text{N}$ und $m_{\text{Buchse}} = 100\ \text{g}$ (Bifurkationspfad 2b) [2]: (a) Dimensionslose Exzentrizitäten ε_V, ε_T; (b) Zapfenpositionen y_{ZV}, y_{ZT}; (c) Frequenzsprektrum von y_{ZV}; (d) Frequenzsprektrum von y_{ZT}; (e) Buchsenpositionen y_{BV}, y_{BT}; (f) Frequenzsprektrum von y_{BV}; (g) Frequenzsprektrum von y_{BT}; (h) Kardanwinkel $\alpha_{\text{tilt},V}$, $\alpha_{\text{tilt},T}$; (i) Frequenzsprektrum von $\alpha_{\text{tilt},V}$; (j) Frequenzsprektrum von $\alpha_{\text{tilt},T}$.

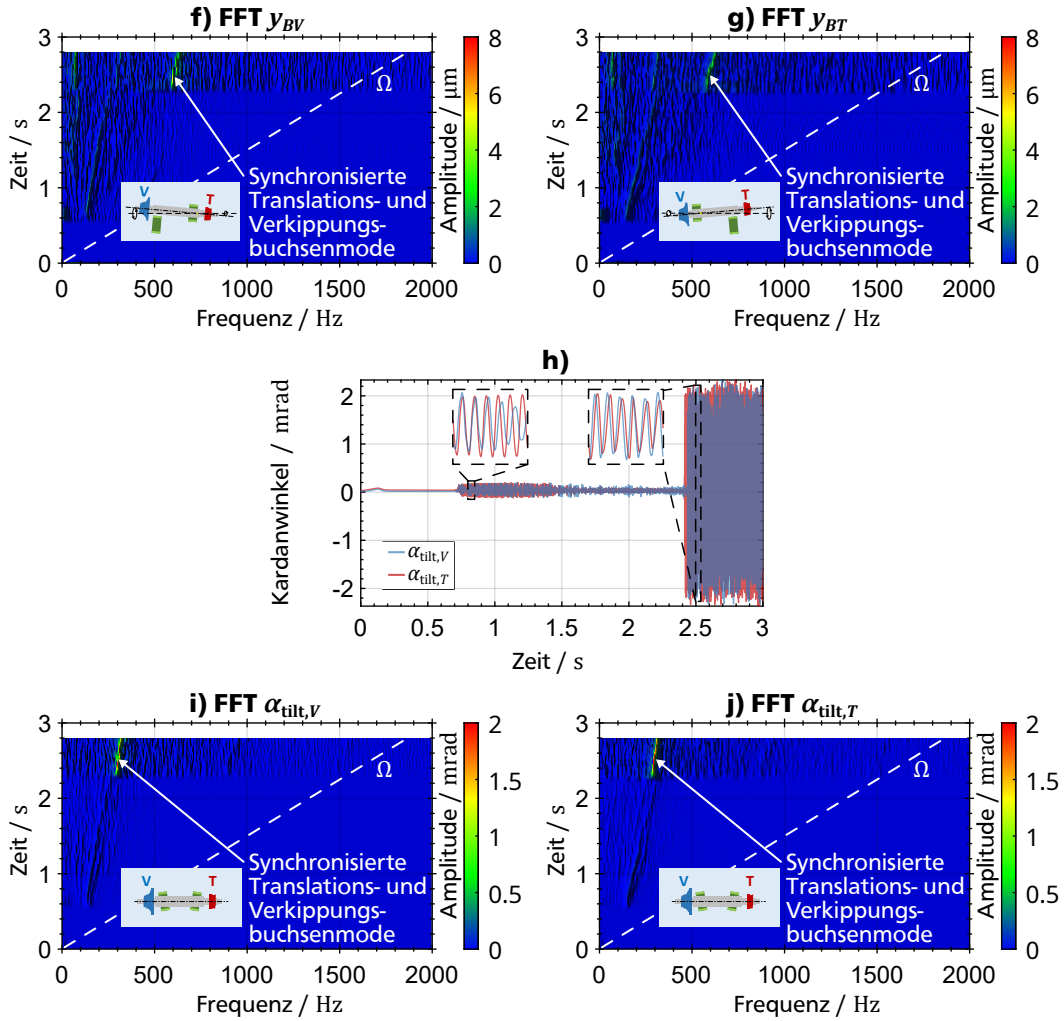

Abbildung 2.4: Hochlaufsimulation Bifurkationspfad 2b (Fortsetzung) [2].

Während der Buchsenmode ist an den Rändern der Buchseninnenfläche aufgrund der hohen Verkippung mit Kontakt zu rechnen. In der ersten und dritten Veröffentlichung [1, 3], in denen die Buchse nicht frei verkippen kann, ist eine translatorische Buchsenmode zu erkennen. Diese weist ebenfalls sehr große Amplituden auf, sodass auch in diesem Fall ein Kontakt sehr wahrscheinlich ist. Aus diesem Grund sollte Bifurkationspfad 2b vermieden werden.

2.3 Die Dynamik, das Stabilitäts- und das Bifurkationsverhalten von Rotorsystemen mit Air Ring Bearings

In diesem Abschnitt wird die Dynamik, das Stabilitäts- und das Bifurkationsverhalten von Rotorsystemen mit Air Ring Bearings anhand der Bifurkationspfade erläutert. Grundlage hierfür sind die Ergebnisse der ersten beiden Veröffentlichungen [1, 2]. Ebenfalls werden Empfehlungen für die Wahl der Systemparameter gegeben, um das System in einen günstigen Bifurkationspfad zu überführen. Ein kurzes Fazit über das dynamische Verhalten und erste Schlussfolgerungen für die Auslegung von Rotorsystemen mit Air Ring Bearings schließen den Abschnitt ab.

Bifurkationspfad 1

Das folgende Verhalten ist charakteristisch für Bifurkationspfad 1:

- Ab einer bestimmten Rotordrehzahl wird das Rotorsystem instabil und es treten Whirl/Whip-Oszillationen auf.
- Die Instabilität tritt zuerst im weniger belasteten, turbinenseitigen Luftfilm auf. Der resultierende Whirl/Whip im Luftfilm regt die turbinenseitige, konische Vorwärtsmode *Mode_(2)* an, siehe Abschnitt 2.1. Kurz darauf bildet sich im verdichterseitigen Luftfilm ein Whirl/Whip aus, der wiederum die verdichterseitige, konische Vorwärtsmode *Mode_(1)* anregt.
- Bei weiterer Drehzahlsteigerung erfolgt eine zweite Bifurkation. In diesem Fall ist eine Synchronisation der Whirl/Whip-Oszillationen beider Luftfilme zu beobachten. Beide Whirl/Whips regen nun eine zylindrische Vorwärtsmode mit sehr großen Amplituden an.
- Mit fortschreitender Simulation können die Whirl/Whips nicht mehr durchlaufen werden. Bei weiterer Erhöhung der Drehzahl nehmen auch die Amplituden der Schwingungen zu.

In Abb. 2.5 ist Bifurkationspfad 1 schematisch dargestellt. Aufgrund der im oberen Drehzahlbereich auftretenden großen Whirl/Whips ist ein Kontakt zwischen Rotor und Buchse sehr wahrscheinlich. Aus diesem Grund sollte für einen technisch sicheren Betrieb von Rotorsystemen mit Air Ring Bearings Bifurkationspfad 1 vermieden werden. Dies kann durch eine Verringerung der Steifigkeit c_{foil} bzw. c_{elast} oder durch eine Erhöhung der Reibkraft F_{fric} bzw. der viskosen Dämpfung d_{visc} erreicht werden. Genauso führt eine

Verringerung des nominellen Lagerspiels C, aber auch eine Vergrößerung der Keilhöhe ΔH zu einer Verbesserung des dynamischen Verhaltens. Eine Synchronisation der beiden Whirl/Whips kann durch eine Vergrößerung der Lagerasymmetrie vermieden werden, siehe Abb. 2.5b. Allerdings hat das Ausbleiben der Synchronisation kaum einen Einfluss auf die gefährlich großen Amplituden des Rotorzapfens.

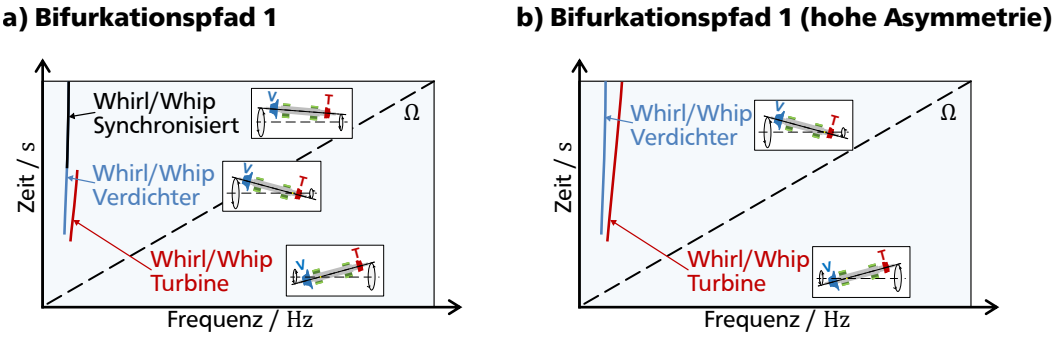

Abbildung 2.5: Bifurkationspfad 1 von Rotorsystemen mit Air Ring Bearings [1, 2].

Bifurkationspfad 2a

Bifurkationspfad 2a lässt sich wie folgt beschreiben:

- Nach Eintritt der Instabilität geht das Rotorsystem in einen Zustand selbsterregter, quasiperiodischer Whirl/Whip-Oszillationen in beiden Luftfilmen über.
- Die Instabilität tritt zunächst im weniger stark belasteten turbinenseitigen Fluidfilm auf. Dieser Zeitversatz nimmt weiter zu, wenn die Asymmetrie des Rotors vergrößert wird [1]. Der turbinenseitige Whirl/Whip regt *Mode_(2)* des Rotorsystems an, der verdichterseitige Whirl/Whip regt *Mode_(1)* des Rotorsystems an, siehe Abschnitt 2.1.
- Bei weiterer Erhöhung der Rotordrehzahl nehmen die Amplituden der Oszillationen ab.

Bifurkationspfad 2a ist in Abb. 2.6 abgebildet. Die im Bifurkationspfad 2a auftretenden Whirl/Whip-Oszillationen weisen allgemeinerweise moderate Amplituden auf, sodass ein technisch sicherer Betrieb des Rotorsystems mit Air Ring Bearings möglich ist. Zur gezielten Nutzung von Bifurkationspfad 2a sollte die Steifigkeit der Folienstruktur c_{foil} bzw.

des Elastomers c_{elast} verringert werden. Ebenfalls kann die Reibkraft F_{fric} bzw. die viskose Dämpfung d_{visc} erhöht werden. Dabei ist jedoch zu beachten, dass eine zu hohe Dämpfung des Systems möglich ist: Sind F_{fric} oder d_{visc} zu groß, kann dies zu einem gefährlichen Anstieg der Amplituden führen. Durch eine Verkleinerung des Lagerspiels C oder durch eine Vergrößerung der Keilhöhe ΔH kann ebenfalls Bifurkationspfad 2a realisiert werden. Insgesamt haben die Simulationen der Veröffentlichungen [1–3] gezeigt, dass der Bereich des Bifurkationspfades 2a recht groß ist, sodass ein Betrieb des Rotorsystems mit moderaten Amplituden vergleichsweise einfach realisierbar ist. Für bestimmte Parameterkombinationen können sogar komplett stabile Hochläufe ohne Oszillationen simuliert werden, wenn das Rotorsystem keine zusätzliche Unwucht aufweist. In diesem Fall können das Lagerspiel C und die Keilhöhe ΔH weiter vergrößert werden, um die Anforderungen an das Thermomanagement und an die Fertigungsgenauigkeit zu reduzieren.

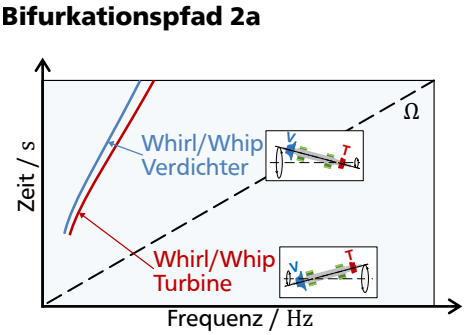

Abbildung 2.6: Bifurkationspfad 2a von Rotorsystemen mit Air Ring Bearings [1, 2].

Bifurkationspfad 2b

Charakteristisch für Bifurkationspfad 2b ist das Auftreten der Buchsenmoden, siehe Abschnitt 2.1. In der zweiten Veröffentlichung [2] wird gezeigt, dass je nach Größe des Hebelarms a die Buchsenmode entweder in Form einer rein translatorischen Buchsenmode oder als Kopplung aus Verkippungs- und Translationsmoden auftreten kann. Darüber hinaus verhält sich Bifurkationspfad 2b je nach Art der elastischen Struktur (Folienstruktur oder Elastomer) unterschiedlich.

Für Air Ring Bearings mit einer Folienstruktur zeigt Bifurkationspfad 2b folgendes Verhalten, siehe Abb. 2.7:

- Beidseitige Whirl/Whip-Oszillation treten nach Eintritt der Instabilität auf.

- Mit zunehmender Drehzahl wird das Frequenzspektrum der Schwingungen zunehmend verrauscht und chaotisch.
- Mit weiter steigender Drehzahl ist eine zweite Bifurkation zu erkennen. Die Whirl/Whips der Luftfilme regen entweder bei großem Hebelarm a eine rein translatorische Mode oder bei kleinem Hebelarm a gekoppelte Verkippungs- und Translationsmoden der Buchsen an:
  - Translatorische Mode:
    Die Frequenz des turbinenseitigen Whirl/Whips bei dieser Mode zeigt einen Sprung. Anschließend wird die translatorische Buchsenmode *Mode_6(f)* durch den Whirl/Whip angeregt. Als Ergebnis sind große Exzentrizitäten auf der Turbinenseite zu erkennen.
  - Verkippungs- und Translationsmoden (1:2 Kopplung):
    Nach der Bifurkation ist sowohl auf der Turbinen- als auch auf der Verdichterseite ein Modewechsel zu erkennen. Es wird nun die Verkippungsmode *Mode_3(f)* angeregt. Gleichzeitig regen die Luftfilme die translatorischen Moden *Mode_5(f)* und *Mode_6(f)* bei einer doppelten Frequenz an. Dieser Effekt ist in der zweiten Veröffentlichung [2] ausführlich beschrieben.

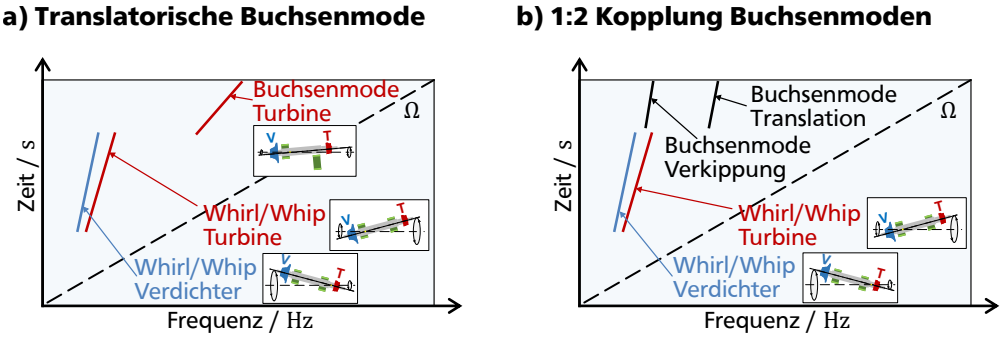

Abbildung 2.7: Bifurkationspfad 2b von Rotorsystemen mit Air Ring Bearings (Folienstruktur) [1, 2].

Für Bifurkationspfad 2b in Kombination mit einem Elastomer ist das folgende Verhalten charakteristisch, siehe Abb. 2.8:

- Nach dem Auftreten der Bifurkation werden entweder eine rein translatorische Buchsenmode (großer Hebelarm a) oder gekoppelte Verkippungs- und Translationsmoden der Buchse (kleiner Hebelarm a) sichtbar:

- Translatorische Mode:
  Nach der Bifurkation findet auf der Verdichterseite eine Anregung von *Mode_5(f)* und auf der Turbinenseite eine Anregung von *Mode_6(f)* statt. Ab einer bestimmten Drehzahl ist eine Synchronisation der Buchsenmoden sichtbar. Es bildet sich eine zylindrische Buchsenmode mit großen Exzentrizitäten.

- Verkippungs- und Translationsmoden (1:2 Kopplung):
  Nach der Bifurkation werden gleichzeitig die Verkippungsmode *Mode_3(f)* und mit einer doppelten Frequenz die translatorischen Moden *Mode_5(f)* und *Mode_6(f)* angeregt, siehe [2].

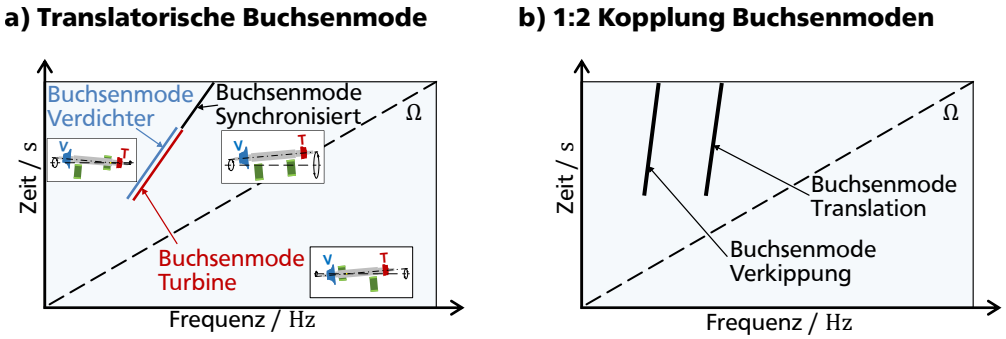

Abbildung 2.8: Bifurkationspfad 2b von Rotorsystemen mit Air Ring Bearings (Elastomer) [1, 2].

Im Bifurkationspfad 2b treten unabhängig von der Art der Buchsenmode und unabhängig von der Art der elastischen Struktur große Exzentrizitäten bzw. große Verkippungen des Rotors in der Buchse auf, die im Betrieb mit hoher Wahrscheinlichkeit zu gefährlichen Kontakten führen. Für einen sicheren Betrieb von Rotorsystemen mit Air Ring Bearings sollte dieser Bifurkationspfad daher vermieden werden. Die beiden Arten der Buchsenmoden können je nach Parameter zu unterschiedlichen Zeitpunkten auftreten und sollten daher auch beide berücksichtigt werden. Sogar ein Wechsel der Buchsenmoden ist bei Betrieb möglich [2]. Bifurkationspfad 2b tritt beim betrachteten Rotorsystem jedoch nur bei vergleichsweise extremen Parametern auf (sehr hohe Buchsenmasse m_{Buchse}, sehr geringe Steifigkeiten c_{foil} bzw. c_{elast} und sehr geringe Reibung F_{fric} bzw. geringe Dämpfung d_{visc}) und ist daher leicht zu vermeiden.

Fazit

Insgesamt lassen sich drei Bifurkationspfade in Rotorsystemen mit Air Ring Bearings erkennen. *Bifurkationspfad 1* weist große Amplituden im Whirl/Whip-Bereich auf und sollte daher vermieden werden. Dieser Bifurkationspfad tritt im Zusammenhang mit hohen Steifigkeiten c_{foil} bzw. c_{elast}, kleinen Disspationsparametern F_{fric} bzw. d_{visc}, einem hohen Lagerspiel C und kleinen Keilhöhen ΔH auf. Für *Bifurkationspfad 2a* sind moderate Amplituden während des Whirl/Whips zu erkennen, sodass ein sicherer Betrieb des Rotorsystems möglich ist. Durch die Wahl geeigneter Parameter kann der Whirl/Whip sogar im gesamten Drehzahlbereich unterdrückt werden. Insgesamt lässt sich Bifurkationspfad 2a für einen weiten Parameterbereich realisieren. In *Bifurkationspfad 2b* treten große Amplituden bei der Anregung der Buchsenmoden auf. Aufgrund der hohen Kontaktgefahr sollte auch dieser Bifurkationspfad vermieden werden. Von Bifurkationspfad 2b gibt es zwei verschiedene Arten: Eine translatorische Buchsenmode und eine 1:2 Kopplung von Verkippungs- und translatorischen Buchsenmoden.

Bei der Auslegung von Rotorsystemen mit Air Ring Bearings sollte Bifurkationspfad 2a angestrebt werden. Die erforderlichen Parameter für Bifurkationspfad 2b sind eher extrem, sodass der Fokus der Auslegung von Rotorsystemen mit Air Ring Bearings weitgehend auf die Vermeidung von Bifurkationspfad 1 fällt.

2.4 Optimierung des Rotorsystems mit Air Ring Bearings

Mit den Erkenntnissen aus dem vorherigen Abschnitt soll das Rotorsystem optimiert werden. Dieser Abschnitt basiert auf den Ergebnissen der dritten Veröffentlichung [3]. Unter einem optimalen Rotorsystem mit Air Ring Bearings wird in dieser Arbeit ein System mit einem maximal großen Luftspalt bei tolerierbaren Whirl/Whip-Oszillationen mit moderaten Amplituden im Betrieb verstanden. Durch den größer dimensionierten Luftspalt können die strengen Anforderungen an das Thermomanagement und an die Fertigungsgenauigkeit reduziert werden. Die Ergebnisse aus Abschnitt 2.3 zeigen, dass für einen optimalen Betrieb Bifurkationspfad 2a angestrebt werden sollte. In der dritten Veröffentlichung [3] wird nun untersucht, mit welchen Parametern Bifurkationspfad 2a für das Rotorsystem dieser Arbeit umsetzbar ist. Neben den Parametern des Elastomers (Steifigkeit c_{elast} und Dämpfung d_{visc}) werden erstmals auch die Parameter des Luftspalts (Lagerspiel C und Keilhöhe ΔH) variiert. Erste Vorstudien haben gezeigt, dass das Verhältnis zwischen Lagerspiel und Keilhöhe von $\Delta H = 2C$ für die Realisierung von Bifurkationspfad 2a besonders gut geeignet ist. Demzufolge werden die Parameter des Luftspalts zu insgesamt vier Kombinationen zusammengefasst: (1) $C = 10$ µm, $\Delta H = 20$ µm; (2) $C = 15$ µm,

$\Delta H = 30$ µm; (3) $C = 20$ µm, $\Delta H = 40$ µm und (4) $C = 30$ µm, $\Delta H = 60$ µm. Für die Steifigkeit c_{elast} des Elastomers werden Werte von 250 N mm^{-1} bis 1500 N mm^{-1} verwendet, die Dämpfung d_{visc} beträgt 50 N s m^{-1} bis 4000 N s m^{-1}. Die Ergebnisse der anschließenden Hochlaufsimulationen sind in Bifurkationskarten zusammengefasst, siehe Abb. 2.9. Dabei können folgende Erkenntnisse festgehalten werden:

- Mit der Vergrößerung des Luftspalts verkleinert sich der Bereich, in dem das Rotorsystem über den gesamten Drehzahlbereich stabil ist. Dagegen vergrößern sich die Bereiche sowohl von Bifurkationspfad 1 als auch Bifurkationspfad 2a
- Eine Erhöhung der Steifigkeit c_{elast} begünstigt Bifurkationspfad 1, insbesondere bei geringer Dämpfung und großem Luftspalt.
- Eine Vergrößerung der Dämpfung d_{visc} ermöglicht einen Wechsel von Bifurkationspfad 1 zu Bifurkationspfad 2a, sodass das Rotorsystem bei moderaten Amplituden im Whirl/Whip-Bereich betrieben werden kann. Allerdings können sehr große Dämpfungen auch zu gefährlich großen Amplituden des Systems führen.
- Bifurkationspfad 2b ist in den Simulationen nicht beobachtet worden und deutet deshalb für die betrachteten Spaltgeometrien nur auf eine geringe Relevanz hin.

Die Ergebnisse zeigen einen großen Parameterbereich, in dem Rotorsysteme mit Air Ring Bearings sicher betrieben werden können. Für bestimmte Kombinationen der Steifigkeits- und Dämpfungskoeffizienten ist selbst beim größten untersuchten Luftspalt ($C = 30$ µm, $\Delta H = 60$ µm) ein komplett stabiler Betrieb des Rotorsystems möglich, sodass bei der Wahl der Spalthöhe eine weitere Vergrößerung in Betracht gezogen werden kann. Die großen Parameterbereiche, in denen ein sicherer Betrieb möglich ist, erleichtern darüber hinaus die Suche nach einem geeigneten Werkstoff für das Elastomer, das neben den Steifigkeits- und Dämpfungsanforderungen noch viele weitere Anforderungen erfüllen muss (Temperaturbeständigkeit, Versprödungsbeständigkeit, etc.).

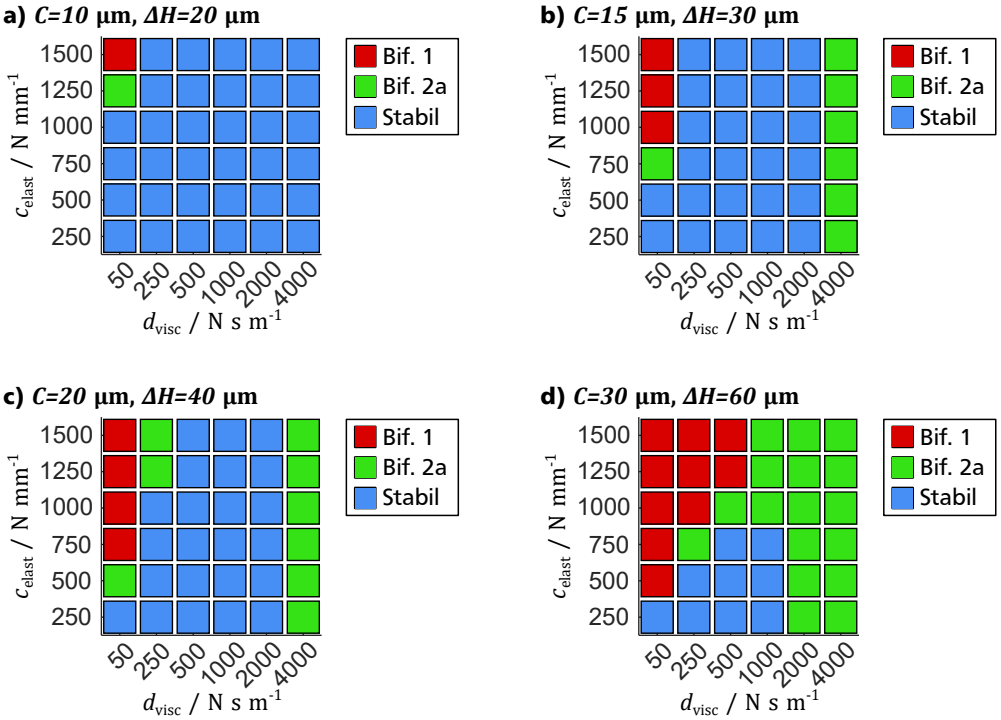

Abbildung 2.9: Bifurkationskarten für unterschiedliche Innengeometrien der Buchse [3]: a) $C = 10$ µm, $\Delta H = 20$ µm; b) $C = 15$ µm, $\Delta H = 30$ µm; c) $C = 20$ µm, $\Delta H = 40$ µm und d) $C = 30$ µm, $\Delta H = 60$ µm.

3 Zusammenfassung und Fazit

Luftlager werden in Umgebungen mit hohen Reinheitsanforderungen eingesetzt, zum Beispiel in Brennstoffzellen oder in Kühlaggregaten von Flugzeugen. Eine Variante sind Luftlager mit starrem Gehäuse, zu denen auch Herringbone-Lager zählen. Diese Lagervariante stellt jedoch hohe Anforderungen an die Fertigungsgenauigkeit und an das Thermomanagement des gesamten Rotorsystems. Die hohen Anforderungen resultieren aus der extrem geringen Höhe des Luftspaltes zwischen Rotorzapfen und Gehäuse, der für den stabilen Betrieb des Gesamtsystems von entscheidender Bedeutung ist.

Durch das Einsetzen einer Folienstruktur zwischen Luftfilm und Gehäuse können die hohen Anforderungen reduziert werden. Allerdings sind bei den sogenannten Folienluftlagern Luftfilm und Struktur sehr stark miteinander gekoppelt. Hohe Vorspannungen in der Folienstruktur, die zum Teil für einen stabilen Betrieb des Systems notwendig sind, können die Abhebedrehzahl und deshalb auch den Verschleiß des Lagers erhöhen. Ebenfalls erschwert die starke Kopplung die numerische Berechnung von Folienluftlagern erheblich. Genaue Vorhersagen zur Dynamik sind allgemein nur mit sehr komplexen und rechenintensiven Modellen möglich.

Bei Air Ring Bearings wird die Kopplung durch den Einsatz einer starren Buchse zwischen Folienstruktur und Luftfilm aufgehoben. Dies verhindert zum einen die Vorspannung der Folien auf den Rotor und verringert damit den Verschleiß bei Start/Stopp-Vorgängen. Zum anderen ermöglicht die Entkopplung des Luftfilms von der elastischen Struktur eine genaue numerische Modellierung mit vertretbaren Simulationszeiten bei transienten Hochläufen. Durch die elastische Struktur können in Air Ring Bearings Fehlstellungen ausgeglichen und Schwingungen ausreichend gedämpft werden.

Das Ziel dieser Arbeit ist es, Rotorsysteme mit Air Ring Bearings oberhalb der Stabilitätsgrenze bei selbsterregten Schwingungen (Whirl/Whip-Oszillationen) mit moderaten Amplituden zu betreiben. Hierdurch können die hohen Anforderungen an das Thermomanagement und an die Fertigungsgenauigkeit im Vergleich zu Rotorsystemen mit Luftlagern mit starrem Gehäuse deutlich reduziert werden.

Das dynamische Verhalten von Rotorsystemen mit Air Ring Bearings ist stark nichtlinear und unterscheidet sich wesentlich von anderen Luftlagertypen. Die genaue Kenntnis des dynamischen Verhaltens, der Stabilität und des Bifurkationsverhaltens ist daher für den

sicheren Betrieb dieser Rotorsysteme unerlässlich. Da das Rotorsystem insbesondere unter Whirl/Whip-Oszillationen betrieben werden soll, sind klassische Stabilitätsberechnungen mit einem linearisierten System nicht ausreichend, um ein vollständiges Bild der dynamischen Eigenschaften zu erhalten. Im Rahmen dieser Dissertation erfolgt die Untersuchung von Rotorsystemen mit Air Ring Bearings durch die transiente Simulation von Hochläufen mit komplexen numerischen Modellen. Der Rotor und die Buchsen werden als Mehrkörpersystem modelliert, die Luftfilme als Finite-Elemente-Systeme. Die sogenannten Subsysteme werden durch einen Co-Simulationsansatz gekoppelt.

Die elastische Struktur des Air Ring Bearings wird in dieser Arbeit in Form einer Folienstruktur oder in Form eines Elastomers realisiert. Bei der Folienstruktur dominiert die Festkörperreibung, beim Elastomer die viskose Dämpfung als Dissipationseffekt. In den ersten beiden Veröffentlichungen [1, 2] wird das dynamische Verhalten von Rotorsystemen mit Air Ring Bearings untersucht. Die Hochlaufsimulationen zeigen, dass solche Rotorsysteme im Allgemeinen drei verschiedene Bifurkationspfade aufweisen: *Bifurkationspfad 1* wird bei hoher Steifigkeit und geringer Reibung bzw. Dämpfung der elastischen Struktur erreicht. Als Folge sind große, unerwünschte Amplituden zu erwarten, sodass dieser Bifurkationspfad für einen sicheren Betrieb des Rotorsystems geeignet ist. *Bifurkationspfad 2a* ist dagegen bei geringeren Steifigkeiten und höheren Dissipationseigenschaften der Struktur erkennbar. Dieser Bifurkationspfad führt zu moderaten Amplituden mit denen ein sicherer Betrieb des Rotorsystems möglich ist. Daher sollte dieser Bifurkationspfad Ziel der Auslegung sein. Im Allgemeinen kann Bifurkationspfad 2a mit moderaten Amplituden durch geeignete Anpassung der Lagerparameter ohne größere Probleme erreicht werden. *Bifurkationspfad 2b* tritt nur bei sehr niedrigen Steifigkeiten und Dämpfungen bzw. Reibungen sowie bei hohen Buchsenmassen auf. Hier wird durch die Whirl/Whips in den Luftfilmen entweder eine rein translatorische Buchsenmode oder eine gekoppelte Translations- und Verkippungsmode der Buchsen angeregt. Die in diesem Zusammenhang entdeckte Kopplung der Translations- und Verkippungsmoden wird in der zweiten Veröffentlichung [2] anschaulich erklärt. Für beide Modenformen bilden sich jedoch gefährlich große Amplituden, sodass auch Bifurkationspfad 2b ausgeschlossen werden sollte.

Optimierungsstudien der dritten Veröffentlichung [3] zeigen, dass ein sicheres Betreiben von Rotorsystemen mit Air Ring Bearings für einen großen Bereich von Parametern möglich ist. In diesen Studien wird erstmals auch die Geometrie des Luftspalts systematisch variiert. Selbst bei vergleichsweise großen Luftspalten liegt bei den durchgeführten Hochlaufsimulationen teilweise ein komplett stabiles Rotorverhalten vor. Die gewonnenen Daten der Untersuchungen werden in Form von Bifurkationskarten dargestellt.

Die Ergebnisse der Arbeit zeigen, dass Rotorsysteme mit Air Ring Bearings mit detaillierten numerischen Werkzeugen einfach auszulegen sind. Zahlreiche Simulationen zeigen,

dass Rotorsysteme für sehr unterschiedliche Steifigkeiten, Reibungs- bzw. Dämpfungseigenschaften und Luftspaltgeometrien sicher betrieben werden können. Dieser weite Parameterbereich ermöglicht einen großen Gestaltungsspielraum und bietet viele Freiheiten zur Lösung von Zielkonflikten in der Auslegung. Auch aufgrund ihrer Vorteile hinsichtlich Thermomanagement und Verschleiß sind Air Ring Bearings eine anzustrebende Alternative für klassische (Folien-)Luftlager in Umgebungen mit höchsten Reinheitsanforderungen.

Literatur

[1] Pascal Zeise und Bernhard Schweizer. „Dynamics, stability and bifurcation analysis of rotors in air ring bearings“. In: *Journal of Sound and Vibration* 521 (2022), S. 116392. ISSN: 0022-460X. DOI: 10.1016/j.jsv.2021.116392.

[2] Pascal Zeise und Bernhard Schweizer. „Vibration and bifurcation analysis of rotor systems with air ring bearings including ring tilting“. In: *Journal of Sound and Vibration* 571 (2024), S. 118079. ISSN: 0022-460X. DOI: 10.1016/j.jsv.2023.118079.

[3] Pascal Zeise und Bernhard Schweizer. „Numerical investigations on high-speed turbo-compressor rotor systems with air ring bearings: Nonlinear vibration behavior and optimization“. In: *Applied and Computational Mechanics* 17.2 (2023), S. 169–190. ISSN: 1802680X. DOI: 10.24132/acm.2023.836.

[4] Farid Al–Bender. *Air Bearings*. Wiley, 2021. ISBN: 9781118926444. DOI: 10.1002/9781118926444.

[5] J. H. Vohr und C. Y. Chow. „Characteristics of Herringbone-Grooved, Gas-Lubricated Journal Bearings“. In: *Journal of Basic Engineering* 87.3 (1965), S. 568–576. ISSN: 0021-9223. DOI: 10.1115/1.3650607.

[6] S. B. Malanoski. „Experiments on an Ultrastable Gas Journal Bearing“. In: *Journal of Lubrication Technology* 89.4 (1967), S. 433–438. ISSN: 0022-2305. DOI: 10.1115/1.3617021.

[7] Elia Iseli und Jürg Schiffmann. „Stability and Unbalance Analysis of Rigid Rotors Supported by Spiral Groove Bearings: Comparison of Different Approaches“. In: *Journal of Engineering for Gas Turbines and Power* 143.12 (2021), S. 121008. ISSN: 0742-4795. DOI: 10.1115/1.4052025.

[8] Henning Schlums, Christian Hühne und Michael Sinapius. „Design of a Herringbone-Grooved Bearing for Application in an Electrically Driven Air Compressor“. In: *Machines* 10.8 (2022), S. 662. DOI: 10.3390/machines10080662.

[9] Philipp K. Bättig, Patrick H. Wagner und Jürg Schiffmann. „Experimental Investigation of Enhanced Grooves for Herringbone Grooved Journal Bearings“. In: *Journal of Tribology* 144.9 (2022). ISSN: 0742-4787. DOI: 10.1115/1.4053978.

[10] L. E. Olmedo u. a. „Thermal management for gas lubricated, high-speed turbomachinery“. In: *Applied Thermal Engineering* 218 (2023), S. 119229. ISSN: 13594311. DOI: 10.1016/j.applthermaleng.2022.119229.

[11] Lili Gu, Eliott Guenat und Jürg Schiffmann. „A Review of Grooved Dynamic Gas Bearings“. In: *Applied Mechanics Reviews* 72.1 (2020). ISSN: 0003-6900. DOI: 10.1115/1.4044191.

[12] Christopher DellaCorte u. a. „Design, fabrication, and performance of open source generation I and II compliant hydrodynamic gas foil bearings“. In: *Tribology Transactions* 51.3 (2008), S. 254–264. ISSN: 1040-2004. DOI: 10.1080/10402000701772579.

[13] H. Heshmat, W. Shapiro und S. Gray. „Development of foil journal bearings for high load capacity and high speed whirl stability“. In: *Journal of Lubrication Technology* 104.2 (1982), S. 149–156. ISSN: 0022-2305. DOI: 10.1115/1.3253173.

[14] Daejong Kim. „Parametric studies on static and dynamic performance of air foil bearings with different top foil geometries and bump stiffness distributions“. In: *Journal of Tribology* 129.2 (2007), S. 354–364. ISSN: 0742-4787. DOI: 10.1115/1.2540065.

[15] Kai Feng, Xueyuan Zhao und Zhiyang Guo. „Design and structural performance measurements of a novel multi-cantilever foil bearing“. In: *Proceedings of the Institution of Mechanical Engineers, Part C: Journal of Mechanical Engineering Science* 229.10 (2015), S. 1830–1838. ISSN: 0954-4062. DOI: 10.1177/0954406214547529.

[16] Changlin Li, Jianjun Du und Yingxue Yao. „Study of load carrying mechanism of a novel three-pad gas foil bearing with multiple sliding beams“. In: *Mechanical systems and signal processing* 135 (2020), S. 106372. ISSN: 0888-3270. DOI: 10.1016/j.ymssp.2019.106372.

[17] Erik E. Swanson und P. Shawn O'Meara. „The wing foil: a novel compliant radial foil bearing design“. In: *Journal of Engineering for Gas Turbines and Power* 140.8 (2018). ISSN: 0742-4795. DOI: 10.1115/1.4038366.

[18] Jason C. Wilkes u. a. „Impact of Bearing Clearance on Measured Stiffness and Damping Coefficients and Thermal Performance of a High-Stiffness Generation 3 Foil Journal Bearing“. In: *Journal of Engineering for Gas Turbines and Power* 140.7 (2018). ISSN: 0742-4795. DOI: 10.1115/1.4038603.

[19] Ju-ho Song und Daejong Kim. „Foil Gas Bearing With Compression Springs: Analyses and Experiments“. In: *Journal of Tribology* 129.3 (2007), S. 628–639. ISSN: 0742-4787. DOI: 10.1115/1.2736455.

[20] Luis San Andrés und Thomas Abraham Chirathadam. „A metal mesh foil bearing and a bump-type foil bearing: Comparison of performance for two similar size gas bearings“. In: *Journal of Engineering for Gas Turbines and Power* 134.10 (2012), S. 102501. ISSN: 0742-4795. DOI: 10.1115/1.4007061.

[21] Jisu Park, Donghee Kim und Kyuho Sim. „Development and Performance Measurements of Gas Foil Polymer Bearings with a Dual-Rotor Test Rig Driven by Permanent Magnet Electric Motor“. In: *Applied Sciences* 12.3 (2022), S. 1505. DOI: 10.3390/app12031505.

[22] Gregor Schilling und Robert Liebich. „The Influence of Bearing Clearance on the Load Capacity of Gas Polymer Bearings“. In: *Applied Sciences* 13.7 (2023), S. 4555. DOI: 10.3390/app13074555.

[23] Kyuho Sim u. a. „Effects of mechanical preloads on the rotordynamic performance of a rotor supported on three-pad gas foil journal bearings“. In: *Journal of Engineering for Gas Turbines and Power* 136.12 (2014), S. 122503. ISSN: 0742-4795. DOI: 10.1115/1.4027745.

[24] Tae Ho Kim und Luis San Andres. „Effects of a mechanical preload on the dynamic force response of gas foil bearings: measurements and model predictions“. In: *Tribology Transactions* 52.4 (2009), S. 569–580. ISSN: 1040-2004. DOI: 10.1080/10402000902825721.

[25] Ibrahim Ghalayini und Philip Bonello. „The Application of the Arbitrary-Order Galerkin Reduction Method to the Dynamic Analysis of a Rotor With a Preloaded Single-Pad Foil-Air Bearing“. In: *Journal of Engineering for Gas Turbines and Power* 144.9 (2022). ISSN: 0742-4795. DOI: 10.1115/1.4055188.

[26] Marcel Mahner u. a. „Numerical and Experimental Investigations on Preload Effects in Air Foil Journal Bearings“. In: *Journal of Engineering for Gas Turbines and Power* 140.3 (2018), S. 032505. ISSN: 0742-4795. DOI: 10.1115/1.4037965.

[27] Jisu Park, Donghee Kim und Kyuho Sim. „Rotordynamic Analysis of Piezoelectric Gas Foil Bearings with a Mechanical Preload Control Based on Structural Parameter Identifications“. In: *Applied Sciences* 11.5 (2021), S. 2330. DOI: 10.3390/app11052330.

[28] Ibrahim Ghalayini und Philip Bonello. „Development of a rotor test rig with a novel controllable preload foil-air bearing“. In: *Precision Engineering* 76 (2022), S. 340–359. ISSN: 01416359. DOI: 10.1016/j.precisioneng.2022.04.002.

[29] Sebastian von Osmanski und Ilmar F. Santos. „Gas foil bearings with radial injection: Multi-domain stability analysis and unbalance response“. In: *Journal of Sound and Vibration* 508 (2021), S. 116177. ISSN: 0022-460X. DOI: 10.1016/j.jsv.2021.116177.

[30] Signe T. Heinemann u. a. „Numerical modelling of compliant foil structure in gas foil bearings: Comparison of four top foil models with and without radial injection“. In: *Journal of Sound and Vibration* 547 (2023), S. 117513. ISSN: 0022-460X. DOI: 10.1016/j.jsv.2022.117513.

[31] Hanns Michel und Robert Liebich. „Challenges in Validating a Thermo-Hydrodynamic Gas Foil Bearing Model“. In: *Journal of Engineering for Gas Turbines and Power* 143.4 (2021). ISSN: 0742-4795. DOI: 10.1115/1.4047769.

[32] Marcel Mahner, Marcel Bauer und Bernhard Schweizer. „Numerical analyzes and experimental investigations on the fully-coupled thermo-elasto-gasdynamic behavior of air foil journal bearings“. In: *Mechanical systems and signal processing* 149 (2021), S. 107221. ISSN: 0888-3270. DOI: 10.1016/j.ymssp.2020.107221.

[33] Marcel Mahner u. a. „An experimental investigation on the influence of an assembly preload on the hysteresis, the drag torque, the lift-off speed and the thermal behavior of three-pad air foil journal bearings“. In: *Tribology International* 137 (2019), S. 113–126. ISSN: 0301-679X. DOI: 10.1016/j.triboint.2019.02.026.

[34] J. W. Lund. „Calculation of Stiffness and Damping Properties of Gas Bearings“. In: *Journal of Lubrication Technology* 90.4 (1968), S. 793–803. ISSN: 0022-2305. DOI: 10.1115/1.3601723.

[35] J.-P. Peng und M. Carpino. „Coulomb friction damping effects in elastically supported gas foil bearings©“. In: *Tribology Transactions* 37.1 (1994), S. 91–98. ISSN: 1040-2004. DOI: 10.1080/10402009408983270.

[36] Jon S. Larsen, Ilmar F. Santos und Sebastian von Osmanski. „Stability of rigid rotors supported by air foil bearings: Comparison of two fundamental approaches“. In: *Journal of Sound and Vibration* 381 (2016), S. 179–191. ISSN: 0022-460X. DOI: 10.1016/j.jsv.2016.06.022.

[37] Sebastian von Osmanski, Jon S. Larsen und Ilmar F. Santos. „Multi-domain stability and modal analysis applied to Gas Foil Bearings: Three approaches“. In: *Journal of Sound and Vibration* 472 (2020), S. 115174. ISSN: 0022-460X. DOI: 10.1016/j.jsv.2020.115174.

[38] Philip Bonello und Talieh Pourashraf. „A comparison of modal analyses of foil-air bearing rotor systems using two alternative linearisation methods“. In: *Mechanical systems and signal processing* 170 (2022), S. 108714. ISSN: 0888-3270. DOI: 10.1016/j.ymssp.2021.108714.

[39] Philip Bonello und H. M. Pham. „The efficient computation of the nonlinear dynamic response of a foil–air bearing rotor system“. In: *Journal of Sound and Vibration* 333.15 (2014), S. 3459–3478. ISSN: 0022-460X. DOI: 10.1016/j.jsv.2014.03.001.

[40] Philip Bonello. „The extraction of Campbell diagrams from the dynamical system representation of a foil-air bearing rotor model“. In: *Mechanical systems and signal processing* 129 (2019), S. 502–530. ISSN: 0888-3270. DOI: 10.1016/j.ymssp.2019.04.018.

[41] Talieh Pourashraf und Philip Bonello. „A new Galerkin Reduction approach for the analysis of a fully coupled foil air bearing rotor system with bilinear foil model“. In: *Journal of Sound and Vibration* 546 (2023), S. 117367. ISSN: 0022-460X. DOI: 10.1016/j.jsv.2022.117367.

[42] Franck Balducchi, Mihai Arghir und Romain Gauthier. „Experimental analysis of the unbalance response of rigid rotors supported on aerodynamic foil bearings“. In: *Journal of Vibration and Acoustics* 137.6 (2015), S. 061014. ISSN: 1048-9002. DOI: 10.1115/1.4031409.

[43] Jon S. Larsen und Ilmar F. Santos. „On the nonlinear steady-state response of rigid rotors supported by air foil bearings—Theory and experiments“. In: *Journal of Sound and Vibration* 346 (2015), S. 284–297. ISSN: 0022-460X. DOI: 10.1016/j.jsv.2015.02.017.

[44] Philip Bonello und M.F. Bin Hassan. „An experimental and theoretical analysis of a foil-air bearing rotor system“. In: *Journal of Sound and Vibration* 413 (2018), S. 395–420. ISSN: 0022-460X. DOI: 10.1016/j.jsv.2017.10.036.

[45] P. Samanta, N. C. Murmu und M. M. Khonsari. „The evolution of foil bearing technology“. In: *Tribology International* 135 (2019), S. 305–323. ISSN: 0301-679X. DOI: 10.1016/j.triboint.2019.03.021.

[46] Atsusuke Tatara, Harutaka Koike und Akira Iwasaki. „The Stability of Flexibly Supported, Externally Pressurized Gas Journal Bearings: Case of a Rigid Rotor“. In: *Bulletin of JSME* 16.100 (1973), S. 1573–1579. ISSN: 0021-3764. DOI: 10.1299/jsme1958.16.1573.

[47] Tobias Waumans u. a. „Aerodynamic journal bearing with a flexible, damped support operating at 7.2 million DN“. In: *Journal of Micromechanics and Microengineering* 21.10 (2011), S. 104014. ISSN: 0960-1317. DOI: 10.1088/0960-1317/21/10/104014.

[48] Norifumi Miyanaga und Jun Tomioka. „Effect of support stiffness and damping on stability characteristics of herringbone-grooved aerodynamic journal bearings mounted on viscoelastic supports“. In: *Tribology International* 100 (2016), S. 195–203. ISSN: 0301-679X. DOI: 10.1016/j.triboint.2016.01.019.

[49] Philipp Bättig und Jürg Schiffmann. „Unstable tilting motion of flexibly supported gas bearing bushings“. In: *Mechanical systems and signal processing* 162 (2022), S. 107981. ISSN: 0888-3270. DOI: 10.1016/j.ymssp.2021.107981.

[50] Kei Somaya u. a. „Threshold Speed of Instability of a Herringbone-Grooved Rigid Rotor With a Bearing Bush Flexibly Supported by Straight Spring Wires“. In: *Volume 7A: Structures and Dynamics*. American Society of Mechanical Engineers, 6152015. ISBN: 978-0-7918-5676-5. DOI: 10.1115/GT2015-43161.

[51] Andras Z. Szeri. *Fluid film lubrication*. 2. ed., 1. publ. Cambridge: Cambridge Univ. Press, 2011. ISBN: 0521898234.

[52] Michael M. Khonsari und E. Richard Booser. *Applied Tribology: Bearing Design and Lubrication*. Wiley, 2017. ISBN: 9781118637241. DOI: 10.1002/9781118700280.

[53] Kathryn Eleda Brenan, S. L. Campbell und Linda Ruth Petzold. *Numerical solution of initial-value problems in differential-algebraic equations*. Bd. 14. Classics in applied mathematics. Philadelphia: Society for Industrial and Applied Mathematics, 1996. ISBN: 0898713536. DOI: 10.1137/1.9781611971224.

[54] Mihai B. Dobrica und Michel Fillon. „Mixed Lubrication“. In: *Encyclopedia of Tribology*. Hrsg. von Q. Jane Wang und Yip-Wah Chung. Boston, MA: Springer US, 2013, S. 2284–2291. ISBN: 978-0-387-92896-8. DOI: 10.1007/978-0-387-92897-5_27.

[55] Mihai Arghir und Omar Benchekroun. „A New Structural Bump Foil Model With Application From Start-Up to Full Operating Conditions“. In: *Journal of Engineering for Gas Turbines and Power* 141.10 (2019). ISSN: 0742-4795. DOI: 10.1115/1.4044685.

[56] Paulo Flores u. a. „On the continuous contact force models for soft materials in multibody dynamics“. In: *Multibody System Dynamics* 25.3 (2011), S. 357–375. ISSN: 1384-5640. DOI: 10.1007/s11044-010-9237-4.

[57] Edward J. Haug. *Computer aided kinematics and dynamics of mechanical systems*. Allyn and Bacon series in engineering. Boston: Allyn and Bacon, 1989. ISBN: 978-0205116690.

[58] Ahmed A. Shabana. *Dynamics of multibody systems*. Fourth edition. Cambridge University Press, 2014. ISBN: 9781107042650.

[59] Luis San Andres und Tae Ho Kim. „Forced nonlinear response of gas foil bearing supported rotors“. In: *Tribology International* 41.8 (2008), S. 704–715. ISSN: 0301-679X. DOI: 10.1016/j.triboint.2007.12.009.

[60] Pascal Zeise u. a. „A Reduced Model for Air Foil Journal Bearings for Time-Efficient Run-Up Simulations“. In: *Proceedings of the ASME Turbo Expo 2019: Turbomachinery Technical Conference and Exposition*. American Society of Mechanical Engineers, 2019, V07BT34A004. DOI: 10.1115/GT2019-90187.

[61] Pascal Zeise u. a. „A reduced semi-analytical gas foil bearing model for transient run-up simulations“. In: *Proceedings of the Virtual Conference on Vibrations in Rotating Machinery*. Hrsg. von Institute of Mechanical Engineers. London: CRC press, 2020, S. 575–587. DOI: 10.1201/9781003132639.

[62] C. W. Gear, B. Leimkuhler und G. K. Gupta. „Automatic integration of Euler-Lagrange equations with constraints“. In: *Journal of Computational and Applied Mathematics* 12-13 (1985), S. 77–90. ISSN: 03770427. DOI: 10.1016/0377-0427(85)90008-1.

[63] Cláudio Gomes u. a. „Co-Simulation“. In: *ACM Computing Surveys* 51.3 (2018), S. 1–33. ISSN: 0360-0300. DOI: 10.1145/3179993.

[64] Bernhard Schweizer, Pu Li und Daixing Lu. „Explicit and Implicit Cosimulation Methods: Stability and Convergence Analysis for Different Solver Coupling Approaches“. In: *Journal of Computational and Nonlinear Dynamics* 10.5 (2015). ISSN: 1555-1415. DOI: 10.1115/1.4028503.

[65] Irene Hafner und Niki Popper. „An Overview of the State of the Art in Co-Simulation and Related Methods“. In: *SNE Simulation Notes Europe* 31.4 (2021), S. 185–200. ISSN: 23059974. DOI: 10.11128/sne.31.on.10582.

[66] Robert Schmoll. *Co-Simulation und Solverkopplung: Analyse komplexer multiphysikalischer Systeme: Zugl.: Kassel, Univ., Diss., 2015*. Bd. 3/2015. Berichte des Instituts für Mechanik. Kassel: Kassel University Press, 2015. ISBN: 978-3-86219-592-3.

Erste Veröffentlichung

Pascal Zeise und Bernhard Schweizer. „Dynamics, stability and bifurcation analysis of rotors in air ring bearings“. In: *Journal of Sound and Vibration* 521 (2022), S. 116392. ISSN: 0022-460X. DOI: 10.1016/j.jsv.2021.116392

https://doi.org/10.1016/j.jsv.2021.116392

Journal of Sound and Vibration 521 (2022) 116392

Contents lists available at ScienceDirect

Journal of Sound and Vibration

journal homepage: www.elsevier.com/locate/jsvi

Dynamics, stability and bifurcation analysis of rotors in air ring bearings

Pascal Zeise *, Bernhard Schweizer

Department of Mechanical Engineering, Institute of Applied Dynamics, Technical University of Darmstadt, Darmstadt, Germany

ARTICLE INFO

Keywords:
Air ring bearings
Air foil bearings
Rotor dynamics
Stability
Bifurcation analysis
Co-simulation model

ABSTRACT

Classical air foil bearings consist of a top foil, which is usually supported by a bump or beam foil structure. For this bearing type, the air gap is a function of the top foil deformation. Here, an alternative air bearing design – called air ring bearing – is investigated, which may be regarded as a straightforward and very obvious modification of the classical air bearing design. The basic idea is to insert a rigid ring between the shaft and the foil structure. The ring may therefore be considered to be elastically mounted in the housing by means of a bump or beam-type structure. Alternatively, a viscoelastic supporting structure (elastomer) may be used to connect the ring with the housing. Hence, the air film is separated by a rigid ring from the supporting structure. As a consequence, the bearing gap for the fluid film has rigid walls, which simplifies the numerical calculation significantly.

In this manuscript, a detailed numerical analysis of rotor systems supported in air ring bearings is presented. The basic nonlinear dynamical effects occurring in such rotor systems are investigated with a particular focus on the stability and bifurcation behavior. Therefore, a detailed co-simulation model of the rotor/bearing system is used. Different possible bifurcation scenarios are described and explained with the help of run-up simulations.

Rotor systems with air ring bearings exhibit a completely different vibration and stability behavior than rotors in classical air foil bearings. Diverse interesting nonlinear vibration phenomena, not known in connection with classical air foil bearings, are discussed in detail and physically explained in a clear manner.

1. Introduction

Air foil bearings are used in many fields of application, especially in rotor systems where oil-free operating conditions are required. Classical air foil bearings consist of a top foil, which is supported by a bump-, beam- or wing-type foil [1,2,3,4,5,6,7,8,9]. For such bearings, the air gap between the rotor journal and the top foil is a function of the top foil deformation. The resulting air gap to be observed in operation is an important quantity that defines the load capacity as well as the stability and bifurcation behavior of the rotor system. Calculation of the top foil deformation is a non-trivial task, which requires very detailed nonlinear air foil bearing models. In literature, foil bearing models have been presented for different bearing design variants, see e.g. [10,11,12,13,14,15,16,17,18].

Here, a very straightforward and simple bearing design variant is considered. The main idea is to insert a rigid ring between the air

* Corresponding author.
E-mail address: zeise@ad.tu-darmstadt.de (P. Zeise).

https://doi.org/10.1016/j.jsv.2021.116392
Received 18 March 2021; Received in revised form 2 August 2021; Accepted 9 August 2021
Available online 28 August 2021

film and the supporting foil structure. As a consequence, the air film is generated between the journal and the inner surface of the rigid ring so that the foil deformations do not directly affect the gap function of the air film. The ring itself is elastically supported by the foil structure so that the necessary dissipation for the rotor system is still provided.

Air ring bearings may be designed in various forms and variations. In the simplest case, the inner surface of the ring is designed cylindrically. Alternatively, a multi-lobe geometry can be used (e.g. a three-lobe bearing) or a herringbone bearing. To support the ring with the housing, bump-, beam- or wing-type foils may be used. In this case, dissipation is mainly generated by dry friction effects in the foils. Alternatively, a viscoelastic supporting structure, e.g. an elastomer, may be considered to connect the ring with the housing. Then, dissipation is caused by viscous damping effects. Usage of air ring bearings instead of classical air foil bearings has different technical/physical advantages and disadvantages, which are in detail discussed in Section 2.2.

The physical behavior of air ring bearings is completely different from that of classical air foil bearings. As a consequence, rotors supported in air ring bearings exhibit a totally different stability and bifurcation behavior than rotors mounted in classical air foil bearings. To the best of the authors' knowledge, rotors in ring air bearings have not been studied and analyzed in literature until now. Here, a detailed analysis of such rotor systems is carried out. Air ring bearings behave highly nonlinear. As a consequence, rotor systems with air ring bearings exhibit a complex dynamical vibration behavior and reveal a very interesting stability and bifurcation behavior. Different nonlinear phenomena and vibration effects are observed, like self-excited oscillations, synchronization effects, jump phenomena, chaotic vibrations, etc.

A special focus of this work lies on a systematic study on the bifurcation behavior of rotor systems with air ring bearings. It will be shown that such rotor systems usually exhibit three basic bifurcation paths (here called bifurcation path 1, bifurcation path 2a and bifurcation path 2b). The influence of different rotor and bearing parameters on the bifurcation behavior is investigated and practical hints for a secure operation of the considered rotor systems are given.

A large number of fluid film bearing designs with different practical advantages and disadvantages have been presented and analyzed in literature. Fluid film bearings are technically very important, but also very interesting from the mechanical viewpoint, since rotors in fluid film bearings often exhibit interesting nonlinear vibration and bifurcation effects. While the rotor itself may often be considered as a linear structure, the fluid films behave highly nonlinear. Frequently and especially in rotor applications with low or moderate rotor speeds, the rotor/bearing system is designed in such a way that the system performs stable imbalance oscillations around a stable equilibrium position. Considering high-speed rotor systems, where the rotor weight is usually comparatively low, the critical speed of instability is often significantly below the operating speed so that self-excited oscillations, diverse bifurcation effects, chaotic vibrations, etc. may be observed in the operating range of speed [19,20,21]. While the onset speed of instability may be calculated with the help of an Eigenvalue analysis of the linearized rotor/bearing system, the calculation of rotor vibrations above the critical speed requires more sophisticated mechanical/mathematical investigations or transient numerical run-up simulations with nonlinear rotor/bearing models.

In rotor dynamic applications, self-excited oscillations produced by the fluid films are frequently called whirl or whip (oil whirl/whip phenomena, air whirl/whip phenomena). Whirl/whip effects have thoroughly been investigated in literature for various rotor systems and different bearing concepts. Here, we omit a detailed review on whirl/whip phenomena in fluid bearings; we only give a brief review and refer to the numerous literature in this field. Early investigations on the stability of rotors in hydrodynamic journal bearings based on simple rotor/bearing models can be found in [22,23]. Fundamental theoretical bifurcation analyses on the oil whirl and oil whip phenomena for simple rotor systems are, for instance, carried out in [20,24–33]. A survey on experimental and theoretical works concerning the stability of rotors in hydrodynamic bearings is given in [19,34–36]. Dynamics and stability of rotors with squeeze-film dampers and floating-ring bearings are discussed in [21,37–47], for instance.

For analyzing the stability and bifurcation behavior of rotor/bearing systems, models with very different detail level are used in literature. The necessary model depth depends, on the one hand, on the concrete design and on the complexity of the considered rotor/bearing system. On the other hand, the model requirements are defined by the objectives of the calculation. In the simplest case, a linear rotor/bearing model is used. Based on pre-calculated stiffness and damping coefficients of the fluid bearing, a classical eigenvalue analysis can be applied to calculate the critical rotor speed, where the stable equilibrium position gets unstable. Calculation of rotor motion above the critical rotor speed of instability – e.g. determination of orbits of limit cycles – is of course not possible with linear models. For rotor systems, which cannot be operated above the critical rotor speed for safety reasons (e.g. large steam turbines), a classical linear stability analysis may be sufficient from the practical point of view. In order to analyze rotor systems above the critical rotor speed, nonlinear models have to be applied. To study basic physical effects and vibration phenomena, nonlinear rotor models with reduced complexity are frequently used in literature. With rather straightforward nonlinear rotor/bearing models, even analytical or semi-analytical analyses can be carried out. Therefore, appropriate approximation techniques – perturbation methods, harmonic balance, etc. – may be applied. Such analyses can provide a good insight into the oscillation effects and may give a very clear description of the different physical phenomena arising in the system. With nonlinear models, also more sophisticated bifurcation analyses may be carried out, e.g. by making use of numerical continuation methods. For rather complex and large rotor systems, application of approximation techniques or numerical continuation methods may, however, be rather cumbersome. Moreover, approximation techniques and continuation methods may not be suited or may be inappropriate to calculate certain oscillation phenomena (e.g. quasiperiodic oscillations, chaotic motions). If very detailed physical models are required or if complicated oscillation effects have to be calculated, direct time integrations – e.g. rotor run-up and run-down simulations – of the equations of motion will be necessary. As a matter of fact, parameter studies, generation of stability maps and bifurcation diagrams will then be more time consuming.

The paper at hand intends to provide a systematic analysis of the whirl/whip phenomena occurring in rotor systems with air ring bearings. To analyze the bifurcation behavior of such systems, analytical stability and bifurcation calculations cannot be accomplished

due to the complexity of the system. Therefore, transient run-up simulations are carried out with the help of detailed nonlinear rotor/bearing models. The main contributions of this manuscript are:

- A physical model for air ring bearings is presented.
- The dynamics, the stability and the bifurcations occurring in rotor systems with air ring bearings are analyzed in detail with the help of nonlinear run-up simulations. Therefore, very accurate co-simulation models of the rotor/bearing system are used.
- The basic nonlinear vibration effects and the main physical phenomena occurring in rotor systems with air ring bearings are physically interpreted and explained in a very clear manner. Different vibration and bifurcation phenomena, not observed in connection with classical air foil bearings, are discussed in detail.
- Based on the simulation results, practical design recommendations for such rotor/bearing systems are deduced.

This manuscript is organized as follows: In Section 2, the air ring bearing design is explained. Two different variants are considered: a design variant, where the ring is supported with a foil structure and an alternative design concept, where the ring is supported by a viscoelastic material. A coupled numerical model for rotor systems with air ring bearings is presented, which consists of two nonlinear finite element models for the air films and a multibody model for the rotor. The multibody subsystem for the rotor and the finite element subsystems for the two air bearings are coupled in time domain with a sequential co-simulation algorithm to be described in Section 3. Run-up simulations for a simple 2D rotor/bearing model are presented in Section 4. With the help of this 2D model, the basic physical vibration and bifurcation effects of rotors in air ring bearings can be explained in a very straightforward and clear manner. Run-up simulations with a 3D rotor/bearing model of a real high-speed turbocompressor are presented in Section 5. A summary is given in Section 6. Results of an Eigenmode analysis for the rotor/bearing system of Section 5 are collected in Appendix A. Additional run-up simulations for a rotor system with increased asymmetry are arranged in Appendix B. The influence of rotor imbalance on the stability and bifurcation behavior is discussed in Appendix C. Additional information on the co-simulation interface and on the numerical time integration of the rotor/bearing model is presented in Appendix D.

2. Rotor/Bearing model

2.1. Classical air foil bearings

Classical air foil bearings consist of a top foil and a supporting foil, where frequently a bump-type [1,3,5,12,15] or beam-type structure is used [4,7,48,49], see Fig. 1. Alternatively, wing-type foils may be considered [9]. Reliable bearing models for classical foil bearings have to take into account that the gap function of the air film is influenced by the foil deformations. To calculate the pressure distribution in air foil bearings, it is therefore necessary to couple the compressible fluid film equations with nonlinear beam/shell models for the foil structure. Furthermore, stick-slip contacts between the foils and the housing have to be taken into account to correctly predict the dissipation effects in such bearings [5,50,51,52,53], which complicates the numerical analysis and the computational effort even more. In addition, appropriate heat balance equations have to be applied to compute the temperature distribution in the bearing. Such complex and highly nonlinear multiphysical models can be used to analyze and optimize air bearings within quasi-static calculations (optimization with respect to load capacity, friction loss, lift-off speed, etc.). Usually, these detailed models can, however, not be applied for fully transient simulations (e.g. run-up simulations for analyzing the stability and bifurcation behavior of the rotor/bearing system), since the computational effort would be extremely high. For transient rotordynamic calculations, reduced air foil bearing models are mandatory. Derivation of reduced models for air foil bearings is, however, a very demanding task.

To correctly predict the rotordynamic behavior and especially the stability and bifurcation behavior of rotor/bearing systems, reduced air bearing models must be able to reflect the basic physical effects. On the one hand, the gap function has to be calculated precisely to correctly predict the pressure field in the foil bearing. Therefore, a fully coupled model of the Reynolds equation and the supporting structure is required. On the other hand, for a prediction of the critical rotor speed of instability (onset speed of fluid film induced whirl/whip phenomena) and for a reliable calculation of self-excited rotor oscillations and orbits above the critical speed of instability, a correct modelling of the friction/damping effects in the bearing is necessary. The development of reduced bearing models

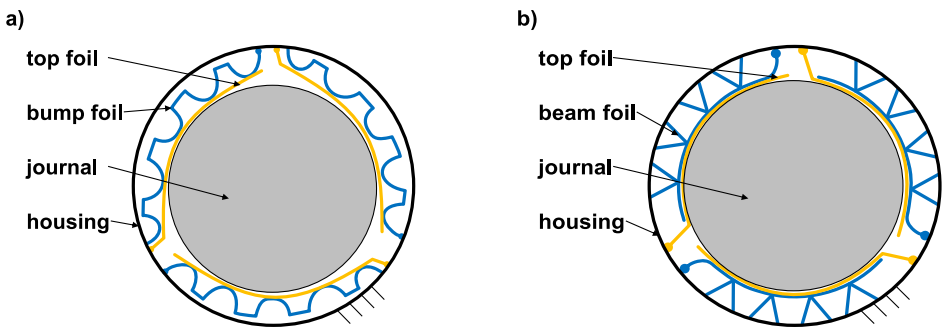

Fig. 1. Classical air foil bearing designs: (a) bump-type and (b) beam-type supporting structure.

for fully dynamic simulations, which take into account all relevant physical effects, is a challenging problem and subject of current research. To the authors' knowledge, this is still an open topic and challenging task. In literature, different reduced bearing models have been developed [54,55,56,57,58]. In the models presented in [54,56,58], damping effects in the air film are neglected and the fluid film is assumed to be infinitely stiff. The stiffness of the foil structure is modelled by a one-dimensional radial force function; dissipation is taken into account with a structural damping approach. More detailed bearing models in connection with transient simulations have been used in [59,60]. In [60], for instance, a transient bearing model is presented, where the fluid film is taken into account. The stiffness of the foil structure and its influence on the air gap is modelled by a linear force model; dissipation is considered with the help of a structural damping approach. Another detailed transient bearing model that takes the fluid film and an elastic fluid gap into account is presented in [59], where a more detailed model for the foil structure is used: the foil model is based on a linear structural model, where dissipation is taken into account by a modal damping approach. Also, a comparison with test rig results is carried out in [59].

A general explanation of the stability and bifurcation behavior of rotors supported in classical air foil bearings is of course not possible, since the occurring vibration effects strongly depend on the actual foil bearing design (bearing parameters) as well as on the rotor design. Nevertheless, regarding run-up/run-down measurements of rotors with different foil bearing designs reported in literature, see e.g. [54,56,59], some basic phenomena can be observed, which frequently occur in rotor systems with classical foil bearings. A characteristic frequency spectra of a run-up measurement is sketched in Fig. 2. At the beginning, only the rotor speed Ω is detected. Later, often subharmonic vibrations with $\Omega/2$ are observed in the lower speed range. Besides the commonly observed subsynchronous oscillations with $\Omega/2$, also subsynchronous vibrations with $n\Omega/m$ (n,m: integers) may be observed as well as supersynchonous oscillations (2Ω, ...). The subharmonic and superharmonic oscillations are caused by the nonlinear characteristic of the foil structure (especially by the nonlinear stiffness behavior). Note that the subharmonics only result from the nonlinear behavior of the foil structure (top foil and bump/beam foil) and are not related with whirl/whip effects from the air film. At higher rotor speeds, whirl/whip instabilities caused by the air films may occur. The amplitudes of the whirl/whip may be moderate so that a secure operation of the rotor in the whirl/whip regime is possible. Depending on the system parameters and on the rotor speed, the whirl/whip amplitudes may, however, also become larger so that a safe technical operation in the whirl/whip regime will not be possible. Depending on the rotor system and the operating conditions, classical foil bearings can also be designed in such a way that subsynchronous oscillations as well as whirl/whip effects may be prevented in the operating speed range (for instance by using a three-lobe bump foil bearing with a mechanical preload [17,62,63]).

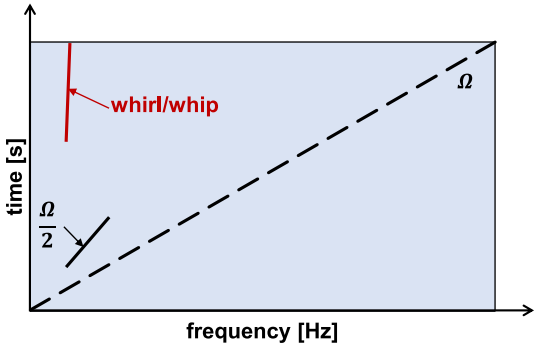

Fig. 2. Characteristic run-up spectrum of a rotor in classical air foil bearings.

2.2. Air ring bearings

2.2.1. Basic idea and design

Within a rotordynamic analysis, calculation of rotor orbits and determination of bifurcation points (stability limit) are important aspects. Therefore, run-up and run-down simulations may be used. Considering classical air foil bearings, reduced models must be developed, which enable transient rotor simulations with acceptable simulation times. The reduced bearing models have to maintain the main physical properties of the bearing. In contrast, alternative bearing concepts and design variants may be regarded, which require simpler models so that transient rotor simulations might be possible without an elaborate model reduction approach. Such alternative bearing design variants may have certain advantages and disadvantages compared to classical air foil bearings. One main advantage might, however, be the possibility to predict the rotordynamic behavior in a reliable manner with moderate computational effort.

As mentioned above, a main difficulty for predicting the dynamic response of rotors in classical air foil bearings lies in the fact that the gap function depends on the foil deformations. To circumvent this problem, it is a very straightforward idea to place a rigid ring between the air gap and the foil structure, see Fig. 3. The ring is able to translate in x- and y-direction; rotation around the z-axis is assumed to be prevented. As a consequence, an air gap with rigid walls is obtained so that the gap function does not explicitly depend on the foil deformations, which considerably reduces the modelling and therefore also the computational effort. The ring itself is supported elastically in the housing. To connect the ring with the housing, various design variants are possible. The ring may, for

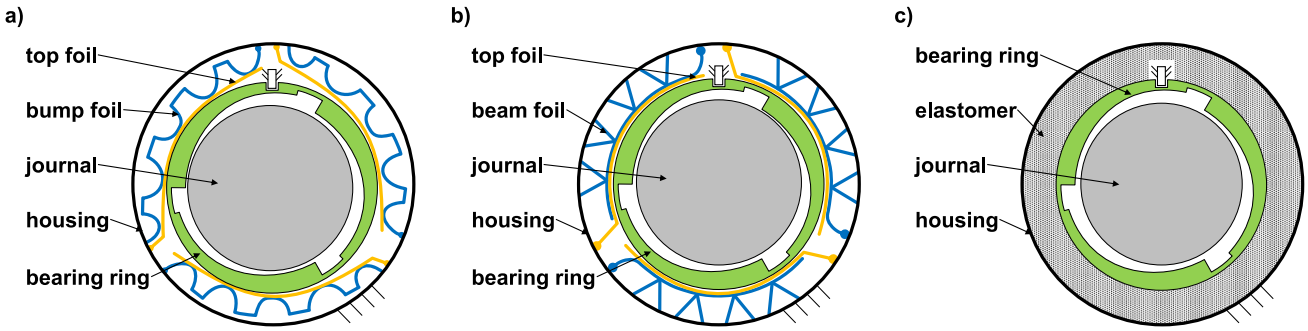

Fig. 3. Design variants of air ring bearings: (a) top/bump foil structure, (b) top/beam foil structure and (c) elastomer (viscoelastic mounting).

instance, be supported with a bump or beam foil structure (with or without top foil). Alternatively, the ring may be supported with an elastomer, see [61]. Using bump- or beam-type structures, dissipation is mainly generated by dry friction. Applying an elastomer, dissipation is basically obtained by viscous damping effects. Note that the physical type of dissipation may have a noticeable effect on the rotordynamic behavior. The inner surface of the ring may be cylindrical so that journal and ring can be considered as a rigid cylindrical air bearing. Alternatively, a three-lobe bearing design can be used, for instance.

Inserting a rigid ring between the journal and the supporting structure entails different benefits and drawbacks.

The main advantages are:

- The additional ring simplifies the dynamic analysis, since the gap function of the air film is only determined by the geometry of the inner ring surface and the relative displacement between journal and ring. As a consequence, reliable, fully transient and efficient models for predicting the critical rotor speed may be derived and solved numerically in time domain. With such models, the nonlinear dynamical behavior of the rotor system may be analyzed and optimized with moderate computational effort. Prediction of the onset speed of whirl/whip motion, detection of further bifurcations at higher rotor speeds (also a possible stabilization of the rotor system at higher rotor speeds), etc. is possible with such models.
- Friction losses during the start/stop phase may be reduced noticeably with the air ring bearing design. Classical air foil bearings are often designed with a mechanical preload in order to improve the stability behavior [17,62,63]. As a consequence of a mechanical preload, the lift-off speed for a fully developed air film is increased. Hence, dry friction or mixed friction is observed in the lower speed range, which produces wear in the coating of the top foil.
- Regarding classical air foil bearings, wear is often observed in the top foil coating in the course of operation. Reduced top foil coating may, one the one hand, entail a destruction of the bearing. On the other hand, a reduced coating may affect the rotordynamic behavior, since reduced coating increases the bearing gap between journal and top foil. Hence, reliable dynamical models have to take into account wear, which complicates the analysis markedly.

The main drawbacks are:

- Using air ring bearings, fluid-film induced instabilities usually occur already at very low rotor speeds. Classical air foil bearings – especially bearing designs with a larger mechanical preload [17,62,63] – may be designed in such a way that self-excited oscillations can even be omitted in the operating rotor speed range.
- Air ring bearing designs are more complex and eventually more expensive than the classical design variants.
- The radial clearance between compressor/turbine wheel and housing may be little larger with an air ring bearing design so that the efficiency of the machine may be (slightly) reduced.

2.2.2. Instability of rotors in hydrodynamic oil bearings

As well-known, rotors in hydrodynamic bearings may become unstable at higher rotor speeds. The stability behavior may be improved, for instance, if a three-lobe bearing design is used instead of the classical cylindrical bore geometry. But even with a three-lobe bearing design, the rotor/bearing system may become unstable at a certain critical speed. If the critical rotor speed is reached – here, the notion critical rotor speed is used for the stability limit of the linearized rotor system with respect to the equilibrium position – a bifurcation occurs and self-excited oscillations are observed: for instance a limit-cycle oscillation for systems with zero imbalance, quasiperiodic oscillations for systems with imbalance, etc.. Considering a rotor in oil bearings with little external (internal) damping/dissipation, the self-excited oscillations usually show very high amplitudes – i.e. dimensionless bearing eccentricities close to 1 – so that a technically save operation will not be possible, although the self-excited oscillations may be regarded as stable oscillations from the mathematical point of view. In order to run a rotor/bearing system above the critical speed of instability, usually additional external damping/friction has to be considered, e.g. by means of an externally arranged squeeze-film damper or by viscoelastic damping elements. Then, the amplitudes of the self-excited oscillations may be reduced so that a safe operation with moderate amplitudes is achieved. If the external damping/friction is chosen appropriately, it may even be possible to stabilize the rotor/bearing system again at higher speeds [19,34,35,36,44].

2.2.3. Instability of rotors in rigid air bearings and rotors in air ring bearings

Considering conventional air bearings with a rigid housing and a cylindrical bore geometry, the critical speed is – in contrast to oil bearings – usually very low, since viscosity of air is very low compared to oil. Using a multi-lobe geometry, the onset speed of instability may be increased, but it usually remains still very low. Without additional damping/friction elements, the rotor cannot be run above the critical rotor speed, since the bearing eccentricities are too large (close to 1). Hence, additional damping/friction has to be supplied in order to run the rotor system in the whirl/whip region with moderate bearing eccentricities. This is the basic idea behind the air ring bearing design considered here. Since the rotor system gets unstable at very low rotor speeds, the rotor is operated above the critical rotor speed. The amplitudes of the self-excited oscillations (amplitudes of the bearing eccentricities) are, however, limited to a technically acceptable magnitude by means of external damping/friction. The numerical investigations presented in the following sections clearly show that rotors in air ring bearings will become unstable at rather low rotor speeds. If additional external friction is supplied by mounting the ring with structural elements so that sufficient dissipation is provided (or by using viscoelastic elements that provide sufficient external damping), a save operation above the critical speed of instability may be possible, i.e. a secure operation with self-excited oscillations and moderate amplitudes.

2.3. Air film model (finite element model)

A schematic sketch of the air film gap in an air ring bearing is shown in Fig. 4. Here, a three-lobe bearing design is considered. The space-fixed x,y-reference system is located in the center O of the bearing housing. The ring is assumed to be able to move in x- and y-direction, rotation around the z-axis is prevented. Note that only a planar ring motion is considered, tilting is neglected. The vector $\boldsymbol{r}_R = [x_R, y_R]^T$ denotes the position vector of the ring center M_R with respect to the reference system; $\boldsymbol{r}_J = [x_J, y_J]^T$ is the vector of the rotor journal M_J with respect to the reference system. The relative displacement vector of M_J with respect to M_R is termed by $\Delta\boldsymbol{r} = \boldsymbol{r}_J - \boldsymbol{r}_R = [\Delta x, \Delta y]^T$; the relative velocity of M_J with respect to M_R is given by $\Delta\dot{\boldsymbol{r}} = \frac{\mathrm{d}}{\mathrm{d}t}\Delta\boldsymbol{r}$.

To characterize the relative displacement of M_J with respect to M_R, ring-fixed polar coordinates – namely the radial coordinate $\Delta r = |\Delta\boldsymbol{r}|$ and the polar angle δ – may be used alternatively to the Cartesian coordinates Δx and Δy. The relationship between $\Delta\boldsymbol{r}$, $\Delta\dot{\boldsymbol{r}}$ and the polar coordinates Δr, δ, $\Delta\dot{r}$, $\dot{\delta}$ is given by

$$\begin{aligned} \Delta r &= |\Delta\boldsymbol{r}| \\ \delta &= \operatorname{atan2}(\Delta y, \Delta x) - \alpha \\ \Delta\dot{r} &= \frac{1}{\Delta r}(\Delta\boldsymbol{r}\cdot\Delta\dot{\boldsymbol{r}}) \\ \dot{\delta} &= \frac{1}{\Delta r^2}\,(\Delta x\,\Delta\dot{y} - \Delta y\,\Delta\dot{x}). \end{aligned} \tag{1}$$

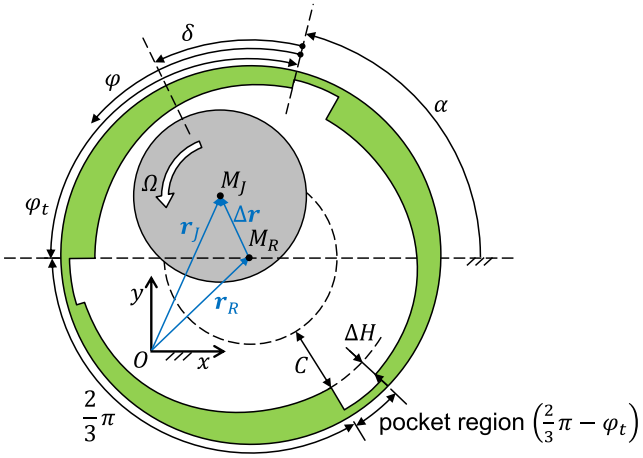

Fig. 4. Three-lobe air ring bearing geometry.

The space-fixed orientation of the ring with respect to the housing is defined by the constant angle α. The angle φ_t defines the lobe region. The three pockets for air supply, where ambient pressure is assumed, have the circumferential extension $\frac{2\pi}{3} - \varphi_t$. As shown in Fig. 4, C denotes the clearance of the three-lobe bearing and ΔH the step height between the pocket and the lobe region. Furthermore, an auxiliary angular coordinate φ is introduced, which is used for calculating the pressure distribution in the air gap with the help of the Reynolds equation.

To calculate the pressure distribution in the air gap, the isothermal Reynolds equation for compressible fluids

$$\frac{1}{r^2}\frac{\partial}{\partial\varphi}\left(\frac{\rho h^3}{\eta}\frac{\partial p}{\partial\varphi}\right)+\frac{\partial}{\partial z}\left(\frac{\rho h^3}{\eta}\frac{\partial p}{\partial z}\right)=6\Omega\frac{\partial(\rho h)}{\partial\varphi}+12\frac{\partial(\rho h)}{\partial t}, \tag{2}$$

is used [28,64]. r denotes the journal radius, $h(\varphi,t)$ is the gap function (journal misalignment is neglected), $p(\varphi,z,t)$ terms the pressure field, η represents the dynamic viscosity of the fluid, $\rho(\varphi,z,t)$ denotes the density field and Ω the rotational speed of the rotor. φ represents the circumferential and z the axial coordinate. The air is considered as an ideal gas. Within an isothermal approach, the relationship between pressure and density is given by $\rho=\frac{1}{R_{\text{air}}T_{\text{air}}}p$ (R_{air} is the specific gas constant of air, T_{air} is the prescribed constant temperature of the air film). With these assumptions, Eq. (2) reads

$$\frac{1}{r^2}\frac{\partial}{\partial\varphi}\left(ph^3\frac{\partial p}{\partial\varphi}\right)+\frac{\partial}{\partial z}\left(ph^3\frac{\partial p}{\partial z}\right)=6\Omega\eta\frac{\partial(ph)}{\partial\varphi}+12\eta\frac{\partial(ph)}{\partial t}. \tag{3}$$

Note that only the pressure in the lobe regions $S_{\text{lobe}}=\left\{[0,\varphi_t],\ \left[\frac{2\pi}{3},\frac{2\pi}{3}+\varphi_t\right],\ \left[\frac{4\pi}{3},\frac{4\pi}{3}+\varphi_t\right]\right\}$ is calculated. In the pockets, ambient pressure p_a is assumed. The gap function h in the lobe regions is given by

$$h(\varphi)=C-\Delta r\cos(\varphi-\delta)+\Delta H\left(1+\frac{2\pi}{3\varphi_t}\left\lfloor\frac{3\varphi}{2\pi}\right\rfloor-\frac{\varphi}{\varphi_t}\right),\qquad \varphi\epsilon S_{\text{lobe}}, \tag{4}$$

where $\lfloor\ldots\rfloor$ denotes the floor function. The boundary conditions for the Reynolds equation are illustrated in Fig. 5. Since journal

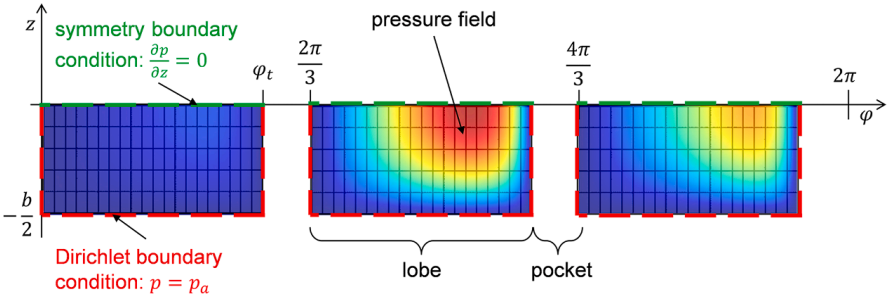

Fig. 5. Boundary conditions for the Reynolds equation.

misalignment is ignored, symmetry boundary conditions can be used with respect to the middle plane of the bearing (note that b denotes the bearing width).

The Reynolds equation, see Eq. (3), is discretized by a finite element approach. Therefore, the time dependent pressure field $p(\varphi,z,t)$ is approximated by $\widetilde{p}_i(\varphi,z,t)=\sum_{i=1}^{n_k}N_i(\varphi,z)p_i(t)$. $N_i(\varphi,z)$ term the ansatz functions, which depend on the chosen element type. $p_i(t)$ are the pressure variables at the finite element nodes. n_k denotes the number of finite element nodes (degrees of freedom). Here, the bearing is discretized with 300 finite elements (quadratic ansatz functions) resulting in $n_k=1353$ pressure degrees of freedom. The discretized Reynolds equation yields a nonlinear system of ordinary differential equations (ODE system) for the pressure variables $p_i(t)$ at the nodes of the finite element mesh, which are collected in the resultant vector $\boldsymbol{p}=[p_1,\ldots,p_{n_k}]^T$. The first order ODE system for the unknown pressure variables can formally be written in implicit form according to

$$\boldsymbol{f}(\boldsymbol{p},\dot{\boldsymbol{p}},t)=\boldsymbol{0}. \tag{5}$$

This nonlinear ODE system is numerically integrated with an implicit time integration scheme. After each time integration step, the resulting bearing forces $F_{px}(t)$, $F_{py}(t)$ in global x- and y-direction can be determined by integrating the pressure field over the bearing surface, i.e.

$$F_{px}=\int_0^{2\pi}\int_0^{b}p(\varphi,\ z)\ r\cos(\varphi+\alpha)\ \mathrm{d}z\ \mathrm{d}\varphi, \tag{6}$$

$$F_{py}=\int_0^{2\pi}\int_0^{b}p(\varphi,\ z)\ r\sin(\varphi+\alpha)\ \mathrm{d}z\ \mathrm{d}\varphi. \tag{7}$$

The resultant bearing forces define the output variables of the finite element subsystem and are collected in the output vector $[F_{px},F_{py}]^{\mathrm{T}}$. The input variables for the finite element subsystem are the angular velocity of the rotor in z-direction (i.e. the rotor speed Ω) as well as the kinematical quantities $\Delta\boldsymbol{r}=[\Delta x,\Delta y]^T$ and $\Delta\dot{\boldsymbol{r}}=[\Delta\dot{x},\Delta\dot{y}]^T$, which describe the relative motion of the rotor journal M_J with respect to the ring center M_R.

Since the rotor/bearing system contains two fluid films, two output vectors $\boldsymbol{y}_{\mathrm{FEM1}} = [F_{px1}, F_{py1}]^{\mathrm{T}}$ and $\boldsymbol{y}_{\mathrm{FEM2}} = [F_{px2}, F_{py2}]^{\mathrm{T}}$ are defined, which are collected into the resulting output vector $\boldsymbol{y}_{\mathrm{FEM}} = [F_{px1}, F_{py1}, F_{px2}, F_{py2}]^{\mathrm{T}}$. It should be mentioned that the output variables $\boldsymbol{y}_{\mathrm{FEM}}$ of the FE subsystems serve as input variables $\boldsymbol{u}_{\mathrm{MBS}}$ for the multibody subsystem of the rotor, i.e. $\boldsymbol{u}_{\mathrm{MBS}} = \boldsymbol{y}_{\mathrm{FEM}}$. It should further be pointed out that the input variables for the two fluid films are given by $\boldsymbol{u}_{\mathrm{FEM1}} = [\Delta\boldsymbol{r}_1^T, \Delta\dot{\boldsymbol{r}}_1^T, \Omega]^{\mathrm{T}}$ and $\boldsymbol{u}_{\mathrm{FEM2}} = [\Delta\boldsymbol{r}_2^T, \Delta\dot{\boldsymbol{r}}_2^T, \Omega]^{\mathrm{T}}$. Note that the input variables for the finite element subsystems are the output variables of the multibody system, i.e. $\boldsymbol{y}_{\mathrm{MBS}} = [\Delta\boldsymbol{r}_1^T, \Delta\dot{\boldsymbol{r}}_1^T, \Delta\boldsymbol{r}_2^T, \Delta\dot{\boldsymbol{r}}_2^T, \Omega]^{\mathrm{T}}$.

2.4. Model for the supporting structure of the ring

The ring is mounted elastically in the housing so that the ring is able to move in horizontal and vertical direction. Rotation is, however, assumed to be prevented. The supporting structure of the ring does not only provide a certain kind of flexibility. A main purpose of the supporting structure is also to provide friction/damping so that the amplitudes of the self-excited whirl/whip vibrations are limited to a technically acceptable magnitude. Here, two basic design alternatives for the supporting structure are considered, namely a foil design variant and a viscoelastic design variant.

A main objective of this manuscript is to give a very clear physical explanation of the vibration and bifurcation phenomena occurring in rotor systems with air ring bearings. Therefore, very straightforward mechanical models are used. Applying models with a highly nonlinear structural behavior or models with a highly nonlinear viscoelastic characteristic, additional nonlinear vibration effects may be introduced so that a clear distinction between the different physical effects might be complicated.

2.4.1. Elastic foils with dry friction

In the first design variant, the ring is elastically mounted in the housing by means of a foil structure. Different foil designs may be used, e.g. a top/bump foil arrangement according to Fig. 3a or a top/beam foil configuration sketched in Fig. 3b. Dissipation is mainly generated by dry friction. Depending on the specific design, the elastic structure may behave almost linear or highly nonlinear, almost isotropic or rather anisotropic. Generally, the structure may be described by nonlinear hysteresis curves [17,52,58,62,63,65,66], see Fig. 6a. To keep the representation concise, a straightforward modelling approach is considered here. We assume an isotropic and linear-elastic behavior of the foil structure. Furthermore, ideal Coulomb friction is used. With these two basic assumptions, the foil structure can be described by idealized hysteresis curves according to Fig. 6b. The figure shows the resultant force of the foil structure as a function of the radial displacement of the ring. The governing equation, which describes the force/displacement relationship of the idealized hysteresis, reads

$$\boldsymbol{F} = -c_{\mathrm{foil}}\,\boldsymbol{r}_R - F_{\mathrm{fric}}\,\frac{\dot{\boldsymbol{r}}_R}{\max\left(|\dot{\boldsymbol{r}}_R|, v_{\mathrm{step}}\right)}\,\mathrm{step}\left(|\dot{\boldsymbol{r}}_R|\right), \tag{8}$$

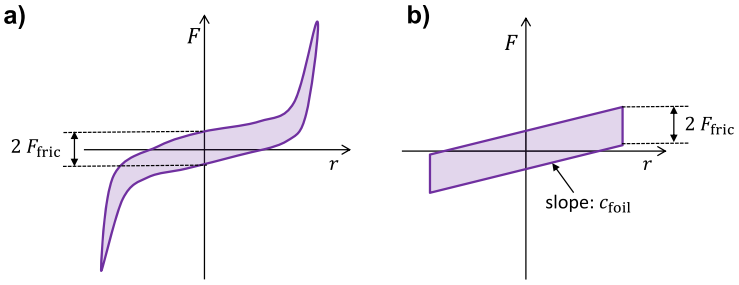

Fig. 6. (a) Nonlinear hysteresis curve; (b) idealized hysteresis curve.

where c_{foil} terms the stiffness coefficient. Coulomb friction is implemented with a regularization approach by using a smoothed step-function according to

$$\mathrm{step}\left(|\dot{\boldsymbol{r}}_R|\right) = \begin{cases} -2\dfrac{|\dot{\boldsymbol{r}}_R|^3}{{v_{\mathrm{step}}}^3} + 3\dfrac{|\dot{\boldsymbol{r}}_R|^2}{{v_{\mathrm{step}}}^2} & \left(0 \le |\dot{\boldsymbol{r}}_R| < v_{\mathrm{step}}\right) \\ 1 & \left(|\dot{\boldsymbol{r}}_R| < v_{\mathrm{step}}\right) \end{cases}, \tag{9}$$

where v_{step} denotes a user-defined numerical constant (e.g. $v_{\text{step}} = 1E-6$ m s^{-1}).

In Sections 4 and 5, run-up simulations of rotors with air ring bearings are presented for different stiffness coefficients c_{foil} and friction forces F_{fric}. Therefore, typical medium-sized high-speed rotors are considered (rotor mass $\approx$ 830 g, maximum rotor speed $\approx$ 2000 Hz, shaft diameter $\approx$ 30 mm). For such an application, reasonable and realistic values for c_{foil} and F_{fric} have to be chosen. Considering classical bump or beam type air foil bearings, typically used for such medium-sized rotors, appropriate values for c_{foil} and F_{fric} can be obtained from measured (simulated) hysteresis curves [4,17,67]. Depending on the actual bearing design (beam or bump type, single or multi-lobe, etc.) and on the bearing parameters (foil thickness, mechanical preload, etc.), stiffness and friction may notably differ. Regarding, for instance, the lightly preloaded three-lobe bump foil bearing investigated in [17] comparatively low stiffness and friction values ($c_{\text{foil}} \approx 125$ N mm^{-1} and $F_{\text{fric}} \approx 1$ N) are obtained in the centered position, whereas for the highly preloaded bearing stiffness and friction will significantly increase ($c_{\text{foil}} \approx 400$ N mm^{-1} and $F_{\text{fric}} \approx 2.5$ N). In [4], for instance, a beam type bearing is analyzed, which shows stiffness and friction values of $c_{\text{foil}} \approx 600$ N mm^{-1} and $F_{\text{fric}} \approx 10$ N in the centered position. Based on the hysteresis curves for classical foil bearings documented in literature, the stiffness coefficients c_{foil} and the friction forces F_{fric} are assumed in the intervals [100 N mm^{-1}, 800 N mm^{-1}] and [1 N, 9 N], respectively. It should be mentioned that the friction forces may simply be increased – without significantly increasing the stiffness – by just raising the mechanical preload between the foils and the ring.

2.4.2. Viscoelastic material (elastomer)

Alternatively to a foil design, a viscoelastic material – e.g. an elastomer – may be used to connect the ring with the housing, see Fig. 3c. To keep the calculation simple, an isotropic linear-viscoelastic material behavior is assumed. Then, the force law reads

$$\boldsymbol{F} = -c_{\text{elast}}\, \boldsymbol{r}_R - d_{\text{visc}}\, \dot{\boldsymbol{r}}_R \tag{10}$$

with the stiffness coefficient c_{elast} and the damping coefficient d_{visc}.

For the run-up simulations in Sections 4 and 5, c_{elast} is chosen in the interval [100 N mm^{-1}, 600 N mm^{-1}]. The damping coefficient d_{visc} is assumed in the interval [30 N ms mm^{-1}, 1500 N ms mm^{-1}]. In contrast to dry friction, the dissipated energy in a force cycle is not independent of the cycling frequency. Therefore, a simple conversion of the assumed force interval for F_{fric} into a corresponding interval for d_{visc} is not possible. Run-up simulations with different values of d_{visc} and a comparison with corresponding run-up simulations with dry friction has shown that assuming d_{visc} in the above specified range will produce plausible and reasonable results. It should be mentioned that for elastomers, damping may very easily be modified – without markedly changing the stiffness – by simply changing the carbon component.

2.5. Multibody model of the rotor

A schematic sketch of the rotor/bearing system is shown in Fig. 7. The rotor is modelled as a multibody system [68,69] and consists of the shaft, the compressor and turbine wheel, the two rigid bearing rings and two small imbalance masses fixed at the wheels. It should be stressed that the multibody subsystem contains the complete rotor (shaft, wheels, imbalance masses, rings including the supporting structure), but not the two air films. The two air films are modelled separately within a finite element environment (two finite element subsystems) and are connected to the multibody subsystem of the rotor by means of a co-simulation approach, see Section 3.

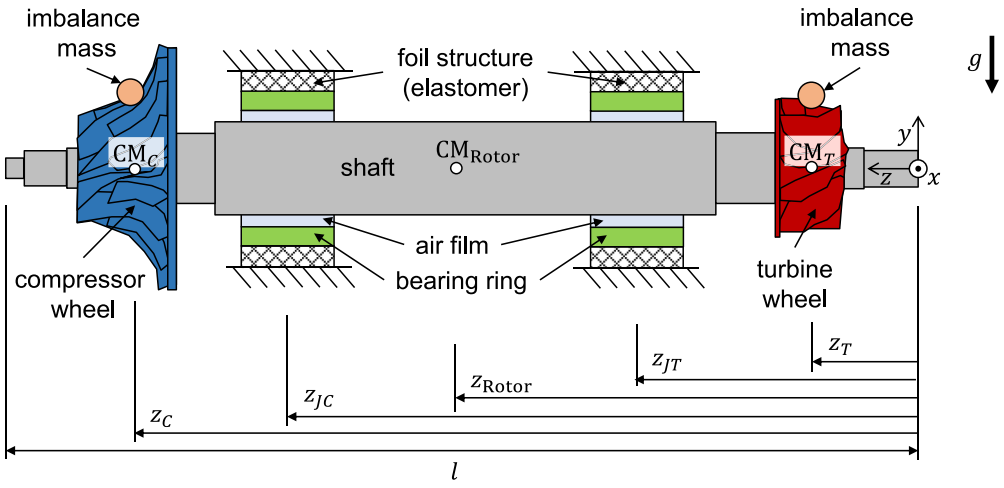

Fig. 7. Schematic sketch of the rotor/bearing system.

In Fig. 7, z_{Rotor} defines the center of mass of the entire rotor (shaft and wheels). The middle planes of the turbine- and compressor-sided bearing are specified by z_{JT} and z_{JC}. Finally, z_T and z_C denote the axial coordinates of the center of mass of the turbine and

compressor wheel.

For the multibody subsystem, the equations of motion in the stabilized index-2 formulation are used [70], which read

$$\begin{aligned} \boldsymbol{M}(t,\boldsymbol{x})\dot{\boldsymbol{x}} &= \boldsymbol{M}(t,\boldsymbol{x})\boldsymbol{v} - \boldsymbol{G}^{\mathrm{T}}(t,\boldsymbol{x})\boldsymbol{\mu} \\ \boldsymbol{M}(t,\boldsymbol{x})\dot{\boldsymbol{v}} &= \boldsymbol{f}_{\mathrm{e}}(t,\boldsymbol{x},\boldsymbol{v},\boldsymbol{u}_{\mathrm{MBS}}) - \boldsymbol{G}^{\mathrm{T}}(t,\boldsymbol{x})\boldsymbol{\lambda} \\ \boldsymbol{0} &= \boldsymbol{g}(t,\boldsymbol{x}) \\ \boldsymbol{0} &= \dot{\boldsymbol{g}}(t,\boldsymbol{x},\boldsymbol{v}). \end{aligned} \tag{11}$$

The vector $\boldsymbol{x} = (x_1, \ldots, x_\upsilon)^T \in \mathbb{R}^\upsilon$ contains the υ generalized coordinates of the multibody system and the vector $\boldsymbol{v} = (v_1, \ldots, v_\upsilon)^T \in \mathbb{R}^\upsilon$ the generalized velocities. Position and velocity coordinates are related by the kinematical differential equations $\dot{\boldsymbol{x}} = \boldsymbol{v}$. The mass matrix is represented by $\boldsymbol{M}(t,\boldsymbol{x}) \in \mathbb{R}^{\upsilon\times\upsilon}$ and assumed to be symmetric and positive definite. The vector $\boldsymbol{f}_{\mathrm{e}}(t,\boldsymbol{x},\boldsymbol{v},\boldsymbol{u}_{\mathrm{MBS}})$ represents the externally applied forces/torques as well as the centrifugal and Coriolis forces. The system is constrained by υ_c rheonomic algebraic constraint equations $g_i(t,\boldsymbol{x}) = 0$ $(i = 1, \ldots, \upsilon_{\mathrm{c}})$, which are arranged in the constraint vector $\boldsymbol{g} \in \mathbb{R}^{\upsilon_{\mathrm{c}}}$. The term $\boldsymbol{G}^T(t,\boldsymbol{x})\boldsymbol{\lambda}$ represents the constraint forces/torques, where $\boldsymbol{G} = \frac{\partial \boldsymbol{g}}{\partial \boldsymbol{x}} \in \mathbb{R}^{\upsilon_{\mathrm{c}}\times\upsilon}$ denotes the constraint-Jacobian and $\boldsymbol{\lambda} = (\lambda_1, \ldots, \lambda_{\upsilon_{\mathrm{c}}})^T \in \mathbb{R}^{\upsilon_{\mathrm{c}}}$ the vector of Lagrange multipliers. Here, the well-established index-2 formulation according to [70] is applied, i.e. the constraint equations $\boldsymbol{0} = \dot{\boldsymbol{g}}(t,\boldsymbol{x},\boldsymbol{v})$ on velocity level are incorporated by means of the additional Lagrange multipliers $\boldsymbol{\mu} = (\mu_1, \ldots, \mu_{\upsilon_{\mathrm{c}}})^T \in \mathbb{R}^{\upsilon_{\mathrm{c}}}$. $\boldsymbol{u}_{\mathrm{MBS}}(t)$ are the input variables of the multibody system, namely the resulting forces of the two fluid film bearings. Note again that the input variables of the multibody subsystem equal the output variables of the finite element subsystems for the two fluid films, i.e. $\boldsymbol{u}_{\mathrm{MBS}}(t) = [\boldsymbol{y}_{\mathrm{FEM1}}^T, \boldsymbol{y}_{\mathrm{FEM2}}^T]^T = [F_{px1}, F_{py1}, F_{px2}, F_{py2}]^T$. The output vector $\boldsymbol{y}_{\mathrm{MBS}}(t) = [\Delta\boldsymbol{r}_1^T, \Delta\dot{\boldsymbol{r}}_1^T, \Delta\boldsymbol{r}_2^T, \Delta\dot{\boldsymbol{r}}_2^T, \Omega]^{\mathrm{T}}$ of the multibody subsystem contains the relative displacement and velocity coordinates of the compressor- and turbine-sided journal as well as the angular velocity of the rotor. The output variables of the multibody subsystem serve as input variables for the two finite element subsystems.

3. Rotor/bearing co-simulation model

In the current work, the rotor/bearing system is numerically integrated with a co-simulation technique [71]. Within this co-simulation approach, the rotor/bearing system is decomposed into three subsystems: one subsystem for the rotor (multibody subsystem, MBS) and two further subsystems for the two air films (2 finite element subsystems, FEM1 and FEM2).

To carry out a co-simulation, appropriate coupling variables (input/output variables) have to be defined, which describe the physical connection between the subsystems. The MBS subsystem is coupled with the two FEM subsystems by means of a weak coupling approach. Therefore, a communication-time grid is introduced by defining macro-time points T_N $(N = 0, 1, 2, \ldots)$. Within a weak coupling approach, the three subsystems are integrated independently from each other during a macro-step from T_N to T_{N+1}. Information, i.e. coupling variables, are only exchanged at the macro-time points T_N. Between the macro-time points, the coupling variables are approximated by using extrapolation and interpolation polynomials.

In the present manuscript, an explicit sequential co-simulation approach (Gauss-Seidel scheme) is applied, where the MBS subsystem is used as master subsystem. Moreover, a force/displacement decomposition technique is applied [72,73]. Hence, the output variables $\boldsymbol{y}_{\mathrm{MBS}}$ of the multibody subsystem are kinematical variables (relative journal displacements in x- and y-direction, their time-derivatives and the angular velocity of the rotor), which serve as input variables for the two FE subsystems. The output variables $\boldsymbol{y}_{\mathrm{FEM1}}$ and $\boldsymbol{y}_{\mathrm{FEM2}}$ of the FE subsystems are the resultant bearing forces in x- and y-direction of the two air films, which together represent the input variables for the multibody subsystem.

The sequential co-simulation procedure used here for carrying out the numerical time integration can simply be described by considering the general macro-time step from T_N to T_{N+1}. At the beginning of the macro-time step, the state variables of the three subsystems and also the coupling variables are assumed to be known at the current time point T_N as well as at the previous macro-time points T_{N-1}, T_{N-2}, …. The sequential co-simulation strategy used here is executed in two steps.

Step 1: Integration of MBS with extrapolated input variables

- Firstly, subsystem 1 (multibody subsystem of the rotor, master subsystem) is integrated from the macro-time point T_N to T_{N+1} with the macro-step size $H_N = T_{N+1} - T_N$. For the numerical time integration of the equations of motion, see Eq. (11), the bearing forces are required. Since the bearing forces are unknown in the time interval $[T_N, T_{N+1}]$, extrapolated bearing forces are used. Therefore, a vector of extrapolation polynomials $\widetilde{\boldsymbol{u}}_{N+1}^{\mathrm{ext,MBS}}(t) = \boldsymbol{P}_{N+1}^k(t; (T_N, \boldsymbol{u}_{\mathrm{MBS}}(T_N)), \cdots, (T_{N-k}, \boldsymbol{u}_{\mathrm{MBS}}(T_{N-k})))$ of degree k is generated, which approximates the coupling variables $\boldsymbol{u}_{\mathrm{MBS}}(t)$ in the time interval $[T_N, T_{N+1}]$.
- Integrating the multibody system, see Eq. (11), from $T_N \rightarrow T_{N+1}$ with the approximation polynomials $\widetilde{\boldsymbol{u}}_{N+1}^{\mathrm{ext,MBS}}(t)$ yields the new variables $\boldsymbol{x}(T_{N+1})$, $\boldsymbol{v}(T_{N+1})$ and $\boldsymbol{\lambda}(T_{N+1})$.
- Finally, new coupling variables $\boldsymbol{y}_{\mathrm{MBS}}(T_{N+1}) = \boldsymbol{u}_{\mathrm{FEM}}(T_{N+1})$ – i.e. new kinematical input variables for the finite element systems – are calculated with the help of $\boldsymbol{x}(T_{N+1})$, $\boldsymbol{v}(T_{N+1})$ and $\boldsymbol{\lambda}(T_{N+1})$.

Step 2: Integration of FEM1 and FEM2 with interpolated input variables

- Secondly, the FE subsystems (slave subsystems) are integrated from T_N to T_{N+1}. For the numerical integration of the FE subsystem, kinematical quantities of subsystem 1 are required. Since the output variables of the multibody system are already known at T_{N+1}

from step 1, interpolated coupling variables can be used for integrating the two finite element subsystems. Therefore, two vectors of interpolation polynomials of degree k are generated, which approximate the coupling variables $\boldsymbol{u}_{\mathrm{FEM1}}(t)$ and $\boldsymbol{u}_{\mathrm{FEM2}}(t)$ in the time interval $[T_N, T_{N+1}]$, namely $\widetilde{\boldsymbol{u}}_{N+1}^{\mathrm{int,FEM1}}(t) = \boldsymbol{P}_{N+1}^{k}(t; (T_{N+1}, \boldsymbol{u}_{\mathrm{FEM1}}(T_{N+1})), (T_N, \boldsymbol{u}_{\mathrm{FEM1}}(T_N)), \cdots, (T_{N-k}, \boldsymbol{u}_{\mathrm{FEM1}}(T_{N-k+1})))$ and $\widetilde{\boldsymbol{u}}_{N+1}^{\mathrm{int,FEM2}}(t) = \boldsymbol{P}_{N+1}^{k}(t; (T_{N+1}, \boldsymbol{u}_{\mathrm{FEM2}}(T_{N+1})), (T_N, \boldsymbol{u}_{\mathrm{FEM2}}(T_N)), \cdots, (T_{N-k}, \boldsymbol{u}_{\mathrm{FEM2}}(T_{N-k+1})))$.

- Integrating the finite element subsystems 1 and 2 according to Eq. (5) from $T_N \rightarrow T_{N+1}$ with the help of the approximation polynomials $\widetilde{\boldsymbol{u}}_{N+1}^{\mathrm{int,FEM1}}(t)$ and $\widetilde{\boldsymbol{u}}_{N+1}^{\mathrm{int,FEM2}}(t)$ yields the new pressure variables $\boldsymbol{p}_1(T_{N+1})$ and $\boldsymbol{p}_2(T_{N+1})$.
- Finally, new coupling variables $\boldsymbol{y}_{\mathrm{FEM1}}(T_{N+1})$ and $\boldsymbol{y}_{\mathrm{FEM2}}(T_{N+1})$ – i.e. new resultant bearing forces at the time point T_{N+1} according to Eq. (6) and Eq. (7) – are calculated with the help of the pressure variables $\boldsymbol{p}_1(T_{N+1})$ and $\boldsymbol{p}_2(T_{N+1})$.

Then, the next macro-time step $T_{N+1} \rightarrow T_{N+2}$ is carried out.

Within the implemented master-slave approach, a variable macro-time grid is used, which is defined by the step-size of the master subsystem, i.e. the macro-step size is identical with the micro-step size of the MBS solver. Further information on the co-simulation interface and the numerical time integration of the subsystems are collected in Appendix D. It should be stressed that the approximation order of the coupling variables influences the accuracy and also the numerical stability of the co-simulation approach. A detailed analysis of the convergence order and a numerical stability analysis of explicit and implicit co-simulation approaches can be found in [74], for instance. In the numerical run-up simulations presented in the following sections, the coupling variables are extrapolated and interpolated with quadratic Lagrange polynomials ($k = 2$).

4. Bifurcation analysis for symmetrical rigid rotor in air ring bearings

To analyze and explain the basic vibration and bifurcation effects of rotors supported in air ring bearings in a very clear manner, we firstly consider a simple rotor system, namely a rigid rotor symmetrically supported in air ring bearings. Due to symmetry and since tilting of the rotor is assumed to be prevented here, only planar motion in x- and y-direction has to be considered. Rotation of the rotor in z-direction is kinematically prescribed according to $\Omega = \frac{2\pi}{3}\ 2000\ \mathrm{t\ s^{-2}}$ (linear rotor run-up in 3 s up to 2000 Hz). For the reason of a very clear representation and a very lucid explanation of the occurring bifurcation effects, rotor imbalance is neglected. Influence of imbalance on the vibration and bifurcation behavior of the rotor system is discussed in Appendix C. For the run-up simulations, rotor and ring are initially centered at the space-fixed z-axes with zero velocity.

4.1. Air ring bearings with elastic foil structure

Firstly, a symmetrical rigid rotor system is considered, where the rings are mounted with a foil structure, see Section 2.4.1. Run-up simulations have been carried out with the following data: rotor mass $m = 830$ g, ring mass $m_R = 50$ g, air viscosity $\eta_{\mathrm{air}} = 20.936E-6\ \mathrm{kg\ m^{-1}s^{-1}}$ (assumed fluid temperature: $T_{\mathrm{air}} = 80°\mathrm{C}$), bearing clearance $C = 30\ \mu$m (warm clearance), step height $\Delta H = 20\ \mu$m, lobe angle $\varphi_t = 110°$, ring orientation angle $\alpha = \pi - \varphi_t$. The stiffness coefficient c_{foil} and the friction force F_{fric} are varied in order to show the different possible bifurcations of the system. Detailed numerical investigations have shown that the system may exhibit three different bifurcations paths (here called bifurcation path 1, bifurcation path 2a and bifurcations path 2b). These three basic bifurcation paths are explained in the subsequent subsections.

4.1.1. Run-up simulation 1 (bifurcation path 1)

Results of a run-up simulation with $c_{\mathrm{foil}} = 600\ \mathrm{N\ mm^{-1}}$ and $F_{\mathrm{fric}} = 5$ N are collected in Fig. 8. The figure shows the dimensionless bearing eccentricity $\varepsilon = \Delta r/C$, the vertical rotor displacement y_J as well as the frequency spectrum of y_J. The simulation results can be summarized as follows:

- In the range $0 \leq t \leq 750$ ms ($0 \leq \Omega \leq 500$ Hz), the rotor rotates around a stable equilibrium position (if rotor imbalance is considered, imbalance oscillations around a stable equilibrium position are observed). After a settling phase up to ≈ 100 ms, the bearing eccentricity ε is reduced continuously and moves towards the bearing center.
- At $t \approx 750$ ms ($\Omega \approx 500$ Hz), the equilibrium position becomes unstable (Hopf bifurcation) and a stable limit cycle oscillation is observed (whirl/whip oscillation). The limit cycle frequency at the onset of the self-excited oscillations is ≈ 140 Hz.
- At $t \approx 1000$ ms ($\Omega \approx 666.6$ Hz), a second bifurcation (saddle node bifurcation) is observed. The rotor remains in self-excited oscillations, however a jump in the limit cycle amplitudes is observed. After this jump, stable limit cycle oscillations with very high amplitudes are detected. Note that the bearing eccentricities are very large so that the journal almost reaches the inner ring surface. While this limit cycle is a stable oscillation from the mathematical point of view, a safe operation of the rotor for $t > 1000$ ms will not be possible from the practical viewpoint. The limit cycle frequency only slightly increases with increasing rotor speed.
- Fig. 8 also contains simulation results of a run-down simulation. After the rotor has reached the maximum speed of $\Omega = 2000$ Hz at $t = 3000$ ms, the rotor speed has been decreased linearly from 2000 Hz to $\Omega = 0$ Hz in 3000 ms. For a better comparison of the run-up and run-down results, the run-down curves have been incorporated into the corresponding run-up curves in reverse direction (additional scales for the run-down curves have been omitted). Comparing the run-up and run-down plots clearly shows that the Hopf-bifurcation is subcritical: during the run-up, the equilibrium gets unstable at a rotor speed of $\Omega \approx 500$ Hz; regarding the run-down curves shows that the equilibrium position is reached again at a rotor speed of $\Omega \approx 340$ Hz. Furthermore, a clear

hysteresis effect can be observed in connection with the saddle node bifurcations (jump at $\Omega \approx 666.6$ Hz during the run-up; jump at $\Omega \approx 560$ Hz during the run-down).

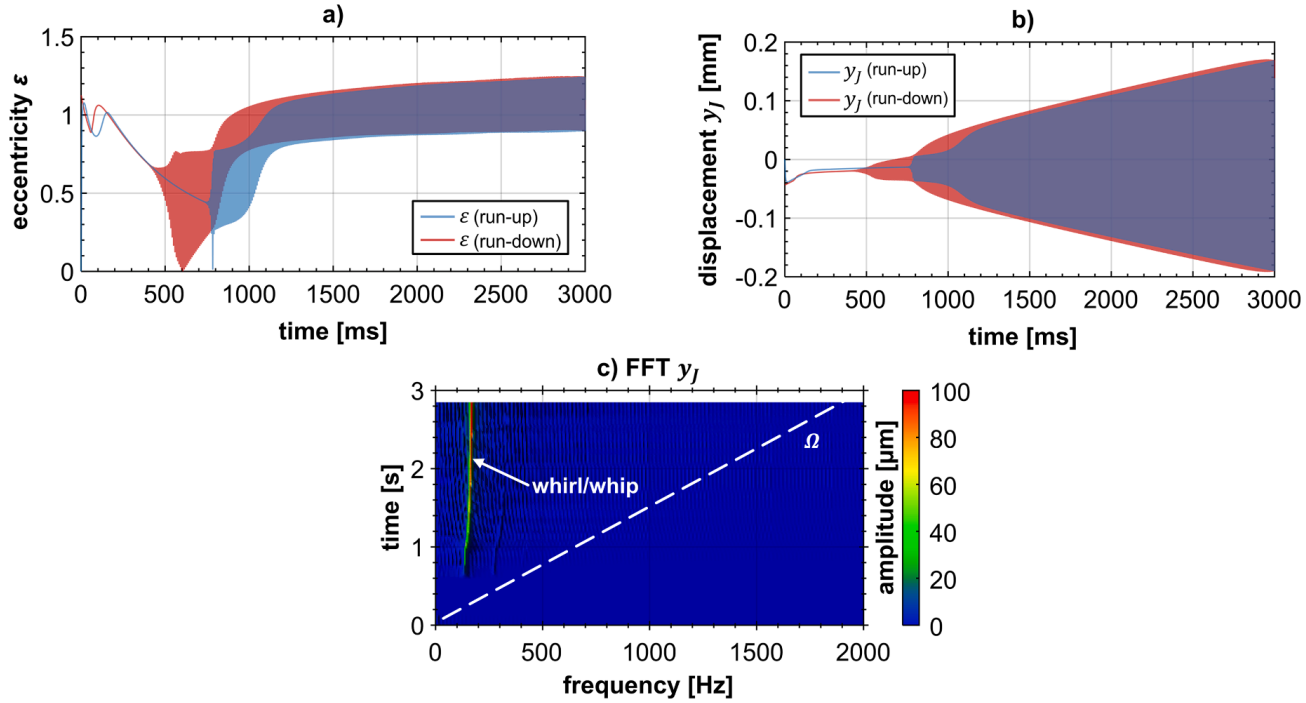

Fig. 8. Run-up (run-down) simulation 1 with $c_{\text{foil}} = 600$ N mm^{-1} and $F_{\text{fric}} = 5$ N: (a) dimensionless bearing eccentricity $\varepsilon(t)$; (b) rotor displacement $y_J(t)$; (c) frequency spectrum of $y_J(t)$ for run-up.

4.1.2. *Run-up simulation 2 (bifurcation path 2a)*

Now, the stiffness c_{foil} is reduced to 400 N mm^{-1}, while the friction force F_{fric} remains unchanged. The run-up simulation shown in Fig. 9 exhibits the following bifurcation scenario:

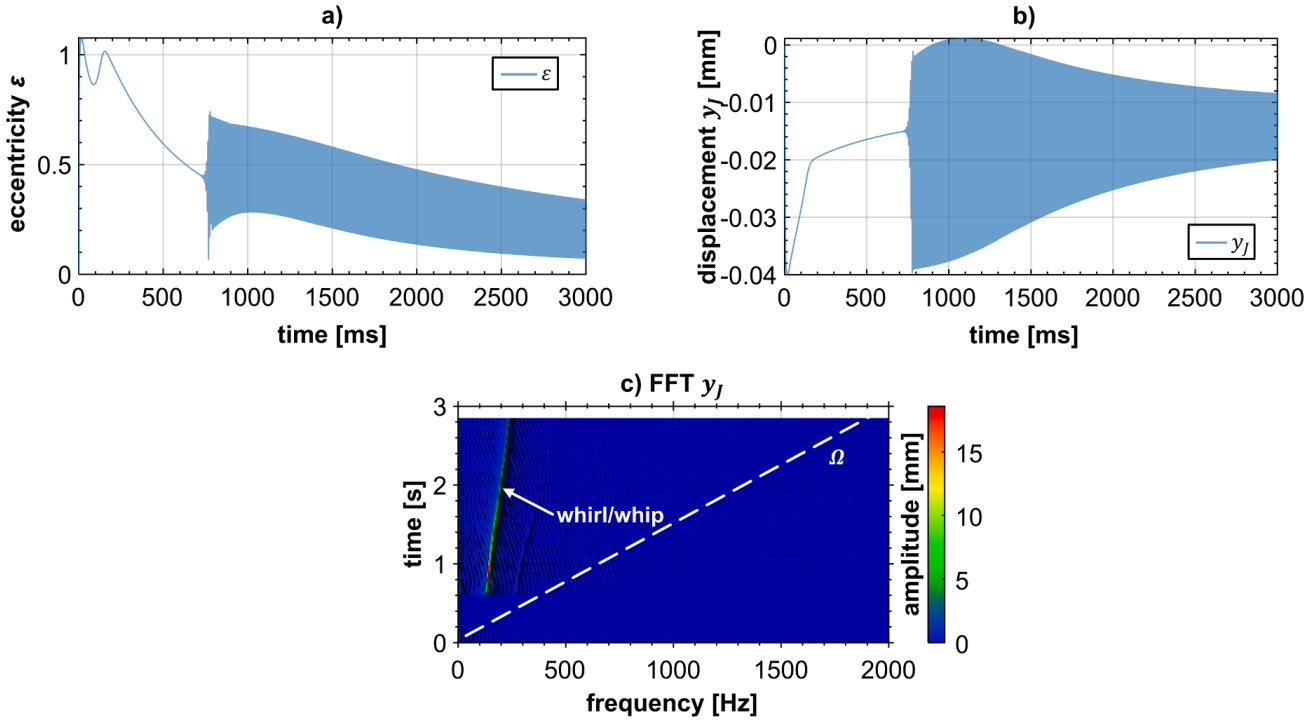

Fig. 9. Run-up simulation 2 with $c_{\text{foil}} = 400$ N mm^{-1} and $F_{\text{fric}} = 5$ N: (a) dimensionless bearing eccentricity $\varepsilon(t)$; (b) rotor displacement $y_J(t)$; (c) frequency spectrum of $y_J(t)$.

- In the range $0 \leq t \leq 700$ ms, the rotor reaches a stable equilibrium position. After an initial phase, the rotor starts to lift up so that the bearing eccentricity ε is getting successively smaller.
- At $t \approx 700$ ms, the equilibrium position becomes unstable (Hopf bifurcation) and a stable limit cycle oscillation is observed (whirl/whip oscillation). The limit cycle frequency at the onset of the self-excited oscillations is ≈ 140 Hz.
- Increasing the rotor speed, the limit cycle frequency increases, while the amplitudes of the self-excited oscillations decrease.

  Remark: Increasing Ω even more, it might be possible that the self-excited oscillations even disappear so that the rotor may reach again a stable equilibrium position.

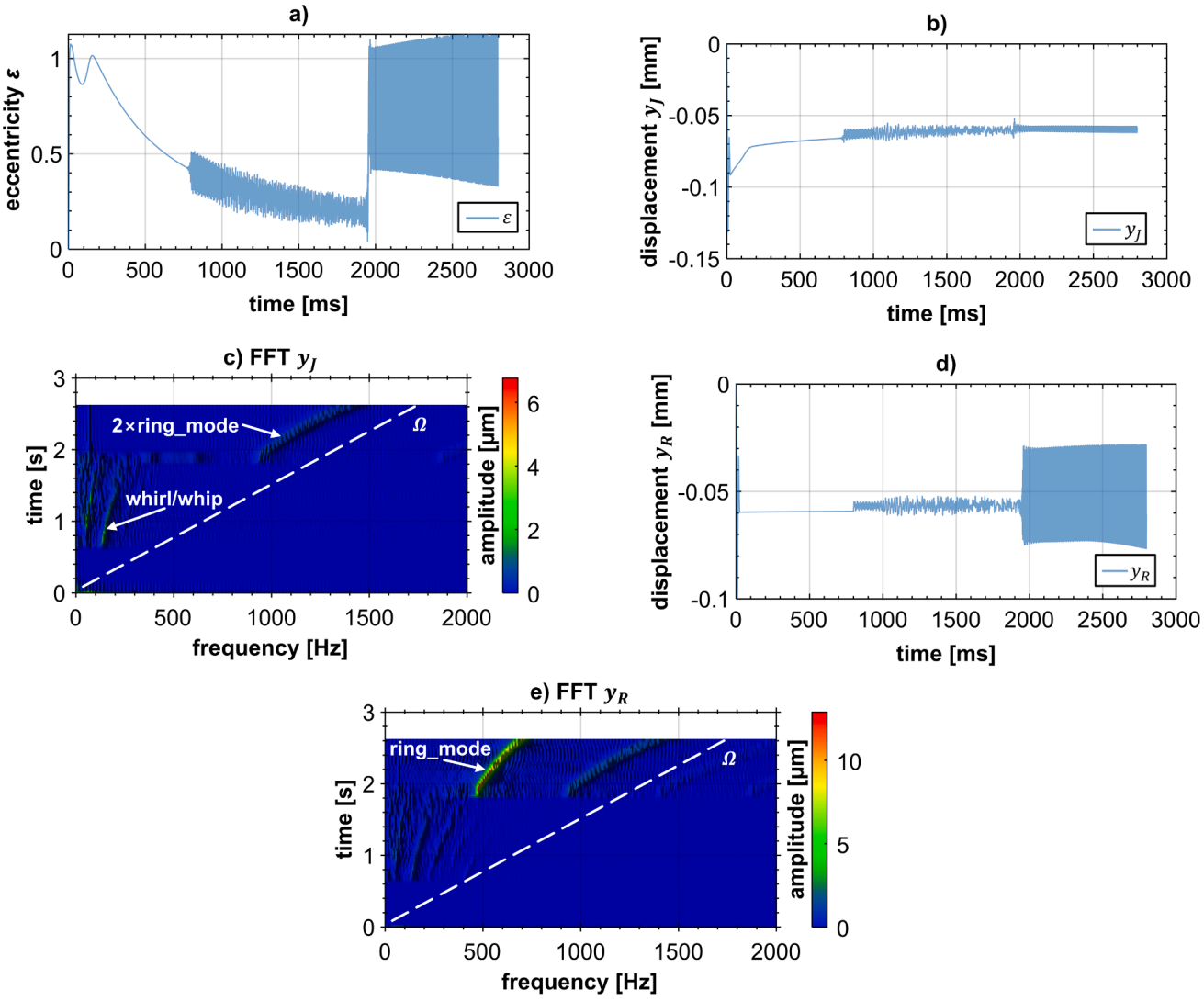

Fig. 10. Run-up simulation 3 with $c_{\text{foil}} = 100$ N mm^{-1}, $F_{\text{fric}} = 1$ N and increased ring mass $m_R = 160$ g: (a) dimensionless bearing eccentricity $\varepsilon(t)$; (b) rotor displacement $y_J(t)$; (c) frequency spectrum of $y_J(t)$; (d) ring displacement $y_R(t)$; (e) frequency spectrum of $y_R(t)$.

4.1.3. Run-up simulation 3 (bifurcation path 2b)

Next, the stiffness c_{foil} is reduced to 100 N mm^{-1} and the friction force to $F_{\text{fric}} = 1$ N. For this special run-up simulation, the ring mass m_R has been increased from 50 g to 160 g. The simulation results are arranged in Fig. 10 and indicate the subsequent bifurcation scenario:

- Up to ≈ 750 ms, the rotor rotates around a stable equilibrium position.
- At $t \approx 750$ ms, a Hopf-bifurcation occurs and whirl/whip oscillations with moderate amplitudes are detected.
- Increasing the rotor speed, the frequency of the whirl/whip oscillations increases, while the amplitudes decrease. Besides the whirl/whip frequency of ≈ 140 Hz, other frequencies below the whirl/whip frequency are detected. A clear physical explanation of these additional frequencies is difficult. In the interval [750 ms, 1950 ms], the spectrum is rather noisy and the motion is possibly chaotic. A more detailed view on the simulation results in this speed range shows that stick/slip-phenomena occur in the foil structure.

- At $t \approx 1950$ ms, a second bifurcation is observed. The rotor remains in self-excited vibrations, however a different mode is excited by the air-film induced whirl/whip. Before the bifurcation at $t \approx 1950$ ms, rotor and ring primarily oscillate inphase. After the jump at $t \approx 1950$ ms, rotor and ring oscillate antiphase. The antiphase oscillation may be interpreted as a "ring mode", where rotor and ring swing opposed, see Appendix A. Operating the system in the "ring mode" regime may be problematic from the technical point of view due to the rather high amplitudes of $\varepsilon(t)$.

4.1.4. *Parameter study 1: Simulations for different friction forces F_{fric}*

Fig. 11 collects results of run-up simulations for different friction forces F_{fric} (1 N,3 N,5 N,7 N,9 N). The stiffness coefficient c_{foil} has been set to 400 N mm^{-1}. The plots show the dimensionless bearing eccentricities $\varepsilon(t)$ and the rotor displacements $y_J(t)$. As can be seen, for small values of the friction force ($F_{\text{fric}} = 1$ N), the saddle node bifurcation into the high amplitude limit cycle oscillation is observed. Increasing F_{fric} reveals limit cycle oscillations with moderate amplitudes that grow with F_{fric}.

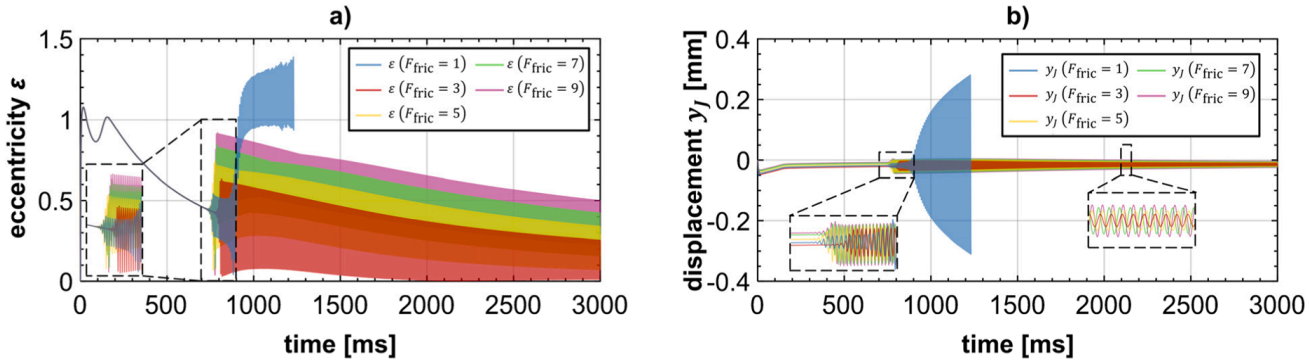

Fig. 11. Parameter study 1: run-up simulations with $c_{\text{foil}} = 400$ N mm^{-1} and different friction forces F_{fric}: (a) dimensionless bearing eccentricity $\varepsilon(t)$; (b) rotor displacement $y_J(t)$.

4.1.5. *Parameter study 2: Simulations for different stiffness coefficients c_{foil}*

Run-up simulations for different values of the stiffness coefficient c_{foil} are arranged in Fig. 12 (F_{fric} has been set to 5 N). Limit cycle oscillations with moderate amplitudes are observed for smaller values of c_{foil} (100 N mm^{-1}, 200 N mm^{-1}, 400 N mm^{-1}). For larger values of c_{foil} (600 N mm^{-1}, 800 N mm^{-1}), a saddle node bifurcation into the high amplitude limit cycle is detected.

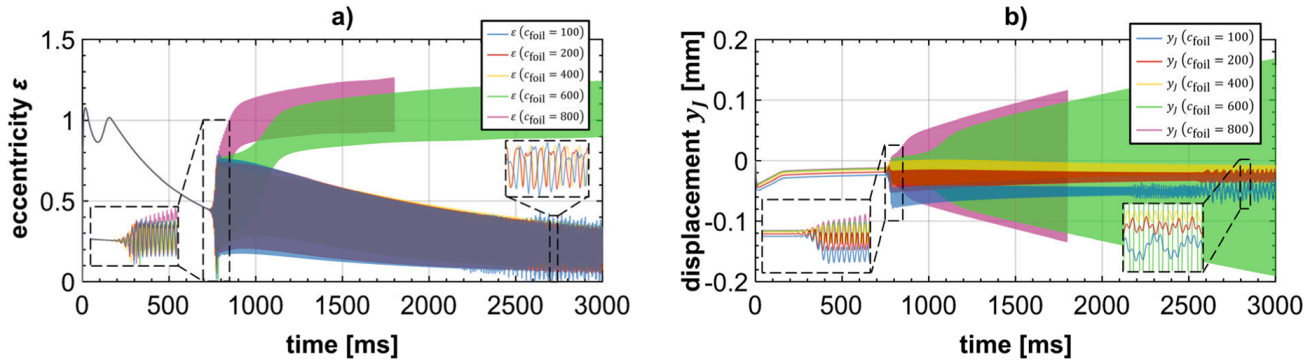

Fig. 12. Parameter study 2: run-up simulations with $F_{\text{fric}} = 5$ N and different stiffness coefficients c_{foil}: (a) dimensionless bearing eccentricity $\varepsilon(t)$; (b) rotor displacement $y_J(t)$.

4.1.6. *Summary of Section 4.1*

Basically, three different bifurcation scenarios can be distinguished:

- For large ring stiffnesses c_{foil} and small friction forces F_{fric}, the dangerous bifurcation path 1 is observed: At first, self-excited oscillations with moderate amplitudes are detected. After a saddle node bifurcation, however, self-excited oscillations with very large bearing eccentricities are observed, which prevent a secure technical operation.
- Reducing the ring stiffness and increasing the friction forces, bifurcation path 2a is detected, where only self-excited vibrations with moderate amplitudes occur.
- For very small ring stiffnesses and fairly large ring masses, bifurcation path 2b may be observed, where the system bifurcates into the rather dangerous ring mode.

4.2. Air ring bearings with viscoelastic mounting

Now, a symmetrical rigid rotor system is analyzed, where the rings are mounted with a viscoelastic material, see Section 2.4.2. The same rotor and bearing parameters have been used as in Section 4.1. Run-up simulations are presented for different stiffness coefficients c_{elast} and damping coefficients d_{visc}.

4.2.1. Run-up simulation 1

Results of a run-up simulation with $c_{\text{elast}} = 600$ N mm^{-1} and $d_{\text{visc}} = 50$ N ms mm^{-1} are arranged in Fig. 13. The plots exhibit the subsequent bifurcation scenario:

- At $t \approx 750$ ms, a Hopf-bifurcation occurs and a limit cycle oscillation with very large amplitudes is detected.
- Increasing the rotor speed, the frequency of the limit cycle almost remains constant (≈ 160 Hz), while the bearing eccentricity slightly decreases; the rotor amplitudes slightly increase.

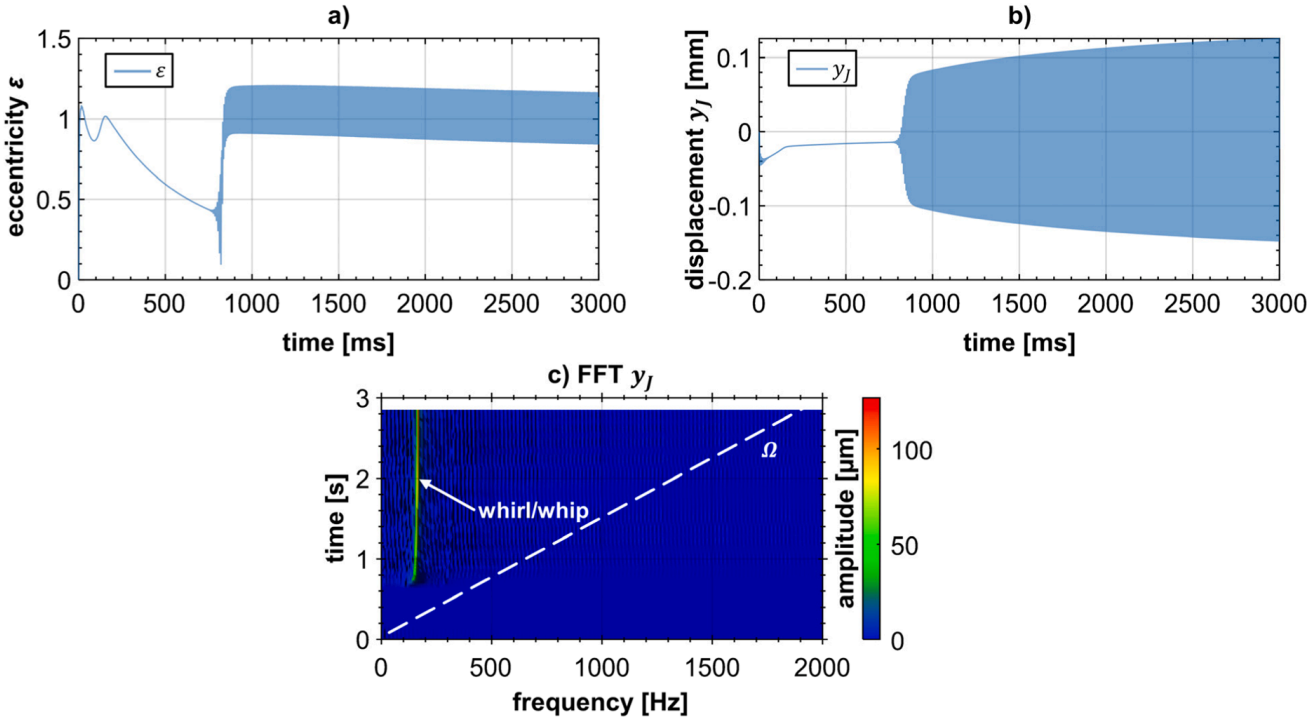

Fig. 13. Run-up simulation 1 with $c_{\text{elast}} = 600$ N mm^{-1} and $d_{\text{visc}} = 50$ N ms mm^{-1}: (a) dimensionless bearing eccentricity $\varepsilon(t)$; (b) rotor displacement $y_J(t)$; (c) frequency spectrum of $y_J(t)$.

4.2.2. Run-up simulation 2

Simulation results for $c_{\text{elast}} = 600$ N mm^{-1} and $d_{\text{visc}} = 500$ N ms mm^{-1} can be seen in Fig. 14:

- At $t \approx 1000$ ms, the equilibrium position gets unstable and the rotor bifurcates into a whirl/whip motion; limit cycle oscillations with moderate amplitudes are observed.
- Increasing the rotor speed, the frequency of the limit cycle slightly increases, while the bearing eccentricities and the rotor amplitudes decrease.
- At $t \approx 2500$ ms, the whirl/whip disappears and the rotor bifurcates again into a stable equilibrium position.

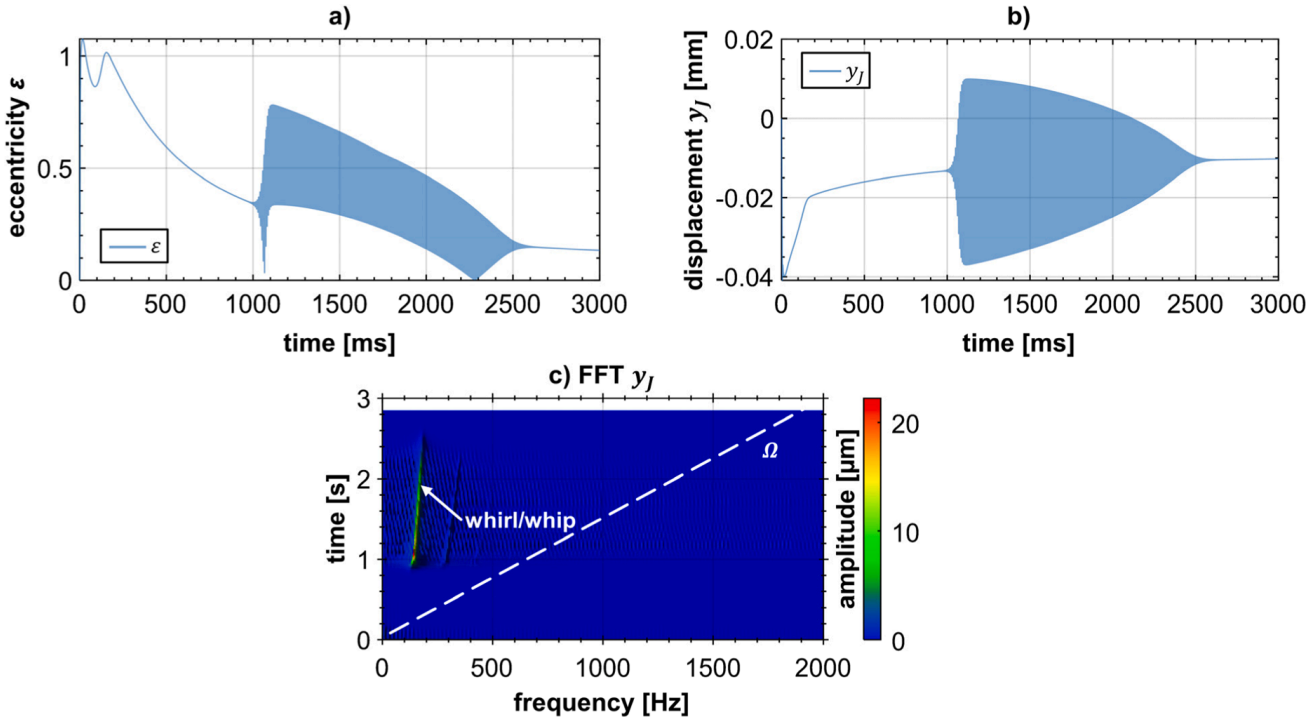

Fig. 14. Run-up simulation 2 with $c_{\text{elast}} = 600$ N mm^{-1} and $d_{\text{visc}} = 500$ N ms mm^{-1}: (a) dimensionless bearing eccentricity $\varepsilon(t)$; (b) rotor displacement $y_J(t)$; (c) frequency spectrum of $y_J(t)$.

Remark: A run-up simulation with $c_{\text{elast}} = 400$ N mm^{-1} and $d_{\text{visc}} = 500$ N ms mm^{-1} – not shown here – does not exhibit any bifurcation effects; the rotor reaches a stable equilibrium position in the complete speed range up to 2000 Hz.

4.2.3. *Run-up simulation 3*

A rotor run-up with $c_{\text{elast}} = 600$ N mm^{-1} and $d_{\text{visc}} = 1500$ N ms mm^{-1} is depicted in Fig. 15:

- At $t \approx 900$ ms, the rotor bifurcates into the whirl/whip motion.
- When the rotor speed is increased, the whirl/whip frequency also increases; the bearing eccentricities and the rotor amplitudes slightly decrease after the bifurcation. The bearing eccentricities and rotor amplitudes are very large in the whirl/whip region; a safe operation is not possible in this regime.

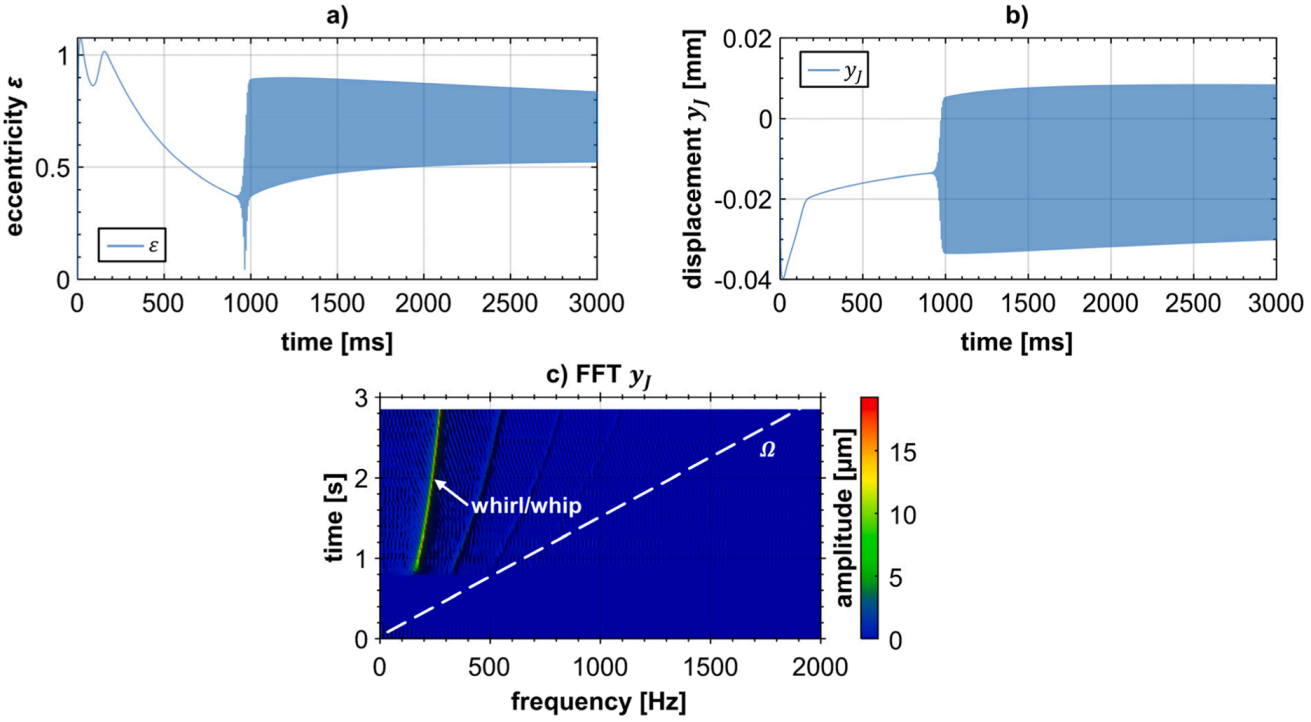

Fig. 15. Run-up simulation 3 with $c_{\text{elast}} = 600$ N mm^{-1} and $d_{\text{visc}} = 1500$ N ms mm^{-1}: (a) dimensionless bearing eccentricity $\varepsilon(t)$; (b) rotor displacement $y_J(t)$; (c) frequency spectrum of $y_J(t)$.

4.2.4. Run-up simulation 4

A simulation with $c_{\text{elast}} = 100$ N mm^{-1} and $d_{\text{visc}} = 30$ N ms mm^{-1} is depicted in Fig. 16. It should be stressed that the ring mass has not been increased (in contrast to Section 4.1.3).

- The equilibrium position is stable up to $t \approx 2150$ ms, where the rotor bifurcates into the whirl/whip motion with a larger whirl/whip frequency. The simulations show that the fluid film induced whirl/whip excites the ring mode, see Appendix A.
- At the beginning, the whirl/whip frequency is ≈ 600 Hz. When the rotor speed is increased, the whirl/whip frequency almost increases linearly. The bearing eccentricities and the rotor amplitudes also increase with increasing rotor speed.

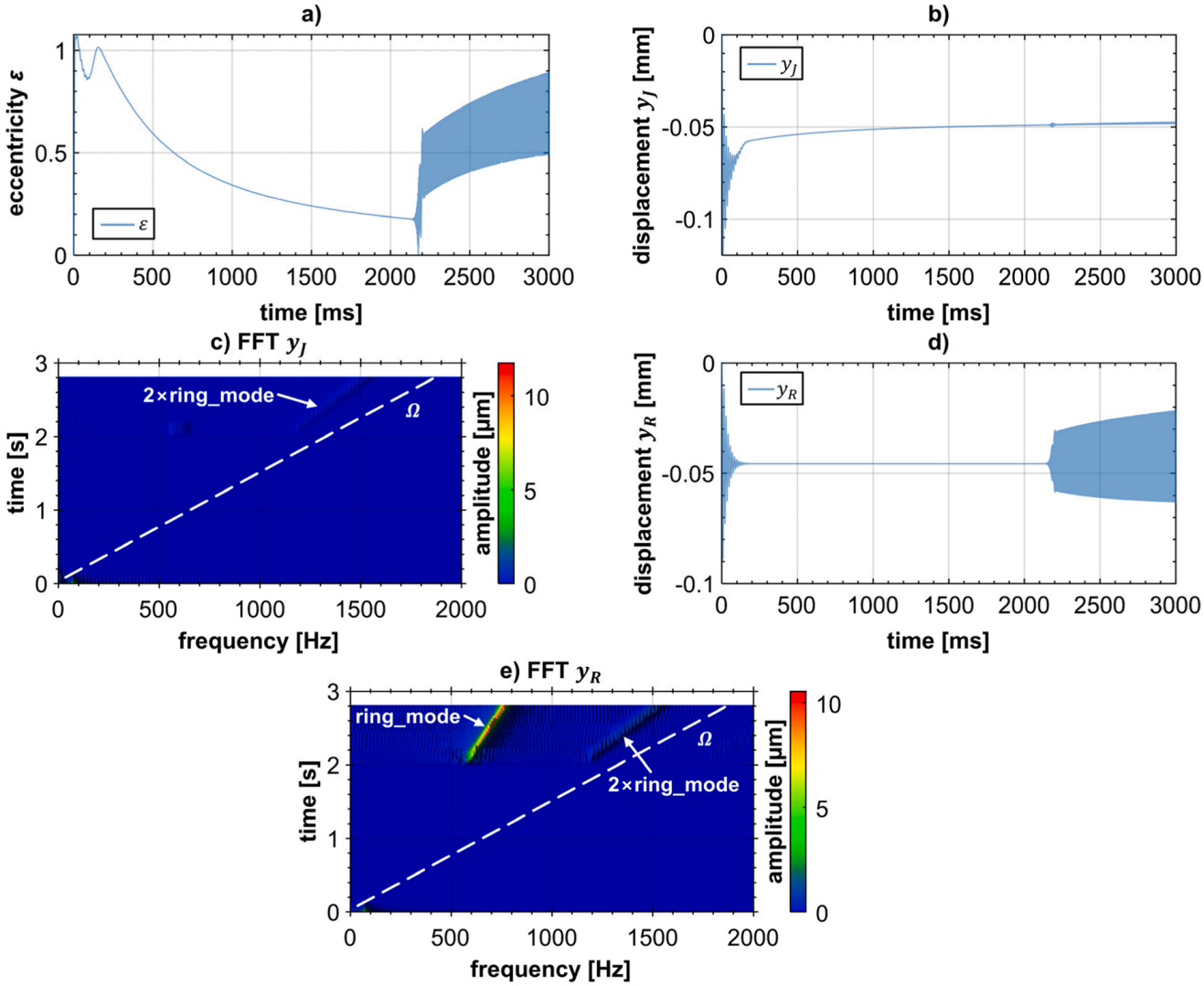

Fig. 16. Run-up simulation 4 with $c_{\text{elast}} = 100$ N mm^{-1}, $d_{\text{visc}} = 30$ N ms mm^{-1} (ring mass: 50 g): (a) dimensionless bearing eccentricity $\varepsilon(t)$; (b) rotor displacement $y_J(t)$; (c) frequency spectrum of $y_J(t)$; (d) rotor displacement $y_R(t)$; (e) frequency spectrum of $y_R(t)$.

4.2.5. Summary of Section 4.2

Essentially, three cases can be distinguished:

- For very small and very large (overdamping) damping coefficients, self-excited vibrations with very large bearing eccentricities are observed (corresponding to bifurcation path 1, see Section 4.1.1). The run-up simulations in Sections 4.2.1-4.2.4 indicate that there exists an optimal damping parameter d_{visc}. Choosing d_{visc} too small (Section 4.2.1) or too large (Section 4.2.3) entails a whirl/whip motion with large amplitudes, which prevents a save operation in this regime
- For damping coefficients in the middle range, self-excited oscillations with technically harmless amplitudes are detected (corresponding to bifurcation path 2a, see Section 4.1.2).
- For very small damping and stiffness coefficients, bifurcation into the critical ring mode is detected (corresponding to bifurcation path 2b, see Section 4.1.3). The risk of reaching a bifurcation into the dangerous ring mode (Section 4.2.4) is comparatively low, since the bifurcation into the ring mode only occurs for rather low stiffness and damping coefficients.

4.3. Comparison: Elastic foil structure versus viscoelastic mounting

Here, we compare the results of Section 4.1 (ring supported in an elastic foil structure) with Section 4.2 (viscoelastically mounted ring). By choosing adequate bearing parameters for the foil structure and for the viscoelastic mounting, both bearing types may exhibit a quite similar vibration and bifurcation behavior (three characteristic bifurcation scenarios). Of course, dry friction and viscous damping represent two different physical dissipation processes. While dry friction produces dissipation, which does not depend on the velocity, dissipation generated by viscous damping is velocity dependent. Hence, if the frequency (e.g. whirl/whip frequency, rotational frequency) changes, differences may be observed for the two bearing types: different onset points of the bifurcations, different whirl/whip amplitudes, etc..

The similarities and differences of the two bearing variants can be summarized as follows:

- Considering the dangerous bifurcation path 1, the run-up simulation in Section 4.1.1 for the foil model firstly exhibits a subcritical Hopf-bifurcation into a limit cycle with moderate amplitudes and then a saddle node bifurcation into the large amplitude limit cycle. In contrast, the corresponding simulation in Section 4.2.1 exhibits a direct subcritical Hopf-bifurcation into the large amplitude limit cycle.
- Regarding bifurcation path 2a, both bearing variants exhibit limit cycle oscillations with moderate amplitudes, which are decaying with increasing rotor speed. With the foil structure, the limit cycle instability cannot be driven through (at least in the considered speed range), while for the viscoelastic variant the instability can be passed through so that the system is stabilized again at higher rotor speeds. As mentioned in Section 4.2.2, it is even possible to find bearing parameters so that the system is stable in the complete speed range, which may be interesting from the practical point of view.
- With rather extreme bearing parameters, both models are able to show the bifurcation into the ring mode. While the viscoelastic bearing model exhibits a direct bifurcation from the equilibrium position, whirl/whip oscillations with moderate amplitudes are observed for the foil model before the system bifurcates into the ring mode.

5. Bifurcation analysis for asymmetrical rotor system: High-speed turbo-compressor supported in air ring bearings

Now, a technical rotor system is considered, namely a high-speed turbo-compressor supported in air ring bearings, see Fig. 7. The rotor consists of a shaft, a compressor wheel (center of mass z_C) and a turbine wheel (center of mass z_T). In addition, small masses might be attached to the wheels to take imbalance effects into account. Here, imbalance is neglected in order to discuss the bifurcation effects in a very clear and straightforward manner (note that large imbalances may notably affect the stability and bifurcation behavior of rotor systems). The center of mass of the entire rotor (mass m, length l) consisting of the shaft and the two wheels is defined by the axial coordinate z_{Rotor}. The two bearings are located at z_{JC} and z_{JT}. The simulations in Section 5 have been carried out with the following parameters: $m = 830$ g, $l = 250$ mm, $z_{\text{Rotor}} = 125$ mm, $z_{JC} = 170$ mm, $z_{JT} = 60$ mm, $m_R = 50$ g. The same bearing parameters as in Section 4.1 have been used ($T_{\text{air}} = 80°\text{C}$, $\eta_{\text{air}} = 20.936E-6$ kg m^{-1}s^{-1}, $C = 30$ μm, $\Delta H = 20$ μm, $\varphi_t = 110°$, $\alpha = \pi - \varphi_t$). For the subsequent run-up simulations, the rotor and both rings are assumed to be initially centered at the space-fixed z-axes with zero velocity.

5.1. Air ring bearings with elastic foil structure

In Section 5.1, the rings are supported with an elastic foil structure according to Section 2.3.1. Stiffness coefficient c_{foil} and friction force F_{fric} are varied to investigate the bifurcation behavior of the system. As in Section 4.1 for the symmetrical rotor system, three main bifurcations paths can be distinguished (bifurcation path 1, bifurcation path 2a and bifurcations path 2b), which are explained in the following.

5.1.1. Run-up simulation 1 (bifurcation path 1)

Fig. 17 collects the results of a rotor run-up carried out with $c_{\text{foil}} = 600$ N mm^{-1} and $F_{\text{fric}} = 6$ N. The figure shows the vertical displacement of the compressor ($y_{JC}(t)$) and turbine wheel ($y_{JT}(t)$), the corresponding frequency spectra as well as the dimensionless bearing eccentricities $\varepsilon_C(t)$ and $\varepsilon_T(t)$ of the two air bearings. The simulation exhibits the subsequent bifurcation behavior:

- In the range $0 \leq t \leq 750$ ms ($0 \leq \Omega \leq 500$ Hz), the rotor rotates in a stable equilibrium position (imbalance oscillations around a stable equilibrium position, if rotor imbalance would be considered). After a settling phase up to ≈ 180ms, the bearing eccentricities ε_C and ε_T are reduced continuously and move towards the bearing center.
- At $t \approx 750$ ms, the equilibrium position gets unstable (Hopf bifurcation) and a stable quasiperiodic oscillation is observed (whirl/whip oscillation). The whirl/whip of the turbine-sided bearing excites the conical forward mode *Mode_2(f)* (≈ 160 Hz at the onset of the whirl/whip motion at $t \approx 750$ ms) and the compressor-sided whirl/whip the conical forward mode *Mode_1(f)* (≈ 140 Hz at the onset of the whirl/whip motion at $t \approx 750$ ms), see Appendix A.
- At $t \approx 1700$ ms, a second bifurcation (synchronization) occurs: the turbine-sided whirl/whip frequency shows a jump. After this jump, the compressor- and turbine-sided whirls/whips have the same frequency. In the synchronized region, a cylindrical mode is detected, see Fig. 17.

- Increasing the rotor speed, the bearing eccentricities and the rotor amplitudes markedly increase, whereas the whirl/whip frequency only slightly increases.

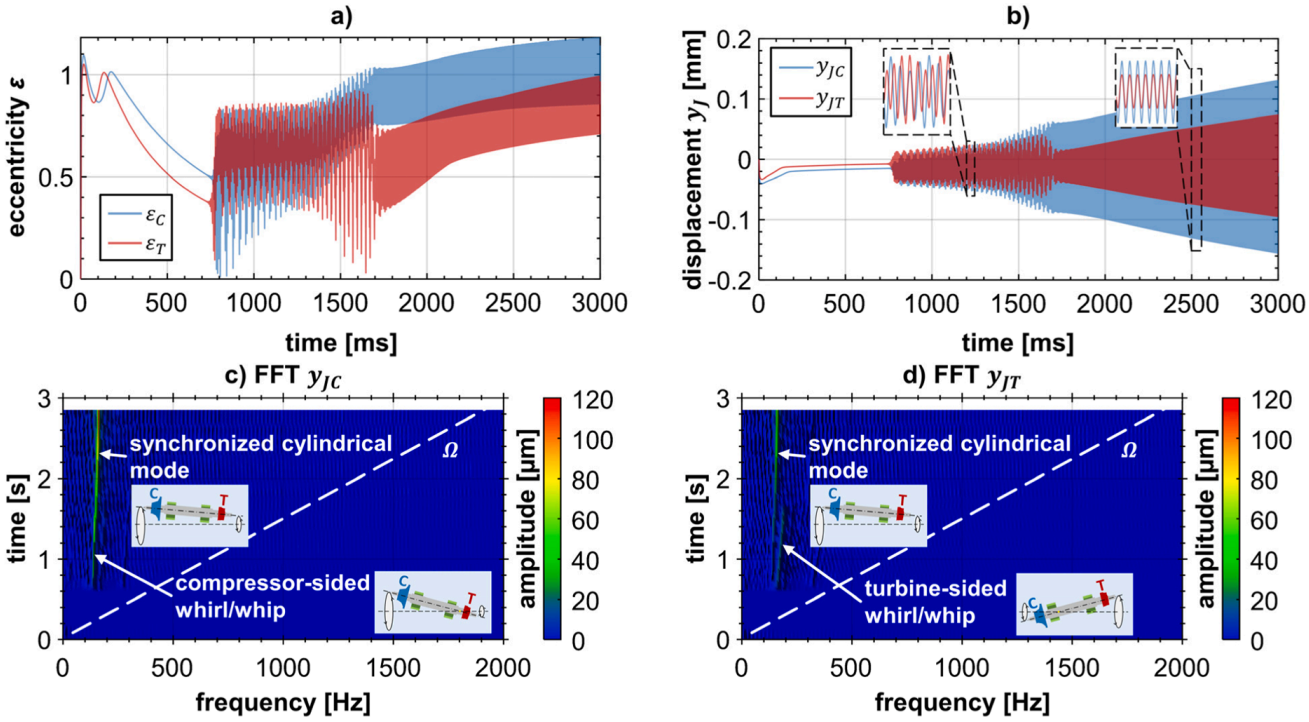

Fig. 17. Run-up simulation 1 with $c_{\text{foil}} = 600$ N mm^{-1}, $F_{\text{fric}} = 6$ N: (a) dimensionless bearing eccentricities $\varepsilon_C(t)$ and $\varepsilon_T(t)$; (b) vertical journal displacements $y_{JC}(t)$ and $y_{JT}(t)$; (c) frequency spectra of $y_{JC}(t)$; (d) frequency spectra of $y_{JT}(t)$.

5.1.2. Run-up simulation 2 (bifurcation path 2a)

Now, the foil stiffness is reduced to $c_{\text{foil}} = 400$ N mm^{-1}; the friction force remains $F_{\text{fric}} = 6$ N. The rotor run-up shows the following bifurcation behavior, see Fig. 18:

- In the range $0 \leq t \leq 750$ ms, a stable equilibrium is detected.
- At $t \approx 750$ ms, the equilibrium position gets unstable (Hopf bifurcation) and a stable quasiperiodic oscillation is observed (whirl/whip oscillation). The whirl/whip of the turbine-sided bearing excites the conical forward mode *Mode_2(f)* (≈ 160 Hz at the onset of the whirl/whip motion at $t \approx 750$ ms) and the compressor-sided whirl/whip the conical forward mode *Mode_1(f)* (≈ 140 Hz at the onset of the whirl/whip motion at $t \approx 750$ ms).
- Increasing the rotor speed, the amplitudes of the compressor- and turbine-sided whirl/whip significantly decrease, while the frequencies of the two whirls/whips notably increase.

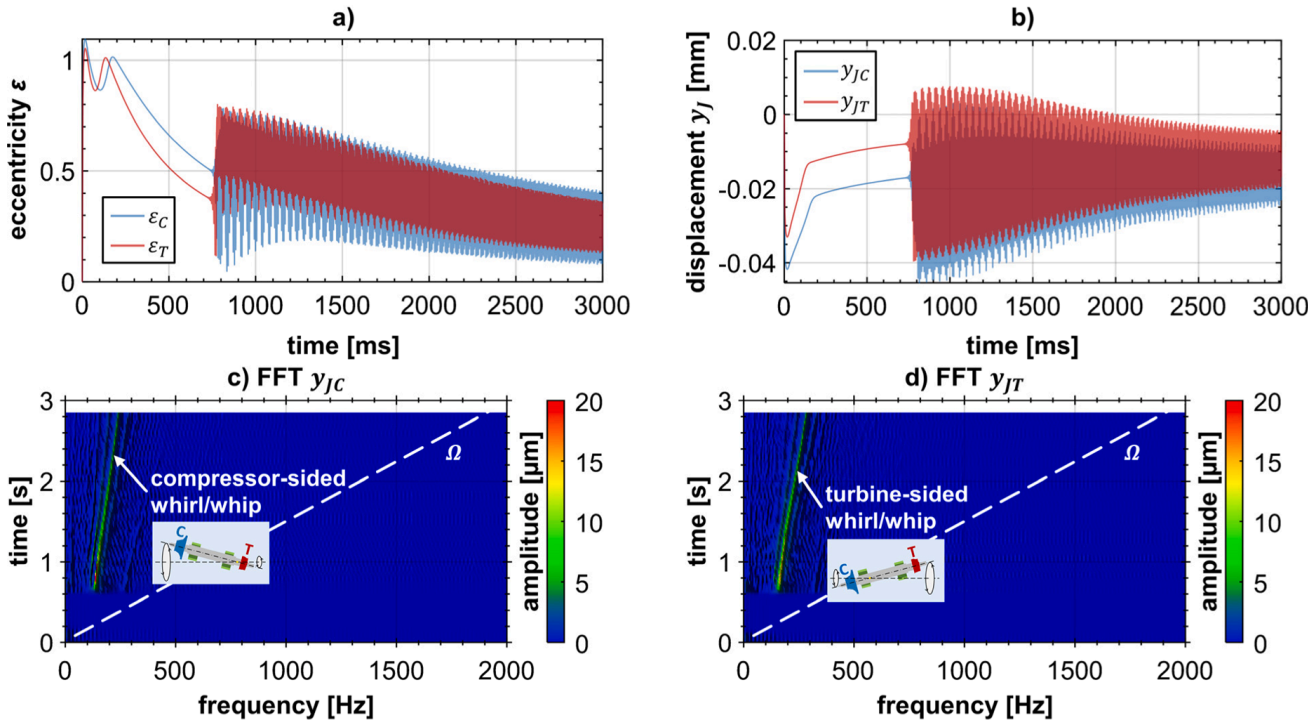

Fig. 18. Run-up simulation 2 with $c_{\text{foil}} = 400$ N mm^{-1} and $F_{\text{fric}} = 6$ N: (a) dimensionless bearing eccentricities $\varepsilon_C(t)$ and $\varepsilon_T(t)$; (b) vertical journal displacements $y_{JC}(t)$ and $y_{JT}(t)$; (c) frequency spectra of $y_{JC}(t)$; (d) frequency spectra of $y_{JT}(t)$.

Fig. 19 shows a similar run-up simulation generated with the parameters $c_{\text{foil}} = 600$ N mm^{-1} and $F_{\text{fric}} = 7$ N, which exhibits an interesting synchronization effect. Up to ≈ 2100 ms, the simulation resembles the above results for $c_{\text{foil}} = 400$ N mm^{-1} and $F_{\text{fric}} = 6$ N. At $t \approx 2100$ ms, the turbine- and compressor-sided whirl/whip synchronize, however. The synchronized whirls/whips excite a cylindrically shaped mode.

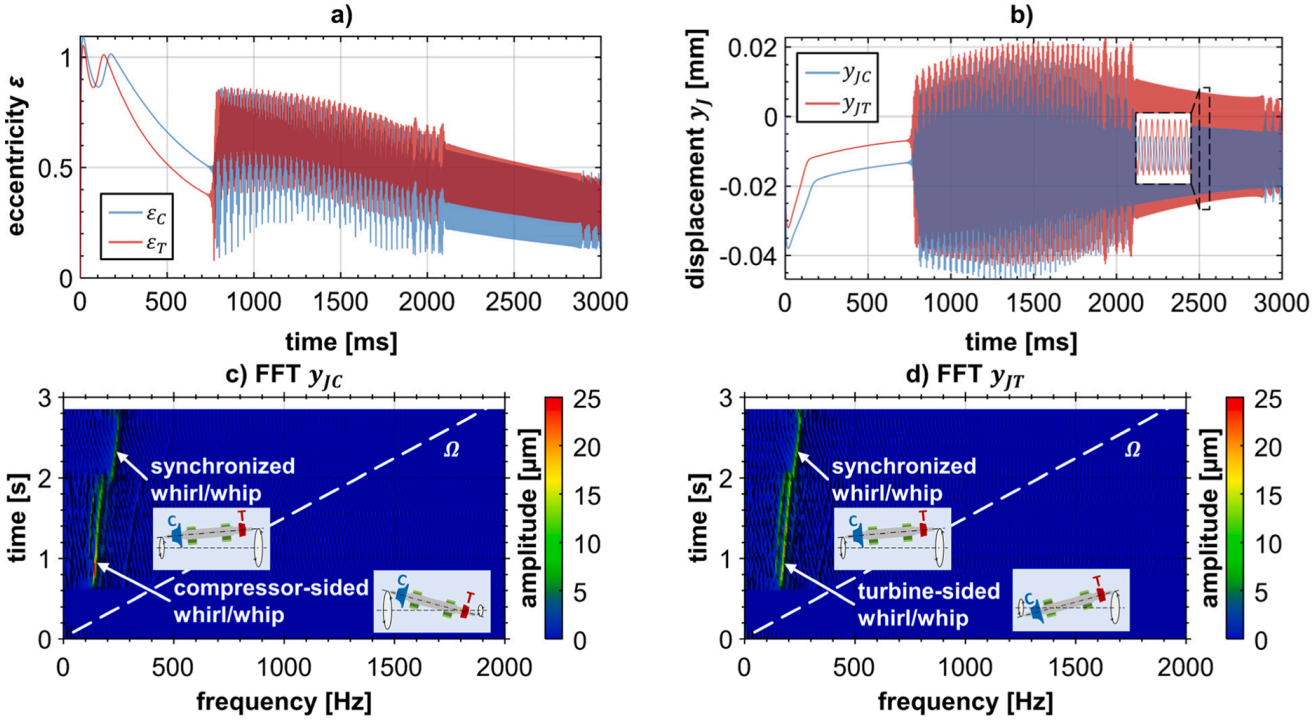

Fig. 19. Run-up simulation with $c_{\text{foil}} = 600$ N mm^{-1}, $F_{\text{fric}} = 7$ N: (a) dimensionless bearing eccentricities $\varepsilon_C(t)$ and $\varepsilon_T(t)$; (b) vertical journal displacements $y_{JC}(t)$ and $y_{JT}(t)$; (c) frequency spectra of $y_{JC}(t)$; (d) frequency spectra of $y_{JT}(t)$.

5.1.3. Run-up simulation 3 (bifurcation path 2b)

In the run-up simulation depicted in Fig. 20, the foil stiffness is reduced to $c_{\text{foil}} = 100$ N mm^{-1} and the friction coefficient to $F_{\text{fric}} = 1$ N. Furthermore, the ring mass m_R is increased to 100 g.

- At $t \approx 750$ ms, the equilibrium position gets unstable (Hopf bifurcation) and stable self-excited oscillations are observed (whirl/whip motion).
- At $t \approx 1200$ ms, further subsynchronous frequencies are detected in the spectra. These additional frequencies may possibly be traced back to stick-slip-effects in the foil structure. For $t > 1200$ ms, the spectra seems noisy and the motion might be chaotic in this region.

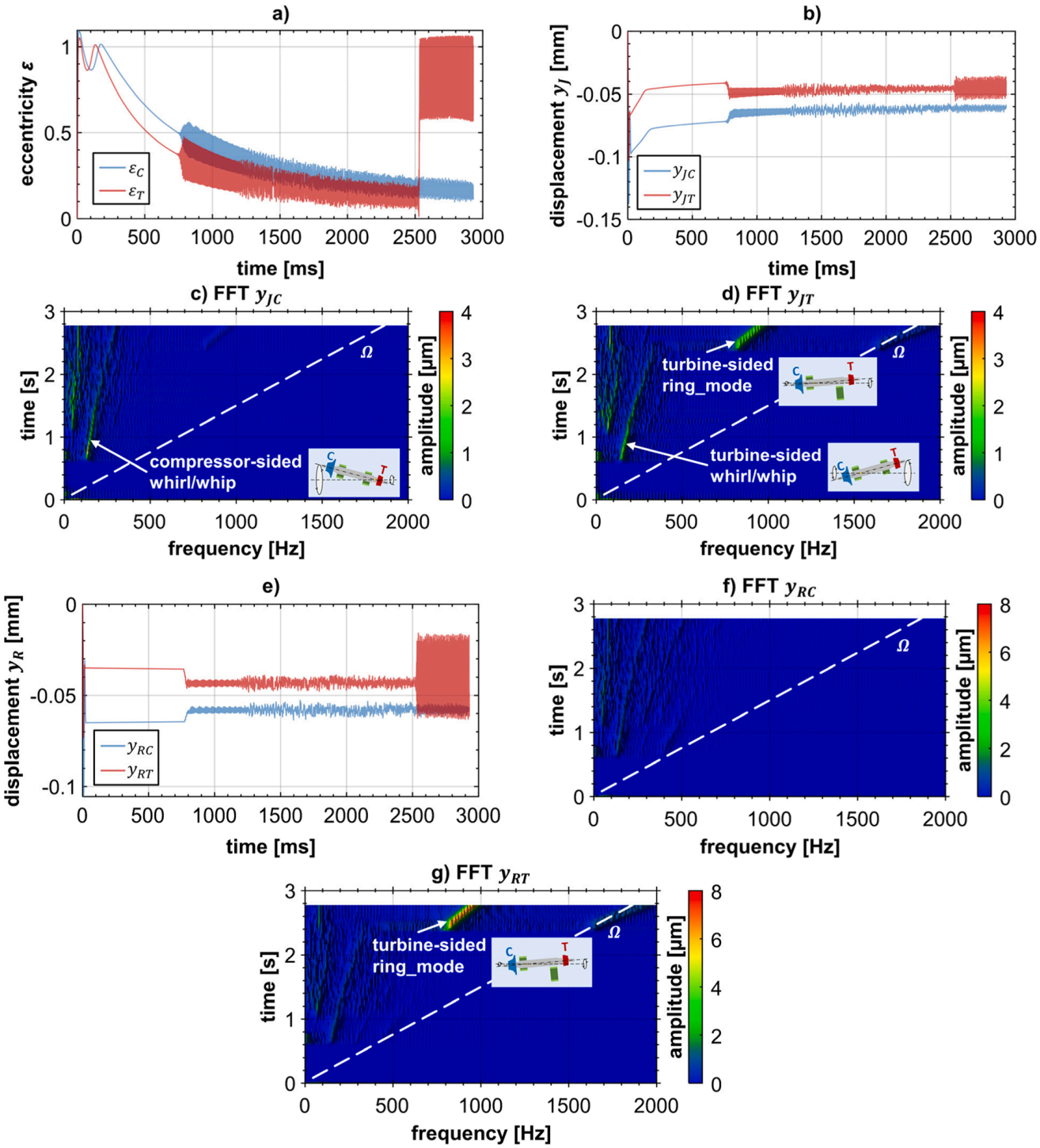

Fig. 20. Run-up simulation 3 with $c_{\text{foil}} = 100$ N mm^{-1}, $F_{\text{fric}} = 1$ N and increased ring mass of 100 g: (a) dimensionless bearing eccentricities $\varepsilon_C(t)$ and $\varepsilon_T(t)$; (b) vertical journal displacements $y_{JC}(t)$ and $y_{JT}(t)$; (c) frequency spectra of $y_{JC}(t)$; (d) frequency spectra $y_{JT}(t)$; (e) vertical ring displacements $y_{RC}(t)$ and $y_{RT}(t)$; (f) frequency spectra of $y_{RC}(t)$; (g) frequency spectra of $y_{RT}(t)$.

- Increasing the rotor speed, the bearing eccentricities decrease; also the amplitudes of the whirl/whip motion slightly decrease.
- At $t \approx 2550$ ms, a bifurcation is detected: the frequency of the turbine-sided whirl/whip shows a jump and the turbine-sided whirl/whip is now exciting a ring mode, namely *Mode_4(f)* of Appendix A. The compressor-sided whirl/whip does not show a jump phenomenon and still excites *Mode_1(f)*. The eccentricities of the turbine-sided bearing are very large and slightly increase with increasing rotor speed. The frequency of the turbine-sided whirl/whip is ≈ 820 Hz at the onset of the ring mode oscillation and increases almost linearly with increasing rotor speed.

It should be stressed that tilting of the rings is not taken into account in the current model. Depending on the ring geometry, the tilting stiffness and the damping properties of the elastic foil structure, considering ring tilting may notably influence the bifurcations in connection with ring modes.

5.1.4. Summary of Section 5.1

The simulations have shown that basically three bifurcation paths can be observed in rotor systems with air ring bearings.

Bifurcation path 1.

I) When a critical rotor speed is reached, the equilibrium position of the rotor/bearing system becomes unstable and self-excited whirl/whip vibrations are observed.

II) The simulations indicate that the instability is initiated by the lower loaded turbine-sided bearing: at the very beginning of the whirl motion, the whirl generated by the turbine-sided bearing excites the gyroscopic conical forward mode *Mode_2(f)* (mode shape with a vibration node close to the compressor-sided bearing). Shortly thereafter, the compressor-sided bearing creates a whirl motion, which excites the gyroscopic conical forward mode *Mode_1(f)* (mode shape with a vibration node close to the turbine-sided bearing). Hence, self-excited vibrations with two whirl frequencies are observed (quasiperiodic motion).

III) Increasing the rotor speed further, a second bifurcation is observed and a synchronization effect, where both whirl motions synchronize. In the synchronized state, the compressor- and turbine-sided whirl both excite the same rotor mode, namely a gyroscopic cylindrical forward mode. In the synchronized state, the bearing eccentricities are very large so that a technically safe operation of the rotor system will most likely be impossible.

Whirl synchronization is detected for the rotor system in Section 5.1, where the center of mass of the rotor lies rather close to the center point of the two bearings. Increasing the rotor asymmetry, see Appendix B, whirl synchronization may be prevented.

IV) The unstable whirl/whip region cannot be driven-through. Increasing the rotor speed, the bearing eccentricities will also increase.

Remark: To avoid the dangerous bifurcation path 1, the friction force (dissipation) should be increased and/or the stiffness of the supporting structure of the ring should be reduced.

Bifurcation path 2a.

I) After the critical rotor speed is reached, the rotor gets unstable and bifurcates into a quasiperiodic rotor motion (self-excited whirl/whip vibrations induced by the fluid films).

II) Simulations with a rotor system with increased asymmetry, see Appendix B, show that the instability is firstly generated by the lower loaded turbine-sided bearing. For the almost symmetrical rotor system of Section 5, the two bearings become unstable almost at the same time. The whirl produced by the turbine-sided bearing will excite *Mode_2(f)*; the whirl of the compressor-sided bearing will excite *Mode_1(f)*. Compared to bifurcation path 1, the bearing eccentricities remain moderate so that a technically safe operation is possible in the whirl/whip regime. Synchronization of the two whirls is not observed.

III) Increasing the rotor speed, the whirl/whip amplitudes continuously decrease.

Bifurcation path 2b.

I) Reaching the critical rotor speed, the rotor system gets unstable and bifurcates into a stable quasiperiodic rotor motion. The turbine-sided whirl excites *Mode_2(f)* and the compressor-sided whirl *Mode_1(f)*. For the system parameters used in Section 5.1.3, whirl synchronization has not been detected.

II) Increasing the rotor speed further, the bearing eccentricities decrease and the whirl will even disappear. The spectrum gets noisy and the motion is possibly chaotic in this region.

III) Increasing the rotor speed even more, a further bifurcation occurs. The frequency of the turbine-sided whirl/whip shows a jump and the turbine-sided whirl/whip is exciting a ring mode (*Mode_4(f)*). The eccentricities of the turbine-sided bearing become very large so that a safe operation in this state will be problematic.

Remark: To avoid the dangerous bifurcation into the ring mode, the stiffness should be increased, the friction (damping) should be increased and the ring mass should be reduced.

The three basic bifurcation paths are schematically illustrated in Fig. 21.

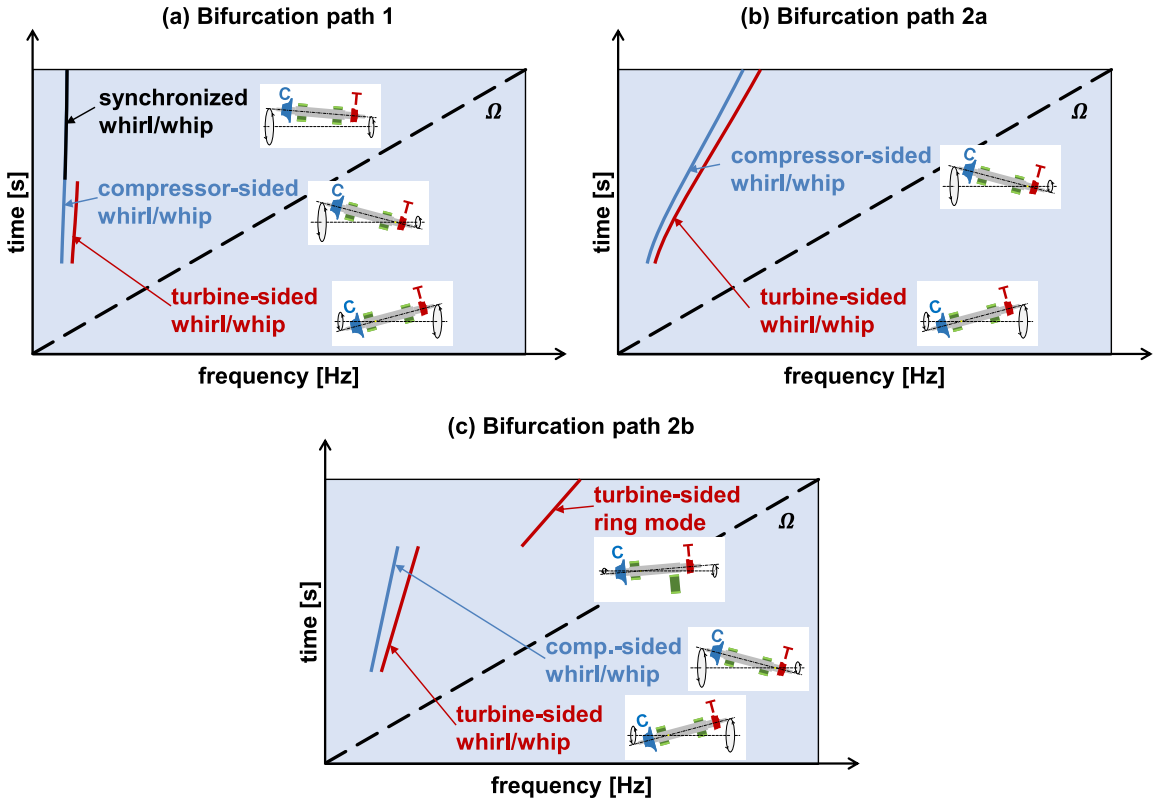

Fig. 21. Basic bifurcation scenarios: (a) bifurcation path 1; (b) bifurcation path 2a; (c) bifurcation path 2b.

5.2. *Air ring bearings with viscoelastic mounting*

In this section, air ring bearings with a viscoelastic supporting material according to Section 2.3.2 are considered. The same rotor and bearing parameters have been used as in Section 5.1. Run-up simulations are presented for different stiffness coefficients c_{elast} and various damping coefficients d_{visc}.

5.2.1. *Run-up simulation 1*

Results of a run-up simulation with $c_{\text{elast}} = 600$ N mm^{-1} and $d_{\text{visc}} = 30$ N ms mm^{-1} are arranged in Fig. 22:

- At $t \approx 750$ ms, the equilibrium position gets unstable (Hopf bifurcation) and a stable quasiperiodic oscillation is observed (whirl/whip oscillation). The whirl/whip of the turbine-sided bearing excites the conical forward mode *Mode_2(f)* and the compressor-sided whirl/whip the conical forward mode *Mode_1(f)*, see Appendix A.
- At $t \approx 1750$ ms, a synchronization effect can be detected. The turbine-sided whirl/whip frequency shows a jump. After the jump of the turbine-sided whirl/whip frequency, the compressor- and turbine-sided whirls/whips exhibit the same frequency. The synchronized whirls/whips excite a cylindrical forward mode.
- Increasing the rotor speed, the system remains in the synchronized oscillation mode with very high bearing eccentricities, which are too large for a save technical operation.

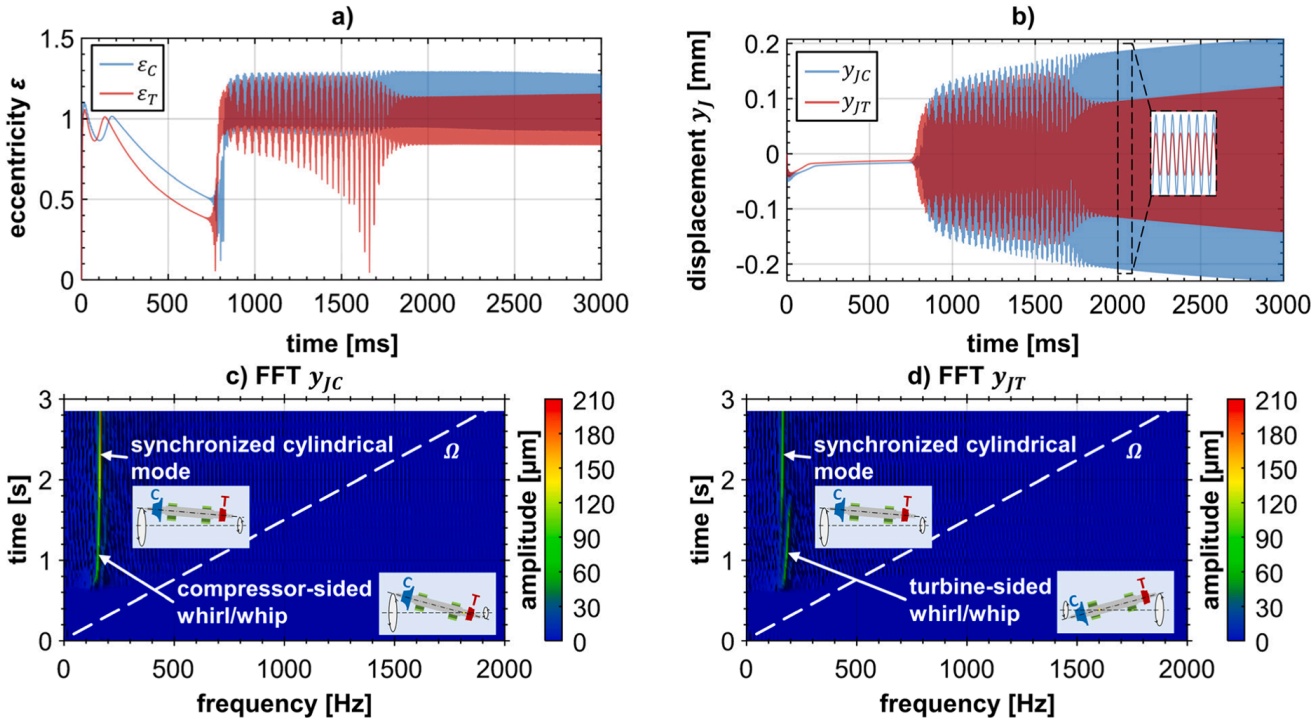

Fig. 22. Run-up simulation 1 with $c_{\text{elast}} = 600$ N mm^{-1} and $d_{\text{visc}} = 30$ N ms mm^{-1}: (a) dimensionless bearing eccentricities $\varepsilon_C(t)$ and $\varepsilon_T(t)$; (b) vertical journal displacements $y_{JC}(t)$ and $y_{JT}(t)$; (c) frequency spectra of $y_{JC}(t)$; (d) frequency spectra of $y_{JT}(t)$.

5.2.2. *Run-up simulation 2*

Now, the damping is increased to $d_{\text{visc}} = 300$ N ms mm^{-1}; the stiffness $c_{\text{elast}} = 600$ N mm^{-1} remains unchanged. The simulation results are collected in Fig. 23:

- At $t \approx 850$ ms, the equilibrium position gets unstable (Hopf bifurcation) and a stable quasiperiodic oscillation is observed (whirl/whip oscillation).
- In contrast to Section 5.2.1, the bearing eccentricities and rotor amplitudes decrease with increasing rotor speed so that a save operation of the rotor system is possible with these bearing parameters.

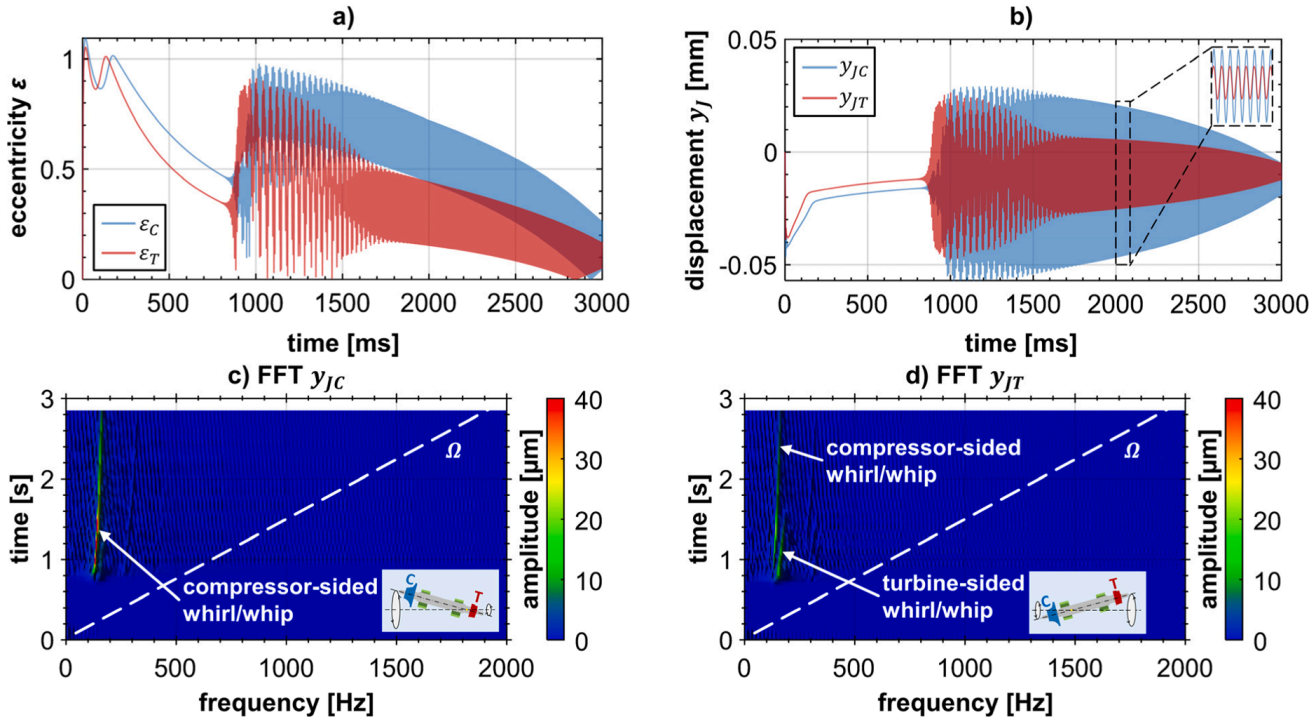

Fig. 23. Run-up simulation 2 with $c_{\text{elast}} = 600$ N mm^{-1} and $d_{\text{visc}} = 300$ N ms mm^{-1}: (a) dimensionless bearing eccentricities $\varepsilon_C(t)$ and $\varepsilon_T(t)$; (b) vertical journal displacements $y_{JC}(t)$ and $y_{JT}(t)$; (c) frequency spectra of $y_{JC}(t)$; (d) frequency spectra of $y_{JT}(t)$.

5.2.3. Run-up simulation 3

Simulation results for $c_{\text{elast}} = 600$ N mm^{-1} and $d_{\text{visc}} = 1500$ N ms mm^{-1} are shown in Fig. 24:

- The equilibrium position gets unstable at $t \approx 850$ ms (Hopf bifurcation). The self-excited oscillations are quasiperiodic: The whirl/whip of the turbine-sided bearing excites the conical forward mode *Mode_2(f)* and the compressor-sided whirl/whip the conical forward mode *Mode_1(f)*, see Appendix A.
- Increasing the rotor speed, the system remains in this state. The bearing eccentricities and rotor amplitudes are very large. A safe technical operation of the rotor is not possible. Obviously, the damping is too large so that the whirl/whip instability cannot be passed through.

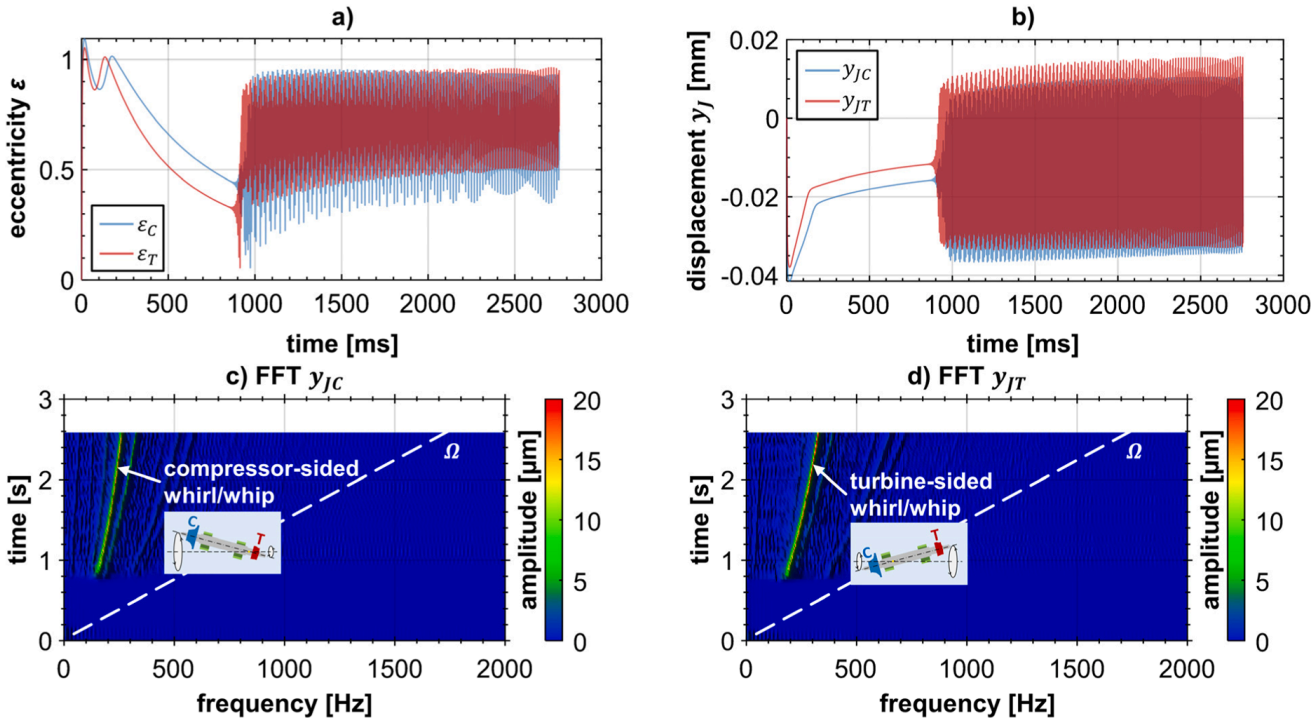

Fig. 24. Run-up simulation 3 with $c_{\text{elast}} = 600$ N mm^{-1} and $d_{\text{visc}} = 1500$ N ms mm^{-1}: (a) dimensionless bearing eccentricities $\varepsilon_C(t)$ and $\varepsilon_T(t)$; (b) vertical journal displacements $y_{JC}(t)$ and $y_{JT}(t)$; (c) frequency spectra of $y_{JC}(t)$; (d) frequency spectra of $y_{JT}(t)$.

5.2.4. Run-up simulation 4

Simulation results for $c_{\text{elast}} = 100$ N mm^{-1} and $d_{\text{visc}} = 30$ N ms mm^{-1} are depicted in Fig. 25. Note that the ring mass has been increased to $m_R = 100$ g in this calculation.

- At $t \approx 1450$ ms, the equilibrium position gets unstable (Hopf bifurcation) and self-excited oscillations are observed (whirl/whip motion exciting ring mode). In the range 1450 ms $\leq t \leq$ 2400 ms, the whirl/whip frequencies of both bearings are almost equal.
- Increasing the rotor speed, the bearing eccentricities increase and reach critical values. Also, the amplitudes of the compressor and turbine wheel increase. The whirl/whip frequencies increase almost linearly.
- For $t >$ 2400 ms, the whirl/whip frequencies are identical (full synchronization); a cylindrically-shaped ring mode is detected.

It should be mentioned again that tilting of the rings is not considered in the model. Depending on the bearing design and the tilting stiffness/damping properties of the viscoelastic mounting, taking into account ring tilting may notably affect the bifurcations in connection with ring modes.

5.2.5. Summary of Section 5.2

Basically, three cases can be distinguished:

- For very small and very large (overdamping) damping coefficients, self-excited vibrations with very large bearing eccentricities are observed, which prevent a secure technical operation (corresponding to bifurcation path 1, see Section 5.1.1).
- For damping coefficients in the middle range, self-excited oscillations with technically harmless amplitudes are detected (corresponding to bifurcation path 2a, see Section 5.1.2).
- For very small damping coefficients, small stiffnesses and rather large ring masses, bifurcation into the critical ring mode is observed (corresponding to bifurcation path 2b, see Section 5.1.3).

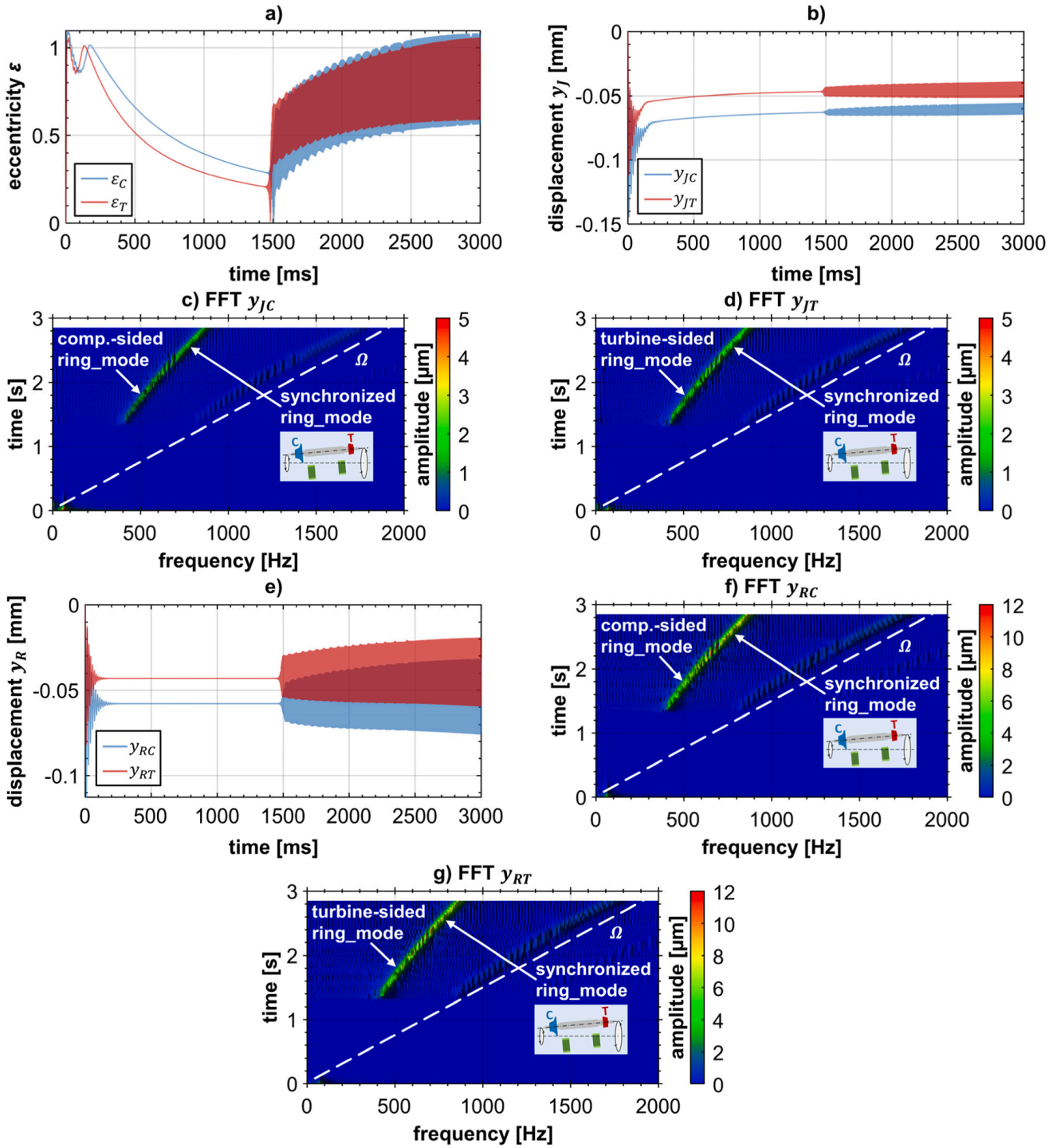

Fig. 25. Run-up simulation 4 with $c_{\text{elast}} = 100$ N mm^{-1}, $d_{\text{visc}} = 30$ N ms mm^{-1} and increased ring mass of 100 g: (a) dimensionless bearing eccentricities $\varepsilon_C(t)$ and $\varepsilon_T(t)$; (b) vertical journal displacements $y_{JC}(t)$ and $y_{JT}(t)$; (c) frequency spectra of $y_{JC}(t)$; (d) frequency spectra of $y_{JT}(t)$; (e) vertical ring displacements $y_{RC}(t)$ and $y_{RT}(t)$; (f) frequency spectra of $y_{RC}(t)$; (g) frequency spectra of $y_{RT}(t)$.

5.3. Comparison: Elastic foil structure versus viscoelastic mounting

Choosing appropriate bearing parameters (stiffness, friction/damping), three basic bifurcation paths can be detected for both bearing designs. A comparison of the simulation results of Section 5.1 and 5.2 shows the subsequent similarities and differences:

- Comparing the run-ups of Section 5.1.1 with Section 5.2.1 (bifurcation path 1), we observe at the onset of the whirl/whip motion smaller amplitudes for the foil structure, which are, however, successively increasing with the rotor speed. For the viscoelastic mounting, larger whirl/whip amplitudes are detected at the beginning, which slowly increase with the rotor speed.

- Regarding bifurcation path 2a (Sections 5.1.2 and 5.2.2), we observe at the onset of the whirl/whip larger amplitudes for the viscoelastic mounting. At the end of the run-up, the whirl/whip almost disappeared, which indicates that the instability may be driven through with the viscoelastic mounting if rotor speed or damping are further increased. However, if damping is chosen too high, see Section 5.2.3, large amplitudes are detected in the complete whirl/whip region, which will not decrease with increasing rotor speed.
- Comparing the two run-up simulations with the ring mode (Section 5.1.3 and 5.2.4), we observe for the foil structure that only the lower loaded turbine-sided bearing is getting unstable and exciting the corresponding turbine-sided ring mode. For the viscoelastic mounting, both bearings get unstable exciting a turbine- and compressor-sided ring mode, whereby both ring modes later synchronize.

It should be stressed that the above listed findings are, of course, only valid for the considered rotor system and for the chosen parameter values. Besides the differences with respect to the vibration characteristics, also the practical and technical advantages and disadvantages of both bearing variants have to be considered for real technical applications of air ring bearings.

6. Conclusion

The paper has presented a thorough study on the dynamics of rotors supported in air ring bearings. Air ring bearings may be considered as an alternative air bearing design, where a rigid ring is used to separate the air film from the elastic foil structure. Alternatively to the foil structure, a viscoelastic material may be used to mount the ring in the housing. The modified design has several technical advantages and disadvantages compared to classical air foil bearings. As a consequence of the modified design, the calculation of the pressure field in the fluid film is significantly simplified, since rigid walls can be assumed to solve Reynolds fluid film equation; the prediction of the nonlinear vibration behavior and the dynamical optimization of the rotor/bearing system over the operating speed range becomes therefore much simpler.

The dynamics, stability and bifurcation behavior of rotors supported in air ring bearings has been systematically analyzed with the help of run-up simulations. The simulations have been carried out with a co-simulation model, where the rotor is represented as a multibody model and the pressure fields in the two bearings by finite element models.

The simulations have shown that rotors in air ring bearings exhibit a very complicated and highly nonlinear vibration and bifurcation behavior. The dynamical behavior differs significantly from the behavior of rotors in classical air foil bearings. Different interesting physical phenomena, which are not observed in connection with classical air foil bearings, have been detected and physically explained in a clear and straightforward manner.

Also, a systematic bifurcation analysis has been carried out. The simulations in Section 5.1 have shown that basically three bifurcation paths can be observed in rotor systems with air ring bearings. For large foil stiffnesses c_{foil} and small friction forces F_{fric}, the dangerous bifurcation path 1 is observed: at higher rotor speeds, whirl/whip vibrations with very large bearing eccentricities are detected. Reducing the foil stiffnesses and increasing the friction forces, bifurcation path 2a is observed, where only self-excited vibrations with moderate amplitudes occur. For very small foil stiffnesses and fairly large ring masses, bifurcation path 2b may be detected, where the system bifurcates into the rather dangerous ring mode.

To achieve a secure operation of a rotor system with air ring bearings, the main task is to avoid bifurcation path 1. This can be simply realized by using a foil structure with higher friction. Furthermore, the foil stiffness should be chosen not too high. From the practical point of view, the friction force in the foil structure can be increased very easily, e.g. by using a higher mechanical preload. If the stiffness and the damping of the foil structure is chosen very small and if the ring mass is comparatively large, a dangerous bifurcation into a ring mode may be observed. For the considered rotor system, the simulations have, however, shown that the bifurcation into the ring mode only occurs for rather extreme system parameters. Hence, the crucial point in the design process of the rotor/bearing design lies in the prevention of bifurcation path 1.

As an alternative to a foil structure, a viscoelastic material may be used to connect the ring with the housing, see Section 5.2. Then, a rather similar vibration and bifurcation behavior is observed.

Declaration of competing interest

The authors declare that they have no known competing financial interests or personal relationships that could have appeared to influence the work reported in this paper.

Appendix A

In this appendix, results of an Eigenmode analysis of the rotor system of Section 5 are presented. Therefore, the nonlinear rotor/bearing system of Section 5 has been linearized. The air film of both bearings has been replaced by two linear springs acting in x- and y-direction with spring constants $c_{\text{air},x} = c_{\text{air},y} = 4900$ N mm^{-1}. The two rings have been mounted elastically in the housing with the linear springs $c_{\text{Ring},x} = c_{\text{Ring},y} = 600$ N mm^{-1}. The modes have been calculated for a rotational speed of $\Omega = 1000$ Hz.

- *Mode_1(b)* and *Mode_1(f)* are conical modes with a vibration node at the compressor-sided bearing: the backward mode *Mode_1(b)* has an eigenfrequency of ≈ 141 Hz; the eigenfrequency of the corresponding forward mode *Mode_1(f)* is ≈ 159 Hz. Rotor and rings oscillate inphase. *Mode_1(f)* is depicted in Fig. 26a.

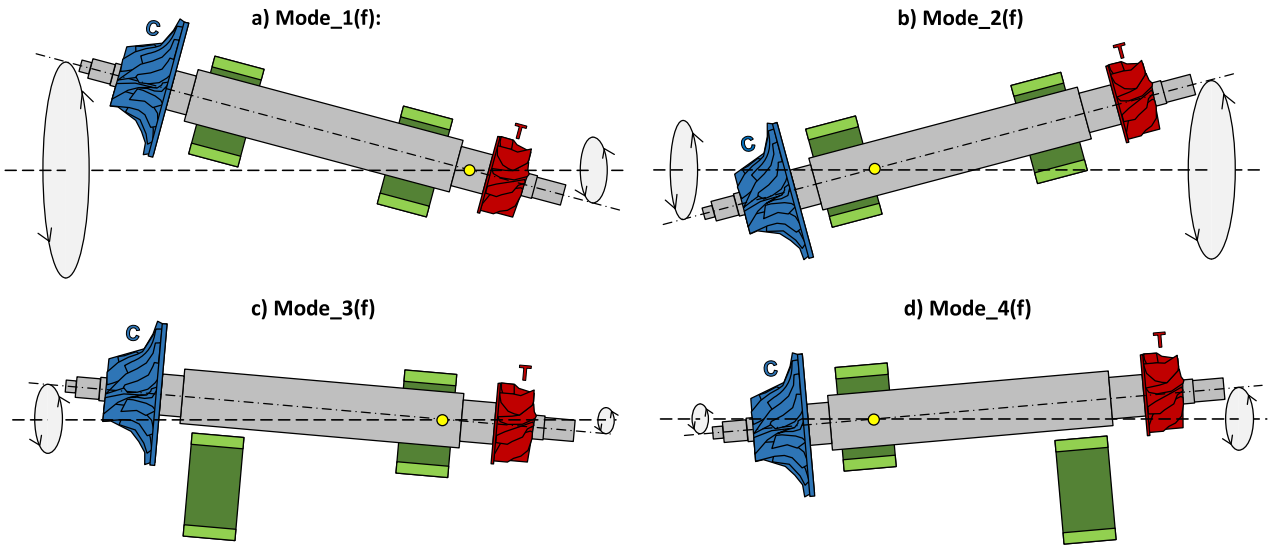

Fig. 26. Rigid body forward mode shapes. (a) and (b): inphase mode shapes *Mode_1(f)* and *Mode_2(f)*; (c) and (d): antiphase mode shapes *Mode_3(f)* and *Mode_4(f)* (ring modes).

- *Mode_2(b)* and *Mode_2(f)* are conical modes with a vibration node at the turbine-sided bearing: the backward mode *Mode_2(b)* shows an eigenfrequency of ≈ 171 Hz; the corresponding forward mode *Mode_2(f)* has an eigenfrequency of ≈ 193 Hz. Rotor and rings oscillate inphase. *Mode_2(f)* is illustrated in Fig. 26b.
- *Mode_3(b)* and *Mode_3(f)* are conical modes with a vibration node at the compressor-sided bearing: the backward mode *Mode_3(b)* has an eigenfrequency of ≈ 1271 Hz; the eigenfrequency of the corresponding forward mode *Mode_3(f)* is ≈ 1274 Hz. Rotor and rings oscillate antiphase. *Mode_3(f)* is shown in Fig. 26c.
- *Mode_4(b)* and *Mode_4(f)* are conical modes with a vibration node at the turbine-sided bearing: the backward mode *Mode_4(b)* has an eigenfrequency of ≈ 1309 Hz; the corresponding forward mode *Mode_4(f)* shows an eigenfrequency of ≈ 1315 Hz. Rotor and rings oscillate antiphase. *Mode_4(f)* is sketched in Fig. 26d.

Remark 1. Modes 1-4 are (almost) rigid body modes. The next higher modes are bending modes. The frequencies of the bending modes are clearly above the maximum rotor speed of 2000 Hz. Run-up simulations show that the bending modes are (almost) not excited in the here considered rotor speed range. To simplify and speed-up the run-up simulations for the current rotor system, a rigid rotor model may therefore be used without a significant loss of accuracy.

Remark 2. As mentioned in Section 2.3, tilting of the rings has not been taken into account in the current rotor/bearing model, i.e. the rings are assumed to perform a planar motion with only two degrees of freedom. Considering ring tilting will affect the eigenfrequency analysis (especially the ring mode shapes and the corresponding eigenfrequencies). As a consequence, the bifurcation points in connection with ring modes (see Section 5.1.3 and Section 5.2.4) may be changed and – depending on the bearing geometry and the stiffness/damping properties of the ring mounting – bifurcation into the dangerous ring modes (bifurcation path 2b) may become more relevant.

Appendix B

For the rotor system examined in Section 5, the center of mass of the rotor lies almost in the middle between the two bearings. Here, simulation results are presented for a rotor/bearing system, where the asymmetry is increased in order to show the influence of rotor asymmetry on the bifurcation behavior. Particularly, the simulations will show that the Hopf bifurcation from the stable equilibrium position into the whirl/whip vibrations originates from the lower loaded turbine-sided bearing. For the following simulations, the rotor center has been moved to the compressor side. Two run-up simulations are presented, where the same data have been used as in Section 5 with only one exception: the location of the rotor center has been moved from $z_{\text{Rotor}} = 125$ mm to $z_{\text{Rotor}} = 140$ mm.

Fig. 27 shows a run-up simulation for $c_{\text{foil}} = 400$ N mm^{-1} and $F_{\text{fric}} = 6$ N. The bifurcation scenario corresponds to bifurcation path

2a in Section 5.1.2.

- At $t \approx 650$ ms, the equilibrium position becomes unstable. Comparing the bearing eccentricities ε_C and ε_T, it can clearly be observed that the instability originates from the turbine-sided bearing, which is significantly lower loaded. The whirl/whip appears at the turbine-sided bearing at $t \approx 700$ ms and slightly later at $t \approx 750$ ms at the compressor-sided bearing. The whirl/whip generated by the turbine-sided air film excites *Mode_2(f)*, while the whirl/whip caused by the compressor-sided air film excites *Mode_1(f)*.
- Increasing the rotor speed, the amplitudes of the bearing eccentricities decrease as well as the amplitudes of compressor and turbine wheel.

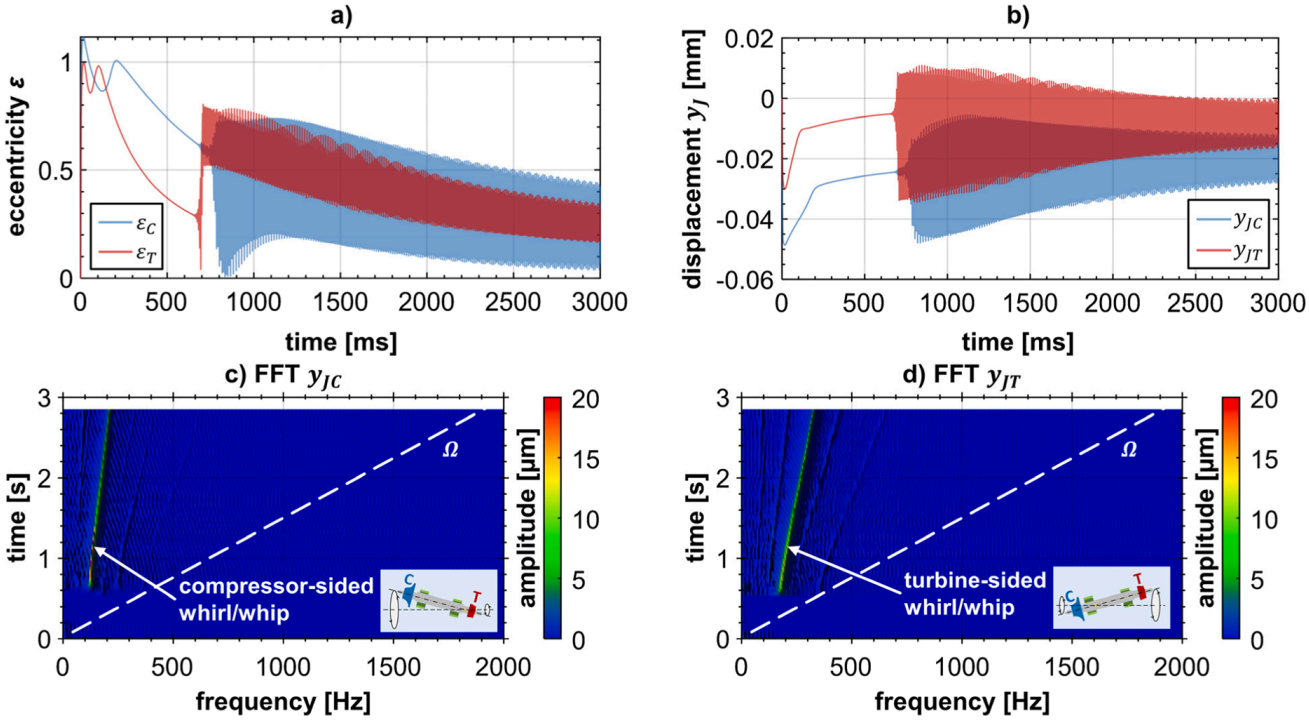

Fig. 27. Run-up simulation for modified rotor with increased asymmetry for $c_{\text{foil}} = 400$ N mm^{-1} and $F_{\text{fric}} = 6$ N: (a) dimensionless bearing eccentricities $\varepsilon_C(t)$ and $\varepsilon_T(t)$; (b) vertical journal displacements $y_{JC}(t)$ and $y_{JT}(t)$; (c) frequency spectra of $y_{JC}(t)$; (d) frequency spectra of $y_{JT}(t)$.

In Fig. 28, a run-up simulation for $c_{\text{foil}} = 800$ N mm^{-1} and $F_{\text{fric}} = 6$ N is depicted, which may be compared with the simulation in Section 5.1.1 (bifurcation path 1).

- At $t \approx 650$ ms, the equilibrium position becomes unstable and the whirl/whip of the turbine-sided bearing excites *Mode_2(f)*. At $t \approx 700$ ms, the compressor-sided air film gets unstable and excites *Mode_1(f)*.
- A saddle node bifurcation, which obviously originates from the compressor-side, occurs at $t \approx 1000$ ms. After the saddle node bifurcation the basic vibration behavior remains unchanged: the whirl/whip of the turbine-sided bearing excites *Mode_2(f)* and the compressor-sided whirl/whip *Mode_1(f)*. In contrast to Section 5.1.1, mode synchronization is not detected for the rotor with increased asymmetry.

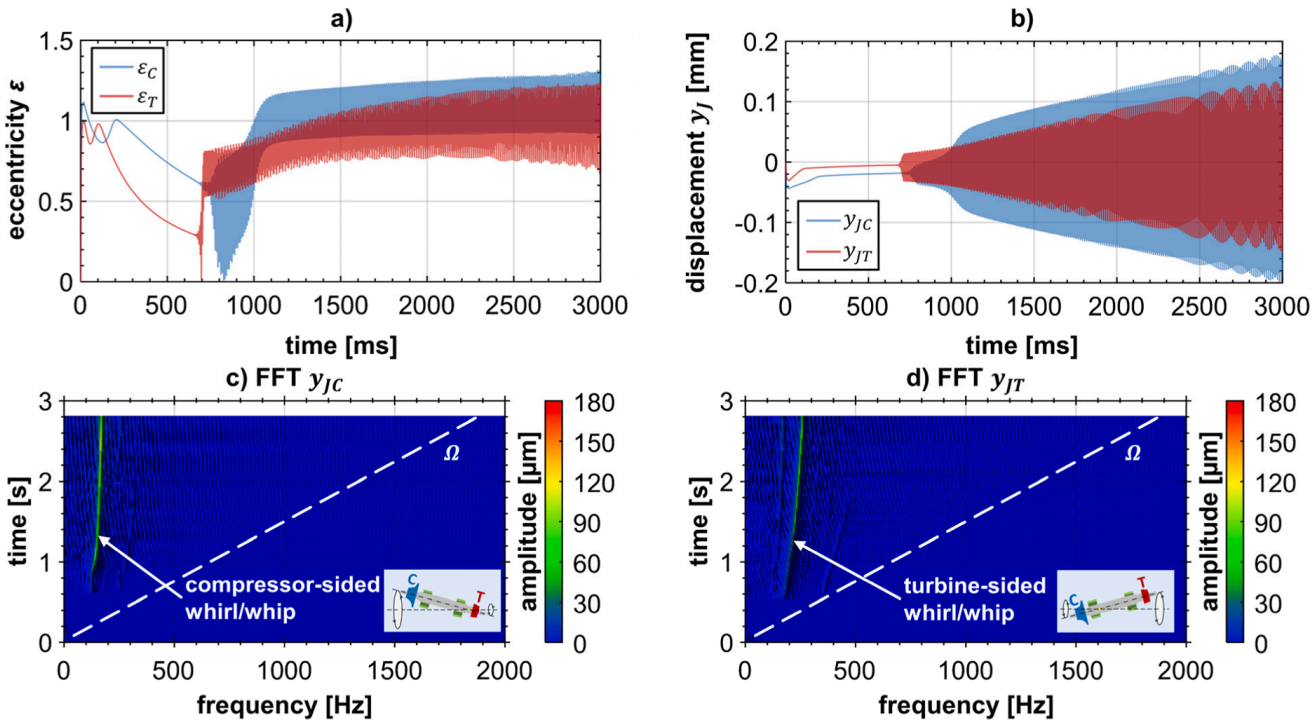

Fig. 28. Run-up simulation for modified rotor with increased asymmetry for $c_{\text{foil}} = 800$ N mm^{-1} and $F_{\text{fric}} = 6$ N: (a) dimensionless bearing eccentricities $\varepsilon_C(t)$ and $\varepsilon_T(t)$; (b) vertical journal displacements $y_{JC}(t)$ and $y_{JT}(t)$; (c) frequency spectra of $y_{JC}(t)$; (d) frequency spectra of $y_{JT}(t)$.

Appendix C

Rotor imbalance influences the vibrations of the rotor system and may also have a noticeable effect on the stability and bifurcation behavior. The run-up simulations in Sections 4 and 5 have been carried out with zero imbalance in order to very clearly illustrate the influence of the bearing parameters on the vibration and bifurcation behavior. In this appendix, the effect of rotor imbalance is discussed. Therefore, two imbalance studies are carried out. Firstly, the symmetrical rotor system of Section 4.1.1 is reconsidered with imbalance. Secondly, an imbalance study for the unsymmetrical rotor system of Section 5.1.1 is presented.

Fig. 29 shows run-up simulations for the symmetrical rotor system of Section 4.1.1 with three different imbalances U_{Rotor}, namely 0.5 g mm, 1 g mm and 1.5 g mm. The results can be summarized as follows:

- The bifurcation point at $t \approx 750$ ms is only slightly influenced by rotor imbalance. Before the Hopf bifurcation, the rotor performs imbalance oscillations around the stable equilibrium position; the higher the imbalance, the larger are the amplitudes. A small rigid body resonance can be detected at $t \approx 250$ ms.
- The second bifurcation point at $t \approx 1000$ ms is also only slightly affected by the rotor imbalance.
- Amplitudes of the quasiperiodic motion (mainly consisting of the rotor speed and the whirl/whip frequency) in the time range 750 ms $\leq t \leq$ 1000 ms are only little larger than the limit cycle amplitudes in the simulation with zero imbalance. The same holds for the quasiperiodic motion in the time range 1000 ms $\leq t \leq$ 3000 ms.

Run-up simulations with different imbalances for the unsymmetrical rotor system of Section 5.1.1 are collected in Fig. 30. Therefore, imbalance masses are attached at the compressor and turbine wheel as illustrated in Fig. 7. Three cases are considered, namely $U_{\text{C}} = U_{\text{T}} = U = 0.25$ g mm, $U_{\text{C}} = U_{\text{T}} = U = 0.5$ g mm as well as $U_{\text{C}} = U_{\text{T}} = U = 0.75$ g mm. The corresponding run-up simulations yield the following results:

- Stable imbalance oscillations are observed before the first bifurcation. At $t \approx 250$ ms, a small rigid body resonance can be seen.
- The Hopf bifurcation point at $t \approx 750$ ms for the simulation with zero imbalance is only slightly changed by the imbalance. With imbalance, the bifurcation occurs little bit earlier.
- The second bifurcation point at $t \approx 1700$ ms is also little affected by the imbalance. Again, the imbalance shifts the bifurcation slightly to smaller rotor speeds.
- Amplitudes of the quasiperiodic motion in the whirl/whip regions are not significantly increased compared to the zero imbalance case.

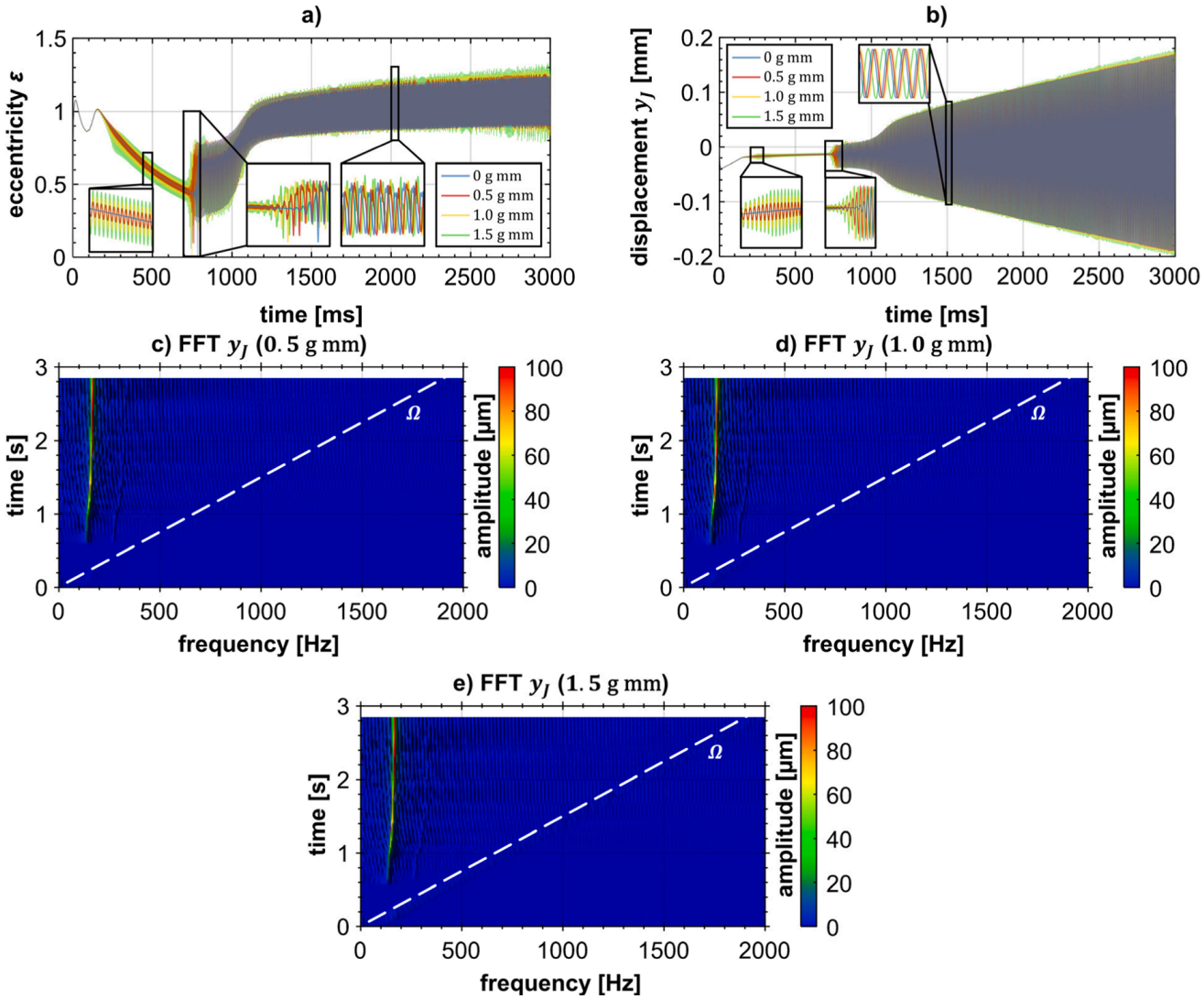

Fig. 29. Run-up simulation of Section 4.1.1 for different rotor imbalances U_{Rotor} (0 g mm, 0.5 g mm, 1 g mm and 1.5 g mm): (a) dimensionless bearing eccentricities $\varepsilon(t)$; (b) rotor displacements $y_J(t)$; (c)-(e) frequency spectra of $y_J(t)$.

Appendix D

This appendix contains some additional information on the co-simulation interface and the numerical time integration of the rotor/bearing model. Also, a convergence study with respect to the error tolerances of the subsystem solvers is presented.

The rotor/bearing co-simulation model consists of 3 subsystems (one multibody subsystem for the rotor and two finite element subsystems for the air films), where each subsystem is integrated with a BDF solver (variable integration order, variable step size) [75, 76,77]. The co-simulations have been carried out on a single processor machine with 12 cores (AMD Ryzen Threadripper 2920X, 12-Core Processor, 3.50 GHz, RAM 128 GB). The multibody subsystem (process 1) is executed firstly according to the sequential Gauss-Seidel scheme explained in Section 3. Then, the two finite element subsystems (processes 2 and 3) are executed in parallel. Communication between the processes 1 and 2 as well as between processes 1 and 3 is realized with TCP/IP.

The integration step-sizes are variable and defined by the error controller. All simulations in Sections 4 and 5 have been carried out with an absolute and relative error tolerance of $\epsilon_{\text{solver}} = \epsilon_{\text{abs}} = \epsilon_{\text{rel}} = 1E-6$. The maximum step size has been set to $h_{\text{max}} = 1E-6$. For the run-up simulation in Section 5.1.1, for instance, the computation time (wall-clock time) is $T_{\text{comp}} \approx 11\text{h}25\text{min}$. The number of macro-steps (i.e. number of MBS solver steps) is $n_{\text{MBS}} = 3,003,138$; the number of micro-steps of the compressor-sided and turbine-sided FE subsystems are $n_{\text{FEM1}} = 3,169,132$ and $n_{\text{FEM2}} = 3,159,155$, respectively.

Detailed numerical studies – carried out for various rotor/bearing co-simulation models and different model parameters – have shown that an error tolerance of $\epsilon_{\text{solver}} = 1E-6$ will usually provide simulation results with a good accuracy. In many cases, even an error tolerance of $\epsilon_{\text{solver}} = 5E-6$ may yield results with acceptable accuracy. Reduction of the error tolerance (e.g. $\epsilon_{\text{solver}} = 5E-7$) often showed only a minor improvement. For the considered model, an error tolerance of $1E-6$ seems to be a good compromise between accuracy and computation time. For the reason of a concise representation, we here omit thorough convergence analyses. We just compare simulation results accomplished with $\epsilon_{\text{solver}} = 5E-6$, $\epsilon_{\text{solver}} = 1E-6$ and $\epsilon_{\text{solver}} = 5E-7$ with the help of the run-up

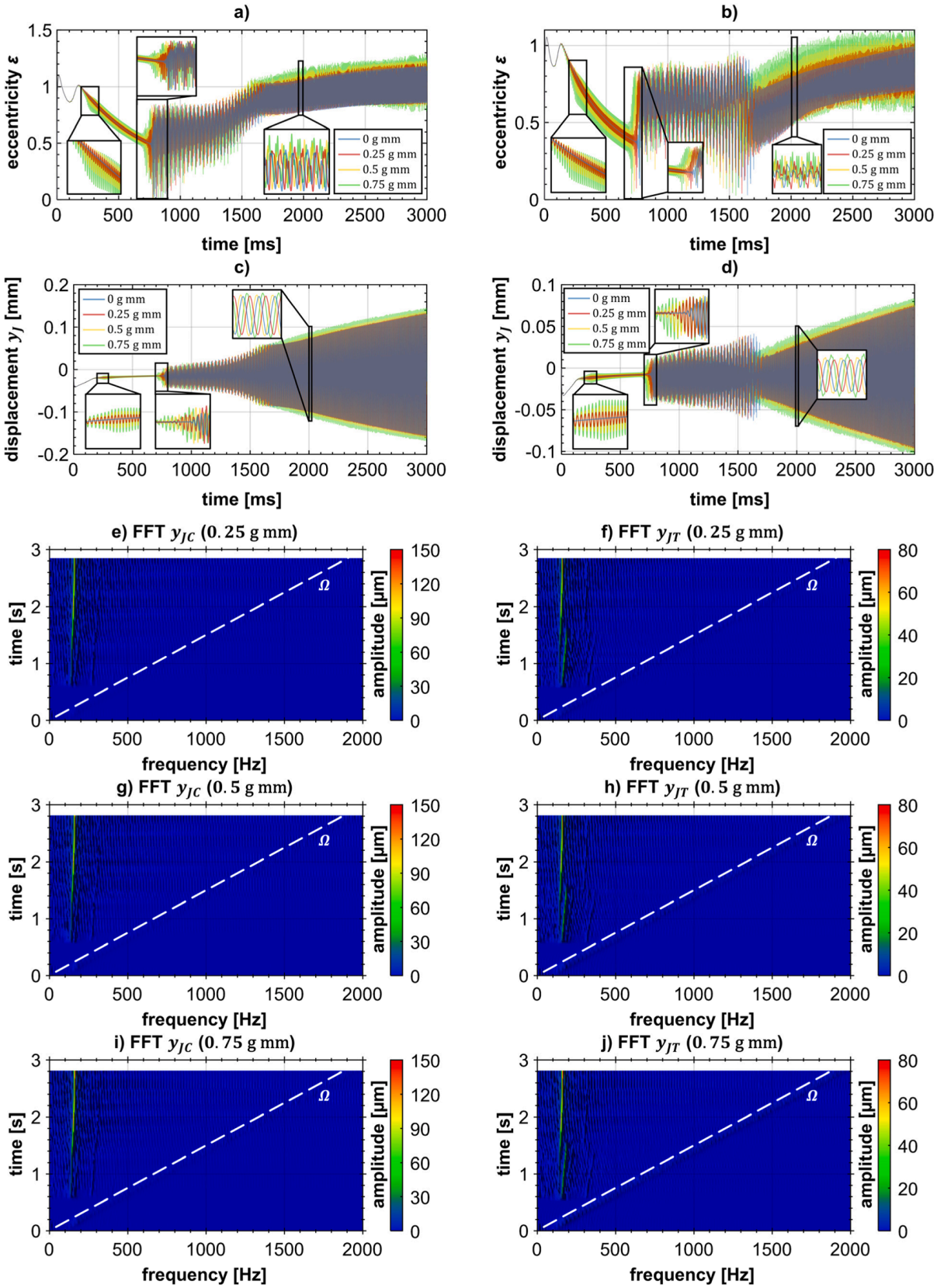

Fig. 30. Run-up simulation of Section 5.1.1 for different imbalances U (0 g mm, $2\times$ 0.25 g mm, 2×0.5 g mm and 2×0.75 g mm): (a) dimensionless bearing eccentricities $\varepsilon_C(t)$; (b) dimensionless bearing eccentricities $\varepsilon_T(t)$; (c) vertical journal displacements $y_{JC}(t)$; (d) vertical journal displacements $y_{JT}(t)$; (e)-(j) frequency spectra of $y_{JC}(t)$ and $y_{JT}(t)$.

simulation in Section 5.1.1. Comparing the spectra of Fig. 17 (c,d) for $\epsilon_{\text{solver}} = 1E-6$ with the corresponding spectra in Fig. 31 for $\epsilon_{\text{solver}} = 5E-6$ and $\epsilon_{\text{solver}} = 5E-7$, only relatively small differences can be detected. The differences with respect to the computation time are, however, rather large. For $\epsilon_{\text{solver}} = 5E-6$, we have $T_{\text{comp}} \approx$ 3h00min, $n_{\text{MBS}} = 604,110$, $n_{\text{FEM1}} = 683,781$ and $n_{\text{FEM2}} = 676,881$. For $\epsilon_{\text{solver}} = 5E-7$, we measure $T_{\text{comp}} \approx$ 20h32min, $n_{\text{MBS}} = 6,002,728$, $n_{\text{FEM1}} = 6,203,357$ and $n_{\text{FEM2}} = 6,160,480$.

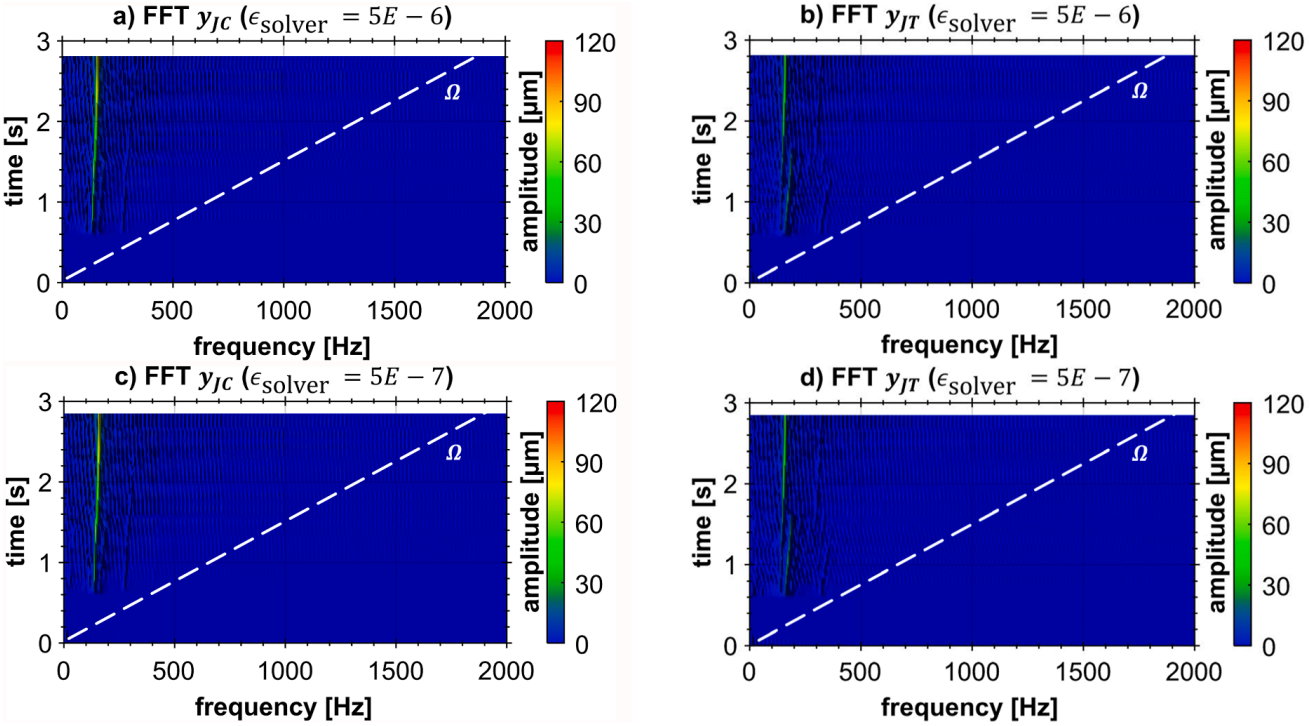

Fig. 31. Convergence study for two different error tolerances ϵ_{solver} ($5E-6$, $5E-7$) with the rotor model of Section 5.1.1: (a),(b) frequency spectra of $y_{JC}(t)$ and $y_{JT}(t)$ for ϵ_{solver}=$5E-6$; (c),(d) frequency spectra of $y_{JC}(t)$ and $y_{JT}(t)$ for ϵ_{solver}=$5E-7$.

References

[1] R. Bruckner, B.J. Puleo, American Society of Mechanical Engineers, Compliant Foil Journal Bearing Performance at Alternate Pressures and Temperatures, ASME Turbo Expo 2008: Power for Land, Sea, and Air (2008).
[2] R. Bruckner, American Society of Mechanical Engineers, An assessment of gas foil bearing scalability and the potential benefits to civilian turbofan engines, ASME Turbo Expo 2010: Power for Land, Sea, and Air (2010).
[3] C. DellaCorte, K. Radil, R. Bruckner, S. Howard, Design, fabrication, and performance of open source generation I and II compliant hydrodynamic gas foil bearings, Tribol. Trans. 51 (3) (2008) 254–264.
[4] K. Feng, X. Zhao, Z. Guo, Design and structural performance measurements of a novel multi-cantilever foil bearing, in: Proceedings of the Institution of Mechanical Engineers, Part C: Journal of Mechanical Engineering Science 229, 2015, pp. 1830–1838.
[5] H. Heshmat, W. Shapiro, S. Gray, Development of foil journal bearings for high load capacity and high speed whirl stability, J. Lubr. Technol. 104 (2) (1982) 149–156.
[6] L. San Andrés, T.A. Chirathadam, A metal mesh foil bearing and a bump-type foil bearing: Comparison of performance for two similar size gas bearings, J. Eng. Gas Turbines Power 134 (10) (2012), 102501.
[7] K. Shalash, J. Schiffmann, Comparative Evaluation of Foil Bearings With Different Compliant Structures for Improved Manufacturability, in: ASME Turbo Expo 2017: Turbomachinery Technical Conference and Exposition, American Society of Mechanical Engineers Digital Collection, 2017.
[8] J.-H. Song, D. Kim, Foil Gas Bearing With Compression Springs: Analyses and Experiments, J. Tribol. 129 (3) (2007) 628–639.
[9] E.E. Swanson, P. Shawn O'Meara, The wing foil: a novel compliant radial foil bearing design, J. Eng. Gas Turbines Power 140 (8) (2018).
[10] M. Arghir, O. Benchekroun, A New Structural Bump Foil Model With Application From Start-Up to Full Operating Conditions, J. Eng. Gas Turbines Power 141 (10) (2019).
[11] P. Bonello, H. Pham, The efficient computation of the nonlinear dynamic response of a foil–air bearing rotor system, J. Sound Vib. 333 (15) (2014) 3459–3478.
[12] D. Kim, Parametric studies on static and dynamic performance of air foil bearings with different top foil geometries and bump stiffness distributions, J. Tribol. 129 (2) (2007) 354–364.
[13] T.H. Kim, L. San Andrés, Effects of a mechanical preload on the dynamic force response of gas foil bearings: measurements and model predictions, Tribol. Trans. 52 (4) (2009) 569–580.
[14] S.Le Lez, M. Arghir, J. Frene, Static and Dynamic Characterisation of a Bump-Type Foil Bearing Structure, in: International Joint Tribology Conference, 2006.
[15] S.Le Lez, M. Arghir, J. Frene, A new bump-type foil bearing structure analytical model, Turbo Expo: Power for Land, Sea, and Air (2007).
[16] D. Lee, D. Kim, Thermohydrodynamic analyses of bump air foil bearings with detailed thermal model of foil structures and rotor, J. Tribol. 132 (2) (2010).
[17] M. Mahner, P. Li, A. Lehn, B. Schweizer, Numerical and Experimental Investigations on Preload Effects in Air Foil Journal Bearings, J. Eng. Gas Turbines Power 140 (3) (2018), 032505.
[18] S. von Osmanski, J.S. Larsen, I.F. Santos, A fully coupled air foil bearing model considering friction–Theory & experiment, J. Sound Vib. 400 (2017) 660–679.
[19] A. Muszynska, Rotordynamics, CRC press, 2005.
[20] C.J. Myers, Bifurcation Theory Applied to Oil Whirl in Plain Cylindrical Journal Bearings, ASME J. Appl. Mech. 51 (1984) 244–250.

[21] B. Schweizer, M. Sievert, Nonlinear Oscillations of Automotive Turbocharger Turbines, J. Sound Vib. 321 (2009) 955–975.
[22] J.W. Lund, B. Sternlicht, Rotor Bearing Dynamics with Emphasis on Attenuation, J. Basic Eng. 84 (4) (1962) 491–502.
[23] J.W. Lund, Stability and Damped Critical Speeds of a Flexible Rotor in Fluid Film Bearings, J. Eng. Indust. (1974) 509–517.
[24] A. Boyaci, H. Hetzler, W. Seemann, C. Proppe, J. Wauer, Analytical bifurcation analysis of a rotor supported by floating ring bearings, Nonlinear Dyn. 57 (2009) 497–507.
[25] A. Chasalevris, Stability and Hopf bifurcations in rotor-bearing-foundation systems of turbines and generators, Tribol. Int. 145 (2020), 106154.
[26] A. Chasalevris, Nonlinear Stability of Turbine and Generator Rotors Applying Hopf Bifurcation Theory, in: E.J. Sapountzakis, M. Banerjee, P. Biswas, E. Inan (Eds.), Proceedings of the 14th International Conference on Vibration Problems. Lecture Notes in Mechanical Engineering, Springer, Singapore, 2021.
[27] J.C. Deepak, S.T. Noah, Experimental Verification of Subcritical Whirl Bifurcation of a Rotor Supported on a Fluid Film Bearing, J. Tribol. Trans. ASME 120 (3) (1998) 605–609.
[28] M.M. Khonsari, E.R. Booser, Applied Tribology, 2nd Edition, John Wiley&Sons, 2008.
[29] J. Shaw, S.W. Shaw, The Effects of Unbalance on Oil Whirl, Nonlinear Dyn. 1 (1990) 293–311.
[30] P. Sundararajan, S.T. Noah, An Algorithm for Response and Stability of Large Order Non-Linear Systems - Application to Rotor Systems, J. Sound Vib. 214 (4) (1998) 695–723.
[31] J.K. Wang, M.M. Khonsari, On the Hysteresis Phenomenon Associated with Instability of Rotor-Bearing Systems, J. Tribol.-Trans. ASME 128 (1) (2006) 188–196.
[32] J.K. Wang, M.M. Khonsari, Bifurcation Analysis of a Flexible Rotor Supported by Two Fluid-Film Journal Bearings, J. Tribol.- Trans. ASME 128 (3) (2006) 594–603.
[33] J.C. Wilkes, J. Wade, A. Rimpel, J. Moore, E. Swanson, J. Grieco, J. Brady, Impact of Bearing Clearance on Measured Stiffness and Damping Coefficients and Thermal Performance of a High-Stiffness Generation 3 Foil Journal Bearing, J. Eng. Gas Turbines Power 140 (7) (2018).
[34] A. Muszynska, Whirl and Whip – Rotor/Bearing Stability Problems, J. Sound Vib. 110 (3) (1986) 443–462.
[35] A. Muszynska, Tracking the Mystery of Oil Whirl, Sound Vib. (1987) 8–12.
[36] A. Muszynska, Stability of Whirl and Whip in Rotor/Bearing Systems, J. Sound Vib. 127 (1) (1988) 49–64.
[37] A. Boyaci, Numerical Continuation Applied to Nonlinear Rotor Dynamics, Procedia IUTAM 19 (2016) 255–265.
[38] A. Boyaci, D. Lu, B. Schweizer, Stability and bifurcation phenomena of Laval/Jeffcott rotors in semi-floating ring bearings, Nonlin. Dyn. (2015) 1535–1561.
[39] A. Chasalevris, Finite length floating ring bearings: Operational characteristics using analytical methods, Tribol. Int. 94 (2016) 571–590.
[40] A. Chasalevris, J.-C. Louis, Evaluation of Transient Response of Turbochargers and Turbines Using Database Method for the Nonlinear Forces of Journal Bearings, Lubricants 7 (9) (2019) 78.
[41] R. Eling, R. van Ostayen, D. Rixen, Multilobe Floating Ring Bearings for Automotive Turbochargers, in: P. Pennacchi (Ed.), Proceedings of the 9th IFToMM International Conference on Rotor Dynamics. Mechanisms and Machine Science 21, Springer, 2015.
[42] R. Eling, M. te Wierik, R. van Ostayen, D. Rixen, Rotordynamic and Friction Loss Measurements on a High Speed Laval Rotor Supported by Floating Ring Bearings, Lubricants 5 (1) (2017) 7.
[43] L. San Andrés, J.C. Rivadeneira, M. Chinta, K. Gjika, G. LaRue, Nonlinear Rotordynamics of Automotive Turbochargers - Predictions and Comparisons to Test Data, ASME J. Eng. Gas Turbines and Power 129 (2007) 488–493.
[44] B. Schweizer, Dynamics and stability of turbocharger rotor, Arch. Appl. Mech. 80 (2010) 1017–1043.
[45] B. Schweizer, Oil Whirl, Oil Whip and Whirl/Whip Synchronization Occurring in Rotor Systems with Full-Floating Ring Bearings, J. Nonlin. Dyn. (2009) 57.
[46] B. Schweizer, Total Instability of Turbocharger Rotors – Physical Explanation of the Dynamic Failure of Rotors with Full-Floating Ring Bearings, J. Sound Vib. 328 (1–2) (2009).
[47] P. Sundararajan, S.T. Noah, Dynamics of Forced Nonlinear Systems Using Shooting/Arc-Length Continuation Method - Application to Rotor Systems, J. Vib. Acoust.- Trans. ASME 119 (1) (1997) 9–20.
[48] C. Li, J. Du, Y. Yao, Study of load carrying mechanism of a novel three-pad gas foil bearing with multiple sliding beams, Mech. Syst. Sig. Process. 135 (2020).
[49] B. Yang, S. Feng, J. Tian, L. Yu, Research on the Static Performance of Multi-Cantilever Foil Bearing with the Fully Coupled Elastic Hydrodynamic Solution, in: 2019 IEEE International Conference on Mechatronics and Automation (ICMA), 2019.
[50] C.-P.R. Ku, H. Heshmat, Compliant Foil Bearing Structural Stiffness Analysis: Part I—Theoretical Model Including Strip and Variable Bump Foil Geometry, J. Tribol. 114 (2) (1992) 394–400.
[51] C.-P.R. Ku, H. Heshmat, Compliant Foil Bearing Structural Stiffness Analysis—Part II: Experimental Investigation, J. Tribol. 115 (3) (1993) 364–369.
[52] J.S. Larsen, A.C. Varela, I.F. Santos, Numerical and experimental investigation of bump foil mechanical behavior, Tribol. Int. 74 (2014) 46–56.
[53] J.-P. Peng, M. Carpino, Coulomb friction damping effects in elastically supported gas foil bearings, Tribol. Trans. 37 (1) (1994) 91–98.
[54] F. Balducchi, M. Arghir, R. Gauthier, Experimental analysis of the unbalance response of rigid rotors supported on aerodynamic foil bearings, J. Vib. Acoust. 137 (6) (2015).
[55] C. Baum, H. Hetzler, S. Schröders, T. Leister, W. Seemann, A computationally efficient nonlinear foil air bearing model for fully coupled, transient rotor dynamic investigations, Tribol. Int. 153 (2021), 106434.
[56] Z. Guo, L. Peng, K. Feng, W. Liu, Measurement and prediction of nonlinear dynamics of a gas foil bearing supported rigid rotor system, Measurement 121 (2018) 205–217.
[57] T. Leister, C. Baum, W. Seemann, Computational Analysis of Foil Air Journal Bearings Using a Runtime-Efficient Segmented Foil Model, J. Fluids Eng. 140 (2) (2018).
[58] L. San Andrés, T.H. Kim, Forced nonlinear response of gas foil bearing supported rotors, Tribol. Int. 41 (8) (2008) 704–715.
[59] P. Bonello, M.B. Hassan, An experimental and theoretical analysis of a foil-air bearing rotor system, J. Sound Vib. 413 (2018) 395–420.
[60] J.S. Larsen, I.F. Santos, On the nonlinear steady-state response of rigid rotors supported by air foil bearings—Theory and experiments, J. Sound Vib. 346 (2015) 284–297.
[61] A. Tatara, H. Koike, A. Iwasaki, The Stability of Flexibly Supported, Externally Pressurized Gas Journal Bearings: Case of a Rigid Rotor, Bull. JSME 16 (100) (1973) 1573–1579.
[62] M. Mahner, M. Bauer, A. Lehn, B. Schweizer, An experimental investigation on the influence of an assembly preload on the hysteresis, the drag torque, the lift-off speed and the thermal behavior of three-pad air foil journal bearings, Tribol. Int. 137 (2019) 113–126.
[63] M. Mahner, M. Bauer, B. Schweizer, Numerical analyzes and experimental investigations on the fully-coupled thermo-elasto-gasdynamic behavior of air foil journal bearings, Mech. Syst. Sig. Process. 149 (2021), 107221.
[64] A.Z. Szeri, Fluid Film Lubrication: Theory and Design, Cambridge University Press, 2005.
[65] P. Zeise, M. Mahner, M. Bauer, R. Rieken, B. Schweizer, A Reduced Model for Air Foil Journal Bearings for Time-Efficient Run-Up Simulations, in: Proceedings of the ASME Turbo Expo 2019: Turbomachinery Technical Conference and Exposition, Volume 7B: Structures and Dynamics, Phoenix, Arizona, USA, 2019.
[66] P. Zeise, M. Mahner, M. Bauer, M. Rieken, B. Schweizer, A Reduced Semi-Analytical Gas Foil Bearing Model for Transient Run-Up Simulations, in: Proceedings of the 12th virtual Conference on Vibrations in Rotating Machinery XII (VIRM 12), October 14-15, 2020.
[67] D. Rubio, L. San Andrés, Structural Stiffness, Dry Friction Coefficient, and Equivalent Viscous Damping in a Bump-Type Foil Gas Bearing, J. Eng. Gas Turbines Power 129 (2) (2007) 494–502.
[68] E.J. Haug, Computer-Aided Kinematics and Dynamics of Mechanical Systems, Allyn and Bacon, 1989.
[69] A. Shabana, Dynamics of Multibody Systems, Cambridge University Press, 2005.
[70] C.W. Gear, G.K. Gupta, B.J. Leimkuhler, Automatic integration of the Euler-Lagrange equations with constraints, J. Comput. Appl. Math. 12-13 (1985) 77–90.
[71] C. Gomes, C. Thule, D. Broman, P.G. Larsen, H. Vangheluwe, Co-simulation: A survey, ACM Comput. Surv. 51 (3) (2018) 1–33.
[72] T. Meyer, J. Kraft, B. Schweizer, Co-Simulation: Error Estimation and Macro-Step Size Control, J. Comput. Nonlinear Dyn. 16 (4) (2021).
[73] B. Schweizer, D. Lu, Semi-Implicit Co-Simulation Approach for Solver Coupling, Arch. Appl. Mech. 84 (12) (2014) 1769–1839.

[74] B. Schweizer, P. Li, D. Lu, Explicit and Implicit Co-Simulation Methods: Stability and Convergence Analysis for Different Solver Coupling Approaches, J. Comput. Nonlinear Dyn. 10 (5) (2015).
[75] K.E. Brenan, S.L. Campbell, L.R Petzold, Numerical solution of initial-value problems in differential-algebraic equations 14 (1996). Siam.
[76] L.F. Shampine, M.K. Gordon, Computer solution of ordinary differential equations: the initial value problem, Freeman (1975).
[77] S. Skelboe, The control of order and steplength for backward differential methods, BIT Num. Math. 17 (1) (1977) 91–107.

Zweite Veröffentlichung

Pascal Zeise und Bernhard Schweizer. „Vibration and bifurcation analysis of rotor systems with air ring bearings including ring tilting“. In: *Journal of Sound and Vibration* 571 (2024), S. 118079. ISSN: 0022-460X. DOI: 10.1016/j.jsv.2023.118079

https://doi.org/10.1016/j.jsv.2023.118079

Journal of Sound and Vibration 571 (2024) 118079

Contents lists available at ScienceDirect

Journal of Sound and Vibration

journal homepage: www.elsevier.com/locate/jsvi

Vibration and bifurcation analysis of rotor systems with air ring bearings including ring tilting

Pascal Zeise *, Bernhard Schweizer

Department of Mechanical Engineering, Institute of Applied Dynamics, Technical University of Darmstadt, Germany

ARTICLE INFO

Keywords:
Air ring bearings
Ring tilting
Rotor dynamics
Stability
Bifurcation analysis
Nonlinear mode coupling
Co-simulation model

ABSTRACT

Air ring bearings may be considered as a further development of classical air bearings. A drawback of classical rigid air bearings is their reduced damping behavior, which usually prevents a secure operation above the linear threshold speed of instability. Considering air ring bearings, the ring-shaped bearing bushing is visco-elastically mounted in the housing so that external damping is provided. Alternatively, the bushing ring may also be mounted in the housing by a foil structure (beam or bump foil design) so that dissipation is generated by dry friction. Due to the external damping/friction provided by the ring mounting, rotor systems with air ring bearings can be operated above the threshold speed of instability so that stable self-excited vibrations with moderate amplitudes are observed. For certain system parameters, however, the rotor system can bifurcate into a rather dangerous vibration mode, where bearing ring modes are excited by the whirl/whip frequency of the air films. To accurately predict the bifurcation into the problematic ring modes, ring tilting has to be taken into account.

Here, a detailed analysis for rotor systems with air ring bearings is presented, which fully incorporates ring tilting effects. The influence of ring tilting on the stability and bifurcation behavior is discussed in detail with the help of nonlinear rotor/bearing models. In connection with the bifurcation into the dangerous ring mode, an interesting nonlinear mode coupling effect (1:2 mode synchronization) is detected. A detailed analysis and a clear physical explanation of this mode coupling phenomenon is given.

1. Introduction

Considering air bearings, basically two categories may be distinguished. The first category comprises air foil bearings, where the air gap between the rotor journal and the top foil is a function of the top foil deformation. The second category collects air bearings with a rigid housing, where the air gap between the rotor journal and the inner surface of the bearing bushing has rigid walls.

Air foil bearings usually consist of a coated top foil, which is supported by a bump-, beam- or wing-type foil structure. Foil bearings are used in many different technical applications. Various design variants have been examined in literature. Air foil bearings with bump foils are, for instance, treated in [1–3], foil bearings with beam foils in [4,5], bearings using a metal mesh in [6], foil bearings with springs in [7] and bearings with wing foils in [8,9]. The stiffness and damping/friction behavior of foil bearings depends on the particular bearing design. Also, the vibration, stability and bifurcation behavior of rotors supported in foil bearings is strongly depending on the specific bearing design and bearing parameters. Bearings with a three-pad design often exhibit an improved stability

* Corresponding author.
E-mail address: zeise@ad.tu-darmstadt.de (P. Zeise).

https://doi.org/10.1016/j.jsv.2023.118079
Received 27 January 2023; Received in revised form 15 August 2023; Accepted 4 October 2023
Available online 13 October 2023

characteristic [2,3] compared to bearings with a single top and bump foil. The stability may also be improved by modifying the bushing bore geometry or by using shims [10–12] or alternatively by creating an assembly preload [13]. Technical approaches to actively stabilize rotor/bearing systems with foil bearings are discussed in [14,15]. Bearings with an active gas injection for heavy rotors are investigated in [16,17]. It should also be mentioned that due to wear in the top foil coating, the dynamical behavior of rotor systems with air foil bearings may change during operation.

The numerical prediction of the dynamical stability of rotor systems with foil bearings is of high importance. Straightforward approaches based on a classical eigenvalue calculation (see e.g. [18]) may, however, not be sufficient [19–21]. More advanced approaches for the prediction of the dynamical performance and stability of rotors with air foil bearings are presented in [22–24], for instance. The thermal behavior of foil bearings is, e.g., treated in [25,26]. An experimental analysis on the lift-off speed of air foil bearings with a mechanical preload can be found in [27].

Air bearings with a rigid housing can be classified with respect to the bore geometry. In the most simple case, a mere circular geometry may be used. However, air bearings with a circular bore geometry exhibit a very poor stability behavior, i.e. the (linear) threshold speed of instability is very low. Using a multi-lobe bore geometry (e.g. a three-lobe bearing bore), the threshold speed may be little increased, but remains still rather low. Operation of rotor systems with rigid air bearings above the linear threshold speed of instability is generally only possible, if external damping is applied. With external damping, the rotor/bearing system may be run above the linear threshold speed of instability so that stable self-excited vibrations (whirl/whip oscillations) with moderate bearing eccentricities and tolerable rotor amplitudes are observed. Depending on the system parameters and especially on the amount of external damping, the rotor system may be even stabilized again at higher rotor speeds, i.e. the region with self-excited vibrations may be driven through.

Instead of using a circular or multi-lobe bore geometry, also a herringbone-geometry may be used, for instance. Properly choosing the design parameters of a herringbone-bearing, stable operation of the rotor system in the complete operating area may be achieved [28,29]. The dynamics and the stability behavior of rotor systems with herringbone-bearings are discussed in [30], investigations on an enhanced groove geometry can be found in [31]. Thermal aspects in connection with herringbone-bearings are, for instance, considered in [32]. For a more detailed literature review on herringbone-bearings, the interested reader is referred to [33]. While rigid air bearings with herringbone-geometry may exhibit an excellent stability behavior, there are different physical, technical and practical reasons, which may prevent the usage of herringbone-bearings [34].

A very obvious and simple way to introduce external damping into rotor systems with rigid air bearings is to use a rigid ring as bearing bushing [35–37]. This bearing type is called *air ring bearing* in the following. The bushing ring itself is visco-elastically mounted in the housing, e.g. by means of an elastomer. Instead of a visco-elastic mounting, the ring may also be supported in the housing by a foil structure (beam or bump foil) so that dissipation is generated by dry friction. Note that the axial rotation of the ring is assumed to be prevented. Using a bushing ring, the air film is generated between the rotor journal and the inner surface of the ring, i.e. the air gap has rigid walls. During operation, the ring will move relative to the housing so that damping/friction is generated in the mounting structure of the ring.

The inner surface of the ring may in the simplest case have a mere circular bore-geometry. Dynamical analyses and rotor simulations with air ring bearings with a circular bore-geometry show that such systems entail a rather poor stability behavior. A significantly improved performance can be obtained, however, if the inner surface of the ring has a three-lobe geometry.

The dynamics, the stability and the bifurcation behavior of air ring bearings with a three-lobe bore geometry has been examined in [37] with the help of numerical models. The analyses in [37] have shown that typical high-speed rotor systems with air ring bearings may basically exhibit three different bifurcation scenarios – here called *bifurcation path 1, bifurcation path 2a* and *bifurcation path 2b* – during a rotor run-up (run-down). If the supporting structure of the ring is rather stiff and the external damping/friction low, the dangerous bifurcation path 1 is detected, where the self-excited rotor vibrations – occurring above the linear threshold speed of instability – show very large amplitudes, preventing a stable technical operation. Reducing the supporting stiffness and increasing the external damping/friction, stable self-excited whirl/whip vibrations are observed with rather moderate rotor amplitudes so that a safe technical operation is possible in the complete operating range (bifurcation path 2a). For rather large ring masses and low external damping/friction, the dangerous bifurcation path 2b is detected, where the whirl/whip frequency of the fluid films excites ring modes with relatively large amplitudes. Hence, a stable operation of rotor systems with air ring bearings is only possible in connection with bifurcation path 2a, i.e. between bifurcation path 1 and 2b. The basin of attraction for bifurcation path 2a is usually rather large. Hence, bifurcation into path 1 or 2b may simply be prevented by choosing appropriate bearing parameters with the help of accurate simulation models.

The simulation model used in [37] and the corresponding results have been derived with a bearing model that does not consider ring tilting effects, i.e. the ring is assumed to perform only a planar motion. In the paper at hand, misalignment effects between the rotor journal and ring are taken into account. It will be shown that misalignment effects – i.e. tilting of the journal with respect to the ring – have only a minor influence on bifurcation path 1 and bifurcation path 2a. The influence of ring tilting may, however, be very significant in connection with bifurcation path 2b. As a consequence, tilting of the ring should be considered in a reliable simulation model.

The main intention of this manuscript is to analyze, how bearing misalignment and ring tilting affects the dynamical and especially the bifurcation behavior of rotor systems with air ring bearings. The novel contributions of the current paper can be summarized as

follows.

- A detailed mechanical model for air ring bearings is presented, which takes into account 3D-misalignment effects between rotor journal and ring.
- The bearing model is discretized by a finite element approach and dynamically coupled with the multibody model of the rotor by means of a co-simulation method (solver-coupling approach). With this rotor/bearing co-simulation model, a detailed dynamical analysis of the fully coupled rotor/bearing system is carried out by means of nonlinear run-up simulations.
- The influence of ring tilting on the bifurcation behavior of the system is investigated in detail. Regarding the three basic bifurcation paths typically observed in rotor systems with air ring bearings, it will be shown that the first and the second bifurcation path (bifurcation path 1 and bifurcation path 2a) are almost not influenced, if ring tilting is taken into account (at least for the here considered typical high-speed rotor system).
- It is shown that the third bifurcation (bifurcation path 2b), where ring modes are excited by the whirl/whip of the air films, may be influenced notably by ring tilting.
- In connection with bifurcation 2b, an interesting nonlinear mode coupling effect is detected, which may be interpreted as a 1:2 mode synchronization effect. This physically interesting and technically relevant nonlinear vibration phenomenon cannot be detected, if misalignment is neglected. The mode coupling effect is discussed in detail and physically explained in a clear and straightforward manner with the help of the simulation model.

This manuscript is structured as follows. The basic dynamical effects occurring in rotor systems with air ring bearing are shortly recapitulated in Section 2. The finite element model of the air ring bearings, the multibody model of the rotor and the coupled rotor/bearing co-simulation model are introduced in Section 3. Run-up simulations with the nonlinear rotor/bearing co-simulation model are arranged in Section 4. Varying different system parameters, the vibration and bifurcation phenomena occurring in typical high-speed rotor systems are analyzed and examined in detail. An Eigenfrequency analysis of the linearized rotor/bearing system is presented in the Appendix.

2. Basic dynamical effects occurring in rotor systems with air ring bearings

In Section 2.1, the concept and the basic design variants of air ring bearings are shortly discussed. Rotors supported in air ring bearings exhibit an interesting and rather complex nonlinear vibration behavior. The dynamical effects and the basic bifurcation scenarios of high-speed rotors supported in air ring bearings are briefly recapitulated in Section 2.2.

2.1. Design of air ring bearings

Air ring bearings consist of a rigid ring, which is mounted in the housing using a foil structure [37], an elastomer [35,38,39], springs [40] or a flexible membrane [36]. Air ring bearings with a foil structure may be designed in different ways, e.g. using a beam- or a bump-foil construction. The supporting structure provides the necessary external friction/damping so that the amplitudes of the air film induced self-excited vibrations will show moderate and technically tolerable amplitudes. Applying a foil structure (see Fig. 1a), dissipation is primarily generated by dry friction. Using an elastomer (see Fig. 1b), dissipation is mainly produced by viscous damping effects. It should be pointed out that the physical type of dissipation may have a notable influence on the dynamical behavior of the rotor/bearing system. In this manuscript, the inner surface of the ring has a three-lobe geometry. The rigid ring has four degrees of freedom; translation in axial direction as well as rotation around the ring axis is assumed to be prevented. Hence, the ring is able to perform planar translations (translation in x- and y-direction) and the ring may tilt around the two axes perpendicular to the ring axis (tilting around the x- and y-axis).

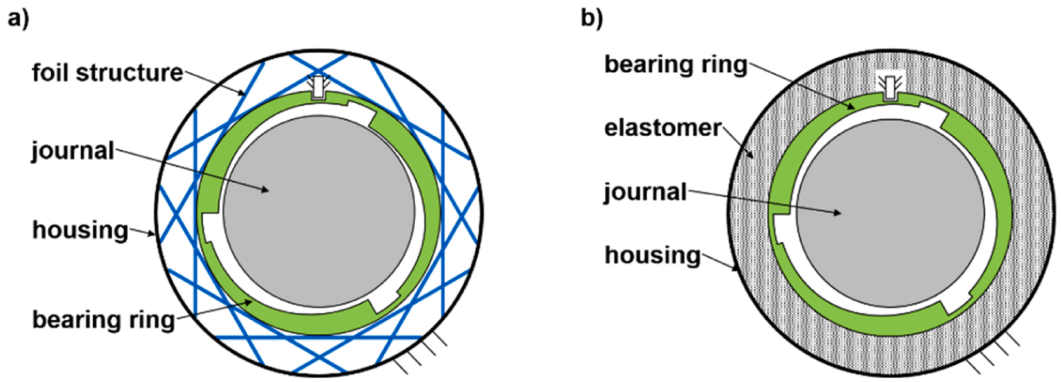

Fig. 1. Design variants of air ring bearings: (a) ring mounted with a foil structure and (b) ring mounted with an elastomer (visco-elastic mounting).

2.2. Bifurcation behavior of typical high-speed rotor systems with air ring bearings (Ring tilting neglected)

High-speed rotors supported in fluid film bearings often exhibit an interesting and complex nonlinear oscillation behavior, which may frequently be traced back to the highly nonlinear stiffness and damping behavior of the fluid films [41–43]. To analyze simple rotor systems, analytical or semi-analytical methods can be applied [44–46]. For more complex systems, transient run-up simulations may be carried out with detailed nonlinear rotor/bearing models in order to examine the rotor vibrations. Numerical and experimental investigations on the nonlinear behavior of rotors supported in air foil bearings are, for instance, discussed in [47–49].

Rotor systems with air ring bearings also show a highly nonlinear vibration and bifurcation behavior. The dynamics of typical high-speed rotor systems supported with three-lobe air ring bearings has been analyzed in [37]. In [37], however, a planar bearing model has been used, i.e. ring tilting has been neglected. It is shown in Section 4 that the occurrence of the three characteristic bifurcation paths will remain unchanged if ring tilting is taken into account. Therefore, we briefly summarize the three basic bifurcation paths, which are typically observed during a rotor run-up (run-down) of rotor systems with air ring bearings. These three characteristic bifurcation scenarios are called *bifurcation path 1, bifurcation path 2a,* and *bifurcation path 2b* here and are shortly explained next.

2.2.1. Bifurcation path 1

A run-up spectrum of bifurcation path 1 can typically be divided into three sections, see Fig. 2a.

I) For low rotor speeds, imbalance vibrations around a stable equilibrium position are observed (neglecting imbalance, the rotor rotates in a stable equilibrium position).
II) Increasing the rotor speed, the equilibrium position becomes unstable and self-excited whirl/whip vibrations are observed. The instability is initiated by the lower loaded turbine-sided bearing. The whirl generated by the turbine-sided bearing excites a conical forward mode with a vibration node close to the compressor-sided bearing. The compressor-sided bearing creates a whirl motion, which excites a conical forward mode with a vibration node close to the turbine-sided bearing. Hence, self-excited vibrations with two whirl frequencies are observed (quasiperiodic motion).
III) Increasing the rotor speed further, a second bifurcation may be observed, namely a synchronization effect where both whirl motions synchronize. In the synchronized state, the compressor- and turbine-sided whirl are both exciting the same rotor mode, namely a cylindrical forward mode. In the synchronized state, the bearing eccentricities are very large so that a technically safe operation of the rotor system will most likely be impossible. The unstable whirl/whip region cannot be driven-through.

The run-up spectrum depicted in Fig. 2a is representative for a rather symmetrical rotor, where the center of mass is close to the

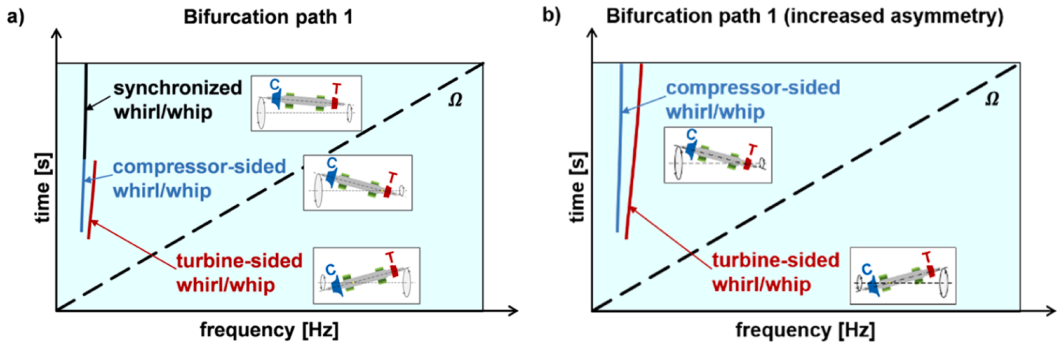

Fig. 2. Typical run-up spectra for bifurcation path 1: (a) almost symmetrical rotor and (b) rotor with increased asymmetry.

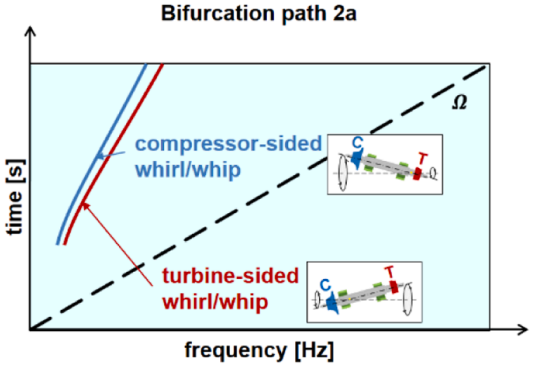

Fig. 3. Typical run-up spectrum for bifurcation path 2a.

middle of the two bearings. For rotor systems with an increased asymmetry, the whirl/whip synchronization between the left and right bearing may be omitted, see Fig. 2b. However, rotor amplitudes and bearing eccentricities remain usually still too large for a secure operation.

To avoid the dangerous bifurcation path 1, the stiffness of the supporting structure should be reduced and the friction/damping force (dissipation) increased.

2.2.2. *Bifurcation path 2a*

A typical frequency spectrum of bifurcation path 2a shows two characteristic domains, see Fig. 3.

I) In the lower speed region, imbalance oscillations around a stable equilibrium position are detected.
II) After the threshold speed of instability is reached, the rotor gets unstable and bifurcates into a quasiperiodic rotor motion (self-excited whirl/whip vibrations induced by the two fluid films). Compared to bifurcation path 1, the bearing eccentricities remain, however, moderate so that a technically safe operation is possible in the whirl/whip regime. Increasing the rotor speed, the whirl/whip amplitudes continuously decrease so that the instability may even be passed through.

2.2.3. *Bifurcation path 2b*

A characteristic run-up spectrum of bifurcation path 2b for the case that the rings are mounted in the housing by a foil structure is sketched in Fig. 4a. Three different sections can be distinguished.

I) Firstly, a stable equilibrium position is detected.
II) Reaching the threshold speed of instability, the rotor system gets unstable and bifurcates into a stable quasiperiodic rotor motion, where the whirls/whips of the two air films are exciting the two conical rigid body modes. Increasing the rotor speed, the bearing eccentricities decrease and the whirls may even disappear.
III) Increasing the rotor speed even more, a further bifurcation occurs. The frequency of the turbine-sided whirl shows a jump and the turbine-sided whirl is now exciting a ring mode. The bearing eccentricities of the turbine-sided bearing become very large so that a safe operation will be very problematic in this state.

If an elastomer is used to mount to the ring in the housing, slightly different bifurcation diagrams may be observed in connection with bifurcation path 2b, see Fig. 4b. Here, a direct bifurcation from the equilibrium position into the ring mode region may be detected, where both the turbine- and the compressor-sided whirl will excite ring modes (see [37] for further details).

To avoid the dangerous bifurcation path 2b, where ring modes are excited by the air whirls, the mounting stiffness of the rings should be increased, the friction/damping increased and the ring mass reduced.

3. Rotor/Bearing model

The nonlinear rotor/bearing model used for the run-up simulations in Section 4 is introduced in this section. The finite element model for the air film is presented in Section 3.1. In Section 3.2, the multibody model for the rotor is explained. The multibody rotor model is coupled with the two finite element bearing models of the fluid films by a co-simulation approach, which is described in Section 3.3. An Eigenmode analysis of the linearized rotor/bearing system is collected in the Appendix.

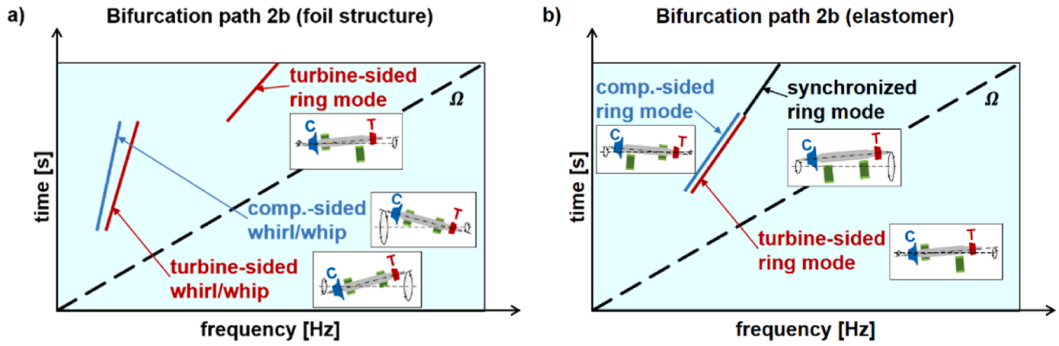

Fig. 4. Typical run-up spectra for bifurcation path 2b: (a) ring mounted with a foil structure and (b) ring mounted with an elastomer (visco-elastic mounting).

3.1. Finite element model of the air film

3.1.1. Hydrodynamic bearing forces and torques

Firstly, the geometry of the air gap between the rotor journal and the bushing ring is considered, whereby 3D ring tilting effects are fully taken into account. Also, some basic kinematical quantities are derived, which describe the relative motion of the rotor journal with respect to the ring. Secondly, the air gap function is incorporated into the compressible Reynolds equation in order to calculate the pressure distribution in the air gap. With the pressure field, the resulting bearing forces and tilting torques are finally determined.

The air gap between the rotor journal and the ring is illustrated in Fig. 5. Note that the inner surface of the here considered ring has a three-lobe bore geometry. The space-fixed x,y-reference system is located in the center O of the bearing housing. We assume that the ring center M_R is able to move in x- and y-direction; translation in z-direction is assumed to be prevented. Furthermore, it is assumed that the ring may rotate about the x- and y-axis (ring tilting motion); rotation about the z_R-axis is assumed to be prevented. Hence, the ring has two translational and two rotational degrees of freedom.

In a first step, we analyze the relative translation of the rotor journal with respect to the ring in the middle plane of the bearing ($z = 0$). The vector $\boldsymbol{r}_R = [x_R, y_R, 0]^T$ denotes the position vector of the ring center M_R with respect to the reference system. The vector $\boldsymbol{r}_J = [x_J, y_J, 0]^T$ describes the vector of the rotor journal M_J with respect to the reference system. The relative displacement vector of M_J with respect to M_R is characterized by $\Delta\boldsymbol{r} = \boldsymbol{r}_J - \boldsymbol{r}_R = [\Delta x, \Delta y, 0]^T$; the relative velocity of M_J with respect to M_R is represented by $\Delta\dot{\boldsymbol{r}} = \frac{\mathrm{d}}{\mathrm{d}t}\Delta\boldsymbol{r}$.

To describe the relative displacement of M_J with respect to M_R, the ring-fixed polar coordinates $\Delta r = |\Delta\boldsymbol{r}|$ and δ may be used alternatively to the Cartesian coordinates Δx and Δy. The relationship between $\Delta\boldsymbol{r}$, $\Delta\dot{\boldsymbol{r}}$ and the polar coordinates Δr, δ, $\Delta\dot{r}$, $\dot{\delta}$ is given by

$$\begin{aligned} \Delta r &= |\Delta\boldsymbol{r}| \ , & \delta &= \operatorname{atan2}(\Delta y, \Delta x) - \alpha \ , \\ \Delta\dot{r} &= \frac{1}{\Delta r}(\Delta\boldsymbol{r}\cdot\Delta\dot{\boldsymbol{r}}) \ , & \dot{\delta} &= \frac{1}{\Delta r^2}(\Delta x\ \Delta\dot{y} - \Delta y\ \Delta\dot{x}) \ . \end{aligned} \tag{1}$$

Note that the orientation of the ring with respect to the housing is defined by the constant angle α. The angle φ_t characterizes the lobe region. The three pockets for air supply, where ambient pressure p_a is assumed, have the circumferential extension $\frac{2\pi}{3} - \varphi_t$. The nominal radial clearance of the three-lobe bearing is denoted by C; the step height between the pocket and the lobe region is termed by ΔH. Furthermore, the auxiliary angular coordinate φ is defined, which is required for calculating the pressure distribution in the air gap with the help of the Reynolds equation.

In a second step, tilting (rotation) of the rotor journal with respect to the ring-fixed x_R,y_R,z_R-system is analyzed. Here, the relative orientation of the rotor journal with respect to the ring is described with the help of relative Bryant angles. The first relative Bryant angles is denoted by α_{tilt} and describes the tilting of the journal about the journal-fixed x_J-axis. The second relative Bryant angle is termed by β_{tilt} and characterizes the journal tilting about the journal-fixed y_J-axis. To derive the gap function of the air film, the third relative Bryant angle is not required. Note that the third relative Bryant angle describes the relative rotation of the rotor journal about the z_J-axis; its time derivative is almost identical with the rotor speed Ω, since $\alpha_{\text{tilt}},\ \beta_{\text{tilt}} \ll 1$. It should be stressed that the ring-fixed x_R, y_R,z_R-system and the journal-fixed x_J,y_J,z_J-system coincide in the initial position (centered position without misalignment).

The rotation matrix, which describes the tilting of the rotor journal with respect to the ring, can be expressed with the help of the two tilting angles according to

$$\boldsymbol{R} = \begin{pmatrix} \cos\beta_{\text{tilt}} & 0 & \sin\beta_{\text{tilt}} \\ \sin\alpha_{\text{tilt}}\sin\beta_{\text{tilt}} & \cos\alpha_{\text{tilt}} & -\sin\alpha_{\text{tilt}}\cos\beta_{\text{tilt}} \\ -\cos\alpha_{\text{tilt}}\sin\beta_{\text{tilt}} & \sin\alpha_{\text{tilt}} & \cos\alpha_{\text{tilt}}\cos\beta_{\text{tilt}} \end{pmatrix} . \tag{2}$$

The additional change of the gap function due to tilting is a function of the distance z_R from the middle plane of the bearing and can be expressed with the subsequent displacement vector

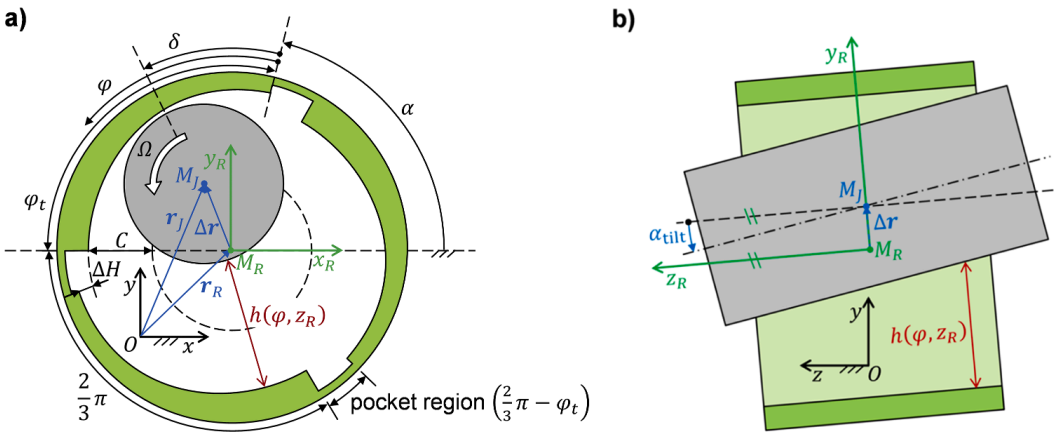

Fig. 5. Three-lobe air ring bearing geometry: (a) front view and (b) side view.

$$\Delta \boldsymbol{r}_{\text{tilt}} = \begin{pmatrix} \Delta x_{\text{tilt}} \\ \Delta y_{\text{tilt}} \\ \Delta z_{\text{tilt}} \end{pmatrix} = \boldsymbol{R} \cdot \begin{pmatrix} 0 \\ 0 \\ z_R \end{pmatrix} = z_R \cdot \begin{pmatrix} \sin \beta_{\text{tilt}} \\ -\sin \alpha_{\text{tilt}} \cos \beta_{\text{tilt}} \\ \cos \alpha_{\text{tilt}} \cos \beta_{\text{tilt}} \end{pmatrix} . \tag{3}$$

Instead of using the cartesian coordinates Δx_{tilt} and Δy_{tilt}, again polar coordinates can be used. The relationship between Δx_{tilt}, Δy_{tilt}, $\Delta \dot{x}_{\text{tilt}}$, $\Delta \dot{y}_{\text{tilt}}$ and the polar coordinates Δr_{tilt}, δ_{tilt}, $\Delta \dot{r}_{\text{tilt}}$, $\dot{\delta}_{\text{tilt}}$ is given by

$$\begin{aligned} \Delta r_{\text{tilt}} &= \sqrt{\Delta x_{\text{tilt}}^2 + \Delta y_{\text{tilt}}^2} , \\ \delta_{\text{tilt}} &= \operatorname{atan2}(\Delta y_{\text{tilt}}, \Delta x_{\text{tilt}}) - \alpha , \\ \Delta \dot{r}_{\text{tilt}} &= \frac{1}{\Delta r_{\text{tilt}}} (\Delta x_{\text{tilt}} \Delta \dot{x}_{\text{tilt}} + \Delta y_{\text{tilt}} \Delta \dot{y}_{\text{tilt}}) , \\ \dot{\delta}_{\text{tilt}} &= \frac{1}{\Delta r^2} (\Delta x_{\text{tilt}} \Delta \dot{y}_{\text{tilt}} - \Delta y_{\text{tilt}} \Delta \dot{x}_{\text{tilt}}) . \end{aligned} \tag{4}$$

With Eq. (1) and Eq. (4), the gap function of the air film can be expressed as

$$h(\varphi, z_R) = C - \Delta r \cdot \cos(\varphi - \delta) - \Delta r_{\text{tilt}} \cdot \cos(\varphi - \delta_{\text{tilt}}) + \Delta H \cdot \left(1 + \frac{2\pi}{3\varphi_t} \left\lfloor \frac{3\varphi}{2\pi} \right\rfloor - \frac{\varphi}{\varphi_t}\right), \quad \varphi \in S_{\text{lobe}} , \tag{5}$$

where $\lfloor \ldots \rfloor$ terms the floor function.

The pressure distribution in the air gap is calculated with the isothermal compressible Reynolds equation [50,51], which reads

$$\frac{1}{r^2} \frac{\partial}{\partial \varphi} \left(\frac{\rho h^3}{\eta} \frac{\partial p}{\partial \varphi} \right) + \frac{\partial}{\partial z_R} \left(\frac{\rho h^3}{\eta} \frac{\partial p}{\partial z_R} \right) = 6\Omega_J \frac{\partial (\rho h)}{\partial \varphi} + 12 \frac{\partial (\rho h)}{\partial t} . \tag{6}$$

In the above equation, $p(\varphi, z_R, t)$ terms the pressure field and $\rho(\varphi, z_R, t)$ the density field. r denotes the radius of the journal and $h(\varphi, z_R, t)$ the gap function (including tilting effects). η represents the dynamic viscosity of the fluid. Ω_J is the z_R-component of the relative angular velocity of the rotor journal with respect to the ring. Note that Ω_J is almost identical with the rotor speed Ω, which is the z-component of the absolute angular velocity of the rotor journal with respect to space-fixed x,y,z-reference system, since α_{tilt}, $\beta_{\text{tilt}} \ll 1$. φ represents the circumferential and z_R the axial coordinate, see Fig. 5. Here, air is treated as an ideal gas. Within an isothermal approach, the relationship between pressure and density is given by $\rho = \frac{1}{R_{\text{air}} T_{\text{air}}} p$ (R_{air} is the specific gas constant of air; T_{air} is the prescribed constant temperature of the air film). With these assumptions, Eq. (6) can be written as

$$\frac{1}{r^2} \frac{\partial}{\partial \varphi} \left(p h^3 \frac{\partial p}{\partial \varphi} \right) + \frac{\partial}{\partial z_R} \left(p h^3 \frac{\partial p}{\partial z_R} \right) = 6\Omega\eta \frac{\partial (ph)}{\partial \varphi} + 12\eta \frac{\partial (ph)}{\partial t} . \tag{7}$$

Pressure is only generated in the lobe regions $S_{\text{lobe}} = \left\{ [0, \varphi_t], \left[\frac{2\pi}{3}, \frac{2\pi}{3} + \varphi_t\right], \left[\frac{4\pi}{3}, \frac{4\pi}{3} + \varphi_t\right] \right\}$. The depth of the pockets is supposed to be large enough so that ambient pressure p_a may be assumed in the pocket regions.

In Fig. 6, the boundary conditions for the Reynolds equation are illustrated: the Dirichlet boundary condition $p = p_a$ is applied at all boundaries. Note that b represents the bearing width.

A finite element approach is used to discretize the Reynolds Eq. (7). Hence, the time dependent pressure field $p(\varphi, z_R, t)$ is approximated by the ansatz $\widetilde{p}_i(\varphi, z_R, t) = \sum_{i=1}^{n_k} N_i(\varphi, z_R) p_i(t)$. Herein, $N_i(\varphi, z_R)$ are the ansatz functions, which depend on the chosen element type and $p_i(t)$ the pressure variables at the finite element nodes. The number of finite element nodes (degrees of freedom) is

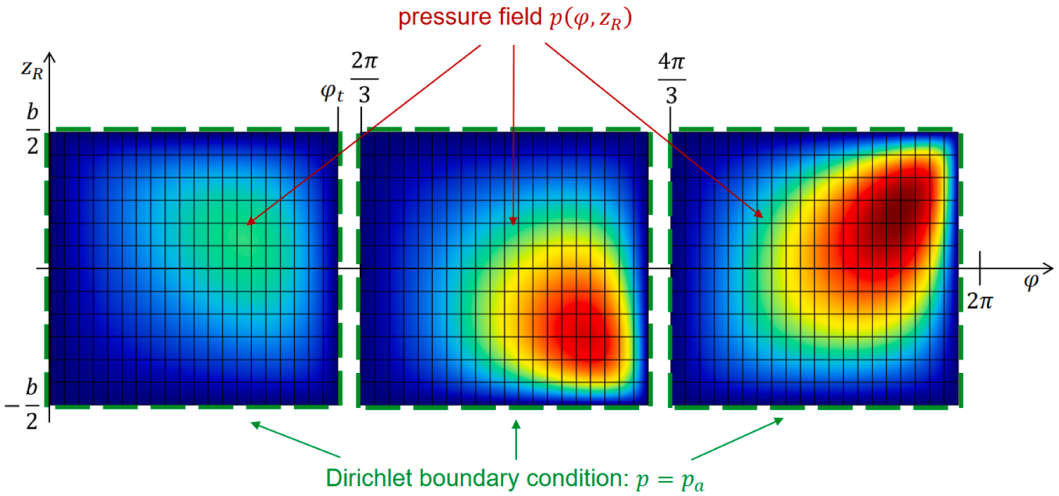

Fig. 6. Boundary conditions for the Reynolds equation.

denoted by n_k. In this work, the bearing is discretized by 720 finite elements (quadratic ansatz functions) resulting in $n_k = 3075$ pressure degrees of freedom. The discretized Reynolds equation represents a nonlinear system of ordinary differential equations (ODE system) for the pressure variables $p_i(t)$ at the nodes of the finite element mesh, which are arranged in the resultant vector $\boldsymbol{p} = [p_1, \ldots, p_{n_k}]^T$. Formally, the first order ODE system for the unknown pressure variables can be written in implicit form according to

$$\boldsymbol{f}(\boldsymbol{p}, \dot{\boldsymbol{p}}, t) = \boldsymbol{0} \ . \tag{8}$$

The nonlinear ODE system (8) is numerically integrated with an implicit time integration scheme. Here, a BDF integrator (backward differentiation formula) with variable integration order and variable step size is applied [52]. The following solver settings and error tolerances have been used for the time integration: absolute error tolerance $\varepsilon_{\text{abs,FEM}} = 1E-6$, relative error tolerance $\varepsilon_{\text{rel,FEM}} = 1E-6$, maximum integration step size $h_{\text{max,FEM}} = 1E-6$. For solving the nonlinear algebraic system of equations within the corrector iteration, the undamped Newton method is used (direct linear solver: MUMPS; maximum number of iterations: 5).

After each time integration step, the components $F_{p,x_R}(t)$ and $F_{p,y_R}(t)$ of the resulting bearing force generated by the pressure field $p(\varphi, z_R)$ are calculated by integrating the pressure over the bearing surface, i.e.

$$\boldsymbol{F}_p = \begin{bmatrix} F_{p,x_R} \\ F_{p,y_R} \end{bmatrix} = \int_0^{2\pi} \int_{-\frac{b}{2}}^{\frac{b}{2}} p(\varphi, z_R) \cdot r \cdot \begin{bmatrix} \cos(\varphi + \alpha) \\ \sin(\varphi + \alpha) \end{bmatrix} \mathrm{d}z_R \ \mathrm{d}\varphi \ . \tag{9}$$

Note that F_{p,x_R} and F_{p,y_R} in Eq. (9) represent the force components acting at the ring expressed in the ring-fixed x_R,y_R,z_R-system. The components of the resulting tilting torque are given by

$$\boldsymbol{M}_p = \begin{bmatrix} M_{p,x_R} \\ M_{p,y_R} \end{bmatrix} = \int_0^{2\pi} \int_{-\frac{b}{2}}^{\frac{b}{2}} z_R \cdot p(\varphi, z_R) \cdot r \cdot \begin{bmatrix} -\sin(\varphi + \alpha) \\ \cos(\varphi + \alpha) \end{bmatrix} \mathrm{d}z_R \ \mathrm{d}\varphi \ . \tag{10}$$

Besides the pressure, also shear stresses are acting at the inner ring surface. To calculate the shear stresses, the additional coordinate $r_{\text{gap}} \in [0, h]$ is introduced to define the height in the air gap ($r_{\text{gap}} = 0$ corresponds to the rotor surface). The velocity component u_φ of the fluid in circumferential φ-direction is given by

$$u_\varphi(\varphi, z_R, r_{\text{gap}}) = \frac{1}{2\eta r} \cdot \frac{\partial p(\varphi, z_R)}{\partial \varphi} \cdot \left(r_{\text{gap}}^2 - h r_{\text{gap}} \right) + r\Omega \cdot \left(1 - \frac{r_{\text{gap}}}{h} \right) \ . \tag{11}$$

Hence, the shear stress distribution in circumferential direction at the inner ring surface is given by

$$\tau(\varphi, z_R) = \eta \cdot \left. \frac{\partial u_\varphi(\varphi, z_R, r_{\text{gap}})}{\partial r_{\text{gap}}} \right|_{r_{\text{gap}} = h} = \eta \cdot \left(\frac{h}{2\eta r} \cdot \frac{\partial p(\varphi, z_R)}{\partial \varphi} - \frac{r\Omega}{h} \right) \ . \tag{12}$$

The components $F_{\tau,x_R}(t)$ and $F_{\tau,y_R}(t)$ of the resulting bearing force produced by the shear stress field $\tau(\varphi, z_R)$ are computed by

$$\boldsymbol{F}_\tau = \begin{bmatrix} F_{\tau,x_R} \\ F_{\tau,y_R} \end{bmatrix} = \int_0^{2\pi} \int_{-\frac{b}{2}}^{\frac{b}{2}} \tau(\varphi, z_R) \cdot r \cdot \begin{bmatrix} \sin(\varphi + \alpha) \\ -\cos(\varphi + \alpha) \end{bmatrix} \mathrm{d}z_R \ \mathrm{d}\varphi \ . \tag{13}$$

The components of the resulting tilting torque generated by the shear stress distribution $\tau(\varphi, z_R)$ read

$$\boldsymbol{M}_\tau = \begin{bmatrix} M_{\tau,x_R} \\ M_{\tau,y_R} \end{bmatrix} = \int_0^{2\pi} \int_{-\frac{b}{2}}^{\frac{b}{2}} z_R \cdot \tau(\varphi, z_R) \cdot r \cdot \begin{bmatrix} \cos(\varphi + \alpha) \\ \sin(\varphi + \alpha) \end{bmatrix} \mathrm{d}z_R \ \mathrm{d}\varphi \ . \tag{14}$$

It should be stressed again that $F_{\tau,x_R}(t)$, $F_{\tau,y_R}(t)$, $M_{\tau,x_R}(t)$ and $M_{\tau,y_R}(t)$ represent resulting force and torque components acting at the ring expressed in the ring-fixed x_R,y_R,z_R-system.

3.1.2. Extension of the bearing model: mixed lubrication

In situations, where the bearing eccentricities are large – and especially in cases where the journal is tilted with respect to the ring – contact may occur between the ring and the journal, see Fig. 7. In such cases, the mere hydrodynamic approach described above for calculating the forces between ring and journal on the basis of the compressible Reynolds equation will not be sufficient, since mixed lubrication effects may occur between ring and journal. Here, a very straightforward approach is used to incorporate mixed lubrication into the bearing model for the air gap. If the gap function $h(\varphi, z_R, t)$ according to Eq. (5) is smaller than a user-defined value h_{con} (e.g. $h_{\text{con}} = 1.2\ \mu\text{m}$), mixed lubrication is assumed to occur [51,53,54].

Assuming that the journal surface as well as the inner ring surface are ideally smooth (i.e. no surface roughness), the gap height $h(\varphi, z_R, t)$ of the air film can exactly be calculated with the help of the actual relative displacement vector $\Delta\boldsymbol{r} = [\Delta x, \Delta y]^T$ and the relative tilting angles α_{tilt}, β_{tilt} according to Eq. (5). Now, two cases have to be distinguished:

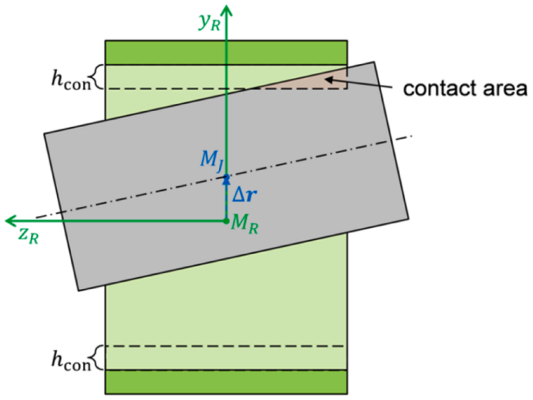

Fig. 7. Mixed lubrication: illustration of the contact area for a tilted journal.

i) If the gap function $h(\varphi, z_R, t)$ is locally larger than the user-defined value h_{con}, mixed lubrication does not occur at this gap point.
ii) If the gap function $h(\varphi, z_R, t)$ is locally smaller than h_{con}, mixed lubrication is assumed to occur at this gap point.

It is important to mention that in both cases ($h(\varphi, z_R, t) > h_{con}$ and $h(\varphi, z_R, t) \leq h_{con}$), the classical Reynolds Eq. (6) is used to calculate the hydrodynamic pressure field. The only difference between two cases is that in the points where $h(\varphi, z_R, t) \leq h_{con}$, additional contact forces at the journal and the ring are superimposed to the pure hydrodynamic forces resulting from the Reynolds equation. Hence, for solving the Reynolds Eq. (6), no distinction between the full hydrodynamic lubrication regime and the mixed lubrication regime is made; the Reynolds Eq. (6) is in both cases solved with the current gap function $h(\varphi, z_R, t)$. Therefore, the resulting forces acting at journal and rotor are calculated in the following way:

i) In the gap regions where $h(\varphi, z_R, t) > h_{con}$ (full hydrodynamic lubrication regime), the classical Reynolds Eq. (6) is used to calculate the hydrodynamic pressure and shear stress as well as the corresponding resultant bearing forces and torques according to Eqs. (9)-(14). Additional contact forces due to mixed friction are not considered.
ii) In the gap regions where $h(\varphi, z_R, t) \leq h_{con}$ (mixed lubrication regime), also the classical Reynolds Eq. (6) is used to compute the hydrodynamic pressure and shear stress and thereby the resultant forces and torques with the help of Eqs. (9)-(14). However, additional contact forces are superimposed at the gap points where $h(\varphi, z_R, t) \leq h_{con}$, which represent the asperity contact forces of the two contacting surfaces.

The here applied mechanical model for the asperity contact considers both normal forces (contact pressure) as well as tangential forces due to dry friction. The normal contact forces are represented by a penalty approach, which takes into account stiffness forces (defined by a penalty stiffness parameter) as well as damping forces (represented by a nonlinear penalty damping approach). The penetration depth δ_{pen} in the areas with mixed lubrication is defined by

$$\delta_{pen}(\varphi, z_R) = \max(h_{con} - h(\varphi, z_R),\ 0)\ . \tag{15}$$

Throughout this paper, h_{con} is set to $h_{con} = 1.2\ \mu$m. The contact pressure p_{con} in normal direction is calculated with the help of the contact stiffness parameter c_{con} (user-defined value) and the contact damping function $d_{con}(\delta_{pen})$ according to

$$p_{con}(\varphi, z_R) = \max\left(c_{con} \cdot \delta_{pen}(\varphi, z_R) - d_{con}\left(\delta_{pen}(\varphi, z_R)\right) \cdot \frac{\mathrm{d}}{\mathrm{d}t} h(\varphi, z_R),\ 0\right)\ . \tag{16}$$

The nonlinear contact damping function $d_{con}(\delta_{pen})$ is defined by

$$d_{con}\left(\delta_{pen}\right) = \begin{cases} d_{max}\left(\frac{6}{\delta_{step}^5} \cdot \delta_{pen}^5 - \frac{15}{\delta_{step}^4} \cdot \delta_{pen}^4 + \frac{10}{\delta_{step}^3} \cdot \delta_{pen}^3\right), & \delta_{pen} \leq \delta_{step} \\ d_{max}, & \delta_{pen} > \delta_{step} \end{cases}\ . \tag{17}$$

In this work, c_{con} has been set to $1E+7$ N mm^{-3} and δ_{step} to 0.24 μm. Note that the damping coefficient d_{con} is a function of the penetration depth δ_{pen} in order to avoid overdamping at the onset of the contact [55]. In the region $\delta_{pen} \leq \delta_{step}$, the damping coefficient is successively increased according to Eq. (17). For $\delta_{pen} > \delta_{step}$, the maximum damping coefficient d_{max} is used (d_{max} is a user-defined value and has been set to $1E+4$ N ms mm^{-3}).

Also, friction forces acting in circumferential direction at the inner ring surface are considered in the mixed lubrication area. Therefore, a tangential contact stress distribution $\tau_{con}(\varphi, z_R)$ is used, which is calculated by multiplying the contact pressure function with the friction coefficient μ, i.e.

$$\tau_{con}(\varphi, z_R) = \mathrm{step}_{SL}(v_{tan}(\varphi, z_R)) \cdot \mu \cdot p_{con}(\varphi, z_R), \tag{18}$$

where v_{tan} denotes the relative velocity between journal and ring in circumferential direction given by

$$v_{\mathrm{tan}}(\varphi, z_R) = r \cdot \Omega - (\Delta\dot{x} + \Delta\dot{x}_{\mathrm{tilt}}) \cdot \sin(\varphi + \alpha) + (\Delta\dot{y} + \Delta\dot{y}_{\mathrm{tilt}}) \cdot \cos(\varphi + \alpha) \ . \tag{19}$$

The smoothed signum function $\mathrm{step}_{SL}(v_{\mathrm{tan}})$ according to

$$\mathrm{step}_{SL}(v_{\mathrm{tan}}) = \begin{cases} -1, & v_{\mathrm{tan}} < -\dfrac{v_{\mathrm{step}}}{2} \\ 1, & v_{\mathrm{tan}} > \dfrac{v_{\mathrm{step}}}{2} \\ \dfrac{96}{8v_{\mathrm{step}}^5} \cdot v_{\mathrm{tan}}^5 - \dfrac{40}{4v_{\mathrm{step}}^3} \cdot v_{\mathrm{tan}}^3 + \dfrac{30}{8v_{\mathrm{step}}} \cdot v_{\mathrm{tan}}, & \text{else} \end{cases} \tag{20}$$

is used so that possible stick/slip-effects may also be considered. For the simulations, the friction coefficient μ has been set to 0.1; the parameter v_{step} has been set to $1E-6$ m s^{-1}. By integrating the contact pressure $p_{\mathrm{con}}(\varphi, z_R)$ and the tangential contact stress $\tau_{\mathrm{con}}(\varphi, z_R)$ over the inner ring surface, the resulting contact forces and torques acting at the ring can be calculated. The resulting contact forces resulting from the normal contact pressure $p_{\mathrm{con}}(\varphi, z_R)$ read

$$\boldsymbol{F}_{\mathrm{con},N} = \begin{bmatrix} F_{\mathrm{con},N,x_R} \\ F_{\mathrm{con},N,y_R} \end{bmatrix} = \int_0^{2\pi} \int_{-\frac{b}{2}}^{\frac{b}{2}} p_{\mathrm{con}}(\varphi, z_R) \cdot r \cdot \begin{bmatrix} \cos(\varphi + \alpha) \\ \sin(\varphi + \alpha) \end{bmatrix} \mathrm{d}z_R \ \mathrm{d}\varphi \ . \tag{21}$$

The resulting contact forces generated by the tangential contact stress $\tau_{\mathrm{con}}(\varphi, z_R)$ are computed by

$$\boldsymbol{F}_{\mathrm{con},T} = \begin{bmatrix} F_{\mathrm{con},T,x_R} \\ F_{\mathrm{con},T,y_R} \end{bmatrix} = \int_0^{2\pi} \int_{-\frac{b}{2}}^{\frac{b}{2}} \tau_{\mathrm{con}}(\varphi, z_R) \cdot r \cdot \begin{bmatrix} -\sin(\varphi + \alpha) \\ \cos(\varphi + \alpha) \end{bmatrix} \mathrm{d}z_R \ \mathrm{d}\varphi \ . \tag{22}$$

The corresponding torques are given by

$$\boldsymbol{M}_{\mathrm{con},N} = \begin{bmatrix} M_{\mathrm{con},N,x_R} \\ M_{\mathrm{con},N,y_R} \end{bmatrix} = \int_0^{2\pi} \int_{-\frac{b}{2}}^{\frac{b}{2}} z_R \cdot p_{\mathrm{con}}(\varphi, z_R) \cdot r \cdot \begin{bmatrix} -\sin(\varphi + \alpha) \\ \cos(\varphi + \alpha) \end{bmatrix} \mathrm{d}z_R \ \mathrm{d}\varphi \tag{23}$$

and

$$\boldsymbol{M}_{\mathrm{con},T} = \begin{bmatrix} M_{\mathrm{con},T,x_R} \\ M_{\mathrm{con},T,y_R} \end{bmatrix} = \int_0^{2\pi} \int_{-\frac{b}{2}}^{\frac{b}{2}} z_R \cdot \tau_{\mathrm{con}}(\varphi, z_R) \cdot r \cdot \begin{bmatrix} -\cos(\varphi + \alpha) \\ -\sin(\varphi + \alpha) \end{bmatrix} \mathrm{d}z_R \ \mathrm{d}\varphi \ . \tag{24}$$

Note that the above forces and torques are calculated with respect to the ring-fixed x_R,y_R,z_R-system.

3.1.3. Resulting bearing forces and torques for the mixed lubrication problem

The resulting force and torque acting on the ring can finally be calculated by superimposing the hydrodynamic forces/torques and the contact forces/torques, which gives

$$\boldsymbol{F}_{\mathrm{res}} = \boldsymbol{F}_p + \boldsymbol{F}_\tau + \boldsymbol{F}_{\mathrm{con},N} + \boldsymbol{F}_{\mathrm{con},T} \tag{25}$$

and

$$\boldsymbol{M}_{\mathrm{res}} = \boldsymbol{M}_p + \boldsymbol{M}_\tau + \boldsymbol{M}_{\mathrm{con},N} + \boldsymbol{M}_{\mathrm{con},T} \ . \tag{26}$$

The resultant bearing force and tilting torque define the output variables of the finite element subsystem. They are collected in the output vector $[\boldsymbol{F}_{\mathrm{res}}^T, \boldsymbol{M}_{\mathrm{res}}^T]^T$. The input variables for the finite element subsystem are the angular velocity Ω, the kinematical quantities $\Delta\boldsymbol{r} = [\Delta x, \Delta y]^T$ and $\Delta\dot{\boldsymbol{r}} = [\Delta\dot{x}, \Delta\dot{y}]^T$ as well as the tilting angles α_{tilt}, β_{tilt} and their time derivatives $\dot{\alpha}_{\mathrm{tilt}}$, $\dot{\beta}_{\mathrm{tilt}}$. These quantities describe the relative motion of the rotor journal with respect to the ring.

The here considered rotor/bearing system is supported in two bearings. Consequently, two output vectors have to be defined, i.e. $\boldsymbol{y}_{\mathrm{FEM1}} = [\boldsymbol{F}_{\mathrm{res1}}^T, \boldsymbol{M}_{\mathrm{res1}}^T]^T$ and $\boldsymbol{y}_{\mathrm{FEM2}} = [\boldsymbol{F}_{\mathrm{res2}}^T, \boldsymbol{M}_{\mathrm{res2}}^T]^T$. They are arranged in the resulting output vector $\boldsymbol{y}_{\mathrm{FEM}} = [\boldsymbol{y}_{\mathrm{FEM1}}^T, \boldsymbol{y}_{\mathrm{FEM2}}^T]^T$. The input variables for the two fluid films are given by $\boldsymbol{u}_{\mathrm{FEM1}} = [\Delta\boldsymbol{r}_1^T, \Delta\dot{\boldsymbol{r}}_1^T, \alpha_{\mathrm{tilt1}}, \beta_{\mathrm{tilt1}}, \dot{\alpha}_{\mathrm{tilt1}}, \dot{\beta}_{\mathrm{tilt1}}, \Omega]^T$ and $\boldsymbol{u}_{\mathrm{FEM2}} = [\Delta\boldsymbol{r}_2^T, \Delta\dot{\boldsymbol{r}}_2^T, \alpha_{\mathrm{tilt2}}, \beta_{\mathrm{tilt2}}, \dot{\alpha}_{\mathrm{tilt2}}, \dot{\beta}_{\mathrm{tilt2}}, \Omega]^T$.

Note that the output variables $\boldsymbol{y}_{\mathrm{FEM}}$ of the finite element subsystems serve as input variables $\boldsymbol{u}_{\mathrm{MBS}}$ for the multibody subsystem of the rotor, i.e. $\boldsymbol{u}_{\mathrm{MBS}} = \boldsymbol{y}_{\mathrm{FEM}}$. On the other hand, the input variables for the finite element subsystems are identical with corresponding output variables of the multibody system, i.e. $\boldsymbol{y}_{\mathrm{MBS}} = [\Delta\boldsymbol{r}_1^T, \Delta\dot{\boldsymbol{r}}_1^T, \alpha_{\mathrm{tilt1}}, \beta_{\mathrm{tilt1}}, \dot{\alpha}_{\mathrm{tilt1}}, \dot{\beta}_{\mathrm{tilt1}}, \Delta\boldsymbol{r}_2^T, \Delta\dot{\boldsymbol{r}}_2^T, \alpha_{\mathrm{tilt2}}, \beta_{\mathrm{tilt2}}, \dot{\alpha}_{\mathrm{tilt2}}, \dot{\beta}_{\mathrm{tilt2}}, \Omega]^T$.

It should finally be mentioned that for the considered rotor/bearing system the bearing forces/torques $F_{p,x_R}(t)$, $F_{p,y_R}(t)$, $M_{p,x_R}(t)$, $M_{p,y_R}(t)$ due to pressure and the bearing forces/torques $F_{\mathrm{con,N},x_R}(t)$, $F_{\mathrm{con,N},y_R}(t)$, $M_{\mathrm{con,N},x_R}(t)$, $M_{\mathrm{con,N},y_R}(t)$ resulting from the normal contact stress are usually significantly larger than the bearing forces/torques $F_{\tau,x_R}(t)$, $F_{\tau,y_R}(t)$, $M_{\tau,x_R}(t)$, $M_{\tau,y_R}(t)$ due to shear stress and the bearing forces/torques $F_{\mathrm{con,T},x_R}(t)$, $F_{\mathrm{con,T},y_R}(t)$, $M_{\mathrm{con,T},x_R}(t)$, $M_{\mathrm{con,T},y_R}(t)$ resulting from the tangential contact stress. In a simplified implementation, the bearing force/torque components $F_{\tau,x_R}(t)$, $F_{\tau,y_R}(t)$, $M_{\tau,x_R}(t)$, $M_{\tau,y_R}(t)$, $F_{\mathrm{con,T},x_R}(t)$, $F_{\mathrm{con,T},y_R}(t)$, $M_{\mathrm{con,T},x_R}(t)$ and $M_{\mathrm{con,T},y_R}(t)$ may therefore be neglected.

3.2. Multibody model of the rotor

In this work, a typical high-speed rotor system is considered, which is schematically sketched in Fig. 8. The rotor consists of the rotor shaft, the compressor wheel (center of mass $[0,0,z_C]^T$) and the turbine wheel (center of mass $[0,0,z_T]^T$). The rotor is supported with two air ring bearings. The rings (ring mass m_R) are mounted in the housing with a foil structure or alternatively with an elastomer. The middle planes of the turbine- and compressor-sided bearing are specified by the axial coordinates z_{JT} and z_{JC}.

The shaft radius r of the considered rotor is 15 mm. The first free-free bending eigenfrequency of the entire rotor (shaft including the compressor and turbine wheel) is ≈ 2600 Hz and clearly above the maximum operation speed of 2000 Hz. Therefore, the rotor can be considered as a rigid body. The center of mass of the entire rotor (mass m_{Rotor}, length l_{Rotor}) consisting of the shaft and the two wheels is defined by the axial coordinate z_{Rotor}.

Here, the rotor system is modelled as a multibody system [56,57], which basically consists of three rigid bodies. The first body is the rotor. The axial displacement of the rotor is prevented by the scleronomic constraint equation $z_{\mathrm{Rotor}} = 0$; the angular velocity in z-direction is prescribed by the rheonomic constraint equation $\omega_{\mathrm{Rotor},z} - \Omega(t) = 0$, where $\Omega(t)$ denotes the rotor speed. The second and the third body are the two rings. Translation in axial direction of the rings is prevented by the constraint equations $z_{JT} = 0$ and $z_{JC} = 0$; rotation of the rings about the z-axis is also prevented by corresponding constraint equations. Hence, the multibody subsystem consists of the complete rotor – shaft, wheels, imbalance masses, rings (including the supporting structure) – but does not contain the two air films. The two air films are modelled separately within a finite element environment (two finite element subsystems). The finite element subsystems are coupled with the multibody subsystem of the rotor by means of a co-simulation approach, see Section 3.3.

For the numerical time integration of the multibody subsystem, the equations of motion in the stabilized index-2 formulation are applied [58], namely

$$\begin{aligned} \boldsymbol{M}(t,\boldsymbol{x})\dot{\boldsymbol{x}} &= \boldsymbol{M}(t,\boldsymbol{x})\boldsymbol{v} - \boldsymbol{G}^T(t,\boldsymbol{x})\boldsymbol{\mu}\ , \\ \boldsymbol{M}(t,\boldsymbol{x})\dot{\boldsymbol{v}} &= \boldsymbol{f}_{\mathrm{e}}(t,\boldsymbol{x},\boldsymbol{v},\boldsymbol{u}_{\mathrm{MBS}}) - \boldsymbol{G}^T(t,\boldsymbol{x})\boldsymbol{\lambda}\ , \\ \boldsymbol{0} &= \boldsymbol{g}(t,\boldsymbol{x})\ , \\ \boldsymbol{0} &= \dot{\boldsymbol{g}}(t,\boldsymbol{x},\boldsymbol{v})\ . \end{aligned} \tag{27}$$

The equations of motion are defined by a system of differential-algebraic equations (DAE system). The vector $\boldsymbol{x} = [x_1,\ldots,x_v]^T \in \mathbb{R}^v$ collects the v (generalized) coordinates of the multibody system; the vector $\boldsymbol{v} = [v_1,\ldots,v_v]^T \in \mathbb{R}^v$ contains the (generalized) velocities. Position and velocity coordinates are related by the kinematical differential equations $\dot{\boldsymbol{x}} = \boldsymbol{v}$. Furthermore, $\boldsymbol{M}(t,\boldsymbol{x}) \in \mathbb{R}^{v\times v}$ represents the symmetric and positive definite mass matrix. The vector $\boldsymbol{f}_{\mathrm{e}}(t,\boldsymbol{x},\boldsymbol{v},\boldsymbol{u}_{\mathrm{MBS}})$ collects the externally applied forces/torques as well as the centrifugal and Coriolis forces. The system is constrained by v_c algebraic constraint equations $g_i(t,\boldsymbol{x}) = 0$ $(i = 1,\ldots,v_c)$, which are arranged in the constraint vector $\boldsymbol{g} \in \mathbb{R}^{v_c}$. The term $\boldsymbol{G}^T(t,\boldsymbol{x})\boldsymbol{\lambda}$ denotes the constraint forces/torques, where $\boldsymbol{G} = \frac{\partial \boldsymbol{g}}{\partial \boldsymbol{x}} \in \mathbb{R}^{v_c\times v}$ is the constraint-Jacobian and $\boldsymbol{\lambda} = [\lambda_1,\cdots,\lambda_{v_c}]^T \in \mathbb{R}^{v_c}$ the vector of Lagrange multipliers. In the framework of the stabilized index-2 formulation [58], the constraint equations $\dot{\boldsymbol{g}}(t,\boldsymbol{x},\boldsymbol{v}) = 0$ on velocity level are incorporated by the additional Lagrange multipliers $\boldsymbol{\mu} = [\mu_1,\cdots,\mu_{v_c}]^T \in \mathbb{R}^{v_c}$. $\boldsymbol{u}_{\mathrm{MBS}}(t)$ are the input variables of the multibody system, namely the resulting bearing forces and tilting torques of the

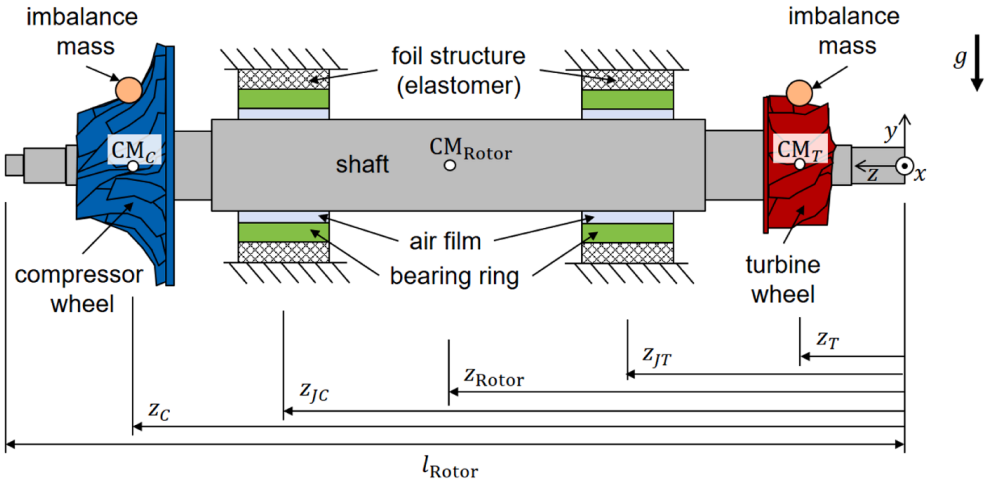

Fig. 8. Sketch of the high-speed rotor/bearing system.

two fluid films.

The equations of motion (27) are discretized with an implicit time integration method. Here, a variable order and variable step size BDF integrator is used [52]. For carrying out the numerical time integration, the subsequent solver parameters have been applied: absolute error tolerance $\varepsilon_{\text{abs,MBS}} = 1E-7$, relative error tolerance $\varepsilon_{\text{rel,MBS}} = 1E-7$, maximum integration step size $h_{\text{max,MBS}} = 1E-7$. The nonlinear algebraic system of equations within the corrector iteration is solved with the undamped Newton method (Jacobian update: at every fourth iteration step; maximum number of corrector iterations: 10; error tolerance for the corrector iteration: $1E-10$).

3.3. Mechanical model for the supporting structure of the ring

As mentioned in Section 2.1, the ring is mounted in the housing either by a foil structure or by an elastomer. In the former case, dissipation is primarily generated by dry friction. In the latter case, visco-elastic effects will provide the necessary dissipation. In practical applications, the friction/damping in the supporting structure has to be chosen in such a way that the amplitudes of the self-excited whirl/whip vibrations are limited to a technically acceptable magnitude.

For the case that the ring is supported by a foil structure, an isotropic, linear-elastic behavior of the supporting structure is assumed; dissipation is modeled by an ideal Coulomb friction approach. As a consequence, the foil structure can be represented by idealized hysteresis curves according to Fig. 9, which depicts the resultant force of the foil structure as a function of the radial displacement of the ring. The force/displacement relationship of the idealized hysteresis is given by

$$\boldsymbol{F} = -c_{\text{foil}}\,\boldsymbol{r}_R - F_{\text{fric}}\,\frac{\dot{\boldsymbol{r}}_R}{\max\left(|\dot{\boldsymbol{r}}_R|, v_{\text{step}}\right)}\,\text{step}(|\dot{\boldsymbol{r}}_R|)\,, \tag{28}$$

where c_{foil} denotes the stiffness coefficient. Coulomb friction is implemented with a regularization approach. Therefore, a smoothed step-function according to

$$\text{step}(|\dot{\boldsymbol{r}}_R|) = \begin{cases} -2\dfrac{|\dot{\boldsymbol{r}}_R|^3}{v_{\text{step}}^3} + 3\dfrac{|\dot{\boldsymbol{r}}_R|^2}{v_{\text{step}}^2}, & 0 \le |\dot{\boldsymbol{r}}_R| < v_{\text{step}} \\ 1, & |\dot{\boldsymbol{r}}_R| \ge v_{\text{step}} \end{cases} \tag{29}$$

is used, where v_{step} denotes a user-defined numerical constant (e.g. $v_{\text{step}} = 1E-6$ m s^{-1}). Note that in practical applications, the friction forces may simply be increased – without significantly increasing the stiffness – by just raising the preload between the foils and the ring.

In this manuscript, it is assumed that the foil structure consists of two independent parts at the left and right bearing ends, see Fig. 10a. Bearing hysteresis forces with $c_{\text{foil}}/2$ and $F_{\text{fric}}/2$ according to Eq. (28) are assumed to act in the middle of the two parts, which are defined by the two ring points $M_{R,\text{left}}$ and $M_{R,\text{right}}$ (distance a from the ring center M_R). Let $\boldsymbol{r}_{R,\text{left}}$ and $\boldsymbol{r}_{R,\text{right}}$ denote the displacement vectors of $M_{R,\text{left}}$ and $M_{R,\text{right}}$ with respect to the space-fixed coordinate system. Then, the left and right foil forces read

$$\begin{aligned} \boldsymbol{F}_{\text{left}} &= -\frac{c_{\text{foil}}}{2}\,\boldsymbol{r}_{R,\text{left}} - \frac{F_{\text{fric}}}{2}\,\frac{\dot{\boldsymbol{r}}_{R,\text{left}}}{\max\left(|\dot{\boldsymbol{r}}_{R,\text{left}}|, v_{\text{step}}\right)}\,\text{step}(|\dot{\boldsymbol{r}}_{R,\text{left}}|)\,, \\ \boldsymbol{F}_{\text{right}} &= -\frac{c_{\text{foil}}}{2}\,\boldsymbol{r}_{R,\text{right}} - \frac{F_{\text{fric}}}{2}\,\frac{\dot{\boldsymbol{r}}_{R,\text{right}}}{\max\left(|\dot{\boldsymbol{r}}_{R,\text{right}}|, v_{\text{step}}\right)}\,\text{step}(|\dot{\boldsymbol{r}}_{R,\text{right}}|)\,. \end{aligned} \tag{30}$$

For the case that the ring is supported by a visco-elastic material (elastomer), an isotropic, linear visco-elastic material behavior is assumed. Then, the force law reads

$$\boldsymbol{F} = -c_{\text{elast}}\,\boldsymbol{r}_R - d_{\text{visc}}\,\dot{\boldsymbol{r}}_R \tag{31}$$

with the stiffness coefficient c_{elast} and the damping coefficient d_{visc}. It should be mentioned that for elastomers, damping may very

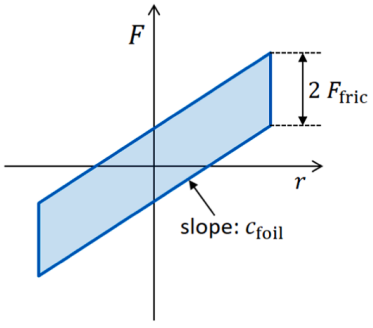

Fig. 9. Idealized hysteresis curve.

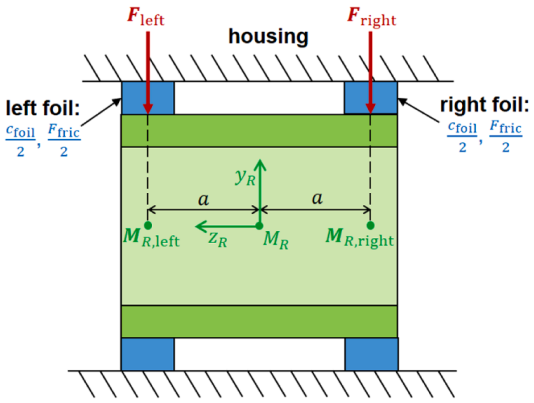

Fig. 10. Sectional view of the supporting structure of the ring.

easily be modified – without markedly changing the stiffness – by simply changing the carbon component. Again, we assume that the elastomer consists of two independent parts at the left and right bearing ends according to Fig. 10 so that the corresponding forces are given by

$$\begin{aligned} \boldsymbol{F}_{\text{left}} &= -\frac{c_{\text{elast}}}{2}\,\boldsymbol{r}_{R,\text{left}} - \frac{d_{\text{visc}}}{2}\,\dot{\boldsymbol{r}}_{R,\text{left}}\,, \\ \boldsymbol{F}_{\text{right}} &= -\frac{c_{\text{elast}}}{2}\,\boldsymbol{r}_{R,\text{right}} - \frac{d_{\text{visc}}}{2}\,\dot{\boldsymbol{r}}_{R,\text{right}}\,. \end{aligned} \tag{32}$$

Final remarks on the supporting structure of the rings:

- In this work, rather straightforward friction and damping models are used in order to keep the representation concise.
- The considered rotor/bearing model is highly nonlinear and shows a large number of interesting nonlinear vibration and bifurcation effects, which are mainly caused by the nonlinearities of the air films. In order to show and discuss the physical effects resulting from the air films in a very clear manner, more complicated models for the supporting structure are not considered within this paper so that physical effects resulting from the air films may clearly be distinguished from possible nonlinear effects resulting from the supporting structure. Therefore, only two basic models – namely the linear-elastic hysteresis model according to Eq. (28) and the linear visco-elastic approach according to Eq. (31) – are considered in the following.
- Depending on the actual design of the supporting structure, these two basic models might be quite suitable or rather inappropriate.

  Regarding a foil supporting structure, special foil designs may entail a highly nonlinear and anisotropic stiffness and friction behavior [13,47]. From the engineering point of view and in order to obtain a robust and predictable rotor/bearing design, it might, however, be useful to choose a foil supporting structure with a mechanical behavior close to the here considered linear-elastic hysteresis approach.

  Regarding the case of an elastomer as supporting structure, a sound modeling approach for elastomers may require much more sophisticated approaches incorporating nonlinear stiffness and damping effects as well as frequency- and temperature-dependent material properties.
- From the practical point of view, air ring bearings with a foil supporting structure may be considered as a rather robust bearing design compared to air ring bearings with an elastomer, where aging of the material or high operating temperatures might lead to problems.
- Compared to classical foil bearings, air ring bearings with a foil supporting structure may also be considered to be advantageous with respect to possible parameter changes during operation. The top foil of classical foil bearings is often coated with Teflon. During operation and especially within the start/stop phase, wear reduces the Teflon coating, which – as a consequence – may also (notably) change the bearing characteristics and the dynamical behavior of the complete rotor/bearing system. Regarding air ring bearings, a Teflon coating is not necessary. To omit wear during the start/stop phase, it might be useful to harden the shaft or the inner ring surface or alternatively to use very thin and hard coatings like DLC so that the bearing characteristic and the dynamical behavior of the rotor/bearing system are not markedly changed during operation. Considering coatings like Teflon, there are also restrictions with respect to the maximum operational temperature. In summary, air ring bearings with a foil supporting structure may be regarded as a rather robust bearing design and well suited to be applied within difficult multi-physical operating environments.

3.4. Simulation of the coupled rotor/bearing system

The rotor/bearing model consists of three subsystems. The first subsystem is the multibody subsystem (MBS) for the rotor. The second and the third subsystem are the two finite element subsystems for the two air films (FEM1 and FEM2). Here, the multibody subsystem and the two finite element subsystems are coupled by an explicit, sequential co-simulation approach (explicit Gauss-Seidel scheme) [59]. The MBS is used as the master subsystem, FEM1 and FEM2 are slave subsystems. The connection between the

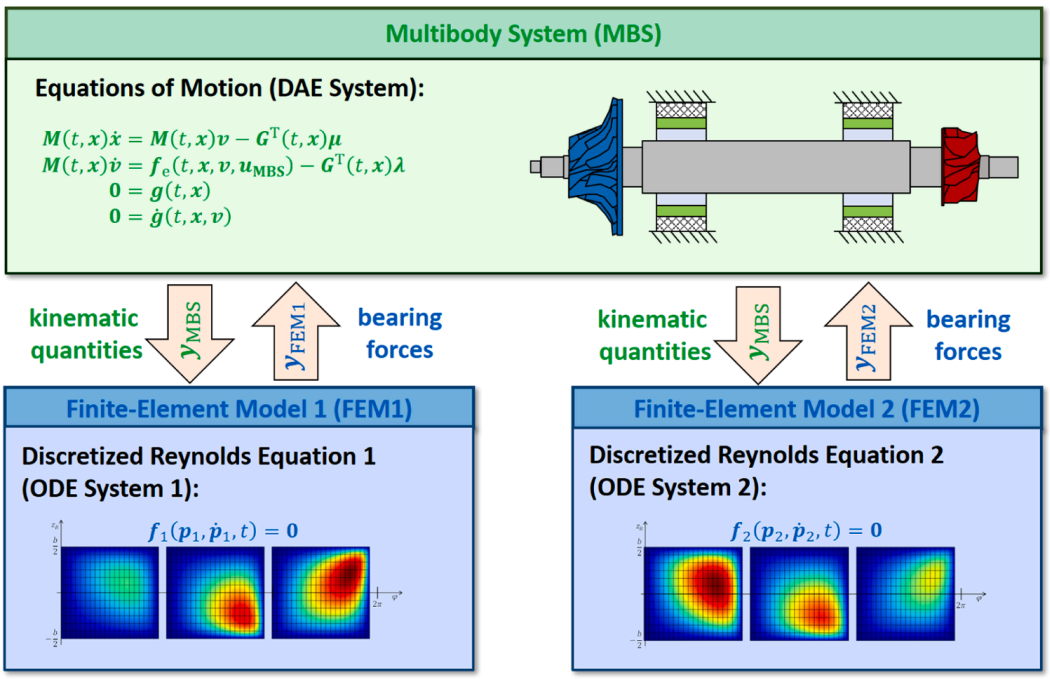

Fig. 11. Coupling structure of the rotor/bearing co-simulation model.

subsystems is physically/mathematically described by appropriate coupling variables (i.e. subsystem input/output variables).

The input variables $\boldsymbol{u}_{\mathrm{MBS}}$ for the multibody subsystem are the resultant bearing forces and tilting torques of the two air films, i.e. $\boldsymbol{u}_{\mathrm{MBS}} = [\boldsymbol{F}^T_{\mathrm{res1}}, \boldsymbol{M}^T_{\mathrm{res1}}, \boldsymbol{F}^T_{\mathrm{res2}}, \boldsymbol{M}^T_{\mathrm{res2}}]^T$. The input variables $\boldsymbol{u}_{\mathrm{FEM1}}$ for the first finite element subsystem (FEM1) are the kinematical quantities for the first air film, i.e. $\boldsymbol{u}_{\mathrm{FEM1}} = [\Delta\boldsymbol{r}^T_1, \Delta\dot{\boldsymbol{r}}^T_1, \alpha_{\mathrm{tilt1}}, \beta_{\mathrm{tilt1}}, \dot{\alpha}_{\mathrm{tilt1}}, \dot{\beta}_{\mathrm{tilt1}}, \Omega]^T$. Correspondingly, the vector $\boldsymbol{u}_{\mathrm{FEM2}} = [\Delta\boldsymbol{r}^T_2, \Delta\dot{\boldsymbol{r}}^T_2, \alpha_{\mathrm{tilt2}}, \beta_{\mathrm{tilt2}}, \dot{\alpha}_{\mathrm{tilt2}}, \dot{\beta}_{\mathrm{tilt2}}, \Omega]^T$ collects the input variables for the second finite element subsystem (FEM2). The coupling structure of the co-simulation model is illustrated in Fig. 11.

To perform a co-simulation, a communication-time grid has to be introduced by defining macro-time points T_N $(N = 0, 1, 2, \ldots)$. During a macro-step from T_N to T_{N+1}, the three subsystems are integrated independently from each other. Only at the macro-time points T_N, information – i.e. coupling variables – is exchanged between the subsystems. Between the macro-time points, the coupling variables are approximated by using extrapolation and interpolation polynomials [60,61]. The here applied sequential co-simulation scheme is executed in two steps.

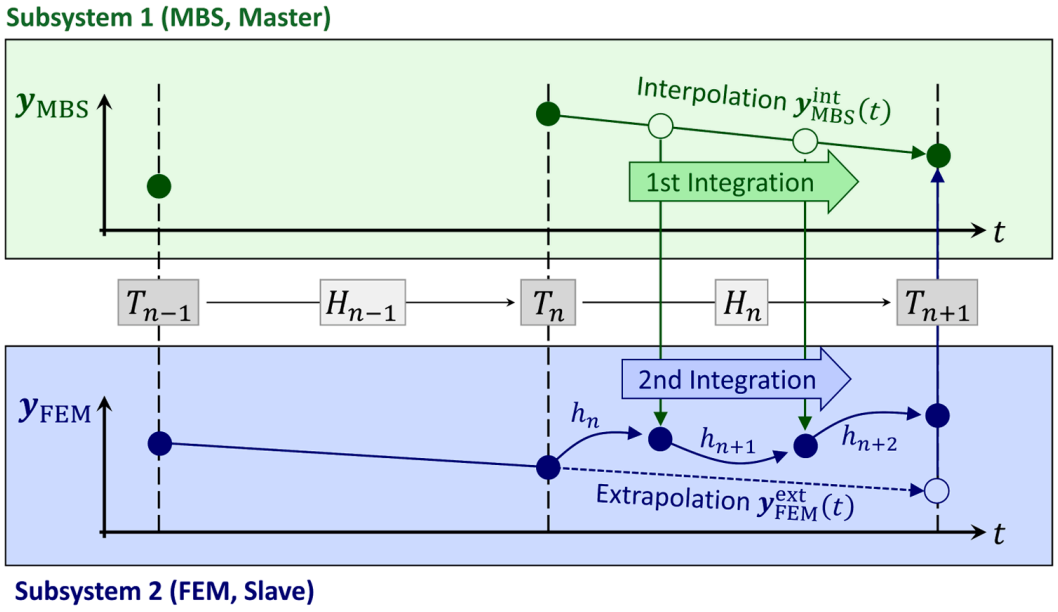

Fig. 12. Explicit co-simulation scheme of Gauss-Seidel type (master-slave approach): illustration for the case of two subsystems and linear approximation polynomials.

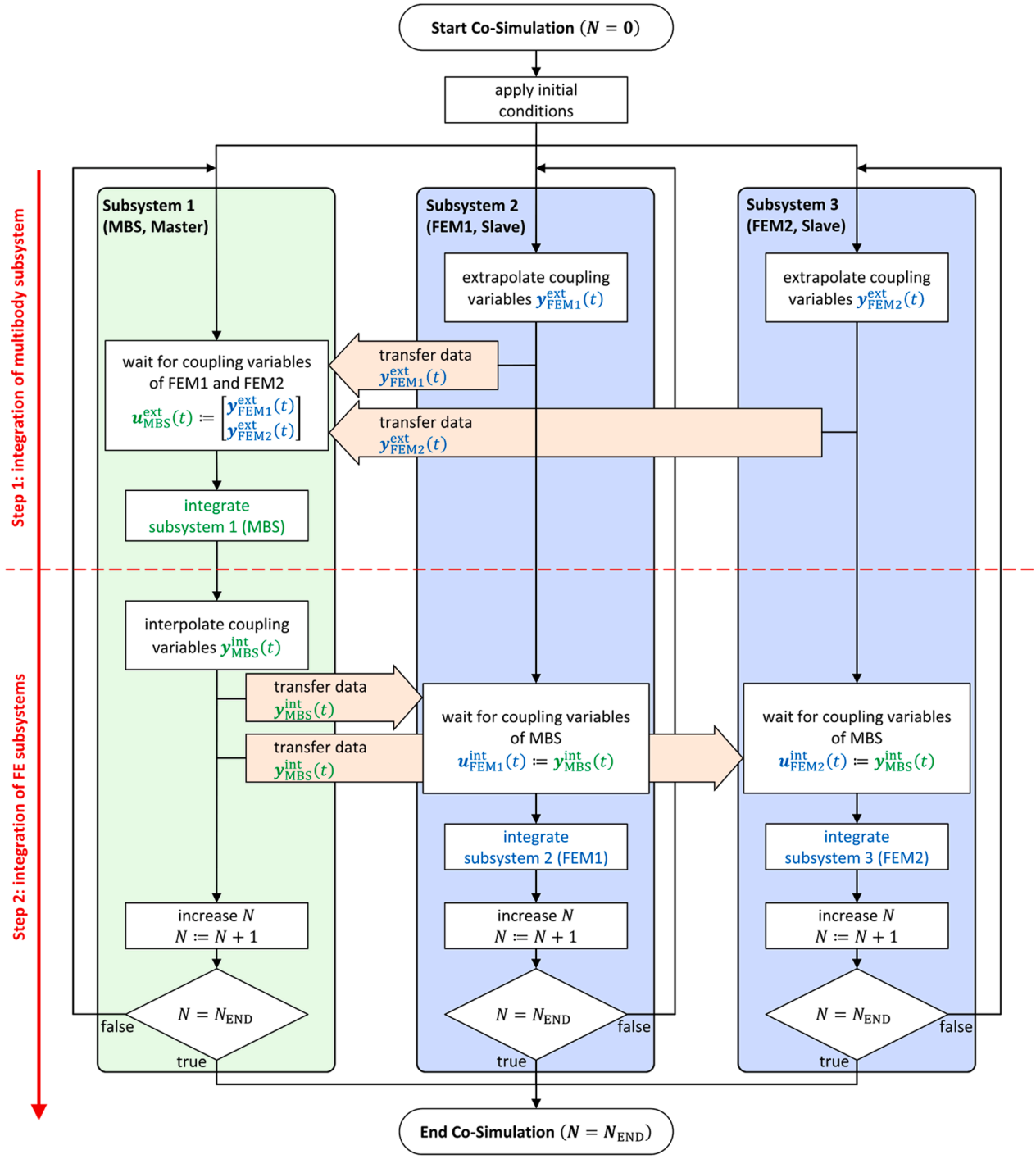

Fig. 13. Flowchart of the overall co-simulation process.

- In the first step, subsystem 1 (multibody subsystem of the rotor, master subsystem) is integrated from the macro-time point T_N to T_{N+1} with the macro-step size $H_N = T_{N+1} - T_N$. For the numerical time integration of the equations of motion according to Eq. (27), the bearing forces/torques are required. Since the bearing forces/torques are unknown in the time interval $[T_N, T_{N+1}]$, extrapolated bearing forces/torques are used. After the MBS subsystem has been integrated from T_N to T_{N+1}, new (updated) coupling variables $\boldsymbol{u}_{\mathrm{FEM}}(T_{N+1})$ are calculated, i.e. new kinematical quantities for the two fluid films.
- In the second step, the FE subsystems (slave subsystems) are integrated from T_N to T_{N+1}. For the numerical integration of the FE subsystems, kinematical quantities of subsystem 1 are required. Since the output variables of the multibody system are already known at T_{N+1} from step 1, interpolated coupling variables can be used for integrating the two finite element subsystems. After the integration of the two FE subsystems, new coupling variables $\boldsymbol{u}_{\mathrm{MBS}}$ – i.e. new resultant bearing forces/torques according to Eqs. (25) and (26) – are calculated at the time point T_{N+1} with the help of the pressure variables $\boldsymbol{p}_1(T_{N+1})$ and $\boldsymbol{p}_2(T_{N+1})$.

Then, the next macro-time step $T_{N+1} \rightarrow T_{N+2}$ is carried out. The basic idea of the approach is sketched in Fig. 12 for the case of linear approximation polynomials.

It should be mentioned that for the here implemented master-slave approach, the macro-step size is identical with the micro-step size of the MBS solver. For approximating the coupling variables $\boldsymbol{u}_{\mathrm{MBS}}$ within the macro-time interval $[T_N, T_{N+1}]$, quadratic extrapolation polynomials are used; quadratic interpolation polynomials are applied to approximate the coupling variables $\boldsymbol{u}_{\mathrm{FEM}}$ in the macro-time interval $[T_N, T_{N+1}]$.

A flowchart of the overall co-simulation process is depicted in Fig. 13.

4. Vibration and bifurcation analysis of high-speed rotor/bearing system

In this section, run-up simulations – carried out with the rotor/bearing system of Section 3 – are used to analyze and explain the basic vibration and bifurcation effects of rotors supported in air ring bearings. Therefore, the rotation of the rotor in z-direction is kinematically prescribed according to $\Omega(t) = \frac{2\pi}{3} \cdot 2000\ t\ \mathrm{s}^{-2}$ (linear rotor run-up in 3 s up to 2000 Hz). The run-up simulations are carried out with zero imbalance in order to very clearly illustrate the influence of the bearing parameters on the vibration and bifurcation behavior. Influence of imbalance has been examined in [37]. The analyses in [37] have shown that the basic vibration and bifurcation behavior is not strongly affected by imbalance (at least for the considered rotor system and for the case of moderate imbalances): both the bifurcation points as well as the amplitudes of the self-excited vibrations are only little influenced by imbalance. For the subsequent run-up simulations, the rotor and both rings are assumed to be initially centered at the space-fixed z-axes with zero velocity. In Section 4.1, a foil structure is assumed as supporting structure of the bearing rings; in Section 4.2, an elastomer is considered.

The simulations in Section 4 have been carried out with the following parameters: $m_{\mathrm{Rotor}} = 830$ g, inertia tensor $\boldsymbol{J}_{\mathrm{Rotor}} = \mathrm{diag}(2500\ \mathrm{kg\ mm^2}, 2500\ \mathrm{kg\ mm^2}, 120\ \mathrm{kg\ mm^2})$ with respect to the center of mass, journal radius $r = 15$ mm, $l_{\mathrm{Rotor}} = 250$ mm, $z_{\mathrm{Rotor}} = 125$ mm, $z_{JC} = 170$ mm, $z_{JT} = 60$ mm, ring mass $m_R = 50$ g, ring inertia tensor $\boldsymbol{J}_R = \mathrm{diag}(10.3\ \mathrm{kg\ mm^2}, 10.3\ \mathrm{kg\ mm^2}, 13.7\ \mathrm{kg\ mm^2})$ with respect to the center of mass, ring width $b = 28.6$ mm, air viscosity $\eta_{\mathrm{air}} = 20.936E-6\ \mathrm{kg\ m^{-1}s^{-1}}$ (assumed fluid temperature: $T_{\mathrm{air}} = 80°\mathrm{C}$), bearing clearance $C = 30\ \mu$m (warm clearance; rotor expansion due to centrifugal forces is neglected), step height $\Delta H = 20\ \mu$m, lobe angle $\varphi_t = 110°$, ring orientation angle $\alpha = \pi - \varphi_t$. The lever length a, which characterizes the tilting stiffness of the ring supporting structure, has been set to 10 mm.

Detailed numerical investigations have shown that in rotor systems with air ring bearings typically three different bifurcations paths may be observed, which are here denoted by *bifurcation path 1, bifurcation path 2a* and *bifurcations path 2b*, see Section 2.2. These three basic bifurcation paths are explained with the help of the subsequent run-up simulations. For this purpose, the stiffness coefficients c_{foil}, c_{elast} and the external friction/damping (friction force F_{fric} in Section 4.1; damping coefficient d_{visc} in Section 4.2) are varied in order to analyze the different possible bifurcations of the system.

The simulations in Section 4 are carried out with the bearing model presented in Section 3, where 3D ring tilting effects are fully taken into account. In order to show and discuss the influence of ring tilting on the vibration and bifurcation behavior of the system, some plots in the Sections 4.1.1–4.1.3 and 4.1.7 as well as in the Sections 4.2.1–4.2.3 and 4.2.7 also contain simulation results, where ring tilting has not been taken into account, i.e. the tilting degrees of freedom of the two rings have been blocked ($\alpha_{\mathrm{tilt}C} = \beta_{\mathrm{tilt}C} = \alpha_{\mathrm{tilt}T} = \beta_{\mathrm{tilt}T} = 0$).

4.1. Air ring bearings with elastic foil structure

In Section 4.1, the rings are supported with an elastic foil structure, see Section 3.3. Stiffness coefficient c_{foil} and friction force F_{fric} are varied in order to investigate the bifurcation behavior of the system. The three basic bifurcations paths are explained in the following subsections.

4.1.1. Run-up simulation 1 (Bifurcation path 1)

Results of a run-up simulation with $c_{\mathrm{foil}} = 600\ \mathrm{N\ mm^{-1}}$ and $F_{\mathrm{fric}} = 6$ N are displayed in Fig. 14. The figure shows the dimensionless bearing eccentricities $\varepsilon_C(t) = \Delta r_C / C$ and $\varepsilon_T(t) = \Delta r_T / C$ of the compressor- and turbine-sided air film as well as the vertical rotor displacements $y_{JC}(t)$ and $y_{JT}(t)$ at the compressor- and turbine-sided bearings, see Fig. 8. Note that the red curves in Fig. 14a-d belong to the run-up simulation including ring tilting, while the blue curves represent corresponding simulation results without ring tilting (planar ring motion with $\alpha_{\mathrm{tilt}C} = \beta_{\mathrm{tilt}C} = \alpha_{\mathrm{tilt}T} = \beta_{\mathrm{tilt}T} = 0$). The simulations show the following vibration behavior.

- In the range $0 \leq t \leq 700$ ms ($0 \leq \Omega \leq 466.7$ Hz), the rotor rotates in a stable equilibrium position.
- At $t \approx 700$ ms, a Hopf bifurcation occurs resulting in a stable quasiperiodic oscillation (whirl/whip oscillation). The compressor-sided whirl/whip excites the conical forward mode *Mode_1(f)* (≈ 130 Hz at the onset of the whirl/whip motion), the turbine-sided whirl/whip excites the conical forward mode *Mode_2(f)* (≈ 160 Hz at the onset), see Appendix.
- At $t \approx 1700$ ms, a second bifurcation is observed. As can be seen, the turbine-sided whirl/whip exhibits a frequency jump. After this jump phenomenon, the turbine- and compressor-sided whirl/whip are synchronized and a cylindrical mode is excited.
- With increasing rotor speed, the rotor amplitudes also markedly increase, while the synchronized whirl/whip frequency only increases slightly.

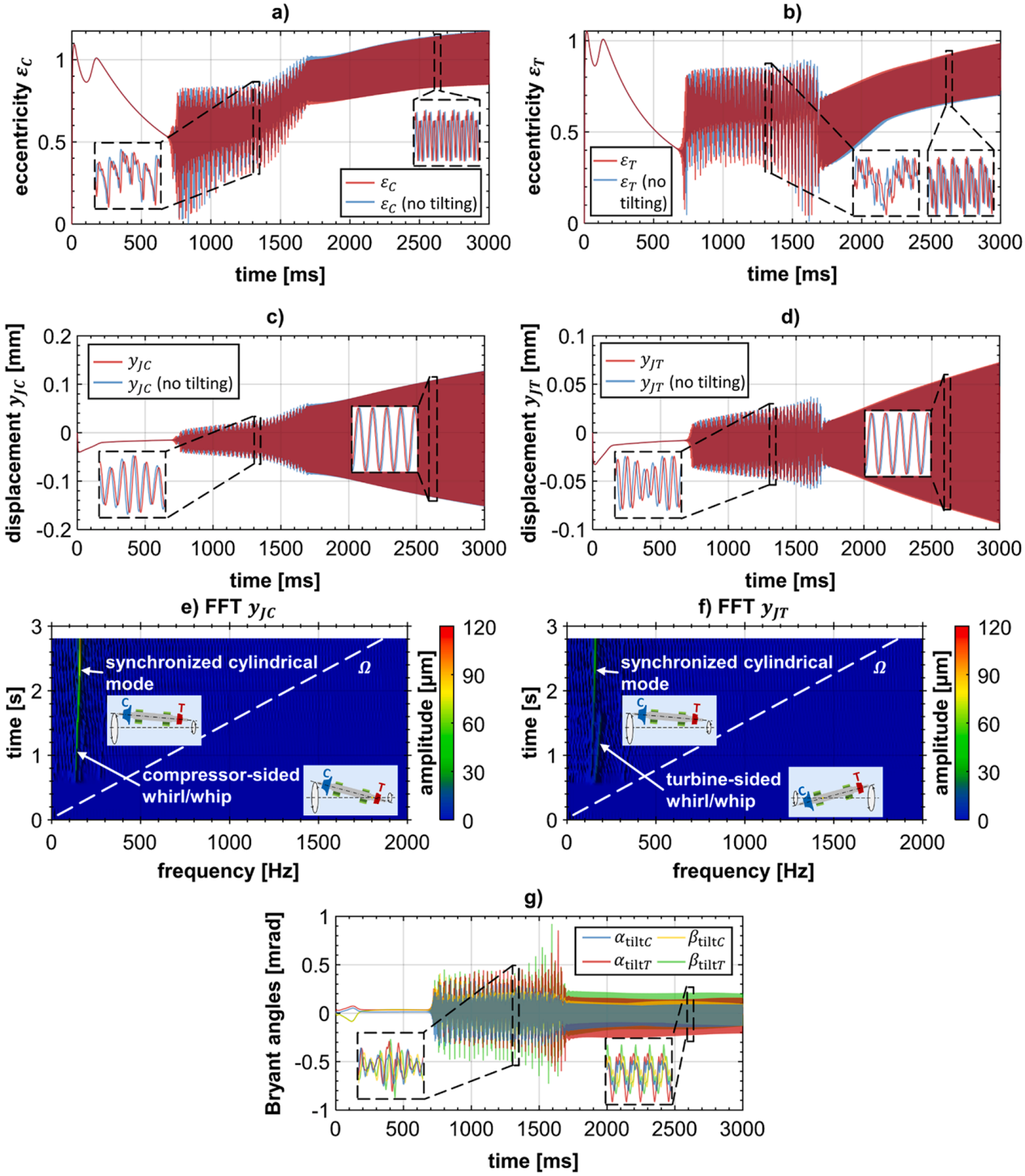

Fig. 14. Run-up simulation with $c_{\mathrm{foil}} = 600$ N mm^{-1} and $F_{\mathrm{fric}} = 6$ N (bifurcation path 1): (a) compressor-sided dimensionless eccentricity $\varepsilon_C(t)$ (with and without ring tilting); (b) turbine-sided dimensionless eccentricity $\varepsilon_T(t)$ (with and without ring tilting); (c) compressor-sided rotor displacement $y_{JC}(t)$ (with and without ring tilting); (d) turbine-sided rotor displacement $y_{JT}(t)$ (with and without ring tilting); (e) frequency spectrum of $y_{JC}(t)$ (with tilting); (f) frequency spectrum of $y_{JT}(t)$ (with tilting); (g) Bryant angles $\alpha_{\mathrm{tilt}C}(t)$, $\alpha_{\mathrm{tilt}T}(t)$, $\beta_{\mathrm{tilt}C}(t)$ and $\beta_{\mathrm{tilt}T}(t)$ (with tilting).

- Throughout the complete speed range, both run-up simulations – with ring tiling (red) and without ring tilting (blue) – almost show the same results: similar bifurcation points and similar rotor amplitudes. Hence, taking into account ring tilting effects only slightly improves the simulation results in connection with bifurcation path 1.

4.1.2. Run-up simulation 2 (Bifurcation path 2a)

To illustrate bifurcation path 2a, the stiffness is decreased to $c_{\mathrm{foil}} = 400$ N mm^{-1}. A run-up simulation with reduced stiffness yields the results collected in Fig. 15.

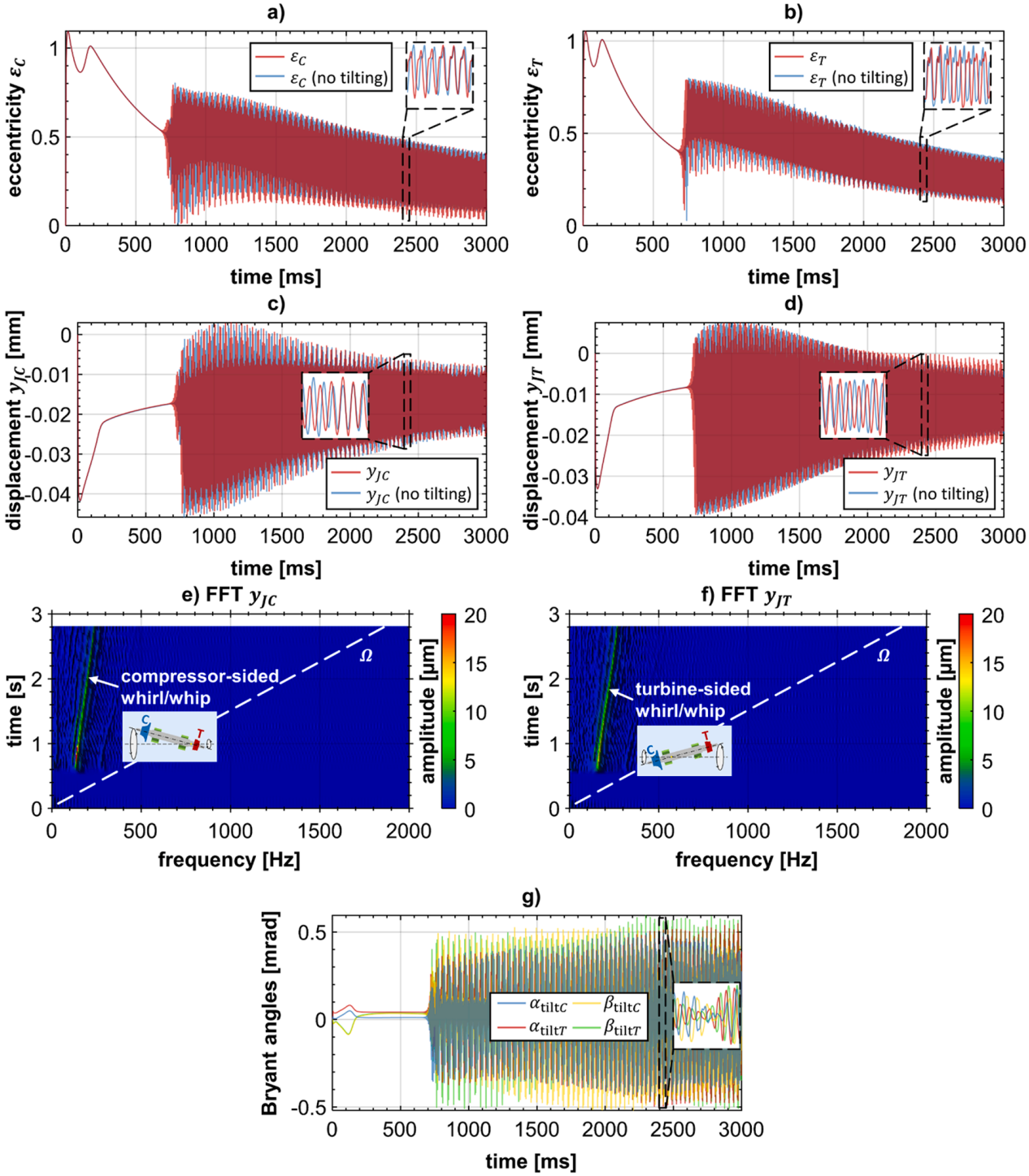

Fig. 15. Run-up simulation with $c_{\mathrm{foil}} = 400$ N mm^{-1} and $F_{\mathrm{fric}} = 6$ N (bifurcation path 2a): (a),(b) compressor- and turbine-sided bearing eccentricities $\varepsilon_C(t)$ and $\varepsilon_T(t)$; (c),(d) compressor- and turbine-sided rotor displacements $y_{JC}(t)$ and $y_{JT}(t)$; (e),(f) frequency spectra of $y_{JC}(t)$ and $y_{JT}(t)$ (with tilting); (g) Bryant angles $\alpha_{\mathrm{tilt}C}(t)$, $\alpha_{\mathrm{tilt}T}(t)$, $\beta_{\mathrm{tilt}C}(t)$ and $\beta_{\mathrm{tilt}T}(t)$.

- In the range $0 \leq t \leq 700$ ms, the rotor rotates in a stable equilibrium position.
- At $t \approx 700$ ms, the equilibrium position bifurcates (Hopf bifurcation) into a stable quasiperiodic motion (whirl/whip vibrations): the compressor-sided whirl/whip excites the conical forward mode *Mode_1(f)* (≈ 130 Hz at the onset), while the turbine-sided whirl/whip excites the conical forward mode *Mode_2(f)* (≈ 150 Hz at the onset).
- Increasing the rotor speed further, the amplitudes of the self-excited oscillations continuously decrease, while the whirl/whip frequencies increase with increasing rotor speed.
- As in Section 4.1.1, taking into account ring tilting effects only little influences the bifurcation behavior and the amplitudes. Hence, ring tilting might be neglected in connection with bifurcation path 2a (at least for the considered rotor and system parameters).

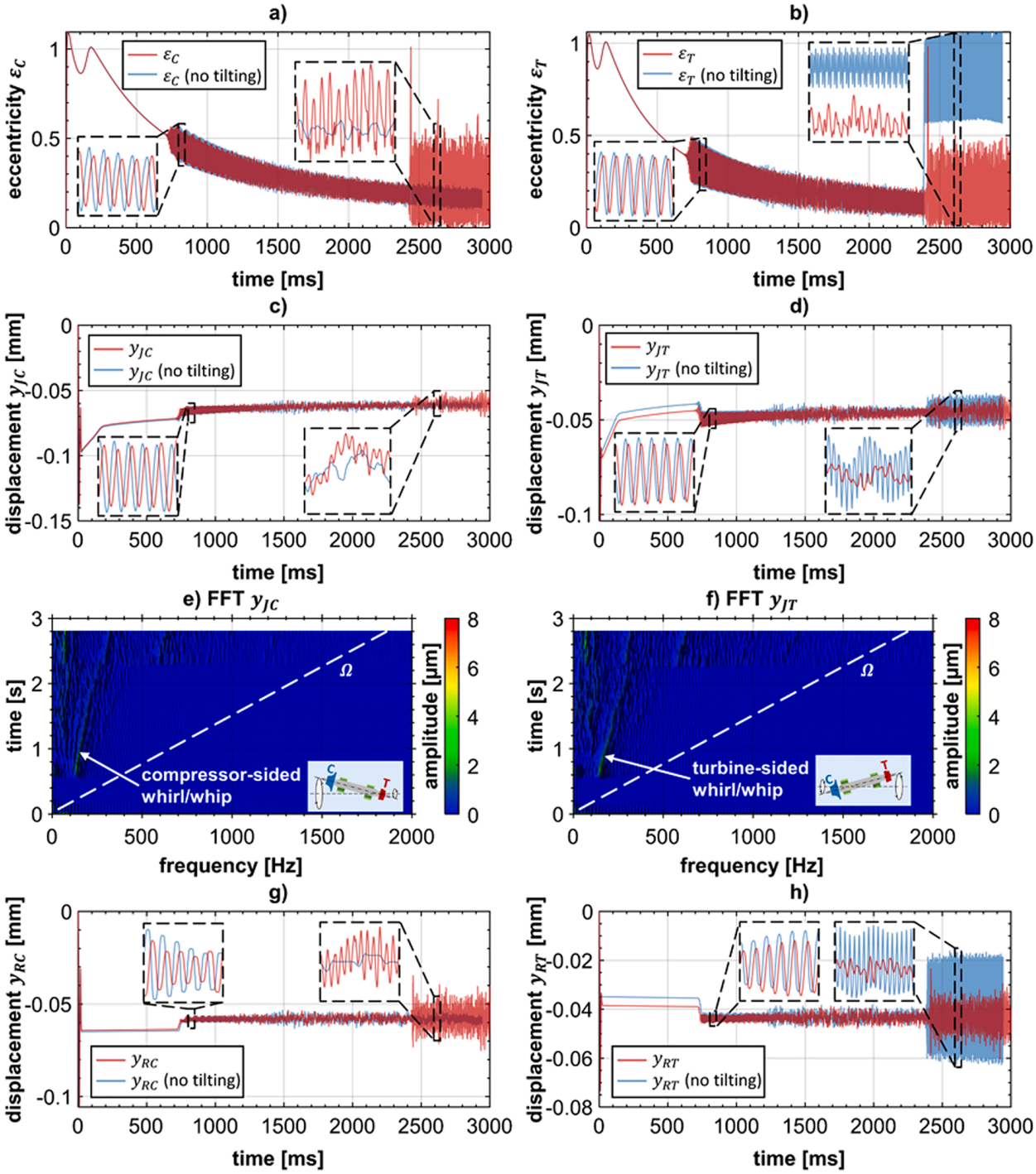

Fig. 16. Run-up simulation with $c_{\text{foil}} = 100$ N mm^{-1}, $F_{\text{fric}} = 1$ N and $m_R = 100$ g (bifurcation path 2b): (a),(b) compressor- and turbine-sided bearing eccentricities $\varepsilon_C(t)$ and $\varepsilon_T(t)$; (c),(d) compressor- and turbine-sided rotor displacements $y_{JC}(t)$ and $y_{JT}(t)$; (e),(f) frequency spectra of $y_{JC}(t)$ and $y_{JT}(t)$ (with tilting); (g),(h) compressor- and turbine-sided ring displacements $y_{RC}(t)$ and $y_{RT}(t)$; (i),(j) frequency spectra of $y_{RC}(t)$ and $y_{RT}(t)$ (with tilting); (k) Bryant angles $\alpha_{\text{tilt}C}(t)$, $\alpha_{\text{tilt}T}(t)$, $\beta_{\text{tilt}C}(t)$ and $\beta_{\text{tilt}T}(t)$; (l),(m) frequency spectra of $\alpha_{\text{tilt}C}(t)$ and $\alpha_{\text{tilt}T}(t)$.

4.1.3. Run-up simulation 3 (Bifurcation path 2b)

For the run-up simulation depicted in Fig. 16, the foil stiffness and the friction force have been reduced to $c_{\text{foil}} = 100$ N mm^{-1} and $F_{\text{fric}} = 1$ N. Furthermore, the ring mass m_R has been increased to 100 g.

- At $t \approx 700$ ms, the equilibrium becomes unstable (Hopf bifurcation) resulting in stable self-excited whirl/whip oscillations. The compressor-sided whirl/whip excites the conical forward mode *Mode_1(f)* (≈ 130 Hz at the onset). The turbine-sided whirl/whip excites the conical forward mode *Mode_2(f)* (≈ 150 Hz at the onset).

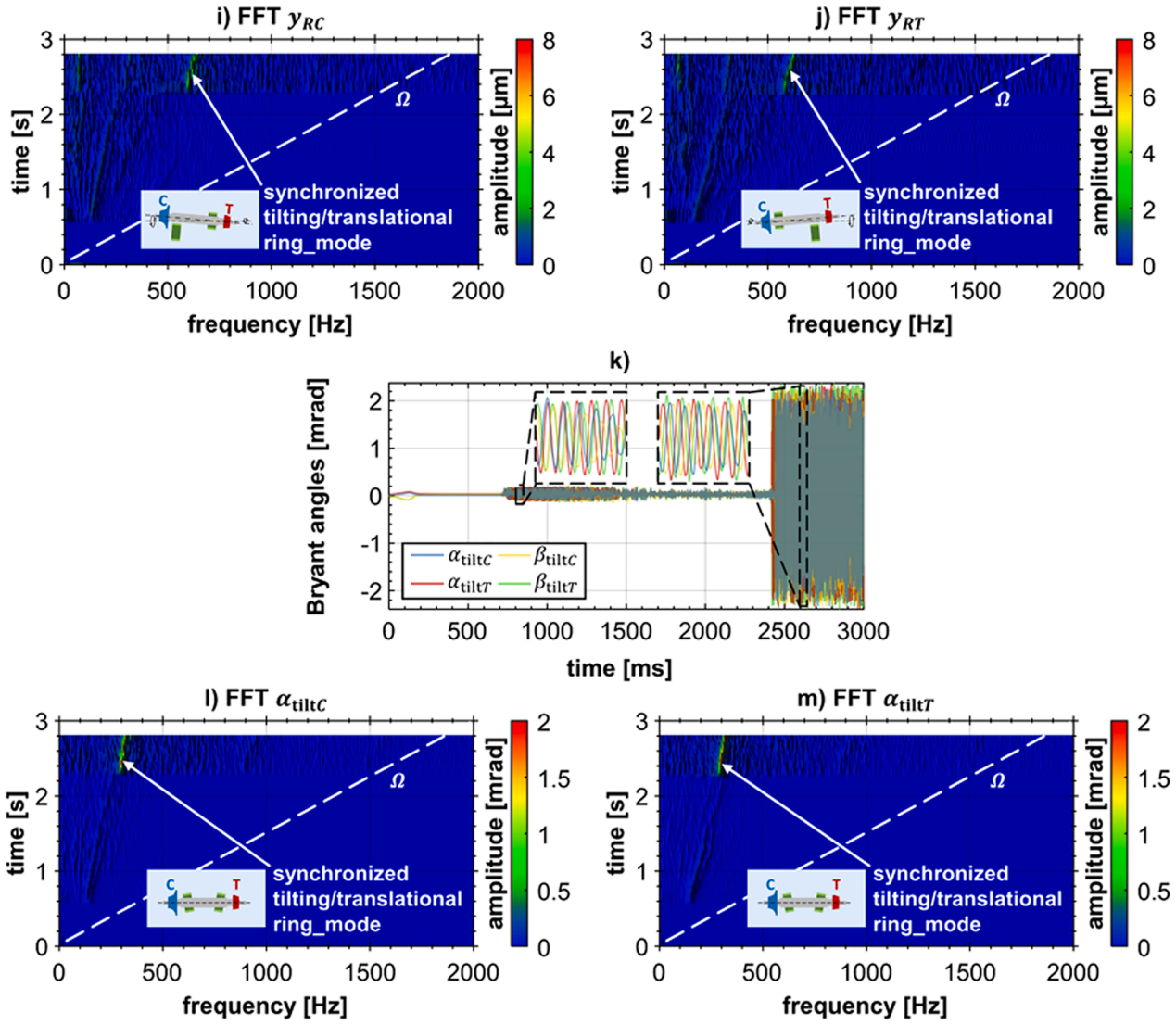

Fig. 16. (*continued*).

- Increasing the rotor speed, further subsynchronous frequencies are detected in the frequency spectra. The cause of these additional frequencies might be traced back to stick-slip effects in the foil structure. The motion is rather noisy and seems to be chaotic in this region.
- In the simulation with ring tilting (red curves), a second bifurcation occurs at $t \approx 2400$ ms. At this time point, a mode jump is detected: the whirl/whip of both fluid films is now exciting the tilting ring mode.

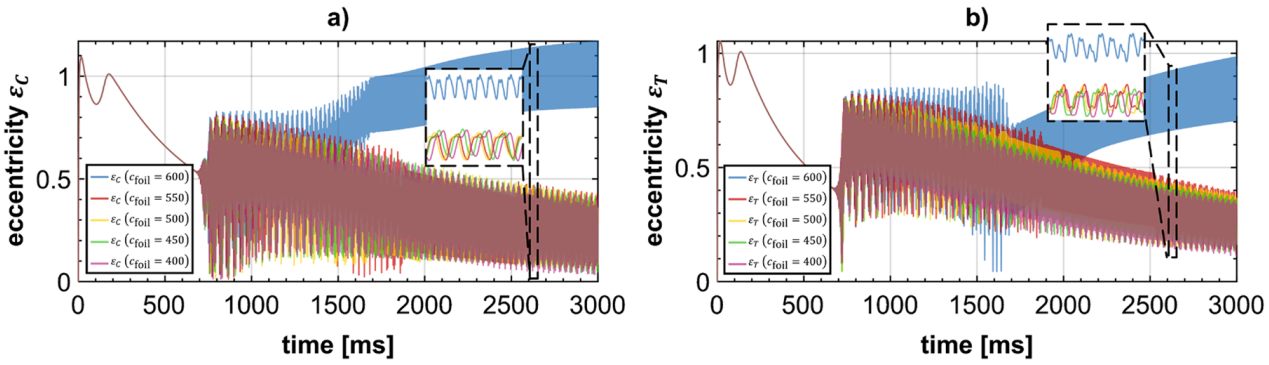

Fig. 17. Parameter study 1: Transition from bifurcation path 1 to bifurcation path 2a for $F_{fric} = 6$ N and different stiffness coefficients c_{foil}. (a),(b) compressor- and turbine-sided bearing eccentricities $\varepsilon_C(t)$ and $\varepsilon_T(t)$.

In Fig. 16k-m, the ring tilting angles and corresponding FFTs for the two tilting angles $\alpha_{\text{tilt}C}(t)$ and $\alpha_{\text{tilt}T}(t)$ are depicted. The frequency spectra clearly show the frequency of the tilting ring mode *Mode_3(f)* ($\approx$ 300 Hz at the onset).

In Fig. 16g-j, the vertical displacements $y_{RC}(t)$ and $y_{RT}(t)$ of the compressor- and turbine-sided rings and the corresponding frequency spectra can be seen. The FFTs in Fig. 16i-j exhibit a subsynchronous frequency of $\approx$ 600 Hz at the onset, which is related to the translational ring modes *Mode_5(f)* and *Mode_6(f)*, see Appendix. A closer view on the simulation results shows that the frequency of the translational ring modes *Mode_5(f)* and *Mode_6(f)* in Fig. 16i-j is exactly two times the frequency of the tilting ring mode *Mode_3(f)* in Fig. 16l-m.

Hence, the frequency spectra of the simulation with ring tilting exhibit two frequencies in the whirl/whip regime, whereas the higher frequency is twice as large as the lower frequency. The lower frequency is associated with the tilting movement of the ring and the higher frequency with the translational movement of the ring. This interesting 1:2 mode synchronization phenomenon is in detail examined and physically explained in Section 4.3.

- In the simulation without tilting (blue curves), the second bifurcation arises also at $t \approx 2400$ ms. The turbine-sided eccentricity shows a large jump and the turbine-side whirl/whip is now exciting the translational ring mode *Mode_6(f)*. Note that this jump phenomenon does not occur at the compressor-sided bearing.
- Comparing the simulation results with and without ring tilting shows that both simulations exhibit very similar results up the point where the second bifurcation into the ring mode occurs. After this bifurcation point, however, a different oscillation behavior is observed. Obviously, ring tilting influences the vibration and bifurcation behavior so that ring tilting effects have to be taken into account to correctly predict the bifurcation into the dangerous ring mode.

4.1.4. Parameter study 1: transition from bifurcation path 1 to bifurcation path 2a

In this section, a parameter study is presented, which illustrates the transition from bifurcation path 1 to bifurcation path 2a. Therefore, the friction force has been set to $F_{\text{fric}} = 6$ N and the stiffness has been successively reduced from $c_{\text{foil}} = 600$ N mm^{-1} (bifurcation path 1, Section 4.1.1) to $c_{\text{foil}} = 400$ N mm^{-1} (bifurcation path 2a, Section 4.1.2).

As can be seen in Fig. 17, bifurcation path 1 is only observed for $c_{\text{foil}} = 600$ N mm^{-1}. For $c_{\text{foil}} \leq 550$ N mm^{-1}, bifurcation path 2a is detected.

4.1.5. Parameter study 2: transition from bifurcation path 2a to bifurcation path 2b

In Fig. 18, the transition from bifurcation path 2a to bifurcation path 2b is examined. Therefore, both the stiffness coefficient c_{foil} and the friction force F_{fric} are successively reduced. The ring mass has been set to $m_R = 100$ g.

The first three curves with higher stiffness and friction parameters ($c_{\text{foil}} = 400$ N mm^{-1}, $F_{\text{fric}} = 6$ N; $c_{\text{foil}} = 325$ N mm^{-1}, $F_{\text{fric}} = 4.75$ N; $c_{\text{foil}} = 250$ N mm^{-1}, $F_{\text{fric}} = 3.5$ N) exhibit bifurcation path 2a. The two curves with lower stiffness and friction parameters ($c_{\text{foil}} = 175$ N mm^{-1}, $F_{\text{fric}} = 2.25$ N; $c_{\text{foil}} = 100$ N mm^{-1}, $F_{\text{fric}} = 1$ N) show bifurcation path 2b, where the whirl/whip of both fluid films is exciting the tilting ring mode (strictly speaking a synchronized tilting/translational ring mode, see Section 4.1.3).

4.1.6. Parameter study 3: influence of ring tilting stiffness (lever length a) in connection with bifurcation path 2b

The influence of the ring tilting stiffness on the bifurcation behavior is discussed with the help of Fig. 19. In this simulation study, the stiffness, friction and ring mass have been set to $c_{\text{foil}} = 100$ N mm^{-1}, $F_{\text{fric}} = 1$ N and $m_R = 100$ g. Only the lever length a (see Section 3.3, Fig. 10), which defines the tilting stiffness, is varied.

All simulations basically exhibit the same vibration behavior, namely bifurcation path 2b, where the whirl/whip of both fluid films is exciting a synchronized tilting/translational ring mode.

4.1.7. Parameter study 4: influence of ring friction in connection with bifurcation path 2b

The influence of the friction force F_{fric} in association with bifurcation path 2b is examined in Fig. 20. Therefore, run-up simulations with $c_{\text{foil}} = 100$ N mm^{-1}, $m_R = 100$ g and different friction forces F_{fric} are considered. In order to highlight the influence of ring tilting on the oscillation behavior, run-up simulations including ring tilting (Fig. 20a,b) are compared with corresponding simulations

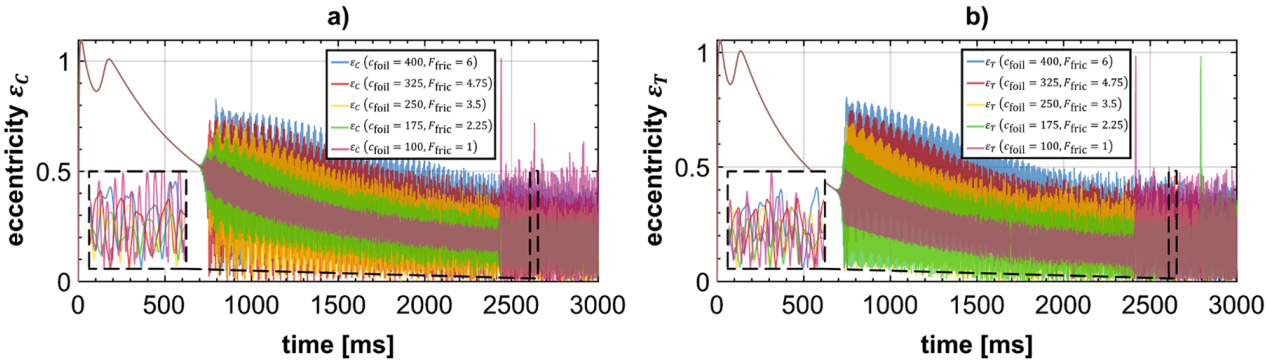

Fig. 18. Parameter study 2: Transition from bifurcation path 2a to bifurcation path 2b using different stiffness coefficients c_{foil} and friction forces F_{fric} (ring mass $m_R = 100$ g). (a),(b) compressor- and turbine-sided dimensionless eccentricities $\varepsilon_C(t)$ and $\varepsilon_T(t)$.

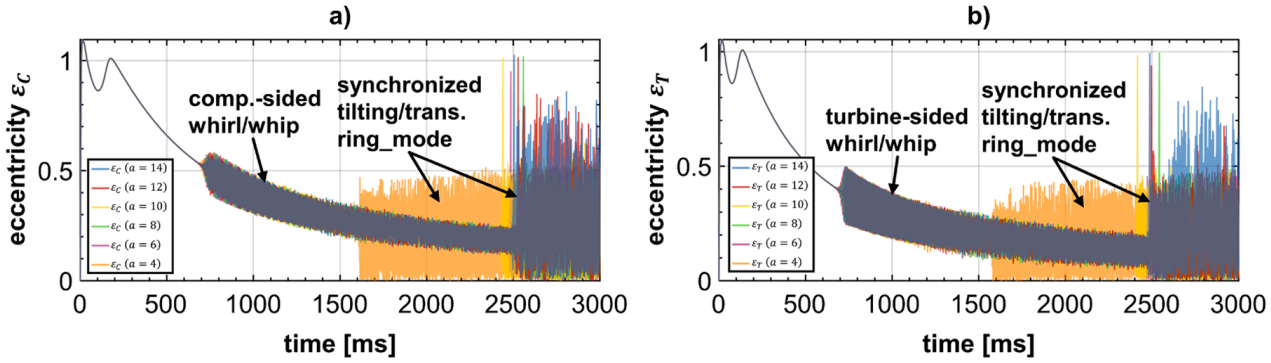

Fig. 19. Parameter study 3: Influence of the ring tilting stiffness in association with bifurcation path 2b. Run-up simulations with $c_{\text{foil}} = 100$ N mm^{-1}, $F_{\text{fric}} = 1$ N, $m_R = 100$ g and different lever lengths a. (a),(b) compressor- and turbine-sided bearing eccentricities $\varepsilon_C(t)$ and $\varepsilon_T(t)$.

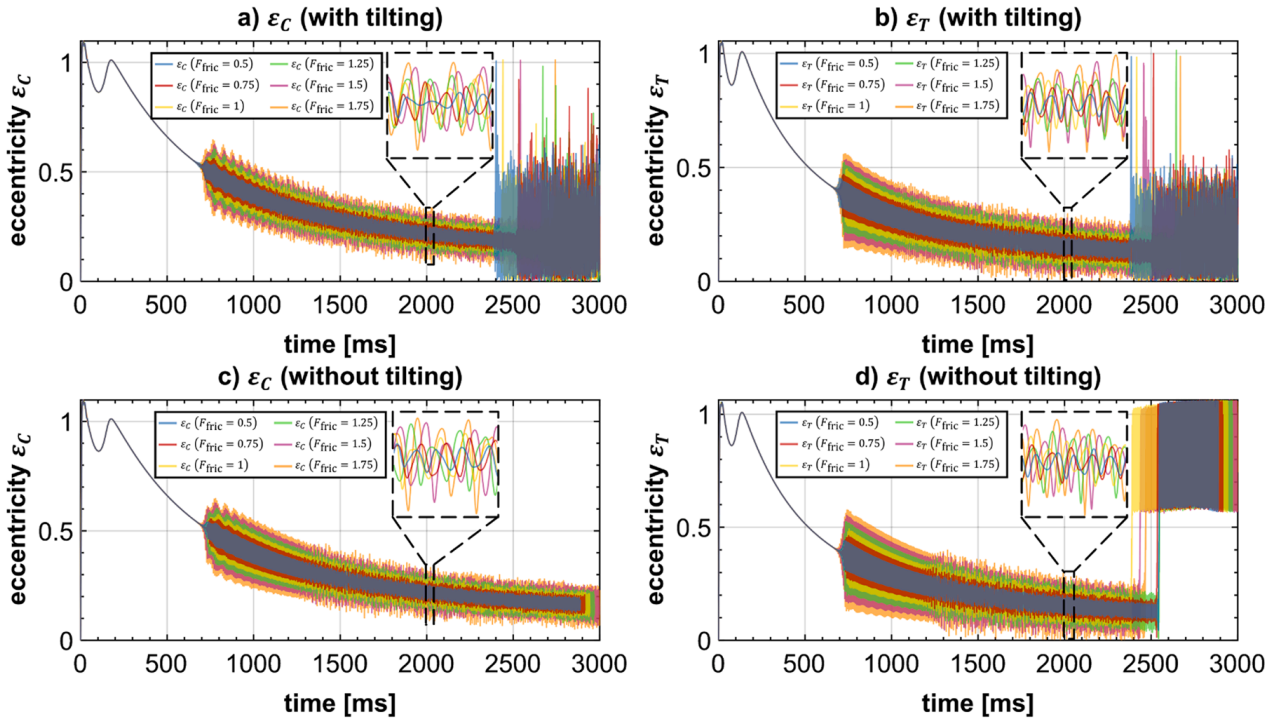

Fig. 20. Parameter study 4: Influence of ring friction in connection with bifurcation path 2b. Run-up simulations with $c_{\text{foil}} = 100$ N mm^{-1} and different friction forces F_{fric} (ring mass $m_R = 100$ g): (a),(b) compressor- and turbine-sided bearing eccentricities $\varepsilon_C(t)$ and $\varepsilon_T(t)$ (with ring tilting); (c),(d) compressor- and turbine-sided bearing eccentricities $\varepsilon_C(t)$ and $\varepsilon_T(t)$ (without ring tilting).

without ring tilting (Fig. 20c,d).

For all friction forces, a bifurcation into the ring mode (i.e. bifurcation path 2b) is observed. Before the jump into the dangerous ring mode arises, whirl/whip oscillations with moderate amplitudes are detected (the lower the friction force, the larger the whirl/whip amplitudes). For the simulations without ring tilting (Fig. 20c,d), it can clearly be observed that only the turbine-sided whirl/whip is exciting the translational ring mode (*Mode_6(f)* in the Appendix). If ring tilting is considered, the whirl/whip of both fluid films is exciting a synchronized tilting/translational ring mode.

4.2. Air ring bearings with visco-elastic mounting (Elastomer)

Now, the rings are assumed to be mounted visco-elastically, see Section 3.3. The stiffness coefficient c_{elast} and the damping coefficient d_{visc} are varied in order to examine the basic bifurcation behavior of the system.

4.2.1. Run-up simulation 1 (Bifurcation path 1)

Results of a run-up simulation with $c_{\text{elast}} = 600$ N mm^{-1} and $d_{\text{visc}} = 30$ N ms mm^{-1} are arranged in Fig. 21.

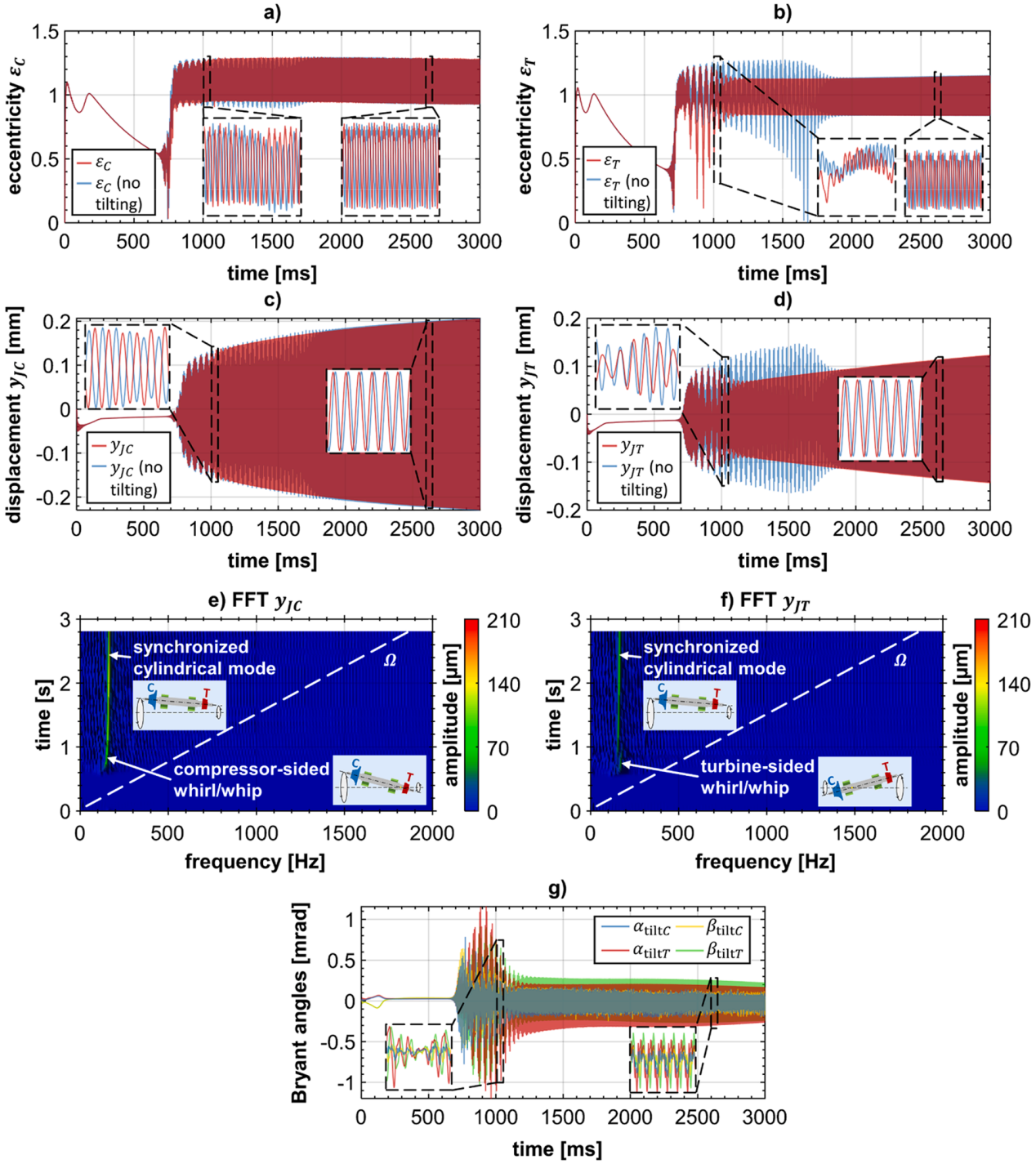

Fig. 21. Run-up simulation with $c_{\text{elast}} = 600$ N mm^{-1} and $d_{\text{visc}} = 30$ N ms mm^{-1}: (a),(b) compressor- and turbine-sided bearing eccentricities $\varepsilon_C(t)$ and $\varepsilon_T(t)$; (c),(d) compressor- and turbine-sided rotor displacements $y_{JC}(t)$ and $y_{JT}(t)$; (e),(f) frequency spectra of $y_{JC}(t)$ and $y_{JT}(t)$ (with tilting); (g) Bryant angles $\alpha_{\text{tilt}C}(t)$, $\alpha_{\text{tilt}T}(t)$, $\beta_{\text{tilt}C}(t)$ and $\beta_{\text{tilt}T}(t)$.

- At $t \approx 700$ ms, the equilibrium position becomes unstable (Hopf bifurcation). After the bifurcation, stable quasiperiodic oscillations (whirl/whip oscillations) with high bearing eccentricities are observed. The whirl/whip of the compressor-sided bearing excites the conical forward mode *Mode_1(f)* (≈ 140 Hz at the onset) and the turbine-sided whirl/whip the conical forward mode *Mode_2(f)* (≈ 160 Hz at onset), see Appendix.
- Regarding the simulation with ring tilting, a synchronization effect can be observed at $t \approx 1100$ ms. Here, the turbine-sided whirl/whip frequency shows a jump and synchronizes with the compressor-sided whirl/whip. After the synchronization, both whirls/whips excite a cylindrical forward mode.
- For the simulation without ring tilting, the synchronization effect occurs later at $t \approx 1700$ ms.

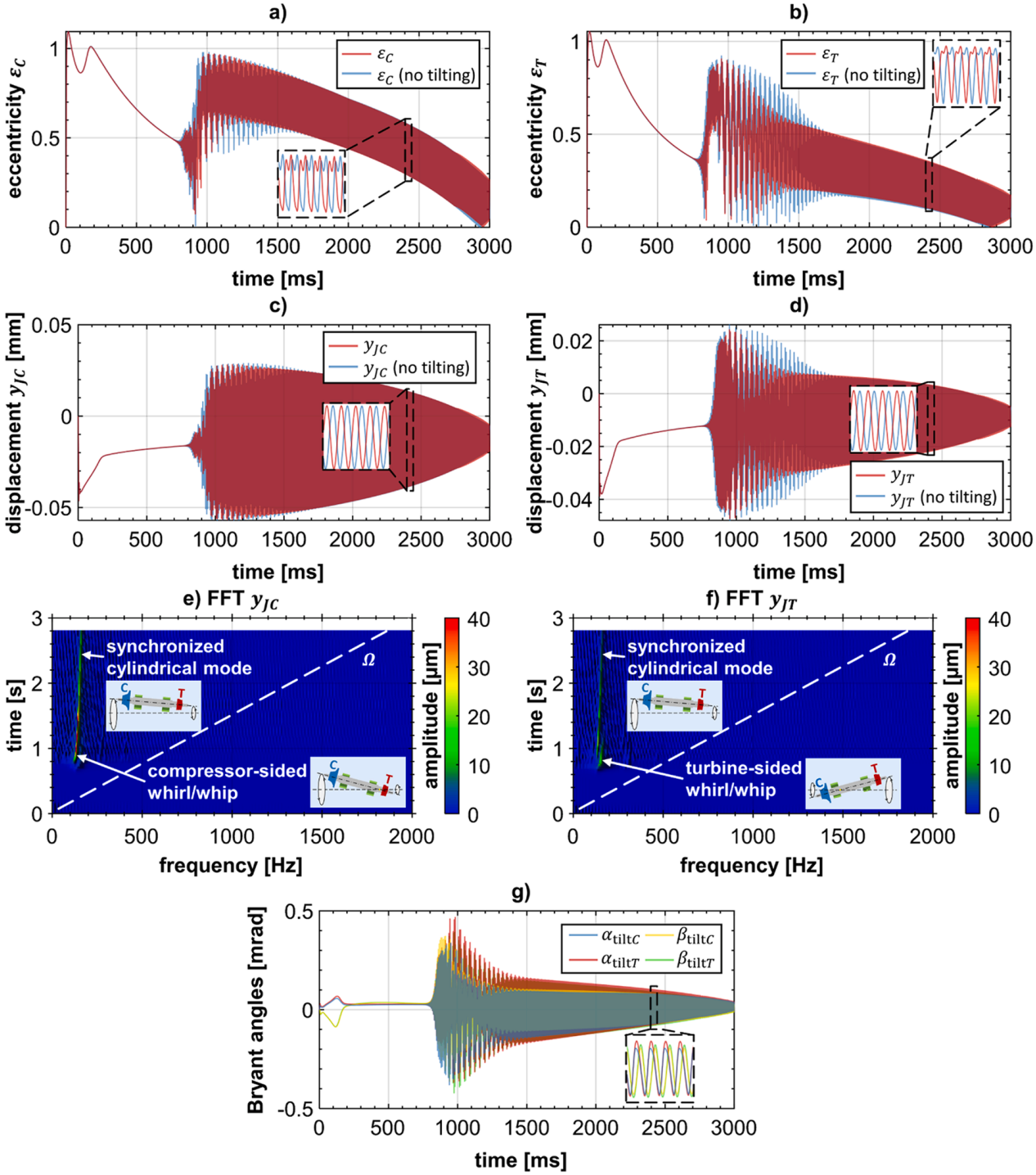

Fig. 22. Run-up simulation with $c_{\mathrm{elast}} = 600$ N mm^{-1} and $d_{\mathrm{visc}} = 300$ N ms mm^{-1}: (a),(b) compressor- and turbine-sided bearing eccentricities $\varepsilon_C(t)$ and $\varepsilon_T(t)$; (c),(d) compressor- and turbine-sided rotor displacements $y_{JC}(t)$ and $y_{JT}(t)$; (e),(f) frequency spectra of $y_{JC}(t)$ and $y_{JT}(t)$ (with tilting); (g) Bryant angles $\alpha_{\mathrm{tilt}C}(t)$, $\alpha_{\mathrm{tilt}T}(t)$, $\beta_{\mathrm{tilt}C}(t)$ and $\beta_{\mathrm{tilt}T}(t)$.

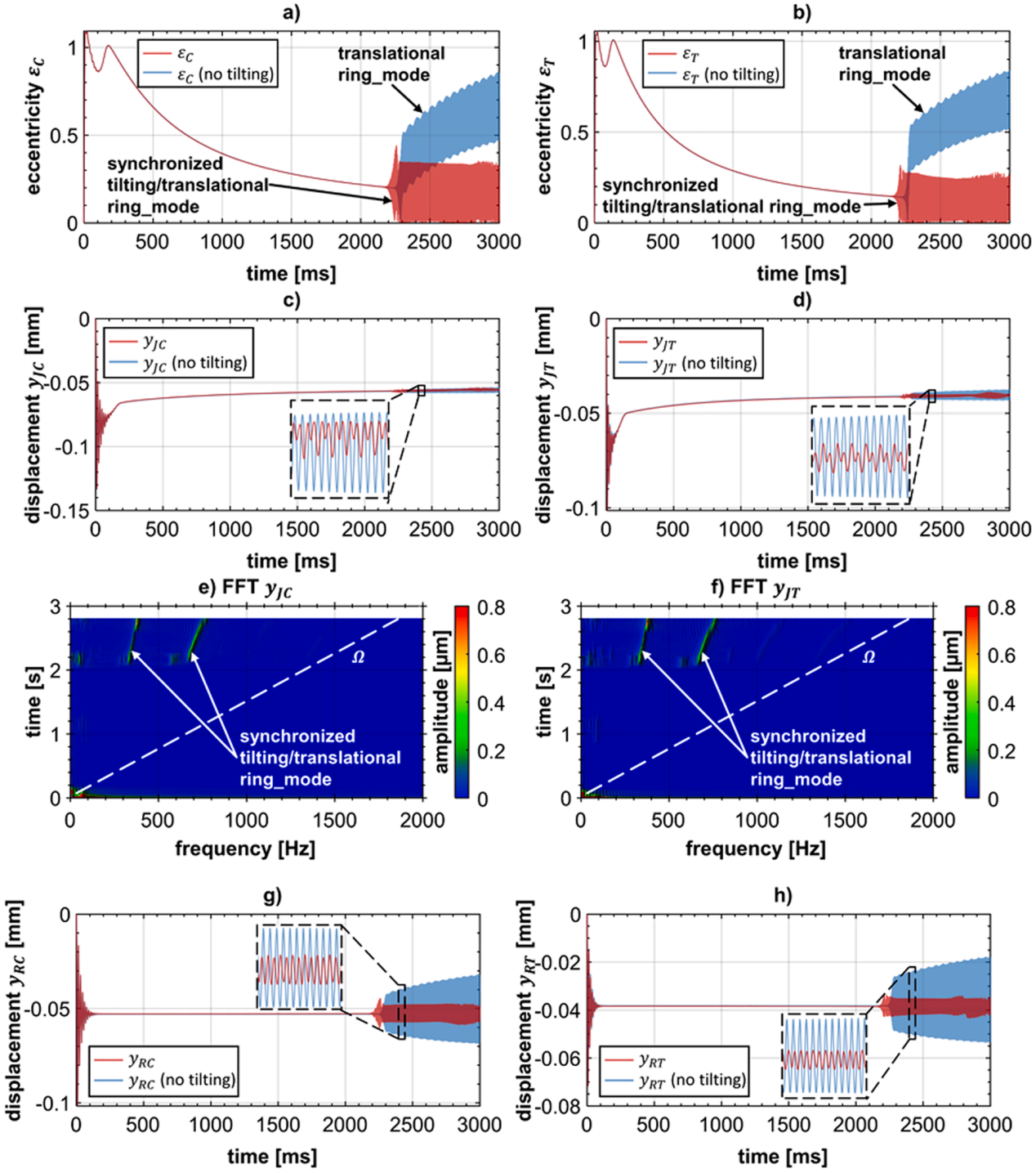

Fig. 23. Run-up simulation with $c_{\text{elast}} = 100$ N mm^{-1} and $d_{\text{visc}} = 40$ N ms mm^{-1}: (a),(b) compressor- and turbine-sided bearing eccentricities $\varepsilon_C(t)$ and $\varepsilon_T(t)$; (c),(d) compressor- and turbine-sided rotor displacements $y_{JC}(t)$ and $y_{JT}(t)$; (e),(f) frequency spectra of $y_{JC}(t)$ and $y_{JT}(t)$ (with tilting); (g), (h) compressor- and turbine-sided ring displacements $y_{RC}(t)$ and $y_{RT}(t)$; (i),(j) frequency spectra of $y_{RC}(t)$ and $y_{RT}(t)$ (with tilting); (k) Bryant angles $\alpha_{\text{tilt}C}(t)$, $\alpha_{\text{tilt}T}(t)$, $\beta_{\text{tilt}C}(t)$ and $\beta_{\text{tilt}T}(t)$; (l),(m) frequency spectra of $\alpha_{\text{tilt}C}(t)$ and $\alpha_{\text{tilt}T}(t)$.

- The synchronized whirl/whip frequency does not significantly change if the rotor speed is increased. In the synchronized region, the bearing eccentricities remain high so that a safe operation of the rotor system is not possible.

4.2.2. *Run-up simulation 2 (Bifurcation path 2a)*

Now, the damping is increased to $d_{\text{visc}} = 300$ N ms mm^{-1}; the stiffness $c_{\text{elast}} = 600$ N mm^{-1} remains unchanged. Simulation results are collected in Fig. 22.

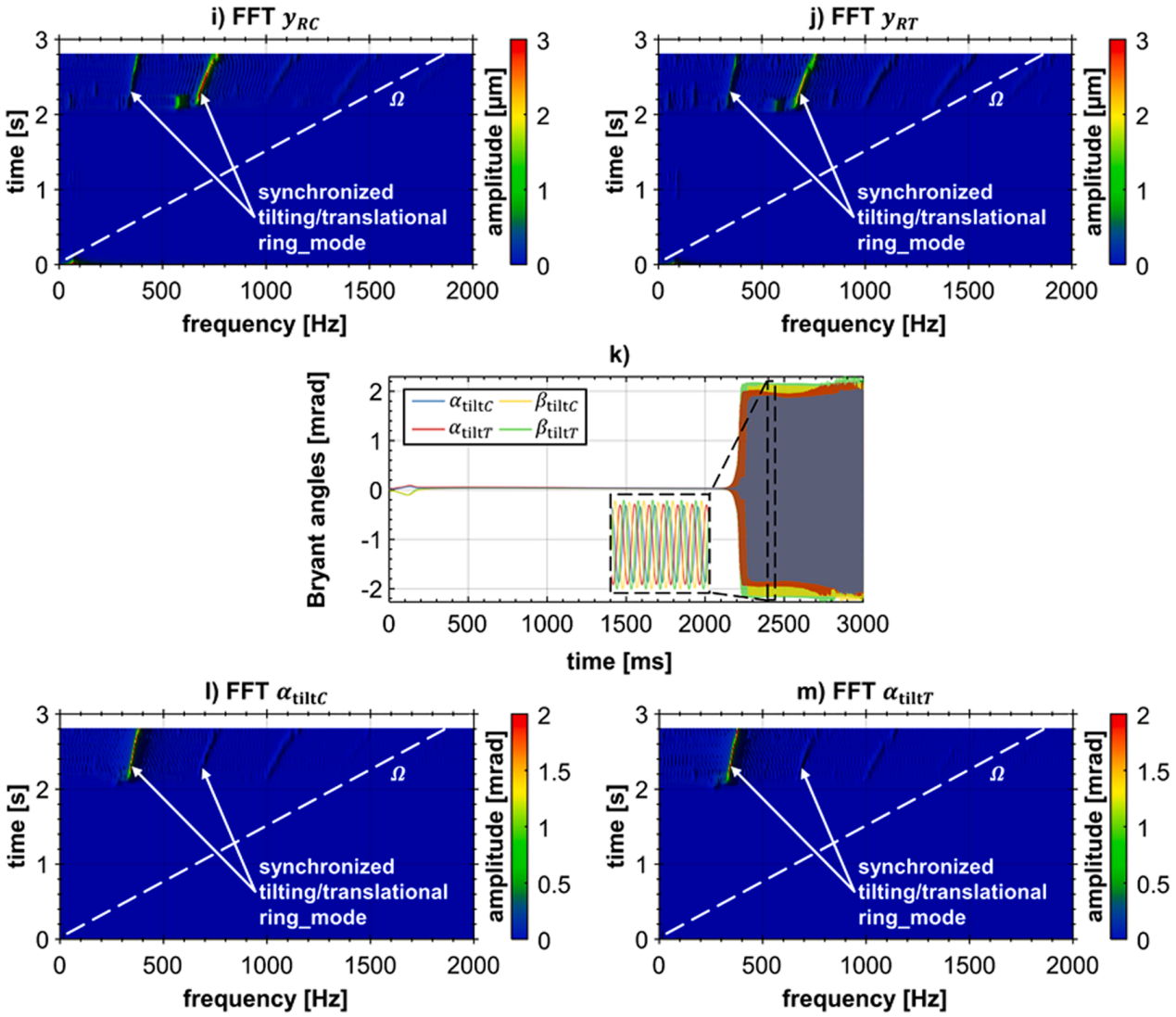

Fig. 23. (*continued*).

- At $t \approx 800$ ms, the equilibrium position becomes unstable (Hopf bifurcation) resulting in stable quasiperiodic oscillations. The whirl/whip of the compressor-sided bearing excites the conical forward mode *Mode_1(f)* (≈ 120 Hz at the onset), while the turbine-sided whirl/whip is exciting the conical forward mode *Mode_2(f)* (≈ 150 Hz at the onset).
- A similar synchronization effect as in Section 4.2.1 can be observed at $t \approx 1300$ ms for the simulation with ring tilting and at $t \approx 1600$ ms for the simulation without ring tilting.

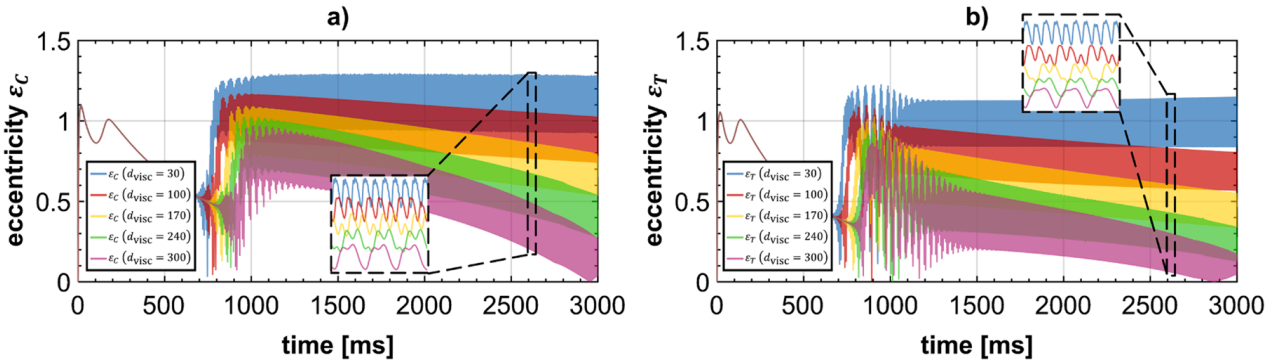

Fig. 24. Parameter study 1: Transition from bifurcation path 1 to bifurcation path 2a with $c_{elast} = 600$ N mm^{-1} and different viscous damping coefficients d_{visc}: (a),(b) compressor- and turbine-sided bearing eccentricities $\varepsilon_C(t)$ and $\varepsilon_T(t)$.

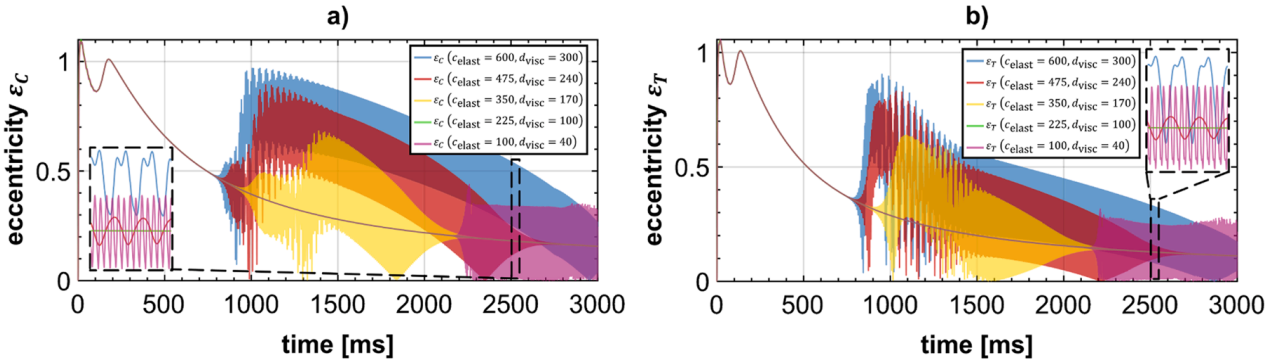

Fig. 25. Parameter study 2: Transition from bifurcation path 2a to bifurcation path 2b for various stiffness and damping coefficients c_{elast} and d_{visc}: (a),(b) compressor- and turbine-sided bearing eccentricities $\varepsilon_C(t)$ and $\varepsilon_T(t)$.

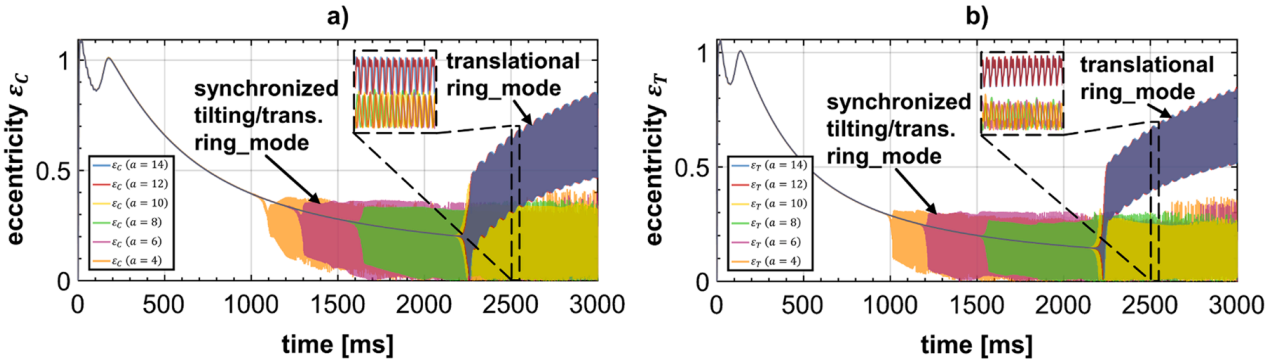

Fig. 26. Parameter study 3: Influence of lever length a (ring tilting stiffness) on bifurcation path 2b for $c_{elast} = 100$ N mm^{-1} and $d_{visc} = 40$ N ms mm^{-1}: (a),(b) compressor- and turbine-sided bearing eccentricities $\varepsilon_C(t)$ and $\varepsilon_T(t)$.

- In contrast to Section 4.2.1, the bearing eccentricities and the rotor amplitudes decrease with increasing rotor speed so that a safe operation of the rotor system is possible.

4.2.3. Run-up simulation 3 (Bifurcation path 2b)

Simulation results for $c_{elast} = 100$ N mm^{-1} and $d_{visc} = 40$ N ms mm^{-1} are depicted in Fig. 23.

- For the simulation including ring tilting, the equilibrium position becomes unstable at $t \approx 2200$ ms (Hopf bifurcation); for the simulation without ring tilting, the bifurcation arises little later at $t \approx 2250$ ms. After the Hopf bifurcation, self-excited oscillations are observed.
- Considering the case with ring tilting, the whirl/whip of the two fluid films excites the tilting ring mode *Mode_3(f)* (more precisely, a synchronized tilting/translational ring mode, see above). A closer view on the simulation results shows that the whirl/whip is initiated by the turbine-sided bearing. The compressor-sided whirl/whip appears shortly later.
- Regarding the run-up simulation without ring tilting, the compressor-sided whirl/whip excites the translational ring mode *Mode_5(f)*. The turbine-sided whirl/whip excites the translational ring mode *Mode_6(f)*, see Appendix.
- As mentioned in Section 4.1.3, the frequency spectra of the simulation with ring tilting show two frequencies in the whirl/whip regime, where the lower frequency is related with the tilting movement and the higher frequency with the translational movement of the ring. The higher frequency is two times as large as the lower frequency (nonlinear 1:2 mode coupling effect, see Section 4.3).

4.2.4. Parameter study 1: transition from bifurcation path 1 to bifurcation path 2a

In this subsection, the transition from bifurcation path 1 to bifurcation path 2a is examined in more detail with the help of a parameter study. Therefore, the stiffness coefficient is set to $c_{elast} = 600$ N mm^{-1}, while the damping coefficient is successively increased from $d_{visc} = 30$ N ms mm^{-1} (see Section 4.2.1) to $d_{visc} = 300$ N ms mm^{-1} (see Section 4.2.2). Fig. 24 depicts the compressor- and turbine-sided bearing eccentricities for run-up simulations carried out with $d_{visc} \in \{30,\ 100,\ 170,\ 240,\ 300\}$ N ms mm^{-1}. The simulations indicate a smooth transition between the two bifurcation paths. As can be seen, the higher the damping is, the lower the amplitudes of the bearing eccentricities become.

4.2.5. Parameter study 2: transition from bifurcation path 2a to bifurcation path 2b

Now, a parameter study is considered to investigate the transition from bifurcation path 2a to bifurcation path 2b, see Fig. 25. For

that purpose, both the stiffness coefficient c_{elast} and the damping coefficient d_{visc} are successively reduced. The first three run-simulations exhibit bifurcation path 2a: reducing c_{elast} and d_{visc}, the bearing eccentricities get continuously smaller. For the parameters $c_{\text{elast}} = 225$ N mm^{-1} and $d_{\text{visc}} = 100$ N ms mm^{-1} (green curve), the rotor system is stable in the complete speed range. For $c_{\text{elast}} = 100$ N mm^{-1} and $d_{\text{visc}} = 40$ N ms mm^{-1} (magenta curve), the system is stable up to $t \approx 2200$ ms. At $t \approx 2200$ ms, a bifurcation occurs and the whirl/whip of the fluid films excite the tilting ring mode *Mode_3(f)* (more accurately, a synchronized tilting/translational ring mode, see above).

4.2.6. *Parameter study 3: influence of ring tilting stiffness (lever length a) in connection with bifurcation path 2b*

The influence of the ring tilting stiffness on the bifurcation behavior of the system is regarded next. The stiffness and damping parameters are kept constant ($c_{\text{elast}} = 100$ N mm^{-1} and $d_{\text{visc}} = 40$ N ms mm^{-1}). However, the lever length a of the left and right part of the supporting structure, see Fig. 10, is varied, which directly changes the tilting stiffness of the supporting structure. Results of run-up simulations for different values of a are collected in Fig. 26. For the lever lengths $a = 14$ mm and $a = 12$ mm, the simulations show a bifurcation into the translational ring mode at $t \approx 2250$ ms. For lever lengths $a \leq 10$ mm, the simulations show a bifurcation into the tilting ring mode (strictly speaking: synchronized tilting/translational ring mode). The smaller the lever length gets, the earlier the bifurcation occurs.

4.2.7. *Parameter study 4: influence of ring damping in connection with bifurcation path 2b*

Fig. 27 highlights the influence of the damping coefficient d_{visc} on bifurcation path 2b. In this subsection, we consider both run-up simulations with and without ring tilting.

- In both cases (with and without ring tilting), a reduction of d_{visc} entails that the bifurcation occurs earlier.
- Regarding the case with ring tilting, two different bifurcation scenarios are observed.

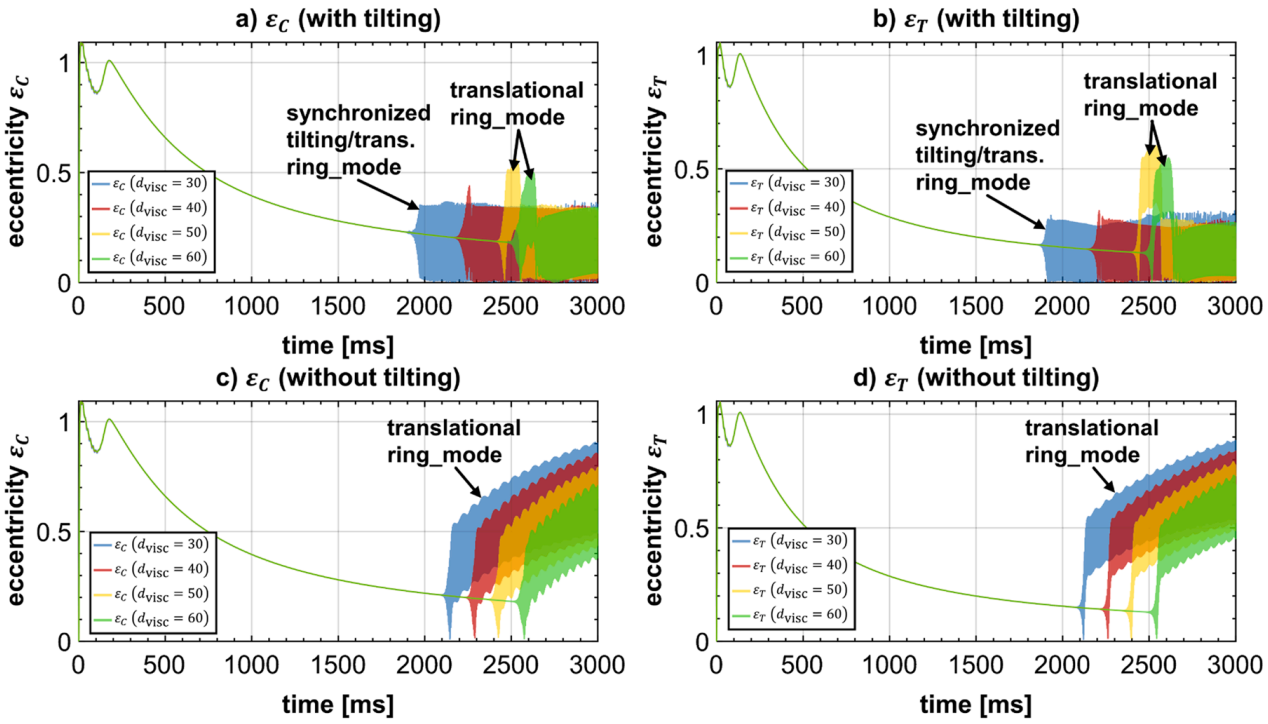

Fig. 27. Parameter study 4: Influence of the ring damping on bifurcation path 2b with $c_{\text{elast}} = 100$ N mm^{-1} and different viscous damping coefficients d_{visc}: (a),(b) compressor- and turbine-sided bearing eccentricities $\varepsilon_C(t)$ and $\varepsilon_T(t)$ (with ring tilting); (c),(d) compressor- and turbine-sided bearing eccentricities $\varepsilon_C(t)$ and $\varepsilon_T(t)$ (without ring tilting).

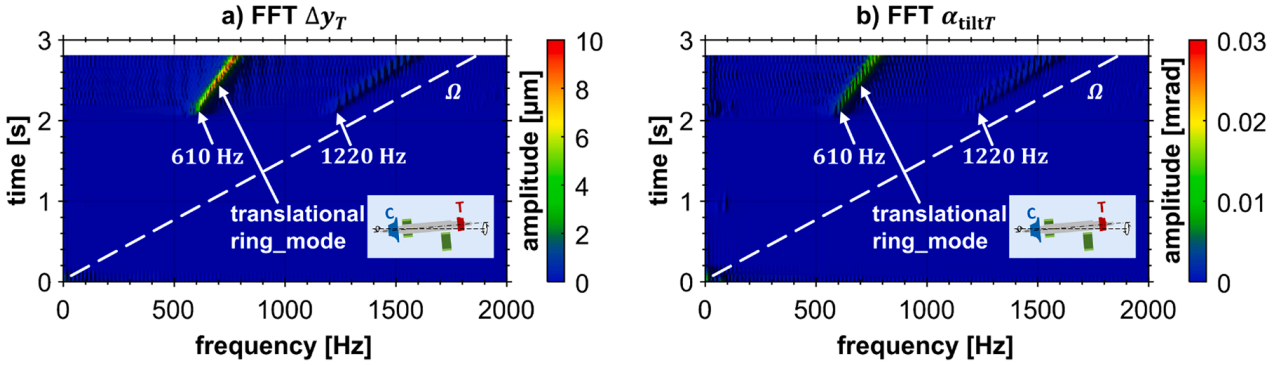

Fig. 28. Case 1: FFTs of $\Delta y_T(t)$ and $\alpha_{tiltT}(t)$ for a lever length of $a = 12$ mm (additional result plots for the run-up simulation of Section 4.2.6).

(i) The run-up simulations with higher damping ($d_{visc} \in \{50,\ 60\}$ N ms mm^{-1}) exhibit two bifurcations: firstly, the whirl/whip is exciting the translational ring mode; shortly afterwards, a mode jump is observed and the whirl/whip is then exciting the synchronized tilting/translational ring mode.

(ii) Regarding the run-up simulations with lower damping ($d_{visc} \in \{30,\ 40\}$ N ms mm^{-1}), the whirl/whip is directly exciting the synchronized tilting/translational ring mode.

- Not considering ring tilting effects, the translational ring mode is excited by the whirl/whip.

4.3. *Physical explanation of the nonlinear mode coupling effect in connection with bifurcation path 2b*

Considering bifurcation path 2b, a physically interesting mode coupling effect can be observed, which is further discussed in this section. Within bifurcation path 2b, ring modes are excited by the whirl/whip frequency of the fluid films. Basically, two types of ring modes can be distinguished, namely the tilting ring modes *Mode_3(f)* and *Mode_4(f)* as well as the translational ring modes *Mode_5(f)* and *Mode_6(f)*, see Fig. 32 in the Appendix. For the here examined rotor/bearing system, mainly the forward modes are excited (note the frequency spectra in Sections 4.1 and 4.2). Therefore, backward modes are not considered in the subsequent discussion.

At first, one would expect that the whirl/whip of a fluid film will excite either a tilting ring mode or a translational ring mode. Moreover, one would expect that the air whirl/whip will initially excite the ring mode with the lower eigenfrequency. The question which ring mode has the smaller frequency – the tilting ring mode or the translational ring mode – depends on the bearing parameters. Specifying the ring supporting stiffness (c_{foil} or c_{elast}), the ratio between the eigenfrequencies of the tilting and translational ring modes can easily be adjusted by changing the lever length a of the ring mounting forces $\boldsymbol{F}_{left}$ and $\boldsymbol{F}_{right}$ (distance a in Fig. 10). For small values

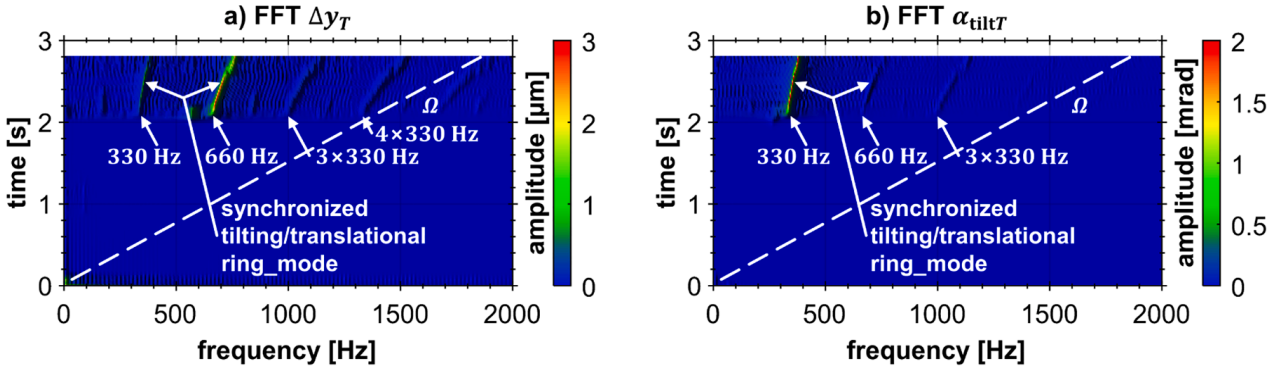

Fig. 29. Case 2: FFTs of $\Delta y_T(t)$ and $\alpha_{tiltT}(t)$ for a lever length of $a = 10$ mm (additional result plots for the run-up simulation of Section 4.2.6).

of a, the eigenfrequencies of the tilting ring modes will be smaller than the eigenfrequencies of the translational ring modes, since the tilting stiffness is rather small. For larger values of a, however, the eigenfrequencies of the tilting modes may become larger than the translational modes, since the tilting stiffness increases with increasing a.

The run-up simulations of Section 4.2.6 have shown that for larger lever lengths a, the air whirl/whip will excite the translational ring modes, since the tilting stiffness is rather large. This situation, where the air whirl/whip is initially exciting the translational ring modes, is called *case 1* in the following.

Fixing the stiffness c_{elast} and reducing the lever length a, the ring tilting eigenfrequencies will become successively lower, while the translational ring eigenfrequencies will remain unchanged.

For a sufficiently small lever length a, the ring tilting eigenfrequencies will get smaller than the translational ring eigenfrequencis and one would therefore expect that the air whirl/whip will – at least initially – excite the tilting ring modes (in the following called *case 2*).

4.3.1. Case 1

The case 1 can, for instance, clearly be observed in the run-up simulations of Section 4.2.6 for $a = \{12,14\}$, see Fig. 26. In Fig. 28, additional result plots are depicted for the simulation with $a = 12$, namely an FFT of the relative vertical journal displacement $\Delta y_T = y_{JT} - y_{RT}$ of the turbine-sided bearing with respect to the ring (Fig. 28a) and an FFT of the ring tilting angle $\alpha_{\text{tilt}T}$ (Fig. 28b). As can be seen in Fig. 28, the ring motion in the whirl/whip regime is almost translational with a whirl frequency of 610 Hz at the onset of the whirl: the compressor-sided whirl is exciting the translational ring mode *Mode_5(f)* and the turbine-sided whirl the translational ring mode *Mode_6(f)*. Since the rotor mode shapes *Mode_5(f)* and *Mode_6(f)* are both conical, the ring motions are not purely translational, but also have a small tilting component. Note, however, that the amplitudes of the tilting angle $\alpha_{\text{tilt}T}$ are very small (< 0.03 mrad).

4.3.2. Case 2

The case 2 – i.e. a pure excitation of the ring tilting modes – has, however, not been detected in any run-up simulation. In contrast, the run-up simulations of Section 4.2.6 for $a = \{4,6,8,10\}$ in Fig. 26 show the following two interesting phenomena:

- The ring tilting modes are always excited together with the translational ring modes.
- The frequencies of the tilting and translational ring modes synchronize so that the frequency ratio is always 2.

In other words, a nonlinear 1:2 mode coupling effect is detected in connection with the occurrence of the tilting ring modes. In order to more clearly explain this mode synchronization phenomenon, two additional plots for the run-up simulation of Section 4.2.6 with $a = 10$ are collected in Fig. 29: an FFT of the relative vertical journal displacement $\Delta y_T = y_{JT} - y_{RT}$ of the turbine-sided bearing with respect to the ring (Fig. 29a) as well as an FFT of the ring tilting angle $\alpha_{\text{tilt}T}$ (Fig. 29b). The relative vertical journal displacement Δy_T clearly shows the frequency of the translation ring mode (≈ 660 Hz at the onset of the whirl), while the ring tilting angle $\alpha_{\text{tilt}T}$ clearly exhibits the frequency of the tilting ring mode (≈ 330 Hz at the onset of the whirl). Note that the amplitudes of the tilting angle $\alpha_{\text{tilt}T}$ are significantly larger compared to case 1 (≈ 2 mrad).

This astonishing mode coupling phenomenon can be explained in a rather straightforward manner with the help of the asymmetric pressure distribution in the air gap, when the journal performs a tilting motion with respect to the ring. To basically describe the 1:2 mode coupling effect, we just consider the simple (academic) case that the rotor journal performs a planar tilting motion with respect to the fixed ring ($\boldsymbol{r}_R \equiv 0$). Therefore, the journal center M_J is placed eccentrically to the ring center according to $\boldsymbol{r}_J = [0, y_{J0}, 0]^T = const.$, where the eccentricity of M_J is assumed to be constant. Then, a planar tilting motion of the journal around the x_J-axis according to $\alpha_{\text{tilt}}(t) = \widehat{\alpha}_{\text{tilt}} \sin(\omega_{\text{tilt}} t)$ is prescribed ($\beta_{\text{tilt}} \equiv 0$).

- At the beginning at time $t = 0$, the tilting between the journal and the ring is zero. The rotating journal (rotor speed Ω) produces a pressure field, which is symmetrical to the center line of the ring (Fig. 30a). The resulting bearing force $F_{p,y_R}(0)$ acts in negative y_R-direction; the resulting bearing torque $M_{p,x_R}(0)$ is zero.
- Then, the time point $t_1 = \frac{\pi}{2\omega_{\text{tilt}}}$ is considered, where the journal is tilted with the angle $+\alpha_{\text{tilt}}$ around the x_J-axis (Fig. 30b). As a consequence, the pressure field gets asymmetric with respect to the bearing center line so that a resulting bearing torque $M_{p,x_R}(t_1) < 0$ is generated.
- Next, the tilting of the journal is reduced so that at the time point $t_2 = \frac{\pi}{\omega_{\text{tilt}}}$ again the initial position is achieved ($F_{p,y_R}(t_2) = F_{p,y_R}(0)$ and $M_{p,x_R}(t_2) = 0$).

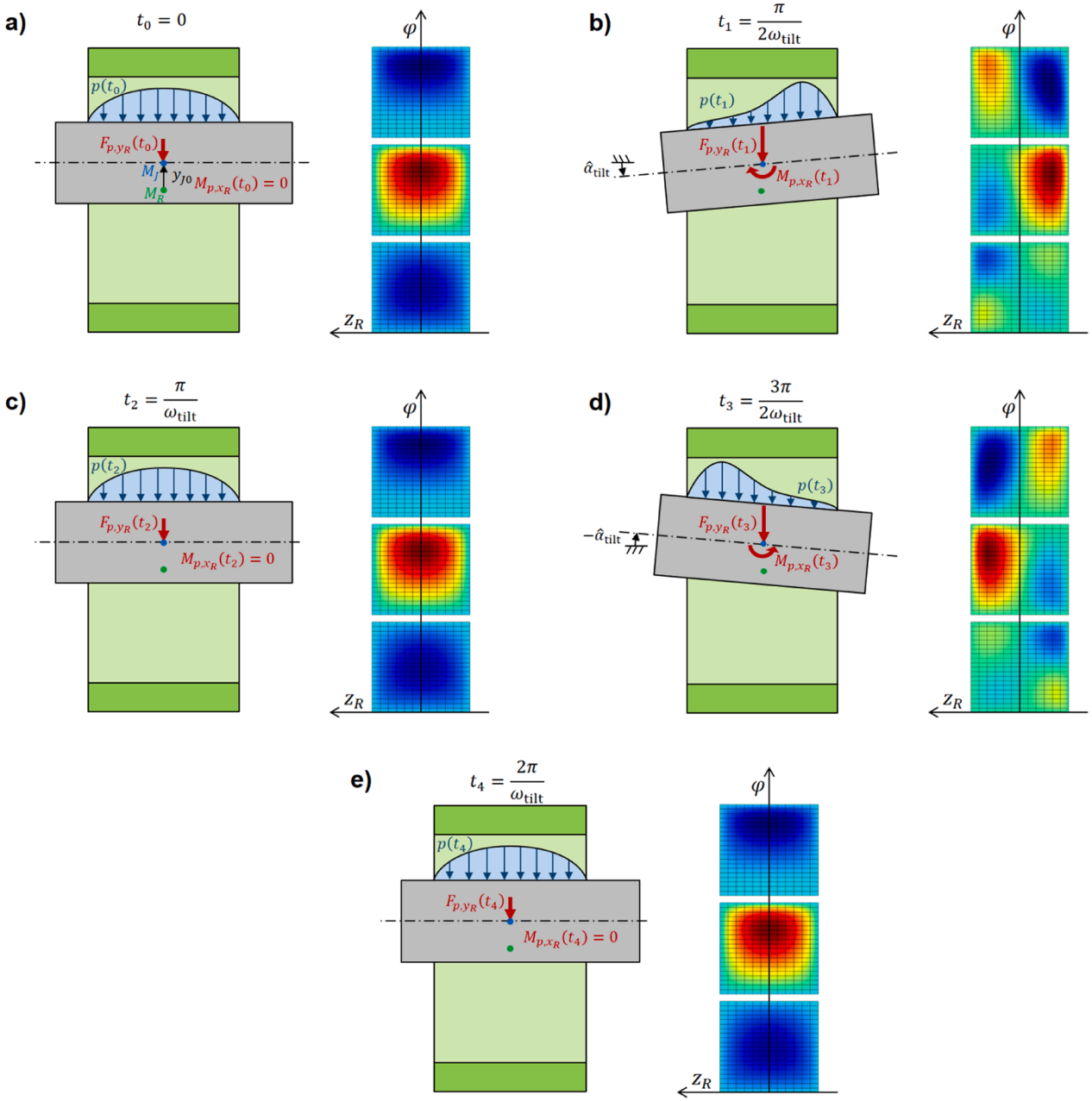

Fig. 30. Physical explanation of the mode coupling effect: ring tilting at five different time points with corresponding bearing forces/torques acting at the rotor journal (left) and pressure field (right).

- At time point $t_3 = \frac{3\pi}{2\omega_{tilt}}$, the journal is tilted with the angle $-\alpha_{tilt}$ in the opposite direction. The resulting bearing force $F_{p,y_R}(t_3)$ equals $F_{p,y_R}(t_1)$; the resulting bearing torque is $M_{p,x_R}(t_3) = -M_{p,x_R}(t_1)$.
- Finally, at the time point t_4, again the initial position is achieved ($F_{p,y_R}(t_4) = F_{p,y_R}(0)$ and $M_{p,x_R}(t_4) = 0$).

As can be seen, within a tilting period ($0 \rightarrow \alpha_{tilt} \rightarrow 0 \rightarrow -\alpha_{tilt} \rightarrow 0$) resulting bearing forces $F_{p,y_R}(t)$ with the double frequency are generated.

The above described planar description of the mode coupling effect may easily be generalized to the case, where rotor and ring perform a spherical motion, which of course occurs when the air whirl/whip is exciting the ring modes. For the sake of brevity, we omit a detailed discussion of the 3D case here. Considering, for instance, the case that the rotor journal performs a conical motion with respect to the ring – i.e. the journal center M_J carries out a circular motion with respect to the ring, which is superimposed by a spherical tilting motion – one can simply see that the frequency of the resulting bearing forces is again twice the frequency of the resulting bearing torques.

5. Conclusions

In high-speed turbomachines, air bearings are often used if oil-free operating conditions are required. Besides the frequently used air foil bearings, also air bearings with a rigid housing may be applied. Considering rigid air bearings, the bore geometry has to be chosen very carefully in order to obtain a stable rotor system. Often, herringbone bearings are used. They exhibit a good stability behavior, but have different practical/technical drawbacks. Rigid air bearings with a circular or with a three-lobe bore geometry, on the other hand, have various advantages compared to herringbone bearings, but exhibit a rather poor stability behavior. Above the threshold speed of instability, rotors in rigid air bearings can usually not be operated, since the rotor amplitudes (bearing eccentricities) are too large.

The problem with the reduced stability can be solved by using air ring bearings, where the bearing bushing is flexibly mounted in the housing so that external friction/damping is provided by the supporting structure of the ring. In this work, air ring bearings with a three-lobe bore geometry have been analyzed. Two cases have been considered:

i) The ring is mounted by a foil structure so that dissipation is generated by dry friction.
ii) The ring is visco-elastically mounted so that dissipation is provided by viscous damping.

If the parameters of the air ring bearings are chosen appropriately, the rotor can be operated above the threshold speed of instability with moderate and technically tolerable rotor amplitudes and bearing eccentricities.

Rotor systems with air ring bearings exhibit a very interesting nonlinear vibration and bifurcation behavior. Depending on the system parameters, typical high-speed rotor systems with air ring bearings can exhibit three different bifurcation paths during a rotor run-up (rotor run-down). If the supporting stiffness of the ring is chosen too large or if the dissipation of the ring mounting is too low, the dangerous *bifurcation path 1* will occur. Using, however, a moderate ring supporting stiffness and an increased ring dissipation, self-excited oscillations with harmless amplitudes or even stable imbalance oscillations around the equilibrium position are observed (*bifurcation path 2a*). If the stiffness is chosen rather low and the ring mass/inertia rather large, the dangerous *bifurcation path 2b* is detected, where the whirl/whip of the air films excites a higher-frequency ring mode (tilting ring mode, translational ring mode) with relatively large amplitudes.

With adequate simulation models, it is rather uncomplicated to find design parameters for the rotor/bearing system, which allow a secure and robust operation of the system within bifurcation path 2a. The basin of attraction of bifurcation path 2a is relatively large so that a robust design may be developed with the help of numerical simulations or experiments.

One of the main findings of this manuscript is that it is usually not necessary to take into account ring tilting effects in the simulation model for accurately predicting bifurcation path 1 and bifurcation path 2a. The analyses in this work have, however, shown that consideration of ring tilting effects is necessary for correctly predicting bifurcation path 2b. Ignoring ring tilting effects, only translational ring mode shapes can be detected. The simulations have, however, shown that the excitation of ring tilting modes may often be more critical than the excitation of translational ring modes, since the eigenfrequencies of the ring tilting modes are often lower than the eigenfrequencies of the translational ring modes.

In connection with bifurcation path 2b, also a physically interesting nonlinear mode coupling effect has been detected. This astonishing synchronization phenomenon is only observed in the case, where ring tilting modes are excited. In the case, where the whirl/whip of the fluid films is just exciting a translational ring mode (see, e.g., Sections 4.1.7 and 4.2.7) – which may happen if the ring tilting stiffness is rather large – the mode coupling effect is not observed. For smaller ring tilting stiffnesses, however, where the whirl/whip frequency initially intends to excite the (lower-frequency) tilting ring modes, the (higher-frequency) translational ring modes are also exited so that the frequency spectra clearly shows both frequencies: the tilting as well as the translational ring mode frequency. Even more interesting than the simultaneous occurrence of both ring modes is the effect that the frequencies synchronize with a frequency ratio of 1:2. In Section 4.3, a rather simple physical explanation of this mode synchronization phenomenon has been provided.

CRediT authorship contribution statement

Pascal Zeise: Conceptualization, Writing – review & editing, Software. **Bernhard Schweizer:** Conceptualization, Writing – review & editing.

Declaration of Competing Interest

The authors declare that they have no known competing financial interests or personal relationships that could have appeared to influence the work reported in this paper.

Data availability

No data was used for the research described in the article.

Appendix

This appendix contains an eigenmode analysis of the linearized rotor/bearing system of Section 3. For this purpose, the two rings are mounted linear-elastically in the housing with the linear springs $c_{\mathrm{Ring},x} = c_{\mathrm{Ring},y} = 100$ N mm^{-1}. The stiffness behavior of the air films is highly nonlinear and generally a function of the relative displacement of the rotor journal with respect to the ring. To estimate the translational air film stiffness, we consider the case that the rotating journal (rotor speed Ω) is quasi-statically moved from the bearing center ($\Delta y = 0$) in negative y-direction; the ring is assumed to be fixed. The resulting bearing force $F_{p,y_R}(\Delta y)$ according to Eq. (9) can be calculated with the Reynolds Eq. (6) as a function of the relative displacement Δy. The slope $\partial F_{p,y_R}(\Delta y)/\partial \Delta y$ may be used for an estimation of the air film stiffness. Fig. 31 shows the air film stiffness as a function of the dimensionless displacement $\varepsilon = \Delta y / C$. For a rotor speed of $\Omega = 1500$ Hz and a relative displacement of $\varepsilon = 0.2$, we obtain a translational stiffness of $c_{\mathrm{trans,air}} \approx 755$ N mm^{-1}. Accordingly, the tilting stiffness of the fluid film may be estimated. For $\Omega = 1500$ Hz, $\varepsilon = 0.2$ and $a = 10$ mm, a tilting stiffness of $c_{\mathrm{tilt,air}} \approx 2.6E+4$ N mm /rad is obtained.

For the subsequent eigenmode analysis, the air film is therefore replaced by the translational stiffnesses $c_{\mathrm{trans,air},x} = c_{\mathrm{trans,air},y} \approx 755$ N mm^{-1} and the tilting stiffnesses $c_{\mathrm{tilt,air},\alpha} = c_{\mathrm{tilt,air},\beta} \approx 2.6E+4$ N mm /rad. Note that due to the high stiffness of the rotor shaft, only rigid body modes are relevant in the considered rotor speed range (maximum rotor speed: 2000 Hz), i.e. rotor elasticity is neglected in the analysis. Also, damping effects are neglected in the eigenmode calculations.

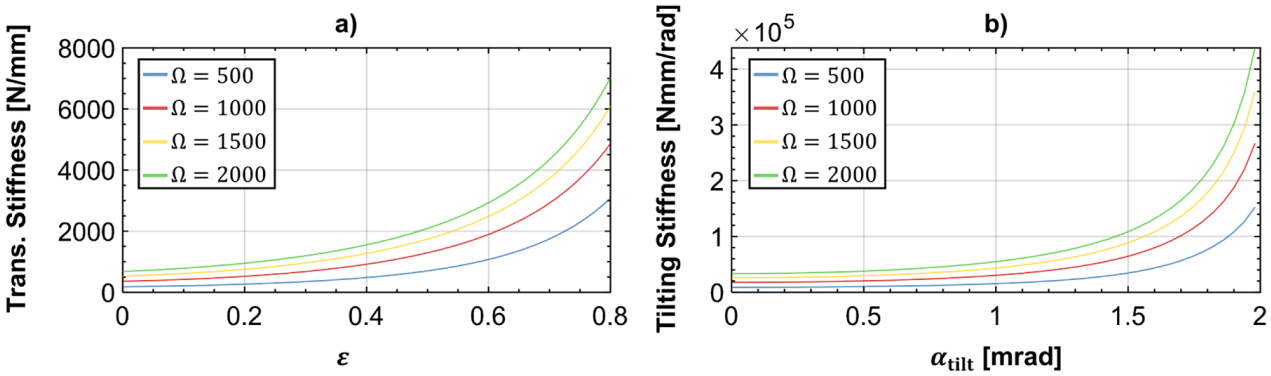

Fig. 31. (a) Translational air film stiffness $c_{\mathrm{trans,air}}$ as a function of the dimensionless journal displacement ε for different rotational speeds Ω ($\alpha_{\mathrm{tilt}} = \beta_{\mathrm{tilt}} = 0$); (b) Tilting stiffness $c_{\mathrm{tilt,air}}$ as a function of the tilting angle α_{tilt} for $\varepsilon = 0.2$.

An eigenmode calculation of the linearized rotor system for a rotor speed of $\Omega = 1500$ Hz shows the following results:

- *Mode_1(b)* and *Mode_1(f)* are conical modes with a vibration node at the compressor-sided bearing: the backward mode *Mode_1(b)* has an eigenfrequency of ≈ 45 Hz; the eigenfrequency of the corresponding forward mode *Mode_1(f)* is ≈ 69 Hz. Rotor and rings oscillate inphase. *Mode_1(f)* is depicted in Fig. 32a.
- *Mode_2(b)* and *Mode_2(f)* are conical modes with a vibration node at the turbine-sided bearing: the backward mode *Mode_2(b)* shows an eigenfrequency of ≈ 71 Hz; the corresponding forward mode *Mode_2(f)* has an eigenfrequency of ≈ 112 Hz. Rotor and rings oscillate inphase. *Mode_2(f)* is illustrated in Fig. 32b.
- *Mode_3(b)* and *Mode_3(f)* are tilting ring modes, where the rings oscillate against the shaft: the backward mode *Mode_3(b)* has an eigenfrequency of ≈ 298 Hz; the eigenfrequency of the corresponding forward mode *Mode_3(f)* is also ≈ 298 Hz. The rings oscillate antiphase; the rotor motion is very small. *Mode_3(f)* is shown in Fig. 32c.
- *Mode_4(b)* and *Mode_4(f)* are also tilting ring modes, where the rings oscillate against the shaft: the backward mode *Mode_4(b)* has an eigenfrequency of ≈ 299 Hz; the corresponding forward mode *Mode_4(f)* shows also an eigenfrequency of ≈ 299 Hz. Rotor and rings oscillate inphase; the rotor motion is very small. *Mode_4(f)* is sketched in Fig. 32d.
- *Mode_5(b)* and *Mode_5(f)* are conical modes with a vibration node at the compressor-sided bearing: the backward mode *Mode_5(b)* has an eigenfrequency of ≈ 682 Hz; the eigenfrequency of the corresponding forward mode *Mode_5(f)* is ≈ 685Hz. Rotor and rings oscillate antiphase (translational ring modes). *Mode_5(f)* is shown in Fig. 32e.
- *Mode_6(b)* and *Mode_6(f)* are conical modes with a vibration node at the turbine-sided bearing: the backward mode *Mode_6(b)* has an eigenfrequency of ≈ 693 Hz; the corresponding forward mode *Mode_6(f)* shows an eigenfrequency of ≈ 697 Hz. Rotor and rings oscillate antiphase (translational ring modes). *Mode_6(f)* is sketched in Fig. 32f.

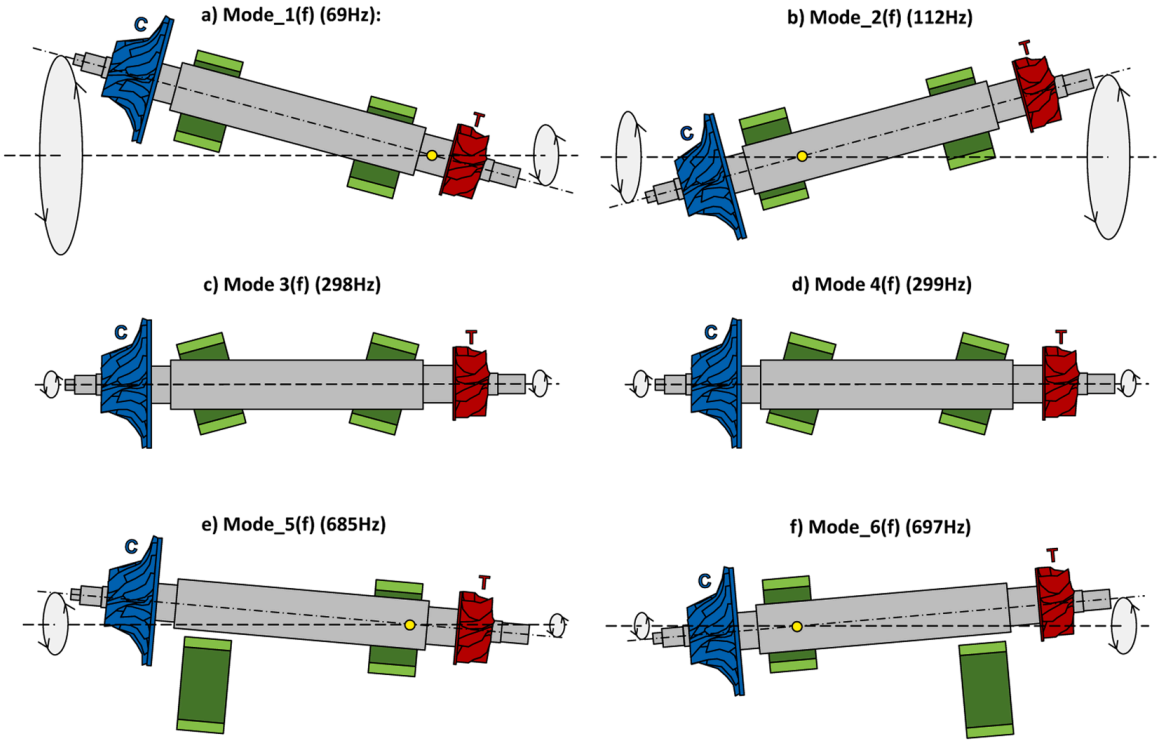

Fig. 32. Rigid body forward mode shapes. (a) and (b): inphase mode shapes *Mode_1(f)* and *Mode_2(f)*; (c) and (d): ring mode shapes *Mode_3(f)* and *Mode_4(f)* (tilting ring modes); (e) and (f): antiphase ring mode shapes *Mode_5(f)* and *Mode_6(f)* (translational ring modes).

References

[1] C. DellaCorte, K. Radil, R. Bruckner, S. Howard, Design, fabrication, and performance of open source generation I and II compliant hydrodynamic gas foil bearings, Tribol. Trans. 51 (3) (2008) 254–264.

[2] H. Heshmat, W. Shapiro, S. Gray, Development of foil journal bearings for high load capacity and high speed whirl stability, J. Lubr. Technol. 104 (2) (1982) 149–156.

[3] D. Kim, Parametric studies on static and dynamic performance of air foil bearings with different top foil geometries and bump stiffness distributions, J. Tribol. 129 (2) (2007) 354–364.

[4] K. Feng, X. Zhao, Z. Guo, Design and structural performance measurements of a novel multi-cantilever foil bearing, Proc. Inst. Mech. Eng. Part C J. Mech. Eng. Sci. 229 (10) (2015) 1830–1838.

[5] C. Li, J. Du, Y. Yao, Study of load carrying mechanism of a novel three-pad gas foil bearing with multiple sliding beams, Mech. Syst. Signal Process 135 (2020).

[6] L. San Andrés, T.A. Chirathadam, A metal mesh foil bearing and a bump-type foil bearing: comparison of performance for two similar size gas bearings, J. Eng. Gas Turbine Power 134 (10) (2012), 102501.

[7] J.-H. Song, D. Kim, Foil gas bearing with compression springs: analyses and experiments, J. Tribol. 129 (3) (2007) 628–639.

[8] E.E. Swanson, P. Shawn O'Meara, The wing foil: a novel compliant radial foil bearing design, J. Eng. Gas Turbine Power 140 (8) (2018).

[9] J.C. Wilkes, J. Wade, A. Rimpel, J. Moore, E. Swanson, J. Grieco, J. Brady, Impact of bearing clearance on measured stiffness and damping coefficients and thermal performance of a high-stiffness generation 3 foil journal bearing, J. Eng. Gas Turbine Power 140 (7) (2018).

[10] T.H. Kim, L. San Andrés, Effects of a mechanical preload on the dynamic force response of gas foil bearings: measurements and model predictions, Tribol. Trans. 52 (4) (2009) 569–580.

[11] K. Sim, Y.-B. Lee, T.H. Kim, Effects of mechanical preload and bearing clearance on rotordynamic performance of lobed gas foil bearings for oil-free turbochargers, Tribol. Trans. 56 (2013) 224–235.

[12] I. Ghalayini, P. Bonello, The application of the arbitrary-order galerkin reduction method to the dynamic analysis of a rotor with a preloaded single-pad foil-air bearing, J. Eng. Gas Turbine Power 144 (2022), 091015.

[13] M. Mahner, P. Li, A. Lehn, B. Schweizer, Numerical and experimental investigations on preload effects in air foil journal bearings, J. Eng. Gas Turbine Power 140 (3) (2018), 032505.

[14] J. Park, D. Kim, K. Sim, Rotordynamic analysis of piezoelectric gas foil bearings with a mechanical preload control based on structural parameter identifications, Appl. Sci. 11 (2021) 2330.

[15] I. Ghalayini, P. Bonello, Development of a rotor test rig with a novel controllable preload foil-air bearing, Precis. Eng. 76 (2022) 340–359.

[16] S. von Osmanski, I.F. Santos, Gas foil bearings with radial injection: multi-domain stability analysis and unbalance response, J. Sound Vib. 508 (2021), 116177.

[17] S.T. Heinemann, J.W. Jensen, S. von Osmanski, I.F. Santos, Numerical modelling of compliant foil structure in gas foil bearings: comparison of four top foil models with and without radial injection, J. Sound Vib. 547 (2023), 117513.

[18] J.W. Lund, Calculation of stiffness and damping properties of gas bearings, J. Lubricat. Tech. 90 (1968) 793–803.

[19] J.S. Larsen, I.F. Santos, S. von Osmanski, Stability of rigid rotors supported by air foil bearings: comparison of two fundamental approaches, J. Sound Vib. 381 (2016) 179–191.

[20] S. von Osmanski, J.S. Larsen, I.F. Santos, Multi-domain stability and modal analysis applied to gas foil bearings: three approaches, J. Sound Vib. 472 (2020), 115174.

[21] P. Bonello, T. Pourashraf, A comparison of modal analyses of foil-air bearing rotor systems using two alternative linearisation methods, Mech. Syst. Signal Process 170 (2022), 108714.
[22] P. Bonello, H. Pham, The efficient computation of the nonlinear dynamic response of a foil–air bearing rotor system, J. Sound Vib. 333 (15) (2014) 3459–3478.
[23] P. Bonello, The extraction of Campbell diagrams from the dynamical system representation of a foil-air bearing rotor model, Mech Syst Signal Process 129 (2019) 502–530.
[24] T. Pourashraf, P. Bonello, A new Galerkin Reduction approach for the analysis of a fully coupled foil air bearing rotor system with bilinear foil model, J. Sound Vib. 546 (2023), 117367.
[25] H. Michel, R. Liebich, Challenges in validating a thermo-hydrodynamic gas foil bearing model, J. Eng. Gas Turbine Power 143 (2021), 041029.
[26] M. Mahner, M. Bauer, B. Schweizer, Numerical analyzes and experimental investigations on the fully-coupled thermo-elasto-gasdynamic behavior of air foil journal bearings, Mech Syst Signal Process 149 (2021), 107221.
[27] M. Mahner, M. Bauer, A. Lehn, B. Schweizer, An experimental investigation on the influence of an assembly preload on the hysteresis, the drag torque, the lift-off speed and the thermal behavior of three-pad air foil journal bearings, Tribol. Int. 137 (2019) 113–126.
[28] J.H. Vohr, C.Y. Chow, Characteristics of herringbone-grooved, gas-lubricated journal bearings, J. Basic Eng. 87 (1965) 568–576.
[29] S.B. Malanoski, Experiments on an ultrastable gas journal bearing, J. Lubr. Technol. 89 (1967) 433–438.
[30] E. Iseli, J. Schiffmann, Stability and unbalance analysis of rigid rotors supported by spiral groove bearings: comparison of different approaches, J. Eng. Gas Turbine Power (2021).
[31] P.K. Bättig, P.H. Wagner, J.A. Schiffmann, Experimental investigation of enhanced grooves for herringbone grooved journal bearings, J. Tribol. 144 (2022), 091801.
[32] L.E. Olmedo, W. Liu, K. Gjika, J. Schiffmann, Thermal management for gas lubricated, high-speed turbomachinery, Appl. Therm. Eng. 218 (2023), 119229.
[33] L. Gu, E. Guenat, J. Schiffmann, A review of grooved dynamic gas bearings, Appl. Mech. Rev. 72 (2020), 010802.
[34] F. Al-Bender, Air Bearings, Wiley, 2021.
[35] T. Waumans, J. Peirs, F. Al-Bender, D. Reynaerts, Aerodynamic journal bearing with a flexible, damped support operating at 7.2 million DN, J. Micromech. Microeng. 21 (2011), 104014.
[36] P. Bättig, J. Schiffmann, Unstable tilting motion of flexibly supported gas bearing bushings, Mech Syst Signal Process 162 (2022), 107981.
[37] P. Zeise, B. Schweizer, Dynamics, stability and bifurcation analysis of rotors in air ring bearings, J. Sound Vib. 521 (2022), 116392.
[38] A. Tatara, H. Koike, A. Iwasaki, The stability of flexibly supported, externally pressurized gas journal bearings: case of a rigid rotor, Bull. JSME 16 (100) (1973) 1573–1579.
[39] N. Miyanaga, J. Tomioka, Effect of support stiffness and damping on stability characteristics of herringbone-grooved aerodynamic journal bearings mounted on viscoelastic supports, Tribol. Int. 100 (2016) 195–203.
[40] K. Somaya, K. Okubo, M. Miyatake, S. Yoshimoto, Threshold speed of instability of a herringbone-grooved rigid rotor with a bearing bush flexibly supported by straight spring wires, in: Proceedings of the ASME Turbo Expo2015: Turbine Technical Conference and Exposition Volume 7A: Structures and Dynamics, ASME, Montreal, Quebec, Canada, 2015. V07AT31A015.
[41] A. Muszynska, Rotordynamics, CRC press, 2005.
[42] A. Chasalevris, Finite length floating ring bearings: operational characteristics using analytical methods, Tribol. Int. 94 (2016) 571–590.
[43] A. Chasalevris, J.-C. Louis, Evaluation of transient response of turbochargers and turbines using database method for the nonlinear forces of journal bearings, Lubricants 7 (9) (2019) 78.
[44] C.J. Myers, Bifurcation theory applied to oil whirl in plain cylindrical journal bearings, J. Appl. Mech. 51 (1984) 244–250.
[45] J. Shaw, S.W. Shaw, The effects of unbalance on oil whirl, Nonlinear Dyn. 1 (1990) 293–311.
[46] A. Chasalevris, Stability and Hopf bifurcations in rotor-bearing-foundation systems of turbines and generators, Tribol. Int. 145 (2020), 106154.
[47] F. Balducchi, M. Arghir, R. Gauthier, Experimental analysis of the unbalance response of rigid rotors supported on aerodynamic foil bearings, J. Vib. Acoust. 137 (6) (2015).
[48] J.S. Larsen, I.F. Santos, On the nonlinear steady-state response of rigid rotors supported by air foil bearings—theory and experiments, J. Sound Vib. 346 (2015) 284–297.
[49] P. Bonello, M.B. Hassan, An experimental and theoretical analysis of a foil-air bearing rotor system, J. Sound Vib. 413 (2018) 395–420.
[50] M.M. Khonsari, E.R. Booser, Applied Tribology, 2nd Edition, John Wiley&Sons, 2008.
[51] A.Z. Szeri, Fluid Film Lubrication, 2nd ed., Cambridge University Press, 2010.
[52] K.E. Brenan, S.L. Campbell, L.R. Petzold, Numerical Solution of Initial-Value Problems in Differential-Algebraic Equations, 14, Siam, 1996. Volume.
[53] M.B. Dobrica, M. Fillon, Mixed Lubrication, in: Q.J. Wang, YW. Chung (Eds.), Encyclopedia of Tribology, Springer, Boston, MA, 2013.
[54] M. Arghir, O. Benchekroun, A new structural bump foil model with application from start-up to full operating conditions, J. Eng. Gas Turbine Power 141 (10) (2019).
[55] P. Flores, M. Machado, M.T. Silva, J.M. Martins, On the continuous contact force models for soft materials in multibody dynamics, Multibody Syst. Dyn. 25 (2011) 357–375.
[56] E.J. Haug, Computer-Aided Kinematics and Dynamics of Mechanical Systems, Allyn and Bacon, 1989.
[57] A. Shabana, Dynamics of Multibody Systems, Cambridge University Press, 2005.
[58] C.W. Gear, G.K. Gupta, B.J. Leimkuhler, Automatic integration of the Euler-Lagrange equations with constraints, J. Comput. Appl. Math. 12-13 (1985) 77–90.
[59] C. Gomes, C. Thule, D. Broman, P.G. Larsen, H. Vangheluwe, Co-simulation: a survey, ACM Comput Surv 51 (3) (2018) 1–33.
[60] B. Schweizer, P. Li, D. Lu, Explicit and implicit co-simulation methods: stability and convergence analysis for different solver coupling approaches, J. Comput. Nonlinear Dyn. 10 (5) (2015).
[61] I. Hafner, N. Popper, An overview of the state of the art in co-simulation and related methods, SNE 31 (2021) 185–200.

Dritte Veröffentlichung

Pascal Zeise und Bernhard Schweizer. „Numerical investigations on high-speed turbocompressor rotor systems with air ring bearings: Nonlinear vibration behavior and optimization“. In: *Applied and Computational Mechanics* 17.2 (2023), S. 169–190. ISSN: 1802680X. DOI: 10.24132/acm.2023.836

https://doi.org/10.24132/acm.2023.836

Applied and Computational Mechanics 17 (2023) 169–190

Applied and Computational Mechanics

Numerical investigations on high-speed turbo-compressor rotor systems with air ring bearings: Nonlinear vibration behavior and optimization

P. Zeise[a,*], B. Schweizer[a]

[a] *Institute of Applied Dynamics, Technical University of Darmstadt, Otto-Berndt-Str. 2, 64287 Darmstadt, Germany*

Received 10 May 2023; accepted 7 November 2023

Abstract

Regarding aerodynamic bearings, mainly two basic types can be distinguished: air bearings with a rigid housing and air foil bearings with an elastic supporting structure. Here, a modified bearing concept – called air ring bearing – is investigated, which may be considered as a further development of rigid air bearings or as a combination of the two basic bearing types. The idea of air ring bearings is to insert a ring-shaped bearing bushing between the shaft and the foil structure. Alternatively, a visco-elastic supporting structure (e.g., an elastomer) can be applied to connect the bushing ring with the housing. In the first case, external dissipation is mainly generated by dry friction. In the latter case, viscous damping is used to provide external dissipation. Due to the external friction/damping generated by the ring mounting structure, rotor systems with air ring bearings can be operated above the linear threshold speed of instability so that stable self-excited vibrations with moderate amplitudes can be achieved in the complete speed range. Here, a detailed transient co-simulation model for rotor systems with air ring bearings is presented. The rotor is represented by a multibody model. The air films of the two bearings are represented by two nonlinear time-dependent finite element systems. The multibody model and the two finite element subsystems are solved simultaneously by means of an explicit sequential co-simulation technique. Due to the strong nonlinearities, the system shows interesting vibration and bifurcation effects, which are investigated in detail with the help of run-up simulations.

Keywords: air ring bearing, nonlinear rotor dynamics, co-simulation model, optimization

1. Introduction

Air bearings may be used in many technical applications, particularly in cases where oil-free operating conditions are necessary. They may be subdivided into two classes: (i) air bearings with a rigid housing and (ii) air foil bearings. Rigid air bearings have a rigid bearing housing and the air film is generated between the rotor journal and the inner bearing surface. The bearing properties (e.g., load capacity) and the dynamic behavior of the rotor/bearing system are mainly determined by the bore geometry [1]. Applying a plain cylindrical bore geometry usually entails a poor rotordynamic stability behavior, i.e., the rotor gets unstable at very low rotor speeds. Stability of the rotor/bearing system can be improved by using a multi-lobe bore geometry and especially by applying a herringbone geometry [13,23,39]. Foil bearings usually consist of a top foil and a compliant substructure [28]. As a consequence, the air gap between the rotor journal and the top foil is depending on the top foil deformation. With respect to the elastic substructure, foil bearings can be subdivided into different categories. Often bump foils [3, 15, 22] are used as

*Corresponding author. Tel.: +49 615 116 234 61, e-mail: zeise@ad.tu-darmstadt.de.
https://doi.org/10.24132/acm.2023.836

compliant substructure. Alternatively, beam foils [9], a metal mesh [29], springs [35] or wing foils [36] can be applied. The dynamic behavior of foil bearings is investigated experimentally and numerically in [4, 7, 16, 19, 27], for instance. Numerical and experimental studies on the lift-off speed can, for instance, be found in [2, 20]. Thermal models for air foil bearings are, e.g., discussed in [21, 25, 30].

Properly designing air foil bearings, a stable operation (or at least self-excited oscillations with moderate amplitudes) of the rotor system can be achieved within the considered speed range. Foil bearings are rather robust and frequently applied in practice. Calculation models for foil bearings are extraordinary involved. The numerical prediction of the stability of rotor systems with air foil bearings is very complicated. The dynamical behavior of such systems can even change during the operation due to wear in the top-foil coating. Regarding bearings with a rigid housing, the bore geometry has to be chosen carefully to achieve a stable rotor behavior. Due to the low viscosity of air, rigid air bearings frequently suffer from a reduced stability behavior. Even if a multi-lobe bore geometry is used, instability problems may occur already for low rotor speeds. Stable operation above the (linear) threshold speed of instability is usually not possible due to the very small damping property of air. To obtain a stable rotor behavior, frequently rigid bearings with a herringbone-geometry are used [6, 10, 17, 23, 39]. While herringbone bearings often provide an excellent rotor stability, they suffer from different technical problems (e.g., small clearances, involved thermo-management, manufacturing costs).

Air ring bearings can be an interesting alternative to air foil bearings and rigid air bearings. They can be considered as a simple and very obvious further development of rigid air bearings. The idea is simply to mount the bearing bushing with an elastomer [26, 38, 40], with a flexible membrane [5], springs [34] or with a foil structure [41] in the housing, see Fig. 1. The elastomer (foil structure) provides additional external damping (friction) to the rotor system so that the vibration behavior is improved. Properly designed air ring bearings may provide a stable rotor operation within the complete speed range or at least self-excited oscillations with moderate amplitudes. Here, air ring bearings with a three-lobe bore geometry are considered, where the ring is visco-elastically mounted in the housing (elastomer). Ring bearings mounted in a foil structure are, for instance, treated in [41].

The vibration and bifurcation behavior of rotor systems with air ring bearings is rather interesting. Typically, three different bifurcation paths may be detected for high-speed rotors supported in air ring bearings:

- For the case that the supporting structure of the ring is rather stiff and the external damping/friction low, *bifurcation path 1* is observed. This bifurcation path is dangerous and

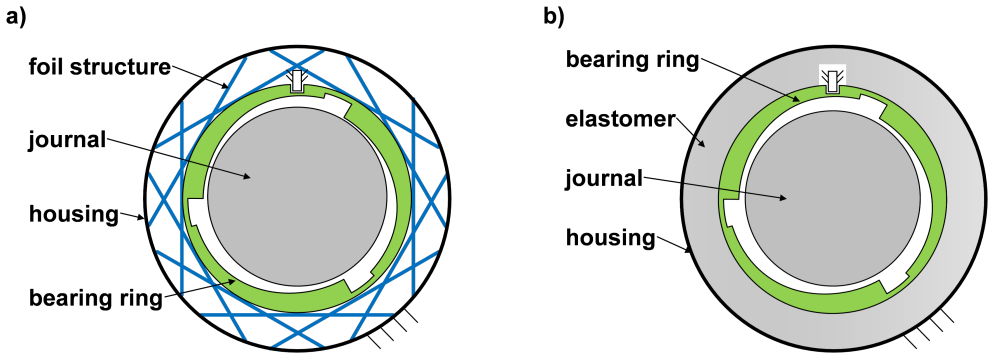

Fig. 1. Air ring bearing with (a) foil structure and (b) elastomer (visco-elastic mounting), see [41]

has to be omitted by a proper design of the rotor/bearing system, because self-excited oscillations with very large amplitudes are detected.
- For moderate ring stiffnesses and larger ring damping/friction, the harmless *bifurcation path 2a* is observed, where self-excited vibrations with moderate amplitudes occur.
- For very low ring stiffnesses, low damping and rather large ring masses, *bifurcation path 2b* can be detected, which should also be prevented in technical applications due to large rotor amplitudes.

It should be stressed that the basin of attraction for *bifurcation path 2a* is typically relatively large. Therefore, the rotor and especially the bearing parameters can in practice be determined in such a way that *bifurcation path 1* and *bifurcation path 2b* can be omitted.

The new contributions of this work are:
- The influence of the bore geometry of the inner ring surface on the stability and bifurcation behavior is analyzed in detail by numerical run-up simulations. Specifically, the effect of the nominal bearing clearance and the slope of the lobes is investigated.
- In [41], only the influence of the stiffness and damping of the ring supporting structure on the rotordynamic behavior has been analyzed. Here, comprehensive numerical studies are presented, where the effect of the bearing bore geometry on the system dynamics is examined.
- It is shown that both parameters – nominal bearing clearance and lobe geometry – have a very significant influence on the vibration and bifurcation behavior of the system.
- Based on the simulation results, practical design recommendations are given.

To carry out the run-up simulations, a detailed physical model for the air films is used, which are discretized by a finite element approach. The rotor is modeled as a 3D multibody system. The multibody model is coupled with the two finite element models of the air films with a co-simulation approach. With the coupled co-simulation model, the nonlinear system behavior is investigated.

The paper is organized as follows: The rotor/bearing co-simulation model is described in Section 2. The three bifurcation paths, typically observed in high-speed rotor systems with air ring bearings, are shortly recapped in Section 3. A detailed parameter and optimization study concerning the optimal choice of the air film geometry is presented in Section 4. The manuscript is concluded in Section 5.

2. Rotor/bearing simulation model of high-speed turbo compressor

2.1. Multibody model of the rotor

The considered rotor/bearing system is sketched in Fig. 2 and modelled as a multibody system, see [14, 32]. It is composed of the rotor shaft, the two wheels (compressor- and turbine-side wheel) and the two rigid bearing rings. In addition, two small imbalance masses are attached at the wheels. The axial coordinate z_{Rotor} characterizes the center of mass CM_{Rotor} of the complete rotor (shaft plus wheels). The middle planes of the turbine- and compressor-side bearing are defined by the axial coordinates z_{JT} and z_{JC}. The center of mass of the turbine CM_T and compressor wheel CM_C are termed by z_T and z_C, respectively.

For integrating the multibody system, the index-2 equations of motion (stabilized index-2 formulation according to [11]) are applied, which are given by

$$\boldsymbol{M}(t,\boldsymbol{x})\dot{\boldsymbol{v}} = \boldsymbol{f}_e(t,\boldsymbol{x},\boldsymbol{v},\boldsymbol{u}_{\text{MBS}}) - \boldsymbol{G}^T(t,\boldsymbol{x})\boldsymbol{\lambda}, \tag{1}$$

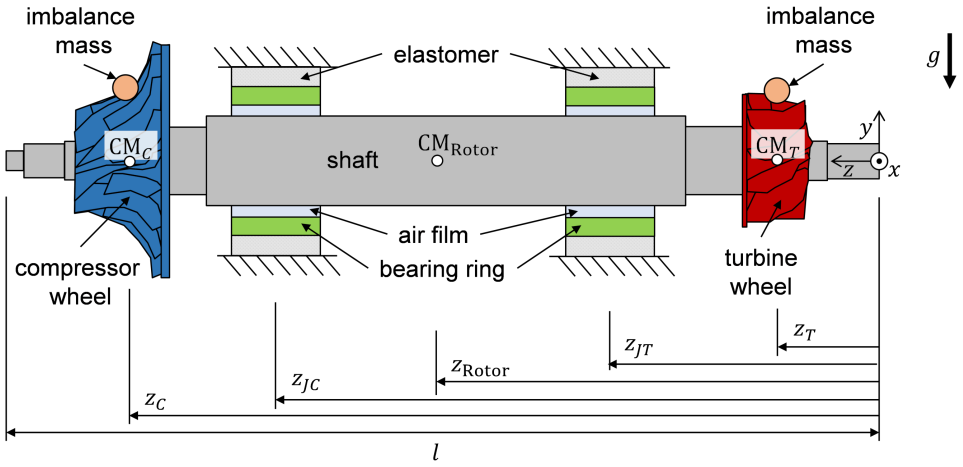

Fig. 2. High-speed rotor system: Turbo-compressor supported in two air ring bearings, see [41]

$$\boldsymbol{M}(t,\boldsymbol{x})\dot{\boldsymbol{x}} = \boldsymbol{M}(t,\boldsymbol{x})\boldsymbol{v} - \boldsymbol{G}^T(t,\boldsymbol{x})\boldsymbol{\mu}, \tag{2}$$

$$\boldsymbol{0} = \boldsymbol{g}(t,\boldsymbol{x}), \tag{3}$$

$$\boldsymbol{0} = \dot{\boldsymbol{g}}(t,\boldsymbol{x},\boldsymbol{v}). \tag{4}$$

The vector $\boldsymbol{x} = [x_1,\ldots,x_\kappa]^T \in \mathbb{R}^\kappa$ collects the κ (generalized) coordinates of the multibody system and the vector $\boldsymbol{v} = [v_1,\ldots,v_\kappa]^T \in \mathbb{R}^\kappa$ the (generalized) velocities. $\boldsymbol{M}\,(t,\boldsymbol{x}) \in \mathbb{R}^{\kappa\times\kappa}$ is the mass matrix. The vector $\boldsymbol{f}_e\,(t,\boldsymbol{x},\boldsymbol{v},\boldsymbol{u}_{\mathrm{MBS}})$ terms the externally applied forces/torques, the centrifugal and Coriolis forces. Gravity g acts in negative y-direction, see Fig. 2. Equation (1) are the force/torques balances. Equation (2) represents the kinematic differential equations, where the mass matrix is used as a scaling matrix to improve the numerical procedure [33]. The multibody system contains κ_c rheonomic algebraic constraint equations $g_i\,(t,\boldsymbol{x}) = 0$ $(i = 1,\ldots,\kappa_c)$, which are collected in the constraint vector $\boldsymbol{g} \in \mathbb{R}^{\kappa_c}$. The term $\boldsymbol{G}^T(t,\boldsymbol{x})\boldsymbol{\lambda}$ characterizes the constraint forces, where $\boldsymbol{G} = \partial\boldsymbol{g}/\partial\boldsymbol{x} \in \mathbb{R}^{\kappa_c\times\kappa}$ represents the constraint-Jacobian. The vector $\boldsymbol{\lambda} = [\lambda_1,\ldots,\lambda_{\kappa_c}]^T \in \mathbb{R}^{\kappa_c}$ contains the Lagrange multipliers. According to the stabilized index-2 formulation [11], the algebraic constraint equations $\boldsymbol{0} = \dot{\boldsymbol{g}}\,(t,\boldsymbol{x},\boldsymbol{v})$ on velocity level are included into the equations of motion with the help of the additional Lagrange multipliers $\boldsymbol{\mu} = [\mu_1,\ldots,\mu_{\kappa_c}]^T \in \mathbb{R}^{\kappa_c}$. The input variables of the multibody system are collected in the vector $\boldsymbol{u}_{\mathrm{MBS}}(t)$ and represent the resulting bearing forces of the two air films. It should be noted that the output vector $\boldsymbol{y}_{\mathrm{MBS}}(t) = \left[\Delta\boldsymbol{r}_1^T, \Delta\dot{\boldsymbol{r}}_1^T, \Delta\boldsymbol{r}_2^T, \Delta\dot{\boldsymbol{r}}_2^T, \Omega\right]^T$ of the multibody subsystem consists of the angular velocity of the rotor and of the relative displacement and velocity coordinates of the compressor- and turbine-side journal. These output variables are directly used as input variables for the two finite element subsystems for calculating the resulting bearing forces of the two air films.

In this work, the ring is assumed to be connected to the housing by a visco-elastic material (elastomer). To simplify the analysis, an isotropic linear visco-elastic material is considered, which is described by the force law $\boldsymbol{F} = -c\,\boldsymbol{r}_R - d\,\dot{\boldsymbol{r}}_R$ with the stiffness coefficient c and the damping coefficient d.

2.2. *Finite element model of the air film*

Fig. 3 depicts the gap of the air film of an air ring bearing with a three-lobe geometry. The space-fixed x, y-reference system is placed in the center O of the bearing housing. It is assumed

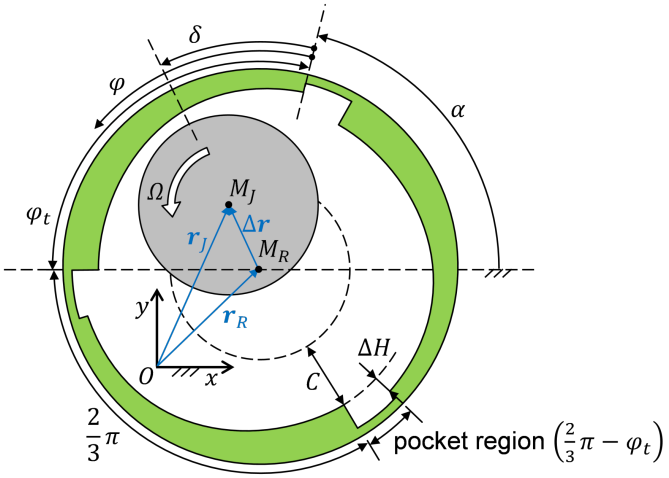

Fig. 3. Three-lobe air ring bearing geometry, see [41]

that the ring is able to move in x- and y-direction. The rotation around the z-axis is blocked (i.e., planar motion with two degrees of freedom). $\boldsymbol{r}_R = [x_R, y_R]^T$ is the position vector of the ring center M_R and $\boldsymbol{r}_J = [x_J, y_J]^T$ the position vector of the rotor journal M_J. The relative displacement vector of M_J with respect to M_R is denoted by $\Delta\boldsymbol{r} = \boldsymbol{r}_J - \boldsymbol{r}_R = [\Delta x, \Delta y]^T$. The relative velocity of M_J with respect to M_R is defined by $\Delta\dot{\boldsymbol{r}} = d/dt\,(\Delta\boldsymbol{r})$. Furthermore, ring-fixed polar coordinates $\Delta r = |\Delta\boldsymbol{r}|$ and $\delta = \text{atan2}\,(\Delta y, \Delta x) - \alpha$ are introduced, which time derivatives are given by $\Delta\dot{r} = 1/\Delta r\,(\Delta\boldsymbol{r}\cdot\Delta\dot{\boldsymbol{r}})$ and $\dot{\delta} = 1/\Delta r^2\,(\Delta x\Delta\dot{y} - \Delta y\Delta\dot{x})$. The orientation of the ring relative to the housing is specified by the angle α ($\alpha = \text{const}$). The lobe region is defined by the angle φ_t. Three pockets are used for the air supply (circumferential extension $2\pi/3 - \varphi_t$). Here, ambient pressure is assumed. Moreover, C is the nominal clearance and ΔH the height of the step between the lobe region and the pocket. The angular coordinate φ, which is an auxiliary coordinate, is used for computing the pressure field with the Reynolds equation.

The pressure field $p(\varphi, z, t)$ in the air film is computed with the isothermal Reynolds equation for compressible fluids [18, 37]

$$\frac{1}{r^2}\frac{\partial}{\partial\varphi}\left(ph^3\frac{\partial p}{\partial\varphi}\right) + \frac{\partial}{\partial z}\left(ph^3\frac{\partial p}{\partial z}\right) = 6\Omega\eta\frac{\partial(ph)}{\partial\varphi} + 12\eta\frac{\partial(ph)}{\partial t}, \tag{5}$$

where the fluid is assumed to be an ideal gas described by the relationship $\varrho = p/(R_{\text{air}}T_{\text{air}})$ (R_{air} – specific gas constant of air, T_{air} – prescribed constant air film temperature), η terms the dynamic viscosity of air, $\varrho(\varphi, z, t)$ is the density field, Ω represents the rotor speed, r is the journal radius, $h(\varphi, t)$ describes the gap function and b denotes the bearing width. φ terms the circumferential and z the axial coordinate. The pressure is only computed in the lobe regions $S_{\text{lobe}} = \{[0, \varphi_t], [2\pi/3, 2\pi/3 + \varphi_t], [4\pi/3, 4\pi/3 + \varphi_t]\}$. Ambient pressure p_a is assumed in the pockets. The gap function h in the lobe regions is characterized by $h(\varphi) = C - \Delta r\cos(\varphi - \delta) + \Delta H\{1 + 2\pi/(3\varphi_t)\lfloor 3\varphi/(2\pi)\rfloor - \varphi/\varphi_t\}$ with $\varphi \in S_{\text{lobe}}$, where $\lfloor\ldots\rfloor$ denotes the floor function. Because journal misalignment is not considered here, symmetry boundary conditions can be applied with respect to the middle plane of the bearing for solving the Reynolds equation. At the remaining boundaries, the Dirichlet boundary condition $p = p_a$ is used.

The Reynolds equation is discretized with the help of a finite element approach, i.e., the time dependent pressure field $p(\varphi, z, t)$ is approximated by $\widetilde{p}_i(\varphi, z, t) = \sum_{i=1}^{n_k} N_i(\varphi, z)\, p_i(t)$. $N_i(\varphi, z)$ represent the ansatz functions and $p_i(t)$ the pressure variables at the finite element nodes (n_k is the number of finite element nodes). Due to symmetry, only half the bearing needs to be discretized. Here, 360 finite elements (quadratic ansatz functions) are used, which result in $n_k = 1\,599$ pressure degrees of freedom. From the mathematical point of view, the discretized Reynolds equation represents a nonlinear ODE system (system of ordinary differential equations) for calculating the unknown pressure variables $p_i(t)$, which are arranged in the vector $\boldsymbol{p} = [p_1, \ldots, p_{n_k}]^T$.

The nonlinear ODE system $\boldsymbol{f}(\boldsymbol{p}, \dot{\boldsymbol{p}}, t) = \boldsymbol{0}$ for the pressure variables $p_i(t)$ is solved with an implicit time integration algorithm. The global components $F_{px}(t)$, $F_{py}(t)$ of the resulting bearing forces are computed by an integration of the pressure field over the bearing surface

$$F_{px} = \int_0^{2\pi} \int_0^{b} p(\varphi, z)\, r \cos(\varphi + \alpha)\, \mathrm{d}z\, \mathrm{d}\varphi, \tag{6}$$

$$F_{py} = \int_0^{2\pi} \int_0^{b} p(\varphi, z)\, r \sin(\varphi + \alpha)\, \mathrm{d}z\, \mathrm{d}\varphi. \tag{7}$$

The output variables of the finite element subsystem are the resultant bearing forces. They are arranged in the output vector $[F_{px}, F_{py}]^T$. The rotor speed Ω and the relative journal displacement vector $\Delta\boldsymbol{r} = [\Delta x, \Delta y]^T$ in combination with its time derivative $\Delta\dot{\boldsymbol{r}} = [\Delta\dot{x}, \Delta\dot{y}]^T$ define the input variables of the finite element subsystem. Because the rotor system has two air films, the two output vectors $\boldsymbol{y}_{\text{FEM1}} = [F_{px1}, F_{py1}]^T$ and $\boldsymbol{y}_{\text{FEM2}} = [F_{px2}, F_{py2}]^T$ and the resulting output vector $\boldsymbol{y}_{\text{FEM}} = [F_{px1}, F_{py1}, F_{px2}, F_{py2}]^T$ are introduced. The output variables $\boldsymbol{y}_{\text{FEM}}$ of the finite element subsystems are the input variables $\boldsymbol{u}_{\text{MBS}}$ for the multibody subsystem ($\boldsymbol{u}_{\text{MBS}} = \boldsymbol{y}_{\text{FEM}}$).

Final remark on the calculation of the bearing forces: The bearing forces according to (6) and (7) represent pure hydrodynamic forces. If the bearing eccentricities become large, the gap height $h(\varphi, t)$ between rotor and journal may get very small so that mixed lubrication effects occur. Then, a mere hydrodynamic approach based on the Reynolds equation will not be sufficient.

Here, a straightforward mixed lubrication approach has been applied [2, 3, 8, 37]. If the distance between the ring and the journal gets below a critical value – i.e., if the gap function $h(\varphi, t)$ is locally smaller than the user-defined value h_{con} – mixed lubrication is assumed to occur at this gap point. In this work, h_{con} has been set to $0.04\,C$. At gap points where $h(\varphi, t) \leq h_{\text{con}}$, additional contact forces at journal and ring are superimposed to the pure hydrodynamic forces resulting from the Reynolds equation. The mechanical approach used here for the asperity contact forces of the two contacting surfaces is described by a penalty force model with a penalty stiffness of $c_{\text{con}} = 10^7\,\text{N}\,\text{mm}^{-3}$.

The simulations in Sections 3 and 4 have shown that mixed lubrication only very rarely occurs with the actual rotor/bearing system. Even in whirl/whip regions with large bearing eccentricities, no mechanical contact is observed between ring and rotor journal as can, for instance, be seen in the orbit plots in Section 3.

2.3. Linearization and modal analysis

The considered rotor/bearing system is highly nonlinear. Nevertheless, different characteristic vibration mode shapes and corresponding frequencies – excited by the rotor imbalance and especially by the whirl/whip frequencies of the air films – can be observed in the frequency spectra of run-up simulations. To get a closer insight into these vibration modes, the rotor/bearing system is linearized and an eigenmode analysis is carried out. For that purpose, the air films have to be linearized. The stiffness behavior of the air film is highly nonlinear and a function of the bearing eccentricity. Fig. 4 depicts an approximate calculation of the radial film stiffness as a function of the relative journal displacement $\varepsilon = |\,[0, -\Delta y]^T\,|/C$ for $C = 20\,\mu$m, $\Delta H = 40\,\mu$m, $\Omega = 1\,000$ Hz and different values of Δy.

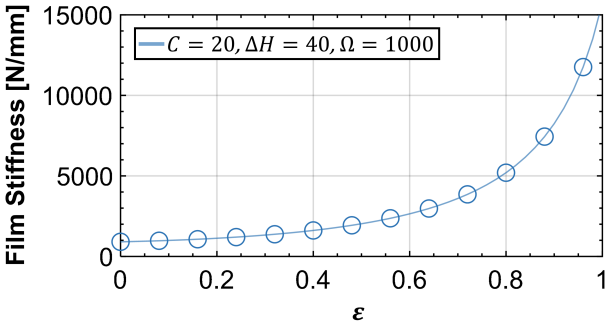

Fig. 4. Approximate calculation of the radial air film stiffness as a function of the bearing eccentricity ε

It should be noted that the rotor is rather stiff (shaft radius $r = 15$ mm) and may therefore be regarded as a rigid body. The first free-free bending eigenfrequency of the rotor is $\approx 2\,600$ Hz and well above the maximum rotor speed of $2\,000$ Hz. Furthermore, it should be mentioned that damping effects have been neglected in the eigenmode analysis. Finally, it should be stressed that tilting of the rings is not considered in the calculation, since the rings can only move in the x, y-plane in our model.

For the eigenmode analysis, the ring mounting stiffness and the ring damping parameter have been set to $c = 500\,\mathrm{N\,mm^{-1}}$ and $d = 0\,\mathrm{N\,s\,m^{-1}}$, respectively. The air film of each bearing has been replaced by two linear springs acting in x- and y-direction with spring constants $c_{\mathrm{air},x} = c_{\mathrm{air},y} = 2\,000\,\mathrm{N\,mm^{-1}}$ (estimated air film stiffness for $\varepsilon \approx 0.5$). The results of the eigenmode calculation are (see Fig. 5):

- *Mode_1(b)* and *Mode_1(f)* are conical modes with a vibration node at the compressor-side bearing (backward mode *Mode_1(b)* ≈ 125 Hz; forward mode *Mode_1(f)* ≈ 145 Hz).
- *Mode_2(b)* and *Mode_2(f)* are conical modes with a vibration node at the turbine-side bearing (backward mode *Mode_2(b)* ≈ 156 Hz; forward mode *Mode_2(f)* ≈ 181 Hz).
- *Mode_3(b)* and *Mode_3(f)* are conical modes with a vibration node at the compressor-side bearing (backward mode *Mode_3(b)* $\approx 1\,161$ Hz; forward mode *Mode_3(f)* $\approx 1\,162$ Hz).
- *Mode_4(b)* and *Mode_4(f)* are conical modes with a vibration node at the turbine-side bearing (backward mode *Mode_4(b)* $\approx 1\,176$ Hz; forward mode *Mode_4(f)* $\approx 1\,179$ Hz).

2.4. Co-simulation model of the overall system

The coupled system consisting of the rotor and the two bearings is integrated in the time domain using a co-simulation approach [12, 24, 31]. Therefore, the overall system is decomposed

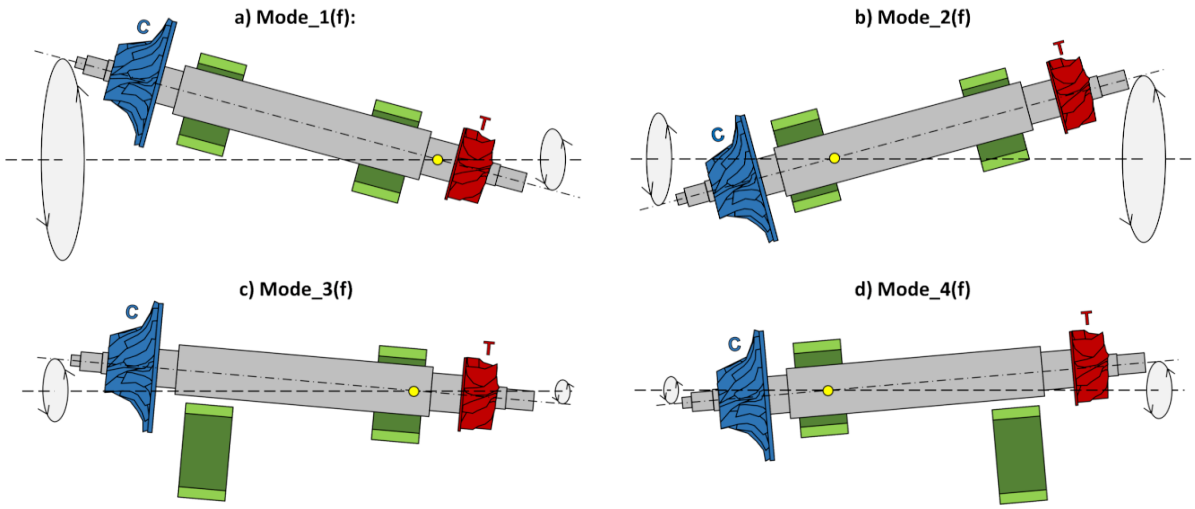

Fig. 5. Rigid body forward mode shapes

into three different subsystems. The first subsystem (multibody subsystem, MBS) contains the rotor. The second and third subsystems are the two finite element subsystems of the discretized Reynolds equations (FEM1 and FEM2).

To accomplish the co-simulation, appropriate coupling variables have to be introduced (input/output variables, see above). They characterize the mathematical connection between the three subsystems. Moreover, a communication-time grid has to be defined. Therefore, the macro-time points T_N $(N = 0, 1, 2, \ldots)$ are introduced. In the framework of a co-simulation, the subsystems can be integrated independently within the macro-step $T_N \rightarrow T_{N+1}$. Information, i.e., coupling variables, are interchanged only at the macro-time points. Within the macro-interval $[T_N, T_{N+1}]$, the coupling variables are approximated. Therefore, appropriate extrapolation and interpolation polynomials are used.

Here, an explicit co-simulation technique, namely the sequential Gauss-Seidel scheme, is used. In the current implementation, the multibody subsystem is considered as the master subsystem.

3. Simulation results: Basic bifurcation behavior

All simulations in Section 3 have been accomplished with the following parameters: $m = 830\,\mathrm{g}$, inertia tensor $\boldsymbol{J}_{\mathrm{Rotor}} = \mathrm{diag}\left(2\,500\,\mathrm{kg\,mm^2},\ 2\,500\,\mathrm{kg\,mm^2},\ 120\,\mathrm{kg\,mm^2}\right)$ with respect to the center of mass, journal radius $r = 15\,\mathrm{mm}$, $l = 250\,\mathrm{mm}$, $z_{\mathrm{Rotor}} = 125\,\mathrm{mm}$, $z_{JC} = 170\,\mathrm{mm}$, $z_{JT} = 60\,\mathrm{mm}$, $m_R = 50\,\mathrm{g}$ ($m_R = 150\,\mathrm{g}$ in Section 3.3), ring width $b = 28.6\,\mathrm{mm}$. The bearing parameters are: air viscosity $\eta_{\mathrm{air}} = 20.936 \times 10^{-6}\,\mathrm{kg\,m^{-1}\,s^{-1}}$ (assumed fluid temperature: $T_{\mathrm{air}} = 80^\circ\,\mathrm{C}$), bearing clearance $C = 20\,\mu\mathrm{m}$ (warm clearance; rotor expansion due to centrifugal forces is neglected), step height $\Delta H = 40\,\mu\mathrm{m}$, lobe angle $\varphi_t = 110^\circ$, ring orientation angle $\alpha = \pi - \varphi_t$. To analyze the possible bifurcations of the high-speed rotor/bearing system, the stiffness parameter c as well as the damping parameter d are varied. At the beginning of the run-up simulations, the rotor and the two rings are centered at the space-fixed z-axis and zero velocity is assumed. The rotor speed $\Omega(t)$ is linearly increased. The maximum speed of $2\,000\,\mathrm{Hz}$ is reached in $3\,\mathrm{s}$, i.e., $\Omega(t) = 2\pi/3 \cdot 2\,000t\,\mathrm{s^{-2}}$. To discuss the occurring bifurcations of the system vividly, the rotor unbalance is assumed to be zero. The effect of imbalance on the dynamical behavior of the system is discussed in [41].

3.1. Rotor run-up simulation: Bifurcation path 1

Simulation results of a rotor run-up with the parameters $c = 1\,000\,\mathrm{N\,mm^{-1}}$ and $d = 50\,\mathrm{N\,s\,m^{-1}}$ are arranged in Fig. 6. The figure depicts the dimensionless bearing eccentricities $\varepsilon_C = \Delta r_C/C$ and $\varepsilon_T = \Delta r_T/C$ of the compressor- and turbine-side bearing, the vertical displacement of the compressor $y_{JC}(t)$ and turbine wheel $y_{JT}(t)$ and the corresponding frequency spectra. Note that the dimensionless eccentricities ε_C and ε_T are defined by using the minimal clearance C. Since the maximum clearance is $C + \Delta H$ at the beginning of the lobe regions, ε_C and ε_T can get larger than 1 without the journal contacting the ring. The figure also contains compressor- and turbine-side orbit plots of the relative journal displacements $\Delta\boldsymbol{r}_C(t)$ and $\Delta\boldsymbol{r}_T(t)$. It should be mentioned that the three green spirals represent the three lobes of the inner ring surface.

- In the range $0 \leq t \leq 1\,150\,\mathrm{ms}$ ($0 \leq \Omega \leq 767\,\mathrm{Hz}$), the rotor is rotating in a stable equilibrium position.

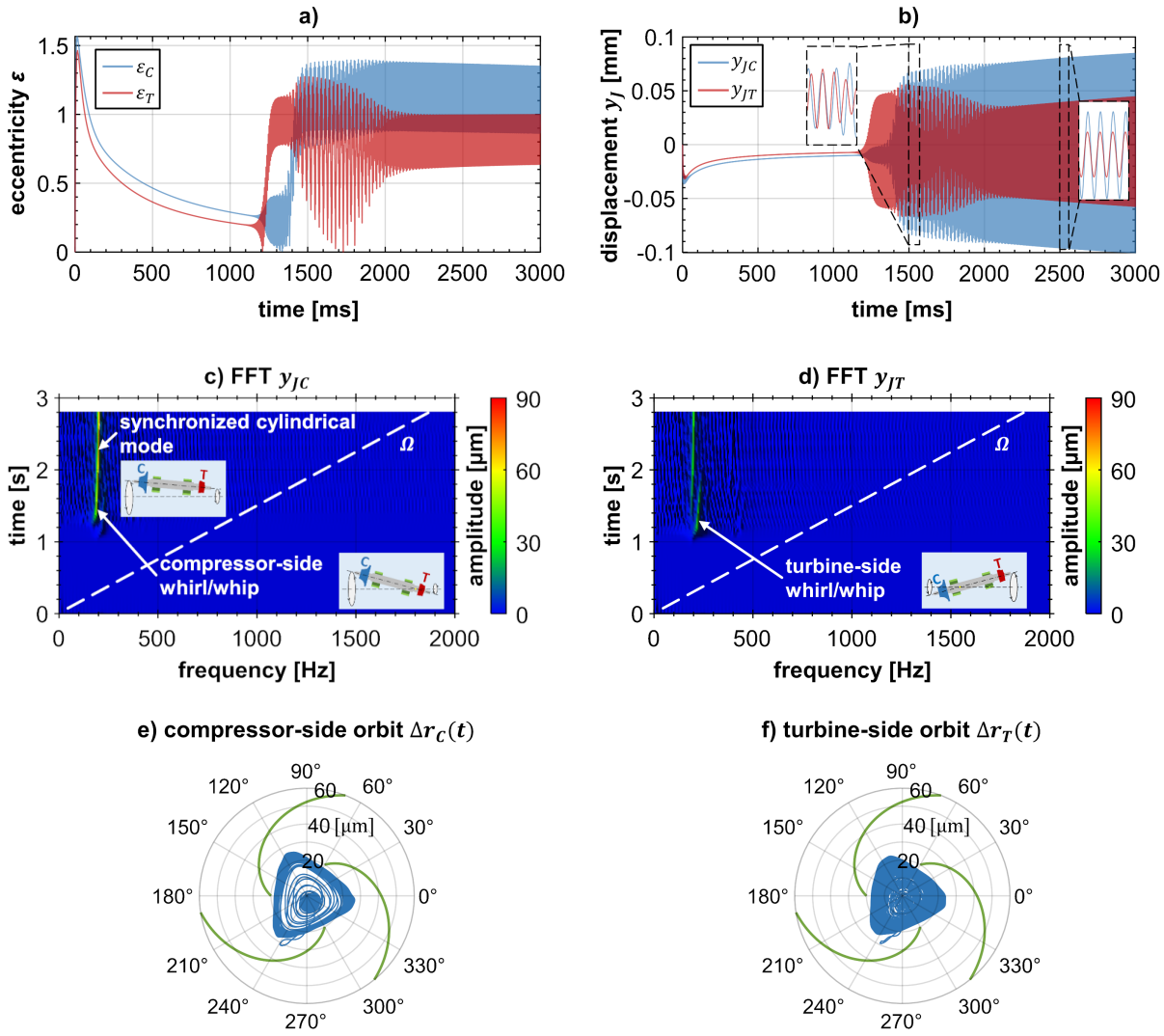

Fig. 6. Bifurcation path 1 with $c = 1\,000\,\mathrm{N\,mm^{-1}}$, $d = 50\,\mathrm{N\,s\,m^{-1}}$: (a) dimensionless bearing eccentricities $\varepsilon_C(t)$ and $\varepsilon_T(t)$, (b) vertical journal displacements $y_{JC}(t)$ and $y_{JT}(t)$, (c) frequency spectrum of $y_{JC}(t)$, (d) frequency spectrum of $y_{JT}(t)$, (e)–(f) compressor- and turbine-side orbit plots of the relative journal displacements $\Delta\boldsymbol{r}_C(t)$ and $\Delta\boldsymbol{r}_T(t)$

- At $t \approx 1\,150$ ms, the equilibrium position becomes unstable by means of a Hopf bifurcation and stable quasiperiodic oscillations are observed (so-called whirl/whip vibrations). Firstly, a whirl/whip primarily generated by the turbine-side bearing is observed. At $t \approx 1\,350$ ms, also a whirl/whip produced by the compressor-side bearing is detected.
- At $t \approx 2\,100$ ms, a synchronization effect takes place: the turbine-side whirl/whip frequency shows a jump and synchronizes with the compressor-side whirl/whip. Then, the synchronized whirls/whips are exciting a cylindrical forward mode.
- Further increasing the speed of the rotor system has only little influence on the frequencies and the amplitudes.
- Since the bearing eccentricities and the rotor amplitudes are typically very large in connection with bifurcation path 1, a secure operation of the rotor/bearing system is usually not possible within bifurcation path 1.

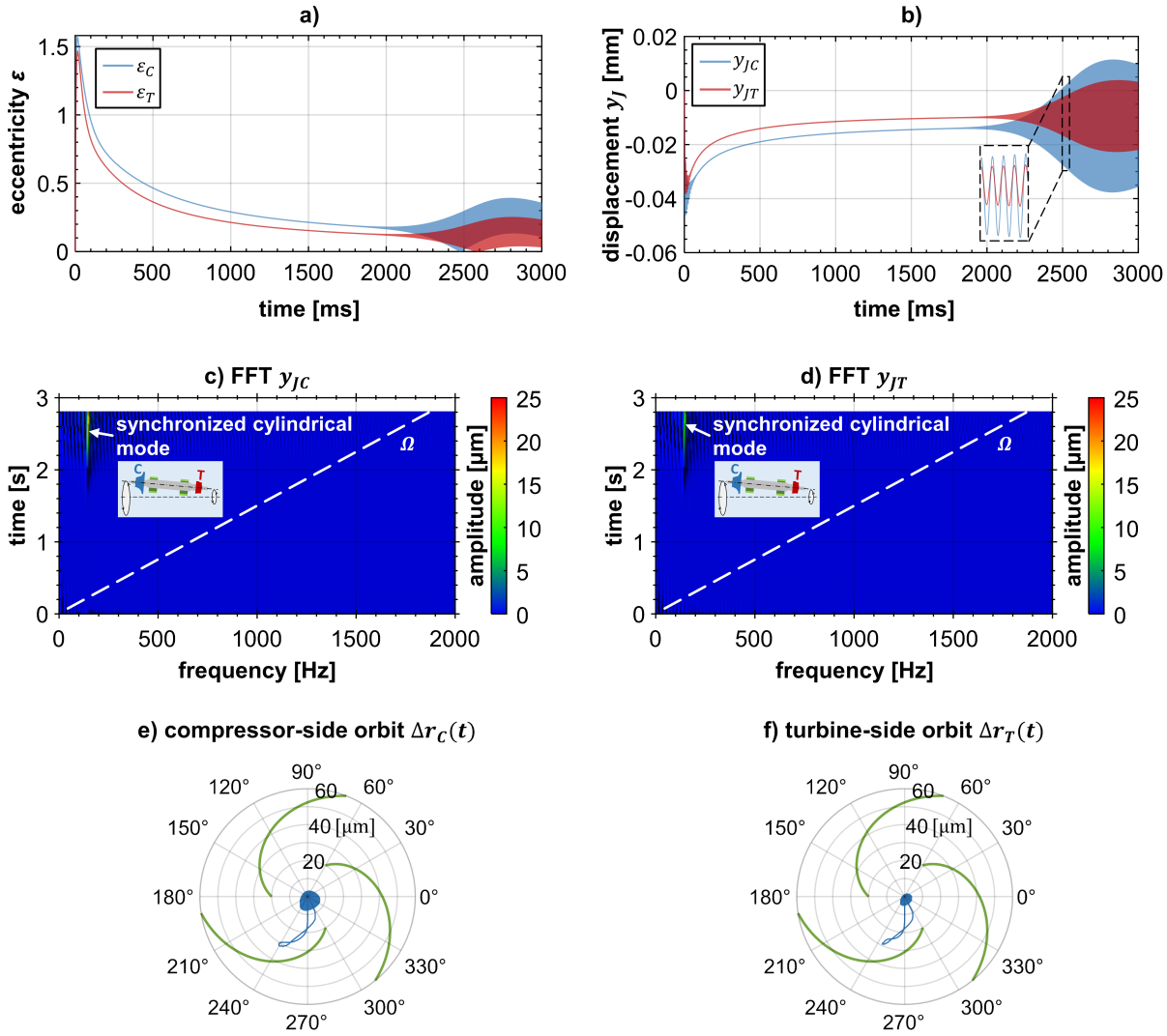

Fig. 7. Bifurcation path 2a with $c = 500\,\mathrm{N\,mm^{-1}}$, $d = 50\,\mathrm{N\,s\,m^{-1}}$: (a) dimensionless bearing eccentricities $\varepsilon_C(t)$ and $\varepsilon_T(t)$, (b) vertical journal displacements $y_{JC}(t)$ and $y_{JT}(t)$, (c) frequency spectrum of $y_{JC}(t)$, (d) frequency spectrum of $y_{JT}(t)$, (e)–(f) compressor- and turbine-side orbit plots of the relative journal displacements $\Delta \boldsymbol{r}_C(t)$ and $\Delta \boldsymbol{r}_T(t)$

3.2. Rotor run-up simulation: Bifurcation path 2a

For this run-up simulation, the stiffness is decreased to $c = 500\,\mathrm{N\,mm^{-1}}$. The damping coefficient remains $d = 50\,\mathrm{N\,s\,m^{-1}}$. The results are collected in Fig. 7.

- At $t \approx 2\,000\,\mathrm{ms}$, the rotor equilibrium position becomes unstable. A stable whirl/whip vibration is detected. The amplitudes of the whirl/whip are rather low so that the system can be run safely in the whirl/whip regime, i.e., in the complete speed range.
- Here, the compressor- and the turbine-side whirl/whip have the same frequency.

3.3. Rotor run-up simulation: Bifurcation path 2b

Now, the stiffness is further decreased to $c = 100\,\mathrm{N\,mm^{-1}}$. The damping coefficient is again $d = 50\,\mathrm{N\,s\,m^{-1}}$. It should be mentioned that the mass of the ring has been increased to $m_R = 150\,\mathrm{g}$ in this run-up simulation. The simulation results can be seen in Fig. 8.

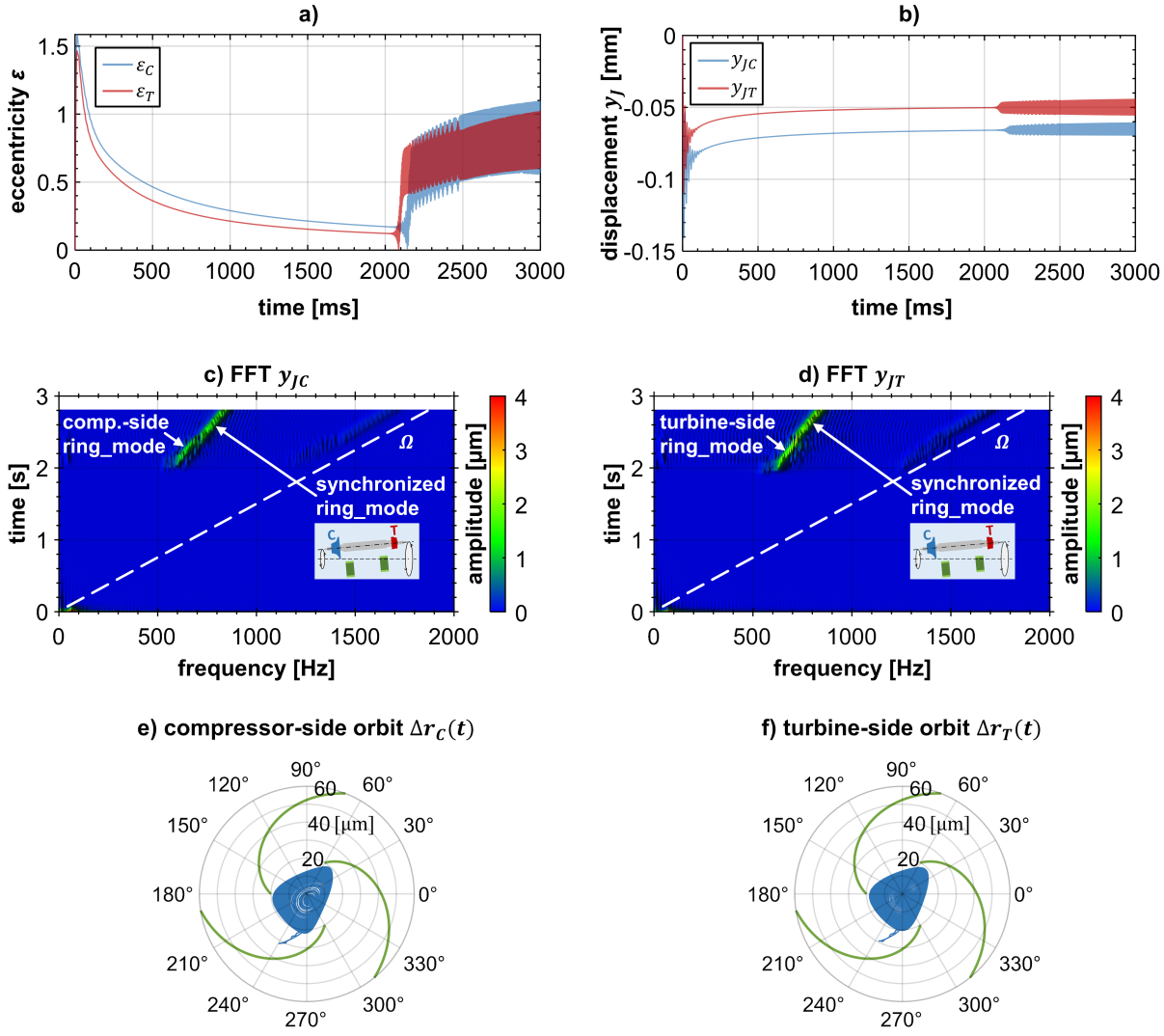

Fig. 8. Bifurcation path 2b with $c = 100\,\mathrm{N\,mm^{-1}}$, $d = 50\,\mathrm{N\,s\,m^{-1}}$, $m_R = 150\,\mathrm{g}$: (a) dimensionless bearing eccentricities $\varepsilon_C(t)$ and $\varepsilon_T(t)$, (b) vertical journal displacements $y_{JC}(t)$ and $y_{JT}(t)$, (c) frequency spectrum of $y_{JC}(t)$, (d) frequency spectrum of $y_{JT}(t)$, (e)–(f) compressor- and turbine-side orbit plots of the relative journal displacements $\Delta\boldsymbol{r}_C(t)$ and $\Delta\boldsymbol{r}_T(t)$

- At $t \approx 2\,050$ ms, the equilibrium position becomes unstable by means of a Hopf bifurcation and self-excited vibrations are observed. Here, the whirl/whip frequencies of the two air films excite special ring mode shapes [41]. In the range $2\,050\,\text{ms} \leq t \leq 2\,500\,\text{ms}$, the frequencies of the whirls/whips generated by the two bearings are almost equal.
- As the rotor speed increases, the bearing eccentricities rise to a critical level. The whirl/whip frequencies increase almost linearly with the rotor speed. Since the bearing eccentricities are usually very large in connection with bifurcation path 2b, a secure operation of the rotor/bearing system within bifurcation path 2b is generally not possible.
- For $t > 2\,500$ ms, the frequencies of the whirls/whips are identical (i.e., a full synchronization occurs). A cylindrically-shaped ring mode shape is observed.

4. Parameter studies and optimization

As mentioned above, a three-lobe bearing geometry is used here, which is mainly specified by the bearing clearance C (warm clearance) and the step height ΔH. In this section, C and

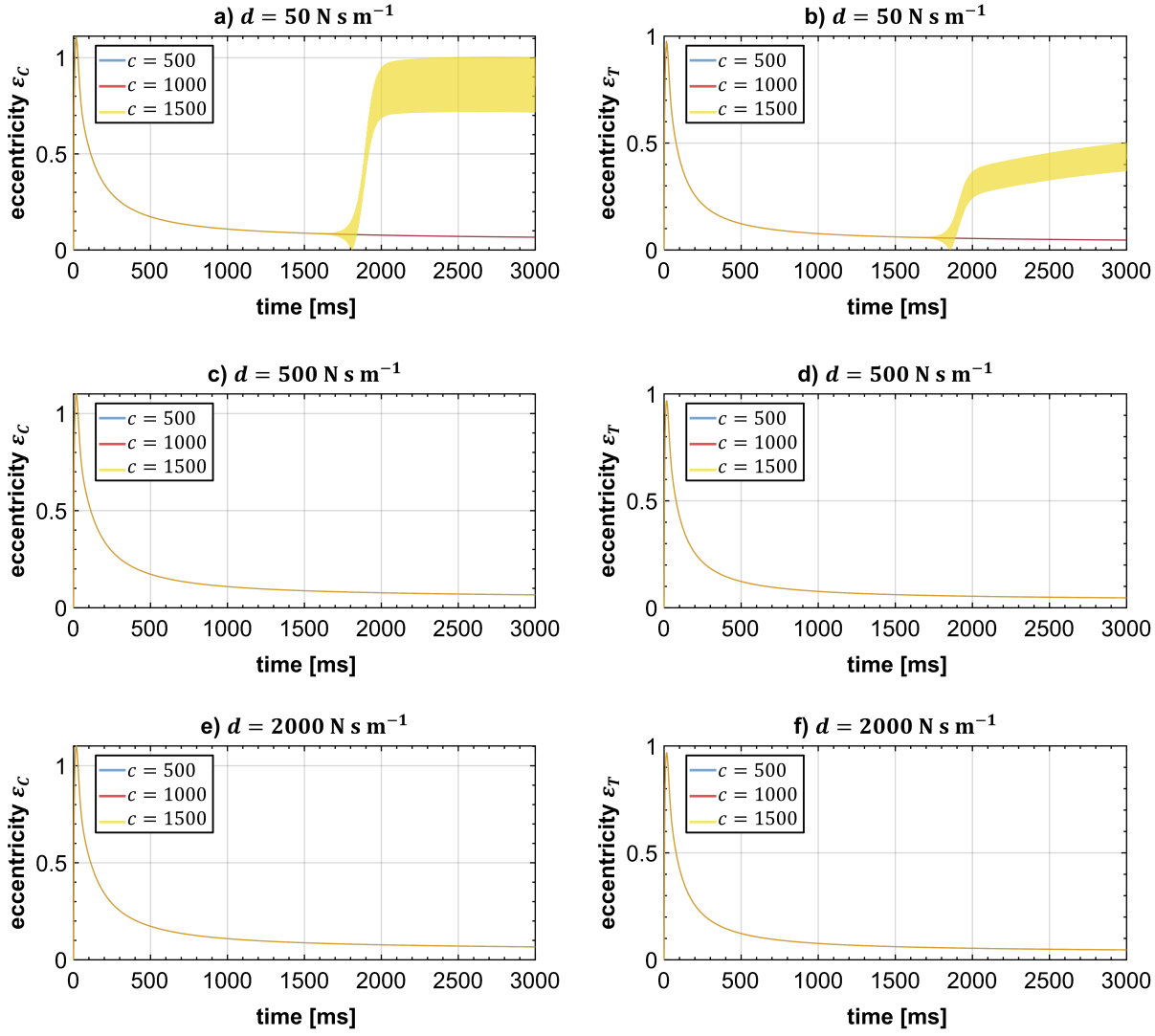

Fig. 9. Case 1 ($C = 10\,\mu$m, $\Delta H = 20\,\mu$m), compressor- and turbine-side bearing eccentricities $\varepsilon_C(t)$ and $\varepsilon_T(t)$: (a)–(b) $d = 50\,\text{N s m}^{-1}$, (c)–(d) $d = 500\,\text{N s m}^{-1}$, (e)–(f) $d = 2\,000\,\text{N s m}^{-1}$

ΔH are varied in order to study their influence on the bifurcation behavior of the rotor/bearing system.

Case 1: Fig. 9 shows the compressor- and turbine-side bearing eccentricities for $C = 10\,\mu$m and $\Delta H = 20\,\mu$m for three different elastomer stiffnesses c ($1\,500\,\mathrm{N\,mm^{-1}}$, $1\,000\,\mathrm{N\,mm^{-1}}$, $500\,\mathrm{N\,mm^{-1}}$) and three different damping parameters d ($2\,000\,\mathrm{N\,s\,m^{-1}}$, $500\,\mathrm{N\,s\,m^{-1}}$, $50\,\mathrm{N\,s\,m^{-1}}$). As can be seen, all simulations are stable (rotor rotation around a stable equilibrium point) with only one exception: for the case $c = 1\,500\,\mathrm{N\,mm^{-1}}$ in combination with the very low damping $d = 50\,\mathrm{N\,s\,m^{-1}}$, the critical *bifurcation path 1* is detected. The corresponding vertical displacements of the compressor $y_{JC}(t)$ and turbine wheel $y_{JT}(t)$ are collected in Fig. 10 and also corresponding frequency spectra for the parameters $d = 50\,\mathrm{N\,s\,m^{-1}}$ and $c = 1\,500\,\mathrm{N\,mm^{-1}}$. Since the run-up simulations have been carried out with zero imbalance, the stable simulations do not exhibit any vibrations so that the frequency spectra become trivial. If imbalance would be taken into account, stable imbalance vibrations around the equilibrium position would be observed (at least for small imbalances). The frequency spectra for $d = 50\,\mathrm{N\,s\,m^{-1}}$ and $c = 1500\,\mathrm{N\,mm^{-1}}$ only exhibit a subsynchronous frequency resulting from the whirl/whip motion. Of course, if

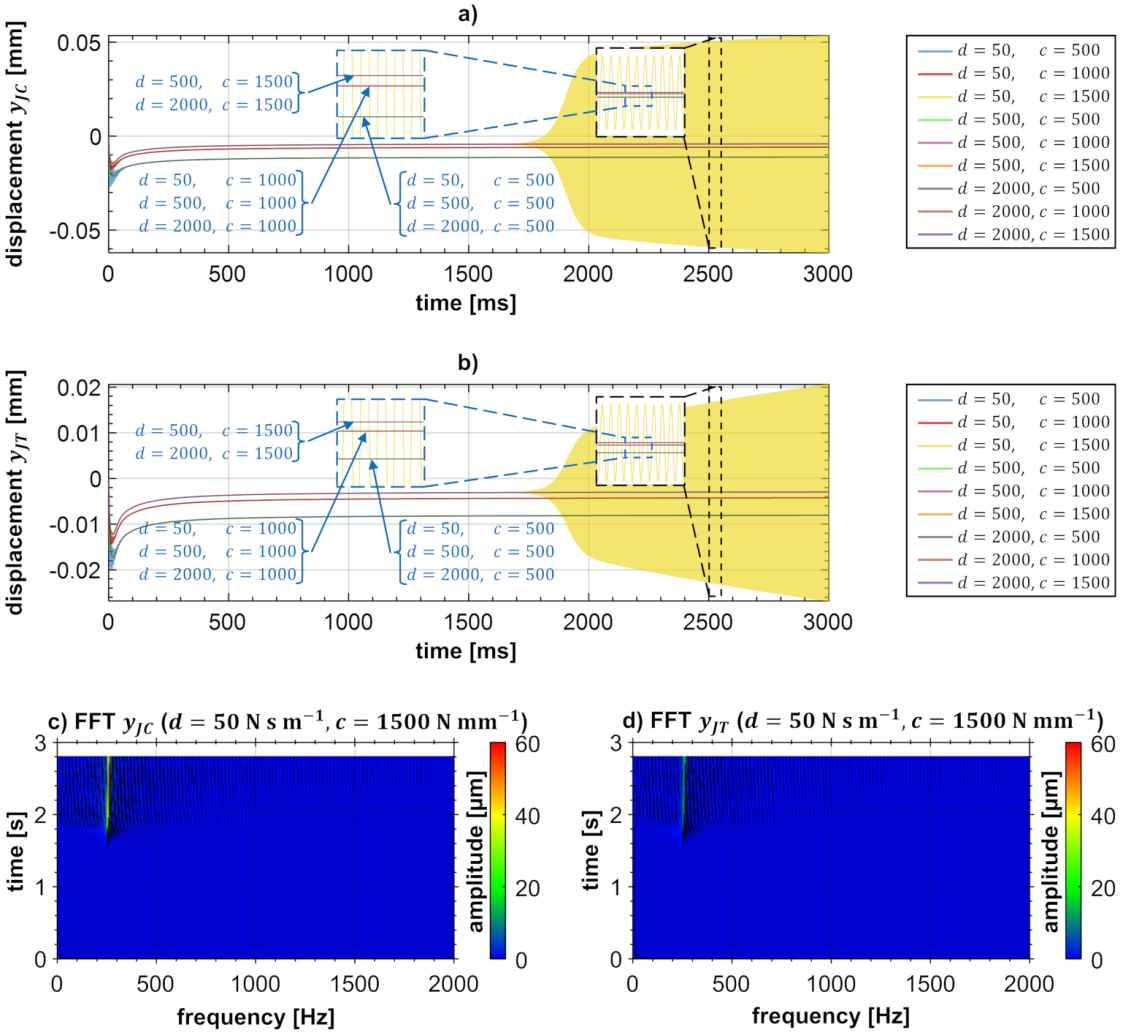

Fig. 10. Case 1 ($C = 10\,\mu$m, $\Delta H = 20\,\mu$m): (a)–(b) compressor and turbine-side rotor displacements $y_{JC}(t)$ and $y_{JT}(t)$, (c)–(d) frequency spectra of $y_{JC}(t)$ and $y_{JT}(t)$ for the parameters $d = 50\,\mathrm{N\,s\,m^{-1}}$ and $c = 1\,500\,\mathrm{N\,mm^{-1}}$

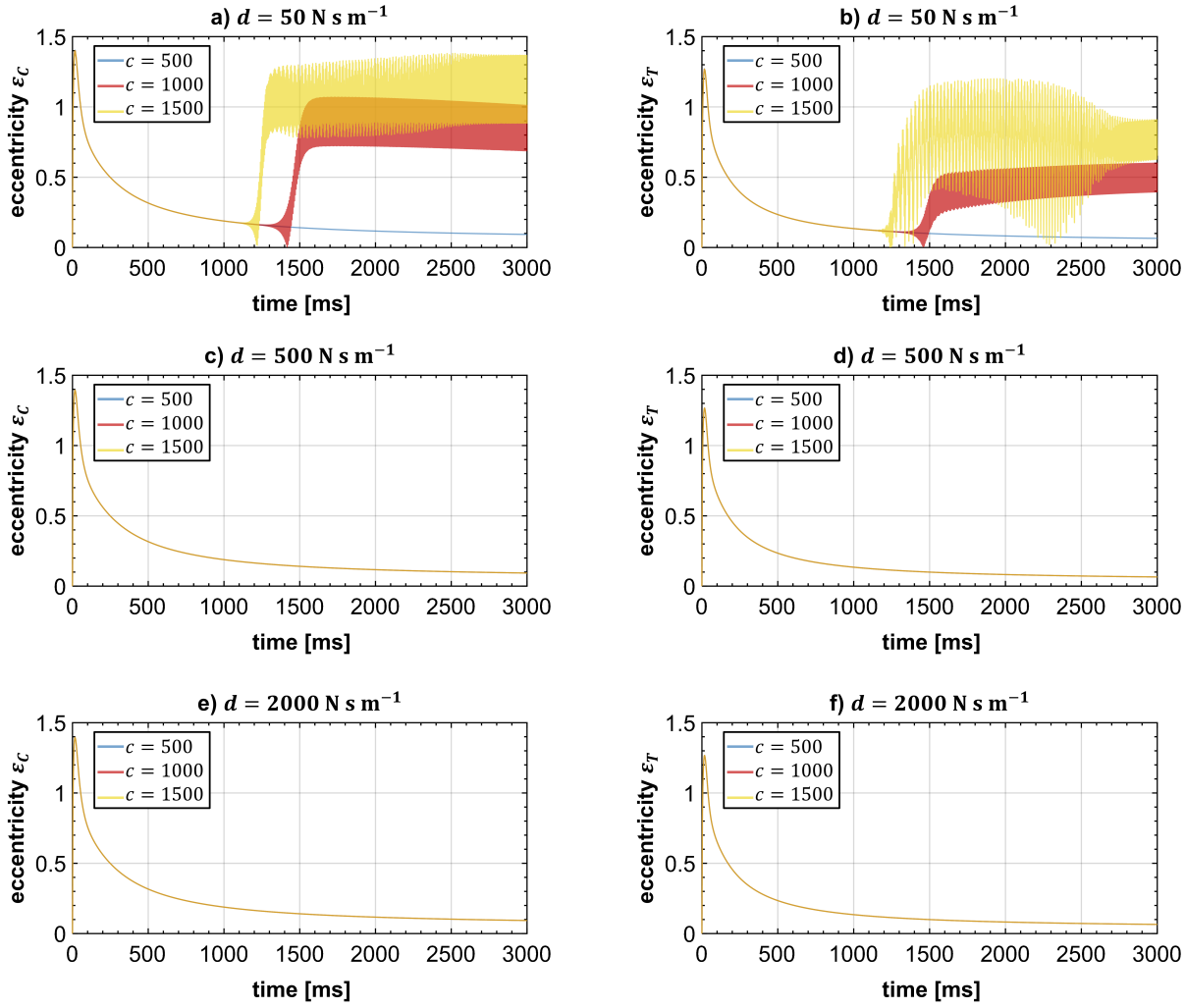

Fig. 11. Case 2 ($C = 15\,\mu$m, $\Delta H = 30\,\mu$m), compressor- and turbine-side bearing eccentricities $\varepsilon_C(t)$ and $\varepsilon_T(t)$: (a)–(b) $d = 50\,\mathrm{N\,s\,m^{-1}}$, (c)–(d) $d = 500\,\mathrm{N\,s\,m^{-1}}$, (e)–(f) $d = 2\,000\,\mathrm{N\,s\,m^{-1}}$

imbalance would be considered, also the rotor speed would be observed in the spectra.

Case 2: Equivalent simulations are carried out for $C = 15\,\mu$m and $\Delta H = 30\,\mu$m, see Figs. 11 and 12. The results are quite similar to the former case. Now, the simulations with $c = 1\,500\,\mathrm{N\,mm^{-1}}$ and $c = 1\,000\,\mathrm{N\,mm^{-1}}$ in combination with the damping coefficient $d = 50\,\mathrm{N\,s\,m^{-1}}$ exhibit the dangerous *bifurcation path 1*.

Case 3: Simulation results for $C = 20\,\mu$m and $\Delta H = 40\,\mu$m are depicted in Figs. 13 and 14. The stability behavior is similar to case 2 with one exception: for $c = 500\,\mathrm{N\,mm^{-1}}$ and $d = 50\,\mathrm{N\,s\,m^{-1}}$, *bifurcation path 2a* is observed.

Case 4: Finally, the bearing parameters $C = 30\,\mu$m and $\Delta H = 60\,\mu$m are considered, see Figs. 15 and 16. For $d = 50\,\mathrm{N\,s\,m^{-1}}$, all three simulations exhibit the problematic *bifurcation path 1*. With the larger damping coefficient $d = 500\,\mathrm{N\,s\,m^{-1}}$, the simulation with the low stiffness of $c = 500\,\mathrm{N\,mm^{-1}}$ is stable in the complete speed range. The simulation with the parameters $c = 1\,000\,\mathrm{N\,mm^{-1}}$ and $d = 500\,\mathrm{N\,s\,m^{-1}}$ exhibits a Hopf bifurcation at $t \approx 1\,800$ ms into *bifurcation path 2a*. For $c = 1\,500\,\mathrm{N\,mm^{-1}}$ and $d = 500\,\mathrm{N\,s\,m^{-1}}$, *bifurcation path 1* is observed. The simulations with the large damping coefficient $d = 2\,000\,\mathrm{N\,s\,m^{-1}}$ show *bifurcation path 2a.* Due to the large damping, the amplitudes of the whirl/whip are not decreasing with

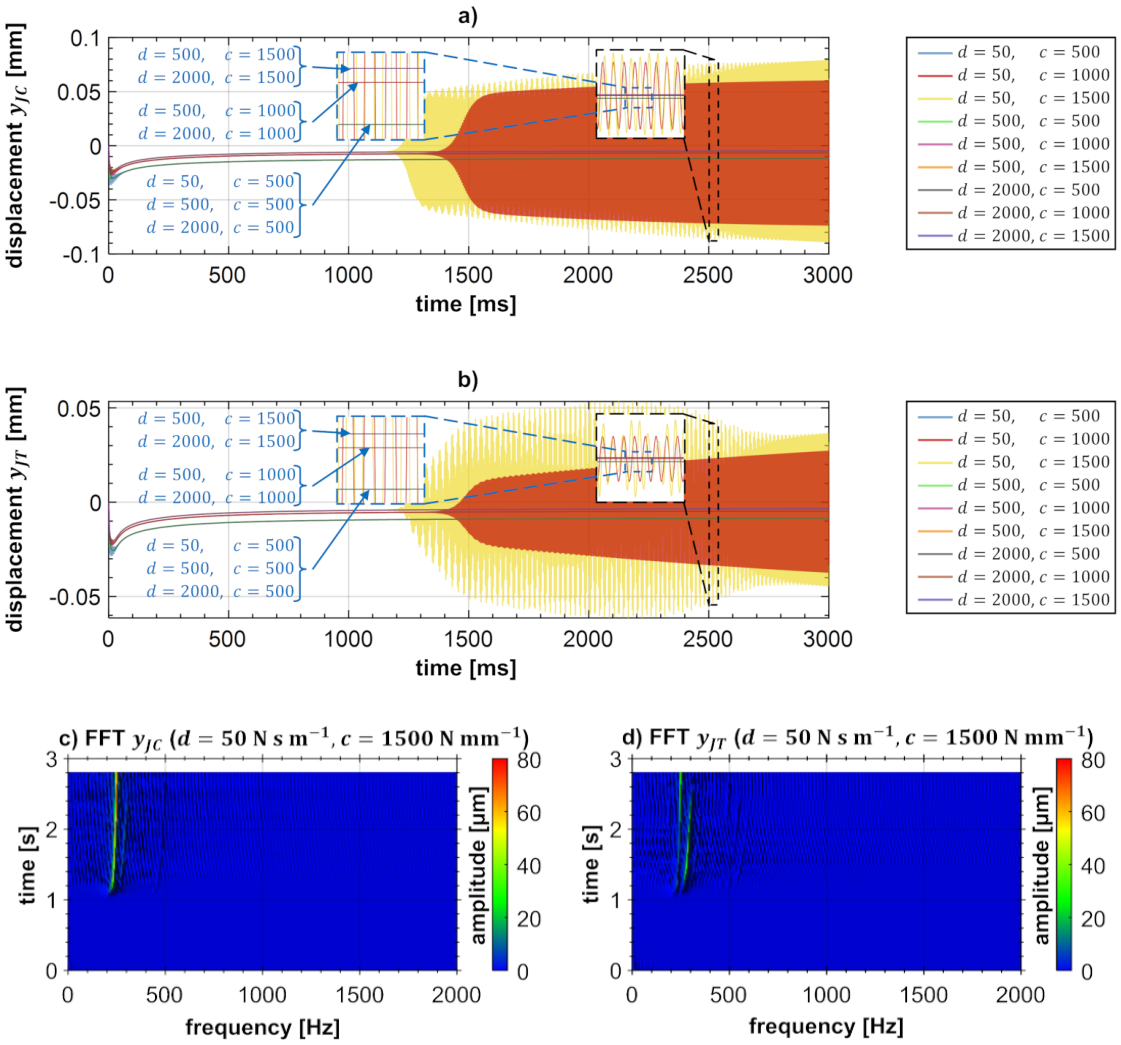

Fig. 12. Case 2 ($C = 15\,\mu$m, $\Delta H = 30\,\mu$m): (a)–(b) compressor and turbine-side rotor displacements $y_{JC}(t)$ and $y_{JT}(t)$, (c)–(d) frequency spectra of $y_{JC}(t)$ and $y_{JT}(t)$ for the parameters $d = 50\,\mathrm{N\,s\,m^{-1}}$ and $c = 1\,500\,\mathrm{N\,mm^{-1}}$

increasing rotor speed.

An overview on the influence of the stiffness and damping coefficients c and d on the stability and bifurcation behavior of the rotor/bearing system is presented in Fig. 17 in the form of bifurcation maps. As can be seen, the smaller the bearing clearance gets, the larger becomes the stable region. Furthermore, two basic trends may be observed in the stability/bifurcation plots:

(i) Increasing the stiffness c, the risk of reaching the dangerous bifurcation path 1 increases (especially for smaller values of d).

(ii) Increasing the damping d (so that the system might even become overdamped), the possibility increases that the system bifurcates into bifurcation path 2a. The whirl/whip amplitudes generally remain moderate so that the system can be operated securely within bifurcation path 2a.

Case study on the step height ΔH: In Fig. 18, a case study for $C = 15\,\mu$m and $c = 1\,000\,\mathrm{N\,mm^{-1}}$ is presented and the influence of the step height ΔH is investigated. As can be seen, for $\Delta H = 0$ all simulations become unstable at very low rotor speeds. Hence, bearing

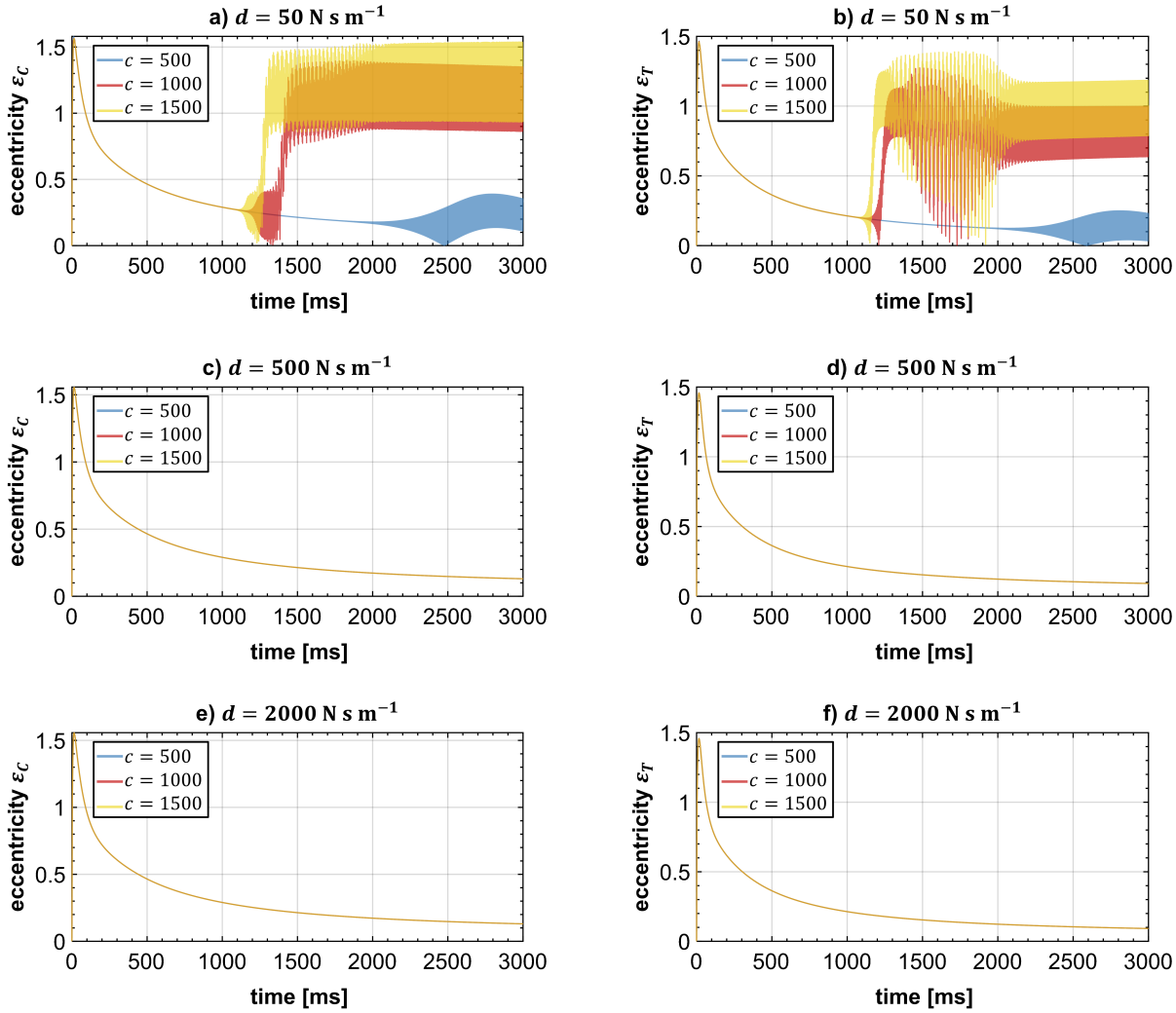

Fig. 13. Case 3 ($C = 20\,\mu$m, $\Delta H = 40\,\mu$m), compressor- and turbine-side bearing eccentricities $\varepsilon_C(t)$ and $\varepsilon_T(t)$: (a)–(b) $d = 50\,\mathrm{N\,s\,m^{-1}}$, (c)–(d) $d = 500\,\mathrm{N\,s\,m^{-1}}$, (e)–(f) $d = 2\,000\,\mathrm{N\,s\,m^{-1}}$

geometries with $\Delta H = 0$ – and also bearing geometries with a plain circular bearing geometry (not shown here) – are from the practical point of view of no interest. For $\Delta H = 15\,\mu$m, the simulation with $d = 50\,\mathrm{N\,s\,m^{-1}}$ exhibits the dangerous *bifurcation path 1*, while the run-up simulation with the larger damping $d = 500\,\mathrm{N\,s\,m^{-1}}$ is stable in the entire speed range. Similar results are observed for the case $\Delta H = 30\,\mu$m and $\Delta H = 45\,\mu$m: the bearing eccentricities for the simulations with $d = 50\,\mathrm{N\,s\,m^{-1}}$ are smaller compared to the simulation with $\Delta H = 15\,\mu$m.

Summary: Air ring bearings with small clearances C show a very good stability behavior even for larger values of c and smaller values d. If very small bearing clearances cannot be realized for practical/technical reasons (e.g., problems due to thermal expansion, manufacturing costs), an increase of d or a decrease of c may enable a stable rotor operation (or at least self-excited vibrations with moderate and technically uncritical amplitudes). However, if d is chosen too large, overdamping may occur, which can yield large and critical amplitudes. The run-up simulations also show that the step height ΔH should be chosen properly, i.e., not too small.

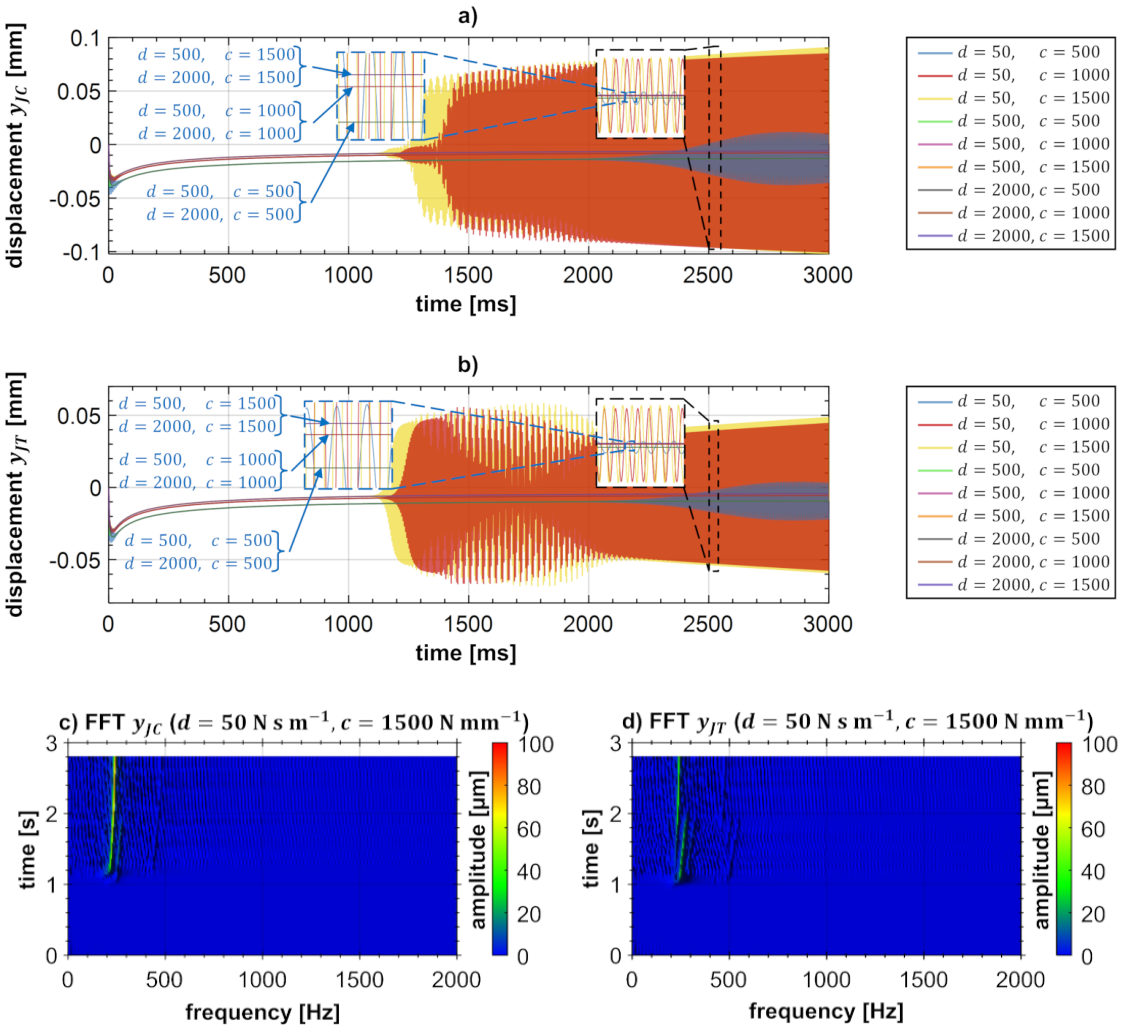

Fig. 14. Case 3 ($C = 20\,\mu$m, $\Delta H = 40\,\mu$m): (a)–(b) compressor and turbine-side rotor displacements $y_{JC}(t)$ and $y_{JT}(t)$, (c)–(d) frequency spectra of $y_{JC}(t)$ and $y_{JT}(t)$ for the parameters $d = 50\,\mathrm{N\,s\,m^{-1}}$ and $c = 1\,500\,\mathrm{N\,mm^{-1}}$

5. Conclusion

Air ring bearings might be considered as a further development of rigid air bearings. The idea is to connect the bearing bushing – i.e., the bushing ring – elastically with the housing. Therefore, an elastomer might be used or a foil structure. Here, a visco-elastically mounting of the bushing ring has been considered. The ring mounting also introduces external damping to the system, which can significantly improve the performance of the rotor/bearing system. The inner surface of the ring considered here has a three-lobed geometry.

Properly choosing the bearing parameters, air ring bearings might be an interesting alternative to classical air foil bearings. Considering air foil bearings, they often suffer from wear occurring in the top foil coating. As a consequence, the mechanical behavior of the bearing will change during operation and the number of start/stop operations is usually limited. Furthermore, the lift-off speed and power loss of foil bearings are comparatively large compared to rigid air bearings.

Air ring bearings also have different advantages compared to rigid herringbone bearings. A main advantage of herringbone bearings is their excellent stability behavior (stable operation

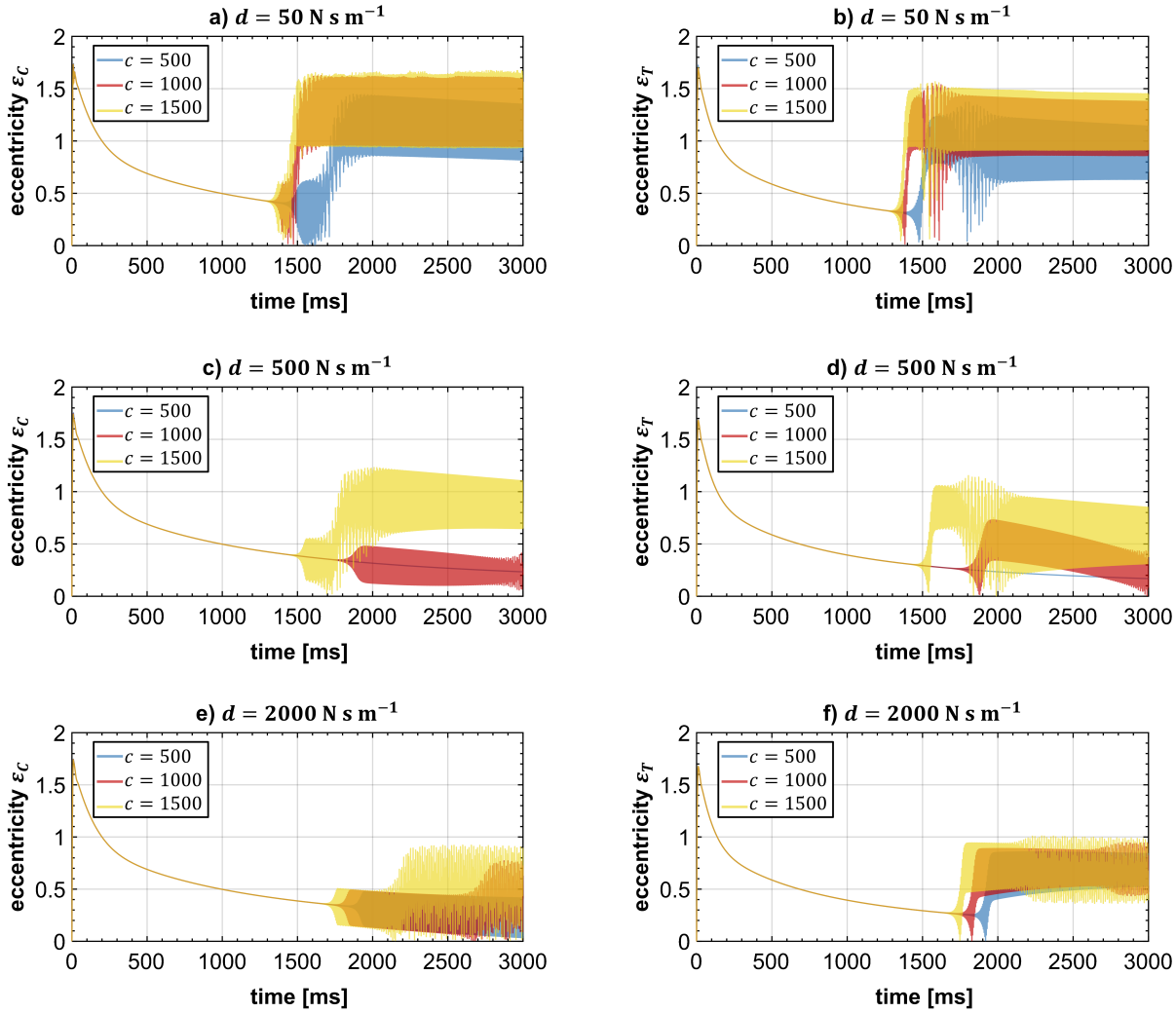

Fig. 15. Case 4 ($C = 30\,\mu$m, $\Delta H = 60\,\mu$m), compressor- and turbine-side bearing eccentricities $\varepsilon_C(t)$ and $\varepsilon_T(t)$: (a)–(b) $d = 50\,\mathrm{N\,s\,m^{-1}}$, (c)–(d) $d = 500\,\mathrm{N\,s\,m^{-1}}$, (e)–(f) $d = 2\,000\,\mathrm{N\,s\,m^{-1}}$

in the complete speed range). Therefore, very small bearing clearances are required and in consequence a rather expensive thermo-management. A very good stability and vibration behavior may also be achieved with air ring bearings. Especially for smaller bearing clearances, a stable operation in the complete speed range can be achieved. Rotors in air ring bearings may – in contrast to rotors in rigid herringbone bearings – however also be operated above the linear threshold speed of instability. By properly choosing the stiffness and damping properties of the ring supporting structure, stable self-excited oscillations with moderate amplitudes may be obtained (bifurcation path 2a) even for larger bearing clearances so that an elaborate thermo-management will not be necessary.

Rotors supported in air ring bearings may therefore be considered as rather robust systems. In a wide parameter range, the system is completely stable (the rotor runs in a stable equilibrium position) or self-excited oscillations with technically harmless amplitudes occur (bifurcation path 2a). The system can, however, not been operated within bifurcation paths 1 and 2b, since the amplitudes usually exceed critical values, which prevents a secure operation.

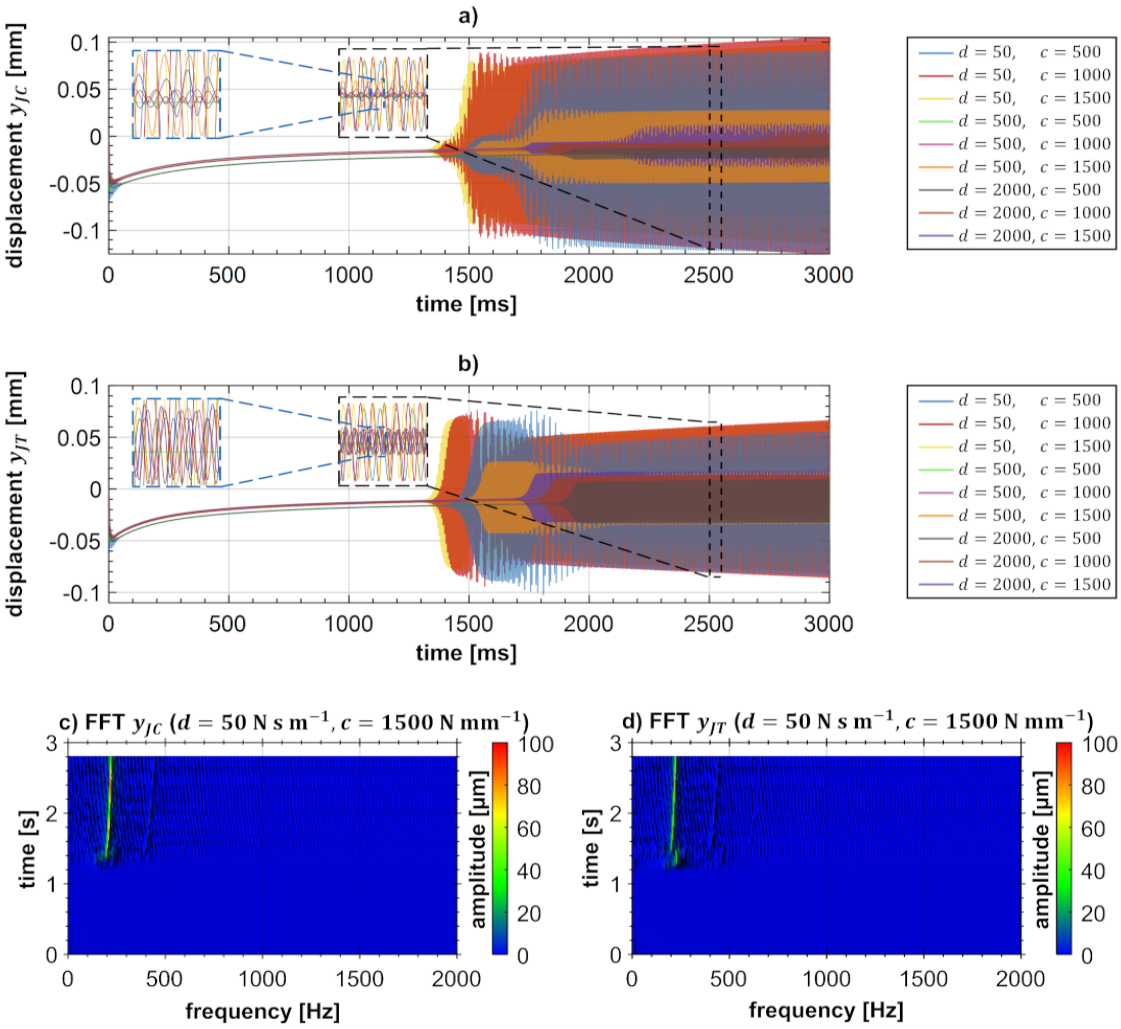

Fig. 16. Case 4 ($C = 30\,\mu$m, $\Delta H = 60\,\mu$m): (a)–(b) compressor and turbine-side rotor displacements $y_{JC}(t)$ and $y_{JT}(t)$, (c)–(d) frequency spectra of $y_{JC}(t)$ and $y_{JT}(t)$ for the parameters $d = 50\,\mathrm{N\,s\,m^{-1}}$ and $c = 1\,500\,\mathrm{N\,mm^{-1}}$

References

[1] Al-Bender, F., Air bearings: Theory, design and applications, John Wiley & Sons, 2021. https://doi.org/10.1002/9781118926444

[2] Arghir, M., Benchekroun, O., A new structural bump foil model with application from start-up to full operating conditions, Journal of Engineering for Gas Turbines and Power 141 (10) (2019) 1–12. https://doi.org/10.1115/1.4044685

[3] Arghir, M., Benchekroun, O., A simplified structural model of bump-type foil bearings based on contact mechanics including gaps, Tribology International 134 (2019) 129–144. https://doi.org/10.1016/j.triboint.2019.01.038

[4] Balducchi, F., Arghir, M., Gauthier, R., Experimental analysis of the unbalance response of rigid rotors supported on aerodynamic foil bearings, Journal of Vibration and Acoustics 137 (6) (2015) 1–11. https://doi.org/10.1115/1.4031409

[5] Bättig, P., Schiffmann, J., Unstable tilting motion of flexibly supported gas bearing bushings, Mechanical Systems and Signal Processing 162 (2022) 1–17. https://doi.org/10.1016/j.ymssp.2021.107981

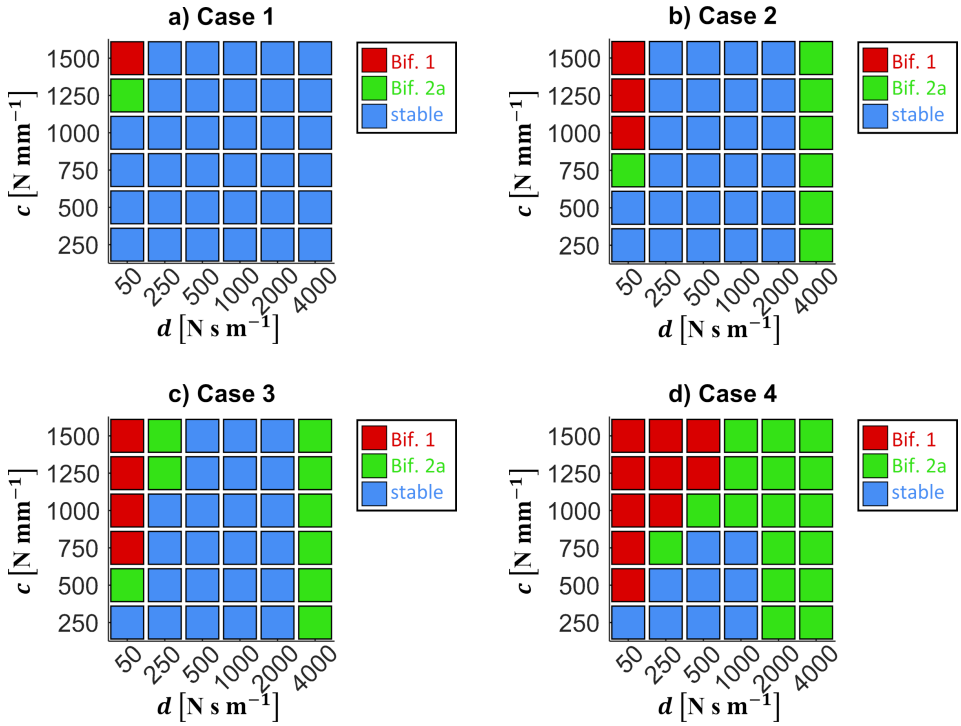

Fig. 17. Bifurcation maps. Influence of the damping and stiffness coefficients d and c on the bifurcation behavior of the system: (a) case 1, (b) case 2, (c) case 3, (d) case 4

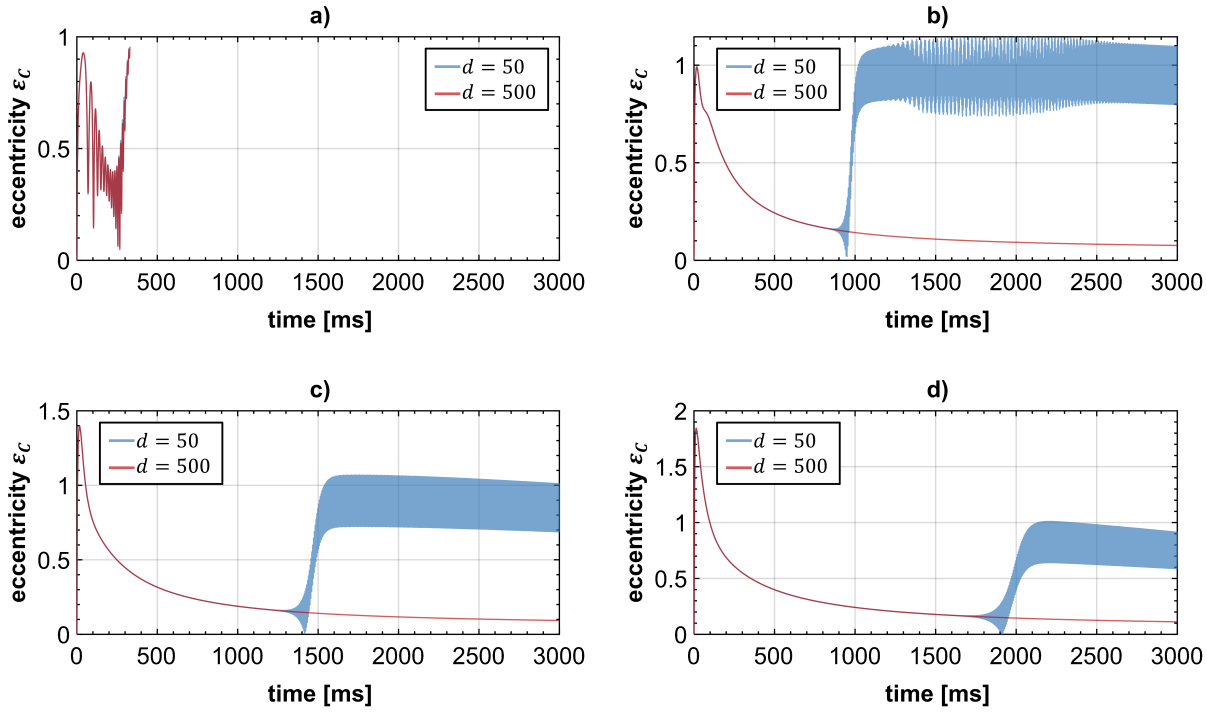

Fig. 18. Case study on different step heights ΔH with $C = 15\,\mu$m, $c = 1\,000\,\mathrm{N\,mm^{-1}}$, compressor-side dimensionless bearing eccentricity $\varepsilon_C(t)$ with: (a) $\Delta H = 0\,\mu$m, (b) $\Delta H = 15\,\mu$m, (c) $\Delta H = 30\,\mu$m, (d) $\Delta H = 45\,\mu$m

[6] Bättig, P. K., Wagner, P. H., Schiffmann, J. A., Experimental investigation of enhanced grooves for herringbone grooved journal bearings, Journal of Tribology 144 (9) (2022) 1–12. https://doi.org/10.1115/1.4053978

[7] Bonello, P., Bin Hassan, M. F., An experimental and theoretical analysis of a foil-air bearing rotor system, Journal of Sound and Vibration 413 (2018) 395–420. https://doi.org/10.1016/j.jsv.2017.10.036

[8] Dobrica, M. B., Fillon, M., Mixed lubrication, In: Encyclopedia of tribology, (eds) Q. J. Wang, Y.-W. Chung, Boston, Springer, 2013. https://doi.org/10.1007/978-0-387-92897-5_27

[9] Feng, K., Zhao, X., Guo, Z., Design and structural performance measurements of a novel multi-cantilever foil bearing, Proceedings of the Institution of Mechanical Engineers, Part C: Journal of Mechanical Engineering Science 229 (10) (2015) 1830–1838. https://doi.org/10.1177/0954406214547529

[10] Fleming, D. P., Hamrock, B. J., Optimization of self-acting herringbone journal bearing for maximum stability, NASA Technical Note D-6351, Washington, 1973.

[11] Gear, C. W., Gupta, G. K., Leimkuhler, B. J., Automatic integration of the Euler-Lagrange equations with constraints, Journal of Computational and Applied Mathematics 12–13 (1985) 77–90. https://doi.org/10.1016/0377-0427(85)90008-1

[12] Gomes, C., Thule, C., Broman, D., Larsen, P. G., Vangheluwe, H., Co-simulation: A survey, ACM Computing Surveys 51 (3) (2018) 1–33. https://doi.org/10.1145/3179993

[13] Gu, L., Guenat, E., Schiffmann, J., A review of grooved dynamic gas bearings, Applied Mechanics Reviews 72 (2020) 1–15. https://doi.org/10.1115/1.4044191

[14] Haug, E. J., Computer-aided kinematics and dynamics of mechanical systems, Allyn and Bacon, Boston, 1989.

[15] Heshmat, H., Shapiro, W., Gray, S., Development of foil journal bearings for high load capacity and high speed whirl stability, Journal of Lubrication Technology 104 (2) (1982) 149–156. https://doi.org/10.1115/1.3253173

[16] Hoffmann, R., Liebich, R., Characterisation and calculation of nonlinear vibrations in gas foil bearing systems–An experimental and numerical investigation, Journal of Sound and Vibration 412 (2018) 389–409. https://doi.org/10.1016/j.jsv.2017.09.040

[17] Iseli, E., Schiffmann, J., Stability and unbalance analysis of rigid rotors supported by spiral groove bearings: Comparison of different approaches, Journal of Engineering for Gas Turbines and Power 143 (12) (2021) 1–12. https://doi.org/10.1115/1.4052025

[18] Khonsari, M. M., Booser, E. R., Applied tribology: Bearing design and lubrication, John Wiley & Sons, 2008. https://doi.org/10.1002/9780470059456

[19] Larsen, J. S., Santos, I. F., On the nonlinear steady-state response of rigid rotors supported by air foil bearings–Theory and experiments, Journal of Sound and Vibration 346 (2015) 284–297. https://doi.org/10.1016/j.jsv.2015.02.017

[20] Mahner, M., Bauer, M., Lehn, A., Schweizer, B., An experimental investigation on the influence of an assembly preload on the hysteresis, the drag torque, the lift-off speed and the thermal behavior of three-pad air foil journal bearings, Tribology International 137 (2019) 113–126. https://doi.org/10.1016/j.triboint.2019.02.026

[21] Mahner, M., Bauer, M., Schweizer, B., Numerical analyzes and experimental investigations on the fully-coupled thermo-elasto-gasdynamic behavior of air foil journal bearings, Mechanical Systems and Signal Processing 149 (2021) 1–32. https://doi.org/10.1016/j.ymssp.2020.107221

[22] Mahner, M., Li, P., Lehn, A., Schweizer, B., Numerical and experimental investigations on preload effects in air foil journal bearings, Journal of Engineering for Gas Turbines and Power 140 (3) (2018) 1–9. https://doi.org/10.1115/1.4037965

[23] Malanoski, S. B., Experiments on an ultrastable gas journal bearing, Journal of Lubrication Technology 89 (4) (1967) 433–438. https://doi.org/10.1115/1.3617021

[24] Meyer, T., Kraft, J., Schweizer, B., Co-simulation: Error estimation and macro-step size control, Journal of Computational and Nonlinear Dynamics 16 (4) (2021) 1–26. https://doi.org/10.1115/1.4048944

[25] Michel, H., Liebich, R., Challenges in validating a thermo-hydrodynamic gas foil bearing model, Journal of Engineering for Gas Turbines and Power 143 (4) (2021) 1–13. https://doi.org/10.1115/1.4047769

[26] Miyanaga, N., Tomioka, J., Effect of support stiffness and damping on stability characteristics of herring-bone-grooved aerodynamic journal bearings mounted on viscoelastic supports, Tribology International 100 (2016) 195–203. https://doi.org/10.1016/j.triboint.2016.01.019

[27] Papafragkos, P., Gavalas, I., Raptopoulos, I., Chasalevris, A., Optimizing energy dissipation in gas foil bearings to eliminate bifurcations of limit cycles in unbalanced rotor systems, Nonlinear Dynamics 111 (2023) 67–95. https://doi.org/10.1007/s11071-022-07837-1

[28] Samanta, P., Murmu, N. C., Khonsari, M. M., The evolution of foil bearing technology, Tribology International 135 (2019) 305–323. https://doi.org/10.1016/j.triboint.2019.03.021

[29] San Andrés, L., Chirathadam, T. A., A metal mesh foil bearing and a bump-type foil bearing: Comparison of performance for two similar size gas bearings, Journal of Engineering for Gas Turbines and Power 134 (10) (2012) 1–13. https://doi.org/10.1115/1.4007061

[30] San Andrés, L., Kim, T. H., Thermohydrodynamic analysis of bump type gas foil bearings: A model anchored to test data, Journal of Engineering for Gas Turbines and Power 132 (4) (2010) 1–10. https://doi.org/10.1115/1.3159386

[31] Schweizer, B., Lu, D., Semi-implicit co-simulation approach for solver coupling, Archive of Applied Mechanics 84 (12) (2014) 1739–1769. https://doi.org/10.1007/s00419-014-0883-5

[32] Shabana, A. A., Dynamics of multibody systems, Cambridge University Press, 2005. https://doi.org/10.1017/CBO9780511610523

[33] Simeon, B., Computational flexible multibody dynamics: A differential-algebraic approach, Springer Berlin, Heidelberg, 2013. https://doi.org/10.1007/978-3-642-35158-7

[34] Somaya, K., Okubo, K., Miyatake, M., Yoshimoto, S., Threshold speed of instability of a herringbone-grooved rigid rotor with a bearing bush flexibly supported by straight spring wires, Proceedings of the ASME Turbo Expo 2015: Turbine Technical Conference and Exposition Volume 7A: Structures and Dynamics, Montreal, ASME, 2015, pp. 1–9. https://doi.org/10.1115/GT2015-43161

[35] Song, J.-H., Kim, D., Foil gas bearing with compression springs: Analyses and experiments, Journal of Tribology 129 (3) (2007) 628–639. https://doi.org/10.1115/1.2736455

[36] Swanson, E. E., Shawn O'Meara, P., The wing foil: A novel compliant radial foil bearing design, Journal of Engineering for Gas Turbines and Power 140 (8) (2018) 1–7. https://doi.org/10.1115/1.4038366

[37] Szeri, A. Z., Fluid film lubrication: Theory and design, Cambridge University Press, 2005.

[38] Tatara, A., Koike, H., Iwasaki, A., The stability of flexibly supported, externally pressurized gas journal bearings: Case of a rigid rotor, Bulletin of JSME 16 (100) (1973) 1573–1579. https://doi.org/10.1299/jsme1958.16.1573

[39] Vohr, J. H., Chow, C. Y., Characteristics of herringbone-grooved, gas-lubricated journal bearings, Journal of Basic Engineering 87 (3) (1965) 568–576. https://doi.org/10.1115/1.3650607

[40] Waumans, T., Peirs, J., Al-Bender, F., Reynaerts, D., Aerodynamic journal bearing with a flexible, damped support operating at 7.2 million DN, Journal of Micromechanics and Microengineering 21 (2011) 1–12. https://doi.org/10.1088/0960-1317/21/10/104014

[41] Zeise, P., Schweizer, B., Dynamics, stability and bifurcation analysis of rotors in air ring bearings, Journal of Sound and Vibration 521 (2022) 1–35. https://doi.org/10.1016/j.jsv.2021.116392